Proximity of Metal and Acid Sites in Bifunctional Catalysts for the Conversion of Hydrocarbons

ISBN: 978-94-6416-597-5
Cover design by Isabelle Cornet, www.isabellecornet.com
Printed by Ridderprint, www.ridderprint.nl

Proximity of Metal and Acid Sites in Bifunctional Catalysts for the Conversion of Hydrocarbons

Nabijheid van Metallische en Zure Plaatsen in Bifunctionele Katalysatoren voor de Omzetting van Koolwaterstoffen

(met een samenvatting in het Nederlands)

Proefschrift

ter verkrijging van de graad van doctor aan de Universiteit Utrecht
op gezag van de rector magnificus, prof. dr. H.R.B.M. Kummeling,
ingevolge het besluit van het college voor promoties in het openbaar te
verdedigen op

woensdag 16 juni 2021
des middags te 2.15 uur

door

Jogchum Oenema
geboren op 26 september 1991
te Groningen

Promotor: Prof. dr. ir. K.P. de Jong

Dit proefschrift werd mede mogelijk gemaakt met financiële steun van de European Research Council (ERC) in het kader van het 7th Framework Programme for Research, ERC Advanced Grant no. 338846.

Table of Contents

Chapter 1

Introduction

1.1 Heterogeneous catalysis

A catalyst is defined as a substance that accelerates a chemical reaction without being consumed.[1] The use and applications of catalysts are widespread; 85 to 90% of all products of the chemical industry are made in catalytic processes, according to recent estimates.[2] Catalysts are also used to abate emissions of harmful gasses or for the production of food and pharmaceuticals.

A catalyst accelerates a chemical reaction by lowering the activation energy with respect to the uncatalyzed reaction by offering an alternative and more energetically favorable route for a chemical reaction. This implies that the catalytic material needs to be in close contact with the reacting molecules. Catalysts allow processes to take place under milder conditions while at the same time, by not catalyzing side reactions, the selectivity towards desired products can be increased. Use of a catalysts can therefore be highly beneficial for the energy efficiency of a process, while simultaneously the amount of produced waste can be lowered. Catalysts that are in a different phase than the reactants and products are known as heterogeneous catalyst. For the majority of processes in the chemical industry solid catalysts are used, while the reactants and products are in the liquid or gas phase. A major reason for the wide application of solid catalysts is that they are relatively easy to handle and are easily separated from the products.[3]

1.2 Role of catalysis in energy conversion

From the start of the industrial revolution (2nd half of the 18th century), the developments in technology, population growth and increasing life-quality standards resulted in a steady increase in the global energy demand. Due to the continuing economic growth, especially in emerging countries, the energy demand is expected to grow further in upcoming decades.[4] At present, the energy demands are largely fulfilled by usage of fossil recourses, i.e., coal, natural gas and crude oil, as can be inferred from Figure 1.1. The increasing use of these carbon based energy resources, that accelerated during the industrial revolution, has resulted in increased CO_2 emissions resulting

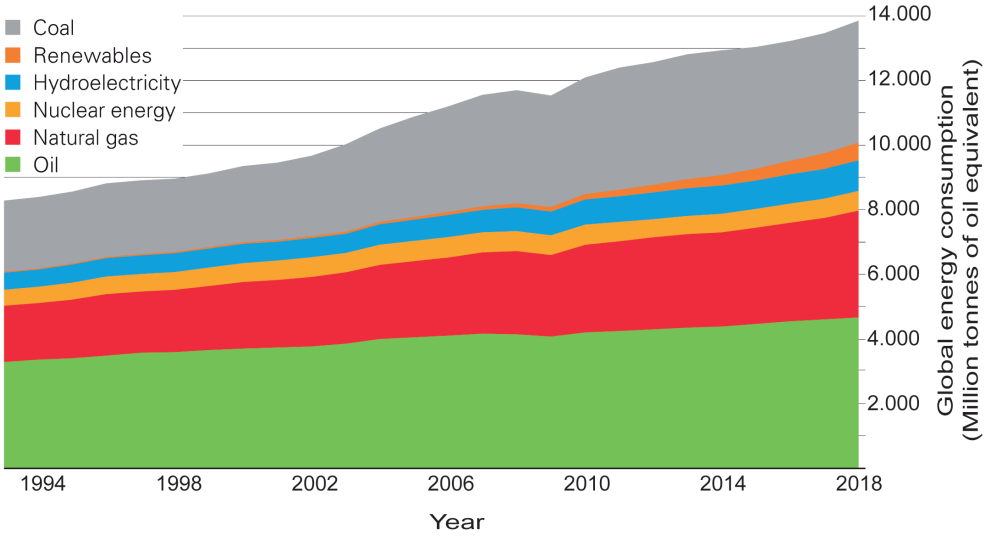

Figure 1.1. Global energy consumption during the period 1994 to 2018 in million tons of oil equivalent. The equivalents of coal, renewables, hydroelectricity, nuclear energy, natural gas and oil are shown. Image adopted from reference [4].

in increased CO_2 concentrations in the atmosphere, that lead to climate change. In the 2015 Paris agreement, many major industrial countries agreed to impose restrictions on CO_2 emissions, in order to remain below a rise of 2 °C in average global temperature.[5] The efficient use of the finite reserves of fossil resources, that also become increasingly difficult to mine, is therefore highly desired.[6,7]

Reduction of CO_2 emissions should result from using renewable forms of energy (hydro, wind, sun, biomass, ect.), but the transition from fossil towards renewable forms of energy comes with hurdles such as intermittency challenges and high costs of new technologies. In 2019 the fraction of renewable energy (including hydroelectricity) constituted about 11% of the global energy consumption, and this percentage is expected to grow in the upcoming years.[8] The ongoing research and development continues to make renewable forms of energy more applicable and it is foreseen that catalysis will a play crucial role in this respect.[9] Despite the foreseen growth of alternative and renewable energy sources, oil and gas are foreseen to remain crucial energy providers for upcoming decades to be able to meet a growing global energy demand.[9]

The transport sector is responsible for 23% of global CO_2 emissions and according to recent estimates is lagging behind in the reduction of CO_2 emissions.[10] The use of liquid fuels for transportation is favored because of their high energy density, ease of handling and well-established production and delivery infrastructure.[9] Especially for truck transport over long distances and aviation, there are currently no good replacements for liquid fuels as energy carrier.[10–12] Synthetic liquid fuels are a promising alternative to oil-based fuels and these can be produced from various carbon containing feedstocks, such as coal, natural gas and biomass. The carbon feedstocks are converted into synthesis gas ($CO+H_2$), which is subsequently converted to hydrocarbons through the Fischer-Tropsch process.[13] The environmental benefit of synthetic fuels mostly depends on the feedstock and overall process efficiency.

Alternatively, liquid fuels can also be made 'directly' from biomass resources, without gasification, often referred to as 'biofuels'.[14–16] The advantage of this method is that it is less energy intensive than Fischer-Tropsch processes, but the product selectivity is limited and dependent on the feedstock that is used. Crops such as rapeseed, sunflower or corn grain and sugarcane are relatively easy to convert into biodiesel or bioethanol, that form the so-called first generation biofuels. However these fuels are controversial because they compete with (land use for) food supplies.[16] The second and third generations biofuels are based on non-edible feedstocks such as lignocellulosic biomass, waste oils or algae. Due to the higher structural complexity of these feedstocks and presence of impurities, they are generally more difficult to convert into fuels and thus require more intensive processing.[17]

Products from Fischer-Tropsch processes or feedstocks for second generation biofuels, generally have a too high molecular weight to be used as liquid fuels. Cracking and upgrading processes are required to decompose the large and heavy hydrocarbon molecules towards smaller ones. For the conversion of crude oil towards liquid fuels and chemicals, processes for hydrocarbon cracking and upgrading over solid catalysts are well-established. Examples of such processes are Fluid Catalytic Cracking that convert approximately 14.5 million barrels of feedstock from crude oil every day, and is applied in over 300 refineries worldwide, or Hydrocracking processes that convert approximately 5.6 million barrels per day in at least 170 refineries.[18]

1.3 Brief history of catalytic processes for the production of liquid fuels

In the beginning of the 20th century liquid fuels, such as gasoline, were mostly produced by distillation and thermal cracking of crude oil.[19,20] Increasing demands for transportation fuels, stimulated the development of the first catalytic cracking processes, that were initiated in the 1920s by Eugene Houdry in the United States.[21] These processes were based on a catalyst consisting of aluminosilicate clay that was significantly better performing than the thermal cracking processes, both in energy efficiency as well as higher octane ratings of the produced gasoline. The latter implied that higher compression ratios could be used for internal combustion engines, which increased their efficiency and performance. During the Second World War, catalytic cracking processes were intensively used to produce high-octane jet fuel for the Allied forces, thereby providing a major strategic advantage.[20]

Further developments in catalytic cracking after the Second World War led to the introduction of zeolite based catalysts.[22] Natural forms of zeolites were already discovered in 1756, by the mineralogist Axel Cronsted, who called them boiling stones ('zeo' and 'lithos' mean 'to boil' and 'a stone'), because he noticed that the mineral Stilbite appeared to boil when heated.[23] The potential for zeolites to be used as catalysts was firstly recognized by Richard M. Barrer in England and researchers at the Union Carbide Corporation in the United states. Between the 1930s up to 1960s, they reported a number of crucial studies on preparation of synthetic zeolites, adsorption properties of zeolites and catalysis, that resulted in the application of zeolites in industrial purification, separation and catalytic processes.[24–26] In the years that followed, research in zeolite based catalysts intensified, resulting in discovery of many new zeolite compositions and structures, while various large-scale zeolite based industrial processes were initiated.[18,27]

1.4 Structure and porosity of zeolite based catalysts

For porous materials, three types of porosity are classified: macropores (>50 nm in diameter), mesopores (2-50 nm) and micropores (<2 nm).[28] In principle, it is preferable to prepare solid catalysts with high porosities and with high specific surface areas (surface area per gram of material) to maximize the number of catalytically active sites that can be accommodated, thereby maximizing catalytic activity. For zeolites however, a high number of active sites and a large specific surface area does not always result in optimal catalytic activity.

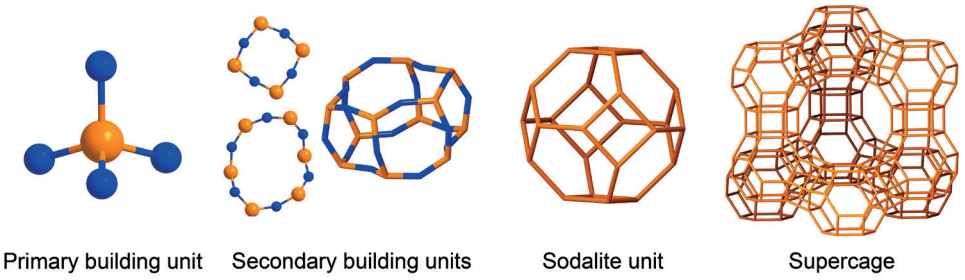

Figure 1.2. Building blocks of zeolites, showing a silica or alumina tetrahedra (primary building unit), a 4- and 6-ring, and a hexagonal prism (secondary building units). The sodalite cage and super cage are larger building units of the faujasite framework, sometimes referred to as tertiary building units. Silicon or aluminum atoms are indicated in orange while oxygen atoms are indicated in blue. Images of the Hexagonal prism, the Sodalite unit and the Supercage were derived from 3D drawings from the IZA-SC Database of Zeolite Structures.[30]

Zeolites are defined as microporous crystalline aluminosilicate materials consisting of silica and alumina tetrahedra connected by shared oxygen atoms.[29] The tetrahedra are also referred to as primary building units and can connect in a number of different fashions resulting in a variety of structures known as secondary or tertiary building blocks of a zeolite. Examples of primary and secondary building blocks are indicated in Figure 1.2, along with the larger sodalite and supercage units that constitute of the faujasite framework. Because every framework has unique properties, new frameworks are actively sought after and regularly reported. To date, there are 248 known zeolite structures according to the International Zeolite Association, of which 67 are naturally occurring.[30]

In a zeolite crystal, the aluminum atoms are in the same position as silicon atoms while having a lower valency, resulting in a negative charge that is compensated by a cation, typically an alkali metal cation or a proton. The latter introduces a Brønsted acidic catalytic site to the zeolite framework. Such acidic protons are often obtained from ion exchange with ammonium ions followed by calcination.[31] The number of zeolite acid sites is inversely proportional to Si/Al ratio of the framework, but zeolites with low Si/Al are not always the most active catalysts. For example, for zeolite Y it has been found that framework aluminum atoms that are in close vicinity with each other lead to weak acid sites compared to isolated sites, resulting in an optimum in Si/Al ratio for catalytic activity.[32]

The size of the micropores is indicated by the number of tetrahedral atoms (T-atoms) in the ring opening of the pores and is used to divide zeolites in subclasses. The most relevant zeolites for catalysis have micropores of either of ten or twelve membered rings that might be present in one, two or three dimensions throughout the crystal. Furthermore, micropores may have a different pore tortuosity, e.g. straight or sinusoidal. Since the size of micropores approaches the size of molecules, zeolites are sometimes referred to as molecular sieves. The most widely applied zeolites in industry, are also known as 'the big five', namely: Ferrierite, ZSM-5, Zeolite Beta, Mordenite and Zeolite Y.[18] The properties of these zeolites are indicated in Table 1.1.

For an optimally functioning catalyst, products and reactants need to be able to diffuse 'freely' towards and from active sites. However, due to the microporous nature of zeolites, diffusion limitations may arise, especially for larger hydrocarbon molecules present in heavier crude

Table 1.1. Characteristics of the five most significant zeolites for industrial applications. Pore size, ring size and pore dimensionality were obtained from the IZA-SC Database of Zeolite structures.[30]

Zeolite	Pore size (nm)[a]	Ring size (#)[a]	Pore dimensionality[b]	Applications
Ferrierite	0.54 × 0.42	10	1	Alkene isomerization
ZSM-5	0.56 × 0.53	10	3	Fluid catalytic cracking, Methanol to hydrocarbons
Zeolite Beta	0.66 × 0.67	12	3	Cumene production, acylation
Mordenite	0.70 × 0.65	12	1	Hydroisomerization
Zeolite Y	0.74 × 0.74	12	3	Fluid catalytic cracking, Hydrocracking

a) Size of the largest micropores are provided.
b) Dimensionality of the largest micropore network of a zeolite.

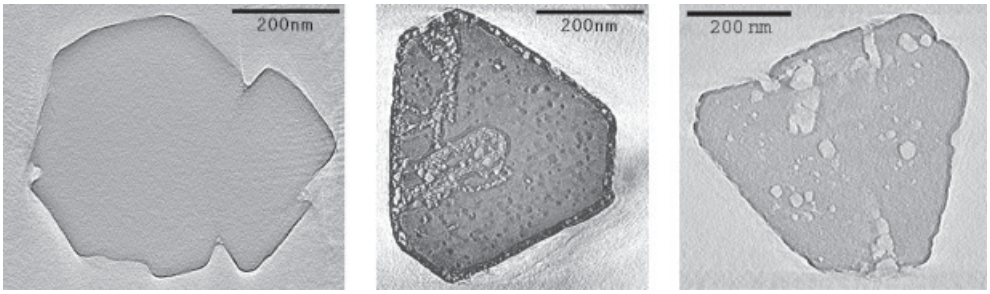

Figure 1.3. Reconstructed images from electron tomography (3D-TEM) of a parent Na-Y crystal (left), a steamed H-Y crystal with extra-framework alumina present as, amongst others, a dark layer around the zeolite crystal (middle) and a mesoporous Zeolite Y crystal after an acid leaching treatment (right). Reprinted with permission from ref [42]. Copyright 2001 Wiley-VHC.

oil or Fischer-Tropsch product fractions. These intracrystalline diffusion limitations may lead to suboptimal catalytic activity and secondary cracking reactions towards undesired lighter hydrocarbons. In order to improve the diffusive transport of molecules through zeolite crystals, nanosized zeolite crystals have been developed to shorten the effective micropore length. These efforts have resulted in the synthesis of zeolite nanosheets[33], self-pillared zeolite nanosheets[34,35], delaminated zeolites[36] or finned zeolite crystals.[37] Also attempts have been made to synthesize new zeolite frameworks with larger micropores, with 14 or more T-atoms, although the success of this approach has been somewhat limited.[38]

Another way for alleviating diffusion limitations in zeolite crystals, is by introduction of a secondary pore system in relatively large zeolite crystals, typically up to 1 micrometer. Mesoporosity throughout a zeolite crystal can be either created directly during zeolite crystallization while using a template, or by performing post treatments on large zeolites crystals, such as steaming, acid or base leaching procedures.[39–41] The advantage of the acid leaching approach is that the procedure is relatively simple and can be easily applied at larger scales for the production of industrial catalysts. In Figure 1.3, electron tomography images are provided of zeolite Y crystals before (left) and after a steam treatment (middle), with subsequent acid leaching (right). By steaming zeolites crystallites, i.e., by exposing zeolites to water vapor at >500 °C, aluminum is extracted from the framework resulting in extra-framework alumina species. By performing a subsequent acid leaching treatment, this extra-framework alumina is removed, resulting in empty mesopores throughout the crystal.[42] Alternatively, by performing a base leaching procedure, silicon is removed from the framework, although this was only shown to work for zeolites with high Si/Al ratios and leads to rather broad pore size distributions.[43] Combinations of acid and base leaching have been successfully used for the synthesis of an so-called trimodal porosity in zeolite Y.[44]

For industrial processes, zeolite powders are relatively hard to handle and mostly require shaping into catalysts bodies. To provide mechanical strength to the catalysts body, a binder material (alumina, silica-alumina or clay) is used that allows shaping into macroscopic structures such as: fluidizable spheres, extrudates, pellets or monoliths. The choice of structure and composition depends mostly on type of reactor that is used and should be optimized for the process conditions,

thereby avoiding pressure drops, mass-transfer and heat-transfer limitations, attrition or sintering. For the preparation of extrudates, the right use of additives (peptizers, plasticizers ect.) and extrusion pressure may impact the porosity of the final extrudates.[45,46] Although the influence of shaping on zeolites as catalysts or adsorbers is often left aside in academic research, a number of studies have indicated that shaping may crucially impact mass transfer and adsorption characteristics of zeolite based catalysts.[47–50]

1.5 Adsorption and diffusion in zeolite based catalyst

The success of zeolites in adsorption, separation and catalysis results mainly from their unique adsorptive and diffusional properties. Because zeolite micropores have a well-defined size, they can be used to selectively adsorb certain molecules from mixtures, a property that is widely used in purification processes. Upon zeolite micropore filling, molecules can be adsorbed relatively strongly and already at low partial pressures. The strength of adsorption in micropores is largely determined by the interaction of the adsorbate with the micropore wall.[51,52] Selective adsorption of molecules by zeolites may be based on differences in adsorption equilibrium between adsorbates (Henry Coefficient) or differences in adsorption rates.[53,54] At higher partial pressures, micropores become fully saturated and adsorbates may be adsorbed in mesopores by capillary forces or at the outer surface, where in both cases the strength of adsorption is generally weaker.[54]

The strength of adsorption (adsorption enthalpy) is studied in experiments whereby the surface coverage (determined directly or indirectly) is monitored as function of temperature. The determination of the specific adsorptive properties of zeolites has been the topic of a large number of experimental and computational research efforts.[55] For example, the presence of aluminum atoms in a siliceous framework leads to a polar and hydrophilic zeolite, while all-silica zeolites are hydrophobic and therefore adsorb preferentially non-polar compounds such as hydrocarbons.[56] Also modifications made to the zeolite can impact the adsorption properties, such as cations that can have a favorable interaction with the adsorbate thereby strengthening adsorption or conversely, block adsorption sites and hampering adsorption.[55]

To determine the accessibility of micropores, a number of methodologies were developed. Breck et al. proposed the concept of the kinetic diameter of molecules, which can be compared with the dimensions a micropore.[57] It provides a relatively crude method to assess if a molecule fits inside a zeolite micropore, since it is assumed that the molecule is spherical and non-polarizable. In order to account for the shape of a molecule, the so-called molecular footprint was proposed, which is a two dimensional projection of the smallest area of a molecule.[58,59] Better approximations can be made with molecular simulations techniques that also include the strain of a molecule in a micropore and the strain within the zeolite framework.[55,60]

Experimental assessments of the accessibility and characterization of the pore space of zeolite frameworks are provided by constraint indexes that can be evaluated during test reactions. This method relies on the ratio of cracking rate between *n*-hexane and 3-methylpentane or the ratio of formation of branched isomers of decane, and are most suitable for 10 membered ring zeolites.[60–64] To characterize 12 membered ring zeolites, the so-called Spaciousness Index was developed. The index is determined by the ratio of *i*-butane to *n*-butane from the cracking of a relatively large

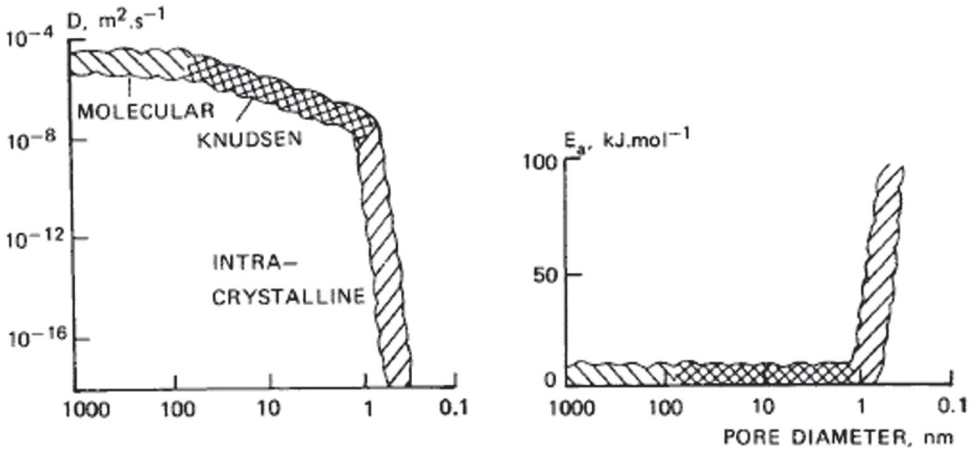

Figure 1.4. Showing the approximate diffusion coefficient and its activation energy as a function of pore diameter in nanometers, in different diffusion regimes. Reprinted with permission from reference [65]. Copyright 2001 Elsevier Science B.V.

molecule: butylcyclohexane.[60] Energetically favorable carbocation cracking reactions (β-scission, Type A) lead solely to the formation of *i*-butane and methylcyclopentane, while less favourable cracking reactions lead to the formation of a broader variety of cracking products. For zeolite Y the Spaciousness Index is typically higher than 20, while for zeolite Beta it is around 18. For 10 membered ring zeolites usually a Spaciousness Index of around 1 is observed.

The diffusivity of molecules within zeolites is indicatively described by Fick's laws, where concentration gradients (or gradients in chemical potential) are the driving force for transport of molecules.[53] The different diffusion regimes that are relevant for zeolite based catalysis are schematically indicated in Figure 1.4. In the molecular diffusion regime molecules move relatively freely and collide only with other molecules. Upon transitioning to the Knudsen diffusion regime, representative for molecules in mesopores, the diffusion coefficient starts to be influenced by the confinement of the pore. In the intra-crystalline regime, representative for molecules in micropores, the molecules are closely surrounded by the pore system, greatly slowing down diffusion. In this regime, sometimes referred to as configurational diffusion, interactions (e.g. van der Waals) between the adsorbate and the micropore wall become dominant. If the size of the diffusing molecule closely approaches the size of the micropore, diffusion may become an activated process due to steric hindrance.[53,65] The exact diffusion coefficient of a molecule in a micropore is very sensitive for the micropore size and even slight changes in shape of molecules, may lead to differences in diffusion coefficients of several orders of magnitude.

Intracrystalline diffusion in zeolites has been studied extensively over the last decades by techniques as: pulsed field gradient nuclear magnetic resonance (PFG-NMR)[66], uptake rate measurements (e.g. combined with a tapered element oscillating microbalance)[67,68], positron emission profiling[69,70], and infrared or interference microscopy[71,72]. Computational studies have also focused on diffusion in zeolite micropores, either by establishment of a microkinetic-model of a catalytic process[73,74], or by molecular modeling using: (dynamically corrected) transition state theory[75], monte carlo simulations[76–78] or molecular dynamics[79]. If the size of the molecules

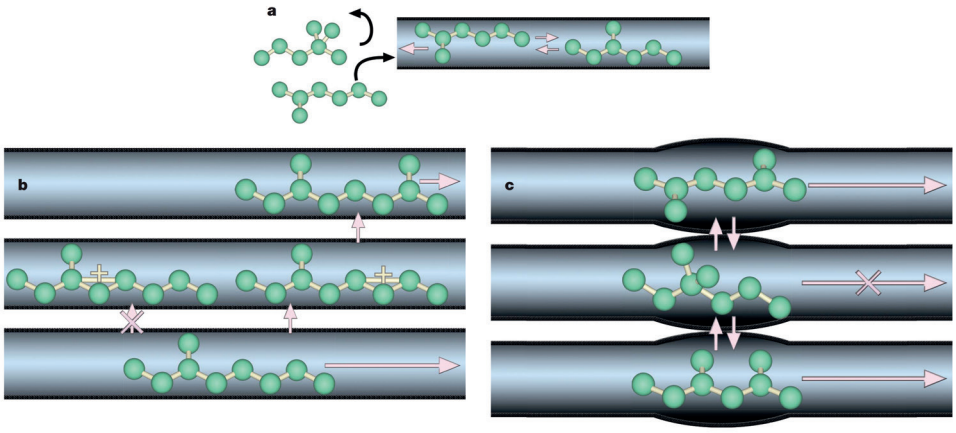

Figure 1.5. Schematic representation of heptane molecules subjected to reactant shape selectivity (a), transition state shape selectivity (b) or product shape selectivity (c). Reprinted with permission from reference [88]. Copyright 2008 Springer Nature.

approaches the size of the cages or channels of the zeolite, a number of phenomena can occur such as resonance diffusion, single-file diffusion, shape selectivity and pore mouth catalysis.

For resonance diffusion, also known as the window effect, the diffusion coefficient of a linear hydrocarbon increases as a function of chain length, while a decreasing trend would be expected since more carbon atoms have to cross the micropore channel.[80,81] This finding is commonly rationalized by a so-called Frenkel-Kontorova model that states that when hydrocarbons in pores absorb in a way that is commensurate with the substrate structure, the barrier for desorption is high resulting in a low diffusion coefficient.[55] If, on the other hand, the adsorption is incommensurate with the substrate structure, this results in a high diffusion coefficient.

Single-File diffusion occurs when molecules in a non-intersecting and small micropore cannot pass each other, and the displacement of a molecule becomes dependent on the displacement of its neighbors, i.e. molecules diffuse through a pore like pearls on a string.[82,83] Therefore, Fick's laws of diffusion do no longer apply and lower diffusion coefficients are obtained. The concept of Single-File diffusion has been proven a number of times both by experimental and computational studies for certain molecule-zeolite combinations.[84–87]

When the adsorption or reaction in a zeolite is directly influenced by the fitting of the molecule in the micropore, shape selectivity effects may arise.[64,88] There are three classes of shape-selectivity, schematically indicated in Figure 1.5. Reactant shape selectivity is based on the ability of a reactant molecule to enter a micropore, while product shape selectivity is based on hindered diffusion of products through the zeolite micropore that prevent or suppress the formation of certain products. Transition state shape selectivity is based on the fact that certain transition states are too large to fit inside a micropore, and therefore the formation of certain products is prevented. In many cases shape selectivity effects have been well established.

In pore mouth catalysis, and the related key-lock catalysis, molecules are partially entering a micropore located at the external surface of a zeolite and subsequently react at acid sites located in the pore mouth. This principle was firstly proposed to rationalize the product distribution for

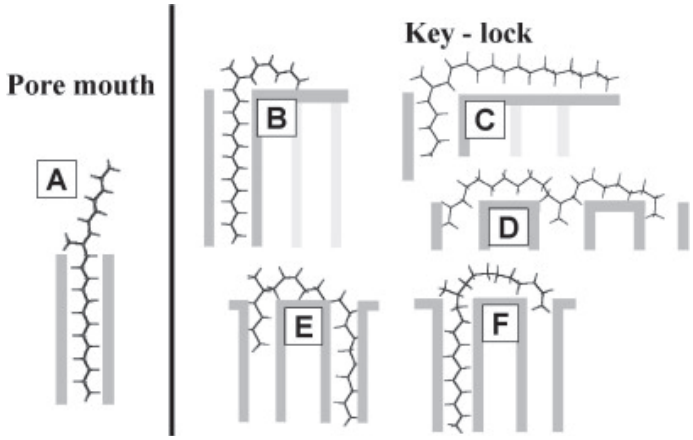

Figure 1.6. Pore mouth (A) and key-lock adsorption configurations (B-F) of long-chain alkanes, as proposed by Martens et al for ZSM-22. Reprinted with permission from ref [91]. Copyright 2001 Elsevier Science B.V.

long-chain hydrocarbons formed on ZSM-22, a 10 membered ring zeolite with a 1 dimensional pore system.[89] For long-chain *n*-alkanes ($>C_{10}$) it was observed that on ZSM-22, in contrary to Zeolite Y, methyl branching at the terminal positions (e.g. 2-methylhexadecane) was strongly favored over internal methyl branches.[90] For *n*-alkanes that have partially entered a micropore, as depicted in Figure 1.6A, the formed methyl branch eases desorption and diffusion out of the micropore. Please note that this anisotropy of the diffusion coefficient, i.e. that diffusion out of the pore is much faster than diffusion into the pore, is key to the understanding of the intimacy effect, which is discussed in more detail in section 1.7. For the conversion of $>C_{12}$ *n*-alkanes on ZSM-22, the preferred formation of isomers with spatially separated methyl branches was observed (e.g. 2,7-, 2,8-, 2,9-, 2,10- 2,11-dimethylpentadecanes), and was ascribed to a key-lock mechanism (Figure 1.6B-F). This involves the secondary isomerization of 2-methylalkenes by a reaction at an active site within a neighboring pore mouth, whereby the distance between the two methyl branches is controlled by the thickness of the micropore wall. Experimentally determined Henry constants of alkanes showed more negative values for *n*-alkanes than for branched alkanes[92,93], which was used as an argument in favor of the pore mouth mechanism.[91] Other variants of pore mouth mechanisms were proposed to rationalize the conversion of *n*-alkanes over small pore zeolites (8 membered ring)[94] where computational studies indicated that the molecules cannot enter the micropores, or for 10 membered ring zeolites for the conversion of large fatty acids[95,96].

There has been a considerable amount of debate in literature about the occurrence of pore mouth catalysis for ZSM-22 and long-chain *n*-alkanes. Studies based on molecular simulations have suggested that the contribution of the external surface to adsorption and catalysis on ZSM-22 is negligible.[94,97] Linear or dibranched alkanes were both able to fully enter micropores of ZSM-22 and the Henry coefficient inside the micropores was almost two orders of magnitude higher than on the external surface while the product distributions could be fully attributed to shape-selectivity. Further evidence was obtained from studies where the acid sites at the external surface of the zeolite were selectively poisoned which had no significant effects on catalysis.[98]

1.6 Multifunctional Catalysis

In a multifunctional catalysis two or more independent catalytic functions are combined within one catalytic particle. Depending on the field of research, multifunctional catalysis can also be referred to as hybrid catalysis, or (orthogonal) tandem catalysis, whereby the latter is more common for the field of biomass conversion.[99–102] When a bifunctional catalysts are employed in batch reactors, it is often referred to as "one-pot tandem catalysis". Ideally, such processes lead to a reduction of the number of experimental steps, such as separation and purification of intermediates, with respect to consecutive processes over monofunctional catalysts. In turn, this leads to higher energy efficiencies of the overall process.[103] The terms domino or cascade catalysis usually refer to multistep processes occurring on catalysts with one type of site occurring sequentially, e.g. multiple hydrogenation reactions on the same molecule.[100] These processes are therefore mechanistically distinct from bifunctional catalysis.

For multifunctional catalysts, all catalytic sites should provide catalytic activity at the same conditions, while the active sites have to be compatible with one another and with the involved species: reactants, intermediates, products, solvents, additives.[99,104] For enzyme catalysts, multifunctionality beyond two types of sites is common, due to well-isolated active sites that have good substrate selectivity. For solid catalysts however, the number of studies on catalysts with three or more distinct sites is rather limited. An example of a trifunctional catalysts is an acid-base-metal catalysts for aldol condensation of aldehydes and ketones, followed by dehydration and subsequent hydrogenation. An hydrotalcite support (MgAlO) supplies both the basic sites and acid sites, and catalyzes the aldol condensation by hydrogen abstraction on a basic site followed by dehydration catalyzed by an acid site.[105,106] Subsequent hydrogenation is catalyzed by a metal site (Ni or Pd), as illustrated in Figure 1.7.

Bifunctional catalysts for the conversion of synthesis gas ($CO + H_2$) have increased in popularity in scientific research, mostly due to the favorable product selectivities bifunctional catalyst may provide with respect to monofunctional catalysts. The catalysts for synthesis gas conversion generally consist of a combination of a metal and an acid functionality. The formation of gasoline-range hydrocarbons has been reported over cobalt based Fischer-Tropsch catalysts combined with ZSM-5 zeolite[107], whereas the production of aromatics and short chain alkenes was observed over iron based Fischer-Tropsch catalysts and ZSM-5.[108] Other forms of bifunctional catalysts are based on silico-aluminophosphates (SAPO's) combined with metal-oxide functions for the production of short chain alkenes[109,110] or a combination of a methanol synthesis catalyst and acidic metal-oxides to produce dimethyl ether[111]. Bifunctional catalysts are also employed for the direct conversion of CO_2 towards hydrocarbons.[112,113]

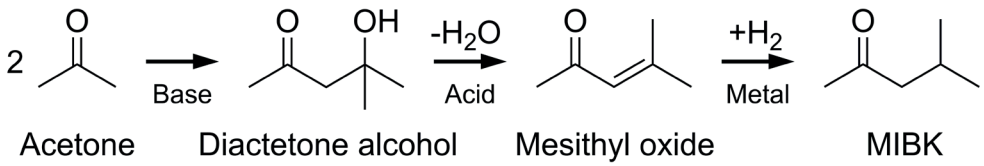

Figure 1.7. Aldol condensation of acetone catalyzed by a basic site followed by dehydration catalyzed by an acid site and hydrogenation on a metal site. Reaction sequence based on refs [105,106].

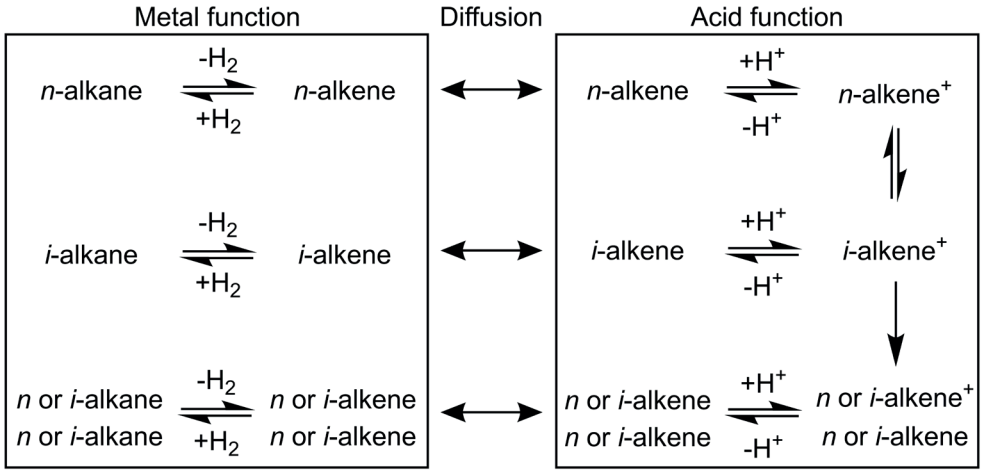

Figure 1.8. The classical bifunctional mechanism for the (de)hydrogenation isomerization and cracking of linear hydrocarbons (*n*-alkanes), whereby mostly branched hydrocarbons (*i*-alkanes) are formed as isomerization or cracking products. Reaction sequence based on refs [114,116].

Bifunctional metal-acid catalysts for the conversion of hydrocarbons are a relatively well-established class of bifunctional catalysts and these catalysts are widely used in industrial processes such as: hydroisomerization, hydrocracking, catalytic dewaxing and catalytic reforming processes.[18]

Although the composition of the catalysts and the reaction mechanisms may vary from process to process, generally, these bifunctional catalysts consist of a metal (sulfide) function catalyzing (de) hydrogenation and Brønsted acid sites catalyzing rearrangement and cracking. Hydrocracking catalysts are mostly based on an ultra-stabilized zeolite Y combined with sulfided forms of NiW, NiMo or CoMo that have average activity for (de)hydrogenation and have good resistance towards sulfur poisons. In absence of feed impurities, also noble metals such as Pt, Pd are used that exhibit superior (de)hydrogenation activity.[18,27] Especially for hydroisomerization processes where concentration of sulfur impurities in feedstocks are usually low, noble metals are used combined as metal function while Mordenite zeolites provide the acid function.

For hydrocracking and hydroisomerization processes, hydrogen is used both as reactant to saturate (cracked) hydrocarbons towards alkanes and to increase the catalysts lifetime by preventing the formation of coke species.[18,107] The isomerization and cracking of hydrocarbons is ascribed to the so-called classical bifunctional mechanism, indicated in Figure 1.8.[114] The first step in the reaction sequence is dehydrogenation of the alkane on metal sites. The formed alkene may then diffuse and adsorb on an acid site to form a carbenium ion that is turned into an alkylated cyclopropane ring and react via the so-called Protonated Cyclopropene mechanism.[115] Subsequent opening of the ring results in either a creation of a methyl branch or the shift of a methyl branch along the hydrocarbon chain.

The resulting alkene isomer may desorb and be hydrogenated over a metal site or undergo further reactions on acid sites. Cracking is attributed to the β-scission mechanism, which favors

the cracking of alkenes with multiple branches.[115,117] Alkylcarbeniumions act as transition states wherein tertiary alkylcarbenium ions are the most stable, followed by secondary while, in principle, the formation of primary alkylcarbenium ions is avoided. As a consequence, mostly branched alkenes are obtained as cracked products that are subsequently hydrogenated on metal sites towards alkanes.

The impact of the ratio of metal and acid sites has been studied intensively. One of the first studies was reported by Guisnet et al. who stated that above a certain metal weight loading the rate on the acid sites would become rate limiting and that further increasing the metal loading did not impact the catalytic performance.[118] When criteria for intimacy and metal-acid ratio are met, the process may become a so-called "ideal" process. Criteria for ideality were defined by Jens Weitkamp for processes that provide an high flexibility in selectivity towards either isomers, primary cracked products and eventually secondary cracked products by increasing the severity of the reaction. [119,120] Besides the catalyst and the reaction temperature, also the process conditions such as total pressure, partial pressures of *n*-alkane and hydrogen and the *n*-alkane carbon number can determine the ideality of a process.[121]

1.7 Inter-site proximity for bifunctional catalyst

The first studies on the effect of inter-site proximity in bifunctional catalysts were performed around 1960 by Paul B. Weisz and coworkers.[122–124] He proposed the so-called 'intimacy criterion', wherein the maximum distance between sites is defined for optimal catalytic activity. In a later study by Martens and Jacobs, the Weisz intimacy criterion was reformulated as [115]:

$$R^2 < 1.2 \cdot 10^5 \frac{P_0 \cdot D_0}{T \cdot dN/dt}$$

In this equation, R (m) is the radius of monofunctional catalyst grains and 2R is therefore the average distance between the two functions, assuming optimally mixed particles. P_0 is the partial pressure of the alkene intermediates (MPa), D_0 is the diffusivity of the alkenes in the pores of the catalyst grains ($m^2 \cdot s^{-1}$), T is the reaction temperature (K), dN/dt is the rate of reaction ($mol \cdot s^{-1} \cdot m^{-3}$) and $1.2 \cdot 10^5$ is the proportionality constant ($K \cdot mol \cdot MPa^{-1} \cdot m^{-3}$). According to the study by Weisz, the equation is relatively insensitive to the shape of the catalyst grains and the kinetics of the reaction.[122] Under typical process conditions for silica alumina or zeolite based catalysts, the intimacy criterion is within the micrometer length scale (2R = 1-1000 μm).[115]

More recent studies on composite zeolite based bifunctional catalysts have pointed out that, besides aforementioned criteria on the ratio and proximity of catalytic sites, locating metal nanoparticles in the zeolite component can be detrimental for the catalytic performance.[125,126] For mesoporous solid acids on the other hand, the location of metal nanoparticles is not relevant. [125–127] The effects reported for composite zeolite based bifunctional catalysts were not in line with the Weisz criterion described above, since intimacy effects were observed within the nanometer length scale. Typically zeolite crystals of 500-1000 nm were used and metal nanoparticles were located either on a γ-alumina binder or in zeolite crystals, thus varying inter-site proximity within the nanoscale rather than the micrometer scale, where detrimental effects are expected based on the intimacy criterion. Moreover, the intimacy criterion is often interpreted as 'the closer

the better', whereas the observations of recent studies show that the closest intimacy (metal in zeolite) led to more extensive secondary cracking than nanoscale intimacy (metal on binder).

The most likely working hypothesis proposed brings us back to the pore mouth mechanism of Figure 1.6 in combination with anisotropic diffusion of branched alkenes from zeolite acid sites to metal sites. It is proposed that the formation of a branched alkene in the pore mouths leads to fast diffusion out of the micropore and slow diffusion into the micropore thus preventing secondary reactions to take place. When a branched alkene is formed inside the micropore and not close to the surface of the zeolite crystal the slow diffusion will lead to more secondary reactions including cracking. The new mechanism proposed here is summarized in Figure 1.9 for metal nanoparticles inside the zeolite (a) or metal nanoparticles on the binder (b).

Please note that the mechanism in Figure 1.9 has not been proven as yet but is the best summary of previous observations, although some of the results summarized in this thesis are challenging it already.

1.8 Scope of thesis

The work described in this thesis aims to provide a deeper understanding of the structure and catalytic properties bifunctional catalysts consisting of zeolite, an alumina binder and platinum. The location of Pt nanoparticles was systematically varied within the composite support, either in the zeolite or on the alumina component. In **Chapter 2** on this thesis, three non-trivial characterization techniques (quantitative XPS, CO infrared spectroscopy, catalysis) are applied to assess the location of Pt nanoparticles in a composite support. The results are compared to results obtained from the previously used TEM characterization. In **Chapter 3**, the influence of metal-acid intimacy on the catalytic performance in *n*-heptane hydroisomerization was studied. Metal-acid intimacies ranged from Pt inside zeolite crystals providing a 'closest' intimacy, Pt on the γ-alumina binder providing a 'nanoscale' intimacy and microscale intimacies provided by physical mixtures of catalyst grains. The study was performed on three different zeolites (ZSM-5, Zeolite Beta, Zeolite Y) with different micropore sizes. In **Chapter 4**, the influence of residual chlorine of the Pt precursor on both acidity and catalytic performance is studied on composite catalysts of zeolite Y. In **Chapter 5** a preliminary study is described on the impact of the location of Pt nanoparticles on the kinetics in the conversion of *n*-alkanes.

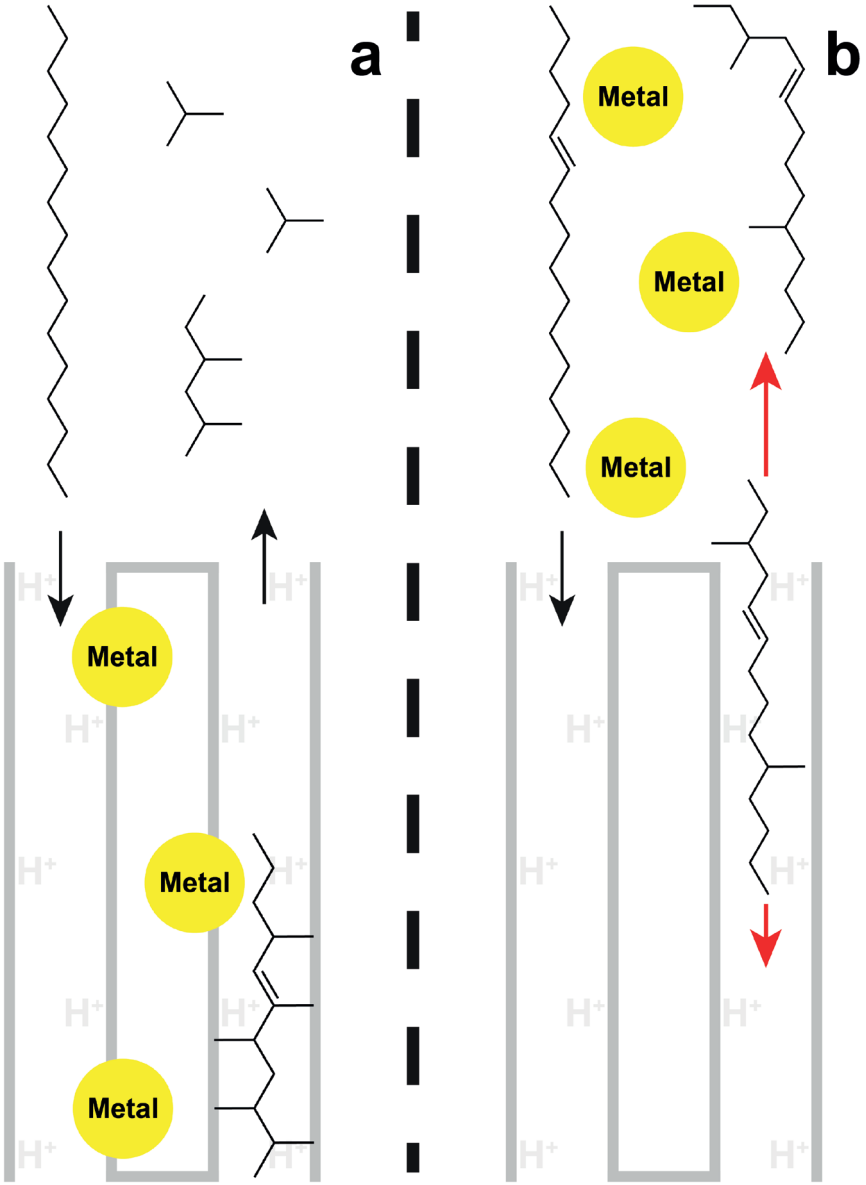

Figure 1.9. Schematic representation of the reaction mechanism of *n*-hexadecane that is converted on a bifunctional zeolite based catalysts with metal nanoparticles located either in the zeolite (a) or outside de zeolite (b), i.e. on the γ-alumina binder. In (a), *n*-hexadecane enters the zeolite as alkane, and is dehydrogenated on metal sites in the zeolite followed by conversion to a branched alkene. Long-chain branched alkenes are likely to get 'trapped' in the zeolite, resulting in cracking towards lighter products that can easily diffuse out of the zeolite micropores. In (b), after dehydrogenation on metal sites on the γ-alumina binder, *n*-hexadecene enters the zeolite and reacts on an acid site close to the zeolite surface. Subsequent diffusion of *i*-hexadecene out of the zeolite is faster than diffusion into the zeolite leading to cracking, i.e. we put forward an anisotropy of the diffusion of *i*-hexadecene, as indicated by red arrows in the figure.

References

[1] G. Ertl, H. Knözinger, F. Schüth, J. Weitkamp, Eds. , Handbook of Heterogeneous Catalysis, 2nd Edition, Wiley-VCH Verlag GmbH& Co. KGaA, Weinheim, Germany, 2008.

[2] I. Chorkendorff, J. W. Niemantsverdriet, Concepts of Modern Catalysis and Kinetics, Wiley-VCH Verlag, 2017.

[3] U. Hanefeld, L. Lefferts, Catalysis: An Integrated Textbook for Students, Wiley-VCH Verlag, 2018.

[4] Statistical Review of World Energy, 2019.

[5] Paris Agreement, United Nations, 2015.

[6] M. Höök, X. Tang, Energy Policy 2013, 52, 797–809.

[7] G. J. Kramer, M. Haigh, Nature 2009, 462, 568–569.

[8] Statistical Review of World Energy, 2020.

[9] R. C. Armstrong, C. Wolfram, K. P. De Jong, R. Gross, N. S. Lewis, B. Boardman, A. J. Ragauskas, K. Ehrhardt-Martinez, G. Crabtree, M. V. Ramana, Nat. Energy 2016, 1, 1–8.

[10] K. Van Kranenburg, Y. Van Delft, A. Gavrilova, R. De Kler, C. Schipper, R. Smokers, M. Verbeek, R. Verbeek, 2020, 1–32.

[11] T. Kandaramath Hari, Z. Yaakob, N. N. Binitha, Renew. Sustain. Energy Rev. 2015, 42, 1234–1244.

[12] J. W. Choi, D. Aurbach, Nat. Rev. Mater. 2016, 1.

[13] K. Cheng, J. Kang, D. L. King, V. Subramanian, C. Zhou, Q. Zhang, Y. Wang, Advances in Catalysis for Syngas Conversion to Hydrocarbons, Elsevier Inc., 2017.

[14] N. H. Tran, J. R. Bartlett, G. S. K. Kannangara, A. S. Milev, H. Volk, M. A. Wilson, Fuel 2010, 89, 265–274.

[15] B. Peng, Y. Yao, C. Zhao, J. A. Lercher, Angew. Chemie - Int. Ed. 2012, 51, 2072–2075.

[16] G. W. Huber, S. Iborra, A. Corma, Chem. Rev. 2006, 106, 4044–4098.

[17] J. Zakzeski, P. C. A. Bruijnincx, A. L. Jongerius, B. M. Weckhuysen, Chem. Rev. 2010, 110, 3552–3599.

[18] E. T. C. Vogt, G. T. Whiting, A. Dutta Chowdhury, B. M. Weckhuysen, Zeolites and Zeotypes for Oil and Gas Conversion, Elsevier Inc., 2015.

[19] M. Hook, The Houdry Process for the Catalytic Conversion of Crude Petroleum to High-Octane Gasoline, 1996.

[20] C. G. Moseley, J. Chem. Educ. 1984, 61, 655–656.

[21] E. Houdry, W. F. Burt, J. A . E. Pew, J. W. A . Peters, Oil Gas J. 1938, 37, 40–45.

[22] E. M. Flanigen, R. W. Broach, S. T. Wilson, in Zeolites Ind. Sep. Catal., 2010.

[23] A. F. Cronsted, Akad. Handl. Stock. 1756, 18, 120–130.

[24] R. M. Barrer, J. Soc. Chem. Ind. 1945, 64, 130.

[25] R. M. Barrer, J. Chem. Soc. 1948, 2158.

[26] T. B. Reed, D. W. Breck, J. Am. Chem. Soc. 1956, 78, 5972–5977.

[27] J. W. Thybaut, G. B. Marin, in Adv. Catal., Elsevier Inc., 2016, pp. 109–238.

[28] K. S. W. Sing, Stud. Surf. Sci. Catal. 1991, 62, 1–9.

[29] A. Corma, Chem. Rev. 1995, 95, 559–614.

[30] C. Baerlocher, L. B. McCusker, "Database of Zeolite Structures," 2017.

[31] R. P. Townsend, E. N. Coker, in Stud. Surf. Sci. Catal., 2001, pp. 467–524.

[32] M. J. Remy, D. Stanica, G. Poncelet, E. J. P. Feijen, P. J. Grobet, J. A. Martens, P. A. Jacobs, J. Phys. Chem. 1996, 100, 12440–12447.

[33] M. Choi, K. Na, J. Kim, Y. Sakamoto, O. Terasaki, R. Ryoo, Nature 2009, 461, 246–249.

[34] X. Zhang, D. Liu, D. Xu, S. Asahina, K. A. Cychosz, K. V. Agrawal, Y. Al Wahedi, A. Bhan, S. Al Hashimi, O. Terasaki, et al., Science. 2012, 336, 1684–1687.

[35] J. Zečević, K. P. de Jong, ChemCatChem 2013, 5, 417–418.

[36] A. Corma, V. Fornes, S. B. Pergher, T. L. M. Maesen, J. G. Buglass, Nature 1998, 396, 353–356.

[37] H. Dai, Y. Shen, T. Yang, C. Lee, D. Fu, A. Agarwal, T. T. Le, M. Tsapatsis, J. C. Palmer, B. M. Weckhuysen, et al., Nat. Mater. 2020, 19, 1074–1080.

[38] J. Jiang, J. L. Jorda, J. Yu, L. A. Baumes, E. Mugnaioli, M. J. Diaz-Cabanas, U. Kolb, A. Corma, Science. 2011, 333, 1131–1134.

[39] J. Pérez-Ramírez, C. H. Christensen, K. Egeblad, C. H. Christensen, J. C. Groen, Chem. Soc. Rev. 2008, 37, 2530–2542.

[40] Y. Wei, T. E. Parmentier, K. P. De Jong, J. Zečević, Chem. Soc. Rev. 2015, 44, 7234–7261.

[41] S. Mitchell, A. B. Pinar, J. Kenvin, P. Crivelli, J. Kärger, J. Pérez-Ramírez, Nat. Commun. 2015, 6.

[42] A. H. Janssen, A. J. Koster, K. P. de Jong, Angew. Chemie Int. Ed. 2001, 40, 1102–1104.

[43] J. C. Groen, J. C. Jansen, J. A. Moulijn, J. Pérez-Ramírez, J. Phys. Chem. B 2004, 108, 13062–13065.

[44] K. P. de Jong, J. Zečević, H. Friedrich, P. E. de Jongh, M. Bulut, S. van Donk, R. Kenmogne, A. Finiels, V. Hulea, F. Fajula, Angew. Chemie Int. Ed. 2010, 49, 10074–10078.

[45] B. Kraushaar-Czarnetzki, S. P. Müller, Synth. Solid Catal. 2009, 173–199.

[46] G. T. Whiting, S. H. Chung, D. Stosic, A. D. Chowdhury, L. I. Van Der Wal, D. Fu, J. Zecevic, A. Travert, K. Houben, M. Baldus, et al., ACS Catal. 2019, 9, 4792–4803.

[47] S. Mitchell, N. L. Michels, J. Pérez-Ramírez, Chem. Soc. Rev. 2013, 42, 6094–6112.

[48] S. Mitchell, N. L. Michels, K. Kunze, J. Pérez-Ramírez, Nat. Chem. 2012, 4, 825–831.

[49] L. Gueudré, M. Milina, S. Mitchell, J. Pérez-Ramírez, Adv. Funct. Mater. 2014, 24, 209–219.

[50] G. T. Whiting, N. Nikolopoulos, I. Nikolopoulos, A. D. Chowdhury, B. M. Weckhuysen, Nat. Chem. 2019, 11, 23–31.

[51] F. Rouquerol, J. Rouquerol, K. S. W. Sing, in Handb. Porous Solids (Eds.: F. Schüth, K.S.W. Sing, J. Weitkamp), Wiley-VCH Verlag, 2002, pp. 236–275.

[52] R. M. Barrer, J. Colloid Interface Sci. 1966, 21, 415–434.

[53] D. M. Ruthven, M. F. M. Post, in Stud. Surf. Sci. Catal. 137 (Eds.: H. Van Bekkum, J.C. Jansen, P.A. Jacobs, E.M. Flanigen), Elsevier Science B.V., 2001, pp. 525–577.

[54] E. M. Flanigen, R. W. Broach, S. T. Wilson, Zeolites in Industrial Separation and Catalysis, Wiley-VCH Verlag GmbH & Co. KGaA, 2010.

[55] B. Smit, T. L. M. Maesen, Chem. Rev. 2008, 108, 4125–4184.

[56] D. Ruthven in Principles of adsorption and adsorption processes, John Wiley & Sons, Inc., 1984.

[57] D. W. Breck, Zeolite Molecular Sieves: Structure, Chemistry, and Use, John Wiley & Sons, Inc., 1973.

[58] C. E. Gounaris, C. A. Floudas, J. Wei, C. A. Floudas, Chem. Eng. Sci. 2006, 61, 7933–7948.

[59] C. E. Gounaris, J. Wei, C. A. Floudas, Chem. Eng. Sci. 2006, 61, 7949–7962.

[60] Y. Traa, S. Sealy, J. Weitkamp, in Mol. Sieves, Springer Berlin Heidelberg, 2006, pp. 103–154.

[61] J. A. Martens, P. A. Jacobs, Zeolites 1986, 6, 334–348.

[62] J. A. Martens, M. Tielen, P. A. Jacobs, Catal. Today 1987, 1, 435–453.

[63] A. Corma, A. Chica, J. M. Guil, F. J. Llopis, G. Mabilon, J. A. Perdigón-Melón, S. Valencia, J. Catal. 2000, 189, 382–394.

[64] W. O. Haag, R. M. Lago, P. B. Weisz, Faraday Discuss. Chem. Soc. 1981, 72, 317–330.

[65] D. M. Ruthven, Chapter 21 Diffusion in Zeolite Molecular Sieves, Elsevier B.V., 2007.

[66] J. Kärger, in Mol. Sieves - Sci. Technol., Springer-Verlag Berlin Heidelberg, Berlin, Heidelberg, 2008, pp. 85–133.

[67] S. Van Donk, A. Broersma, O. L. J. Gijzeman, J. A. Van Bokhoven, J. H. Bitter, K. P. De Jong, J. Catal. 2001, 204, 272–280.

[68] W. Zhu, F. Kapteijn, J. . Moulijn, Microporous Mesoporous Mater. 2001, 47, 157–171.

[69] E. J. M. Hensen, A. M. de Jong, R. A. van Santen, 2007, pp. 277–328.

[70] R. A. van Santen, B. G. Anderson, R. H. Cunningham, A. V. G. Mangnus, L. J. van Ijzendoorn, M. J. A. de Voigt, Angew. Chemie Int. Ed. English 1996, 35, 2785–2787.

[71] C. Chmelik, J. Kärger, Chem. Soc. Rev. 2010, 39, 4864–4884.

[72] U. Schemmert, J. Kärger, J. Weitkamp, Microporous Mesoporous Mater. 1999, 32, 101–110.

[73] B. D. Vandegehuchte, J. W. Thybaut, G. B. Marin, Ind. Eng. Chem. Res. 2014, 53, 15333–15347.

[74] B. D. Vandegehuchte, I. R. Choudhury, J. W. Thybaut, J. A. Martens, G. B. Marin, J. Phys. Chem. C 2014, 118, 22053–22068.

[75] D. Dubbeldam, E. Beerdsen, T. J. H. Vlugt, B. Smit, J. Chem. Phys. 2005, 122.

[76] T. L. M. Maesen, M. Schenk, T. J. H. Vlugt, J. P. De Jonge, B. Smit, J. Catal. 1999, 188, 403–412.

[77] A. Poursaeidesfahani, M. F. de Lange, F. Khodadadian, D. Dubbeldam, M. Rigutto, N. Nair,

T. J. H. Vlugt, J. Catal. 2017, 353, 54–62.
[78] D. Dubbeldam, A. Torres-Knoop, K. S. Walton, Mol. Simul. 2013, 39, 1253–1292.
[79] D. Dubbeldam, S. Calero, D. E. Ellis, R. Q. Snurr, Mol. Simul. 2016, 42, 81–101.
[80] T. L. M. Maesen, E. Beerdsen, S. Calero, D. Dubbeldam, B. Smit, J. Catal. 2006, 237, 278–290.
[81] D. Dubbeldam, S. Calero, T. L. M. Maesen, B. Smit, Angew. Chemie - Int. Ed. 2003, 42, 3624–3626.
[82] J. Kärger, Mol. Sieves - Sci. Technol. 2008, 7, 329–366.
[83] D. G. Levitt, Phys. Rev. A 1973, 8, 3050–3054.
[84] K. Hahn, J. Kärger, V. Kukla, Phys. Rev. Lett. 1996, 76, 2762–2765.
[85] V. Gupta, S. S. Nivarthi, D. Keffer, A. V Mccormick, G. M. Shearer, D. Keffer, H. T. Davis, Science. 1996, 274, 164.
[86] H. Jobic, K. Hahn, J. Kärger, M. Bée, A. Tuel, M. Noack, I. Girnus, G. J. Kearley, J. Phys. Chem. B 1997, 101, 5834–5841.
[87] G. Sastre, A. Corma, Top. Catal. 2003, 24, 7–12.
[88] B. Smit, T. L. M. Maesen, Nature 2008, 451, 671–678.
[89] J. A. Martens, W. Souverijns, W. Verrelst, R. Parton, G. F. Froment, P. A. Jacobs, Angew. Chemie Int. Ed. English 1995, 34, 2528–2530.
[90] S. Ernst, J. Weitkamp, J. A. Martens, P. A. Jacobs, Appl. Catal. 1989, 48, 137–148.
[91] J. A. Martens, G. Vanbutsele, P. A. Jacobs, J. Denayer, R. Ocakoglu, G. Baron, J. A. Muñoz Arroyo, J. Thybaut, G. B. Marin, Catal. Today 2001, 65, 111–116.
[92] J. F. Denayer, G. V. Baron, J. A. Martens, P. A. Jacobs, J. Phys. Chem. B 1998, 102, 3077–3081.
[93] J. F. Denayer, W. Souverijns, P. A. Jacobs, J. A. Martens, G. V. Baron, J. Phys. Chem. B 1998, 102, 4588–4597.
[94] T. L. M. Maesen, R. Krishna, J. M. van Baten, B. Smit, S. Calero, J. M. Castillo Sanchez, J. Catal. 2008, 256, 95–107.
[95] S. C. C. Wiedemann, Z. Ristanovic, G. T. Whiting, V. R. Reddy Marthala, J. Kärger, J. Weitkamp, B. Wels, P. C. A. Bruijnincx, B. M. Weckhuysen, Chem. - A Eur. J. 2016, 22, 199–210.
[96] S. C. C. Wiedemann, J. A. Stewart, F. Soulimani, T. Van Bergen-Brenkman, S. Langelaar, B. Wels, P. De Peinder, P. C. A. Bruijnincx, B. M. Weckhuysen, J. Catal. 2014, 316, 24–35.
[97] T. L. M. Maesen, M. Schenk, T. J. H. Vlugt, J. P. d. Jonge, B. Smit, J. Catal. 1999, 188, 403–412.
[98] G. Sastre, A. Chica, A. Corma, J. Catal. 2000, 195, 227–236.
[99] M. J. Climent, A. Corma, S. Iborra, Chem. Rev. 2011, 111, 1072–1133.
[100] T. L. Lohr, T. J. Marks, Nat. Chem. 2015, 7, 477–482.
[101] P. S. F. Mendes, J. M. Silva, M. F. Ribeiro, A. Daudin, C. Bouchy, Catal. Today 2019, 1–23.
[102] C. M. A. Parlett, M. A. Isaacs, S. K. Beaumont, L. M. Bingham, N. S. Hondow, K. Wilson, A. F. Lee, Nat. Mater. 2016, 15, 178–182.
[103] E. Iglesia, D. G. Barton, J. A. Biscardi, M. J. L. Gines, S. L. Soled, Catal. Today 1997, 38, 339–360.
[104] M. J. Climent, A. Corma, S. Iborra, M. J. Sabater, ACS Catal. 2014, 4, 870–891.
[105] Y. Z. Chen, C. M. Hwang, C. W. Liaw, Appl. Catal. A Gen. 1998, 169, 207–214.
[106] M. de J. Martínez-Ortiz, D. Tichit, P. Gonzalez, B. Coq, J. Mol. Catal. A Chem. 2003, 201, 199–210.
[107] S. Sartipi, M. Makkee, F. Kapteijn, J. Gascon, Catal. Sci. Technol. 2014, 4, 893–907.
[108] J. L. Weber, I. Dugulan, P. E. de Jongh, K. P. de Jong, ChemCatChem 2018, 10, 1107–1112.
[109] K. Cheng, B. Gu, X. Liu, J. Kang, Q. Zhang, Y. Wang, Angew. Chemie Int. Ed. 2016, 55, 4725–4728.
[110] F. Jiao, J. Li, X. Pan, J. Xiao, H. Li, H. Ma, M. Wei, Y. Pan, Z. Zhou, M. Li, et al., Science. 2016, 351, 1065–1068.
[111] C. H. Mejía, D. M. A. Verbart, K. P. de Jong, Catal. Today 2020, 0–1.
[112] P. Gao, S. Li, X. Bu, S. Dang, Z. Liu, H. Wang, L. Zhong, M. Qiu, C. Yang, J. Cai, et al., Nat. Chem. 2017, 9, 1019–1024.
[113] J. Wei, Q. Ge, R. Yao, Z. Wen, C. Fang, L. Guo, H. Xu, J. Sun, Nat. Commun. 2017, 8, 15174.
[114] H. L. Coonradt, W. E. Garwood, Ind. Eng. Chem. Process Des. Dev. 1964, 3, 38–45.
[115] J. A. Martens, P. A. Jacobs, in Stud. Surf. Sci. Catal., 2001, pp. 633–671.
[116] C. Bouchy, G. Hastoy, E. Guillon, J. A. Martens, Oil Gas Sci. Technol. 2009, 64, 91–112.

[117] J. A. Martens, P. A. Jacobs, J. Weitkamp, Appl. Catal. 1986, 20, 283–303.

[118] M. Guisnet, F. Alvarez, G. Giannetto, G. Perot, Catal. Today 1987, 1, 415–433.

[119] J. Weitkamp, Erdol Kohle Erdgas Petrochem 1978, 31, 13–22.

[120] J. Weitkamp, ChemCatChem 2012, 4, 292–306.

[121] J. W. Thybaut, C. S. Laxmi Narasimhan, J. F. Denayer, G. V. Baron, P. A. Jacobs, J. A. Martens, G. B. Marin, Ind. Eng. Chem. Res. 2005, 44, 5159–5169.

[122] P. B. Weisz, Adv. Catal. 1962, 13, 137–190.

[123] P. B. Weisz, Science. 1956, 123, 887–888.

[124] P. B. Weisz, E. W. Swegler, Science. 1957, 126, 31–32.

[125] J. Zečević, G. Vanbutsele, K. P. De Jong, J. A. Martens, Nature 2015, 528, 245–254.

[126] K. Cheng, L. I. Wal, H. Yoshida, J. Oenema, J. Harmel, Z. Zhang, G. Sunley, J. Zečević, K. P. Jong, Angew. Chemie Int. Ed. 2020, 59, 3592–3600.

[127] J. Harmel, L. I. van der Wal, J. Zečević, P. E. de Jongh, K. P. de Jong, Catal. Sci. Technol. 2020, 10, 2111–2119.

Chapter 2

Assessment of the Location of Pt Nanoparticles in Pt/Zeolite Y/γ-Al_2O_3 Composite Catalysts

This chapter is based on: J. Oenema, J.P. Hofmann, E.J.M. Hensen, J. Zečević, K.P. de Jong, ChemCatChem 12 (2020) 615–622.

Abstract

The location of Pt nanoparticles was studied in Pt/zeolite Y/γ-Al_2O_3 composite catalysts prepared by $H_2PtCl_6 \cdot 6H_2O$ (CPA) or $Pt(NH_3)_4(NO_3)_2$ (PTA) as Pt precursors. The aim of this study is to validate findings from Transmission Electron Microscopy (TEM) by using characterization techniques that sample larger amounts of catalyst per measurement. Quantitative X-ray Photoelectron Spectroscopy (XPS) showed that the catalyst prepared with CPA led to a significantly higher Pt/Al atomic ratio than the catalyst prepared with PTA confirming that the 1-2 nm sized Pt nanoparticles in the former catalyst were located on the open and mesoporous γ-Al_2O_3 component, whereas they were located in the micropores of zeolite Y in the latter. By using infrared spectroscopy, a shift in the absorption band maximum of CO chemisorbed on Pt nanoparticles was observed, which can be attributed to a difference in electronic properties depending on the support of the Pt nanoparticles. Finally, model hydrogenation experiments were performed using β-phenylcinnamaldehyde, a reactant molecule with low diffusivity in zeolite Y micropores, resulting in a 5 times higher activity for the catalyst prepared by CPA compared to PTA. The combined use of these characterization techniques allow us to draw more robust conclusions on the ability to control the location of Pt nanoparticles by using either CPA or PTA as precursors in zeolite/γ-Al_2O_3 composite catalyst materials.

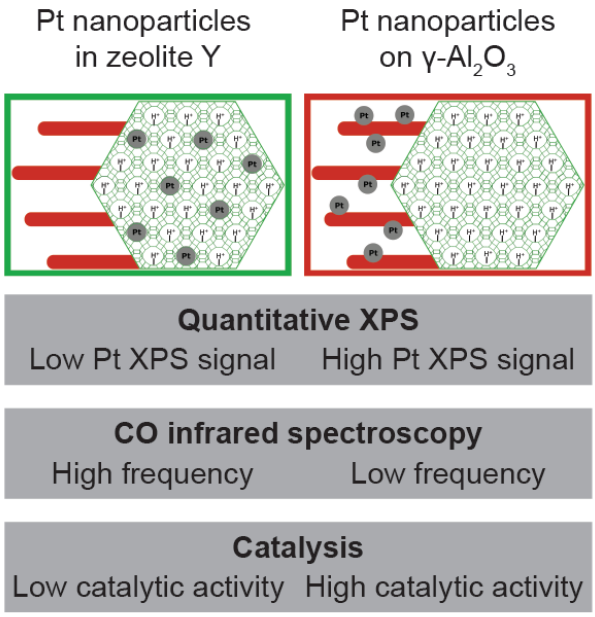

2.1. Introduction

The structural properties of supported metal catalysts, e.g.: metal loading, metal nanoparticle size and their distribution across the catalyst support, as well as the support acidity and porosity, strongly affect their selectivity, activity and stability in catalytic reactions.[1–3] Bifunctional catalysts with zeolite acid sites and metal sites are a special class of solid catalysts that are used for the conversion of crude oil fractions or renewable hydrocarbon feedstocks into fuels and chemicals.[4–6] For optimal catalytic performance of these catalysts, a close intimacy between the metal and acid sites is essential.[7–9] When metal nanoparticles, responsible for dehydrogenation-hydrogenation, are located inside zeolite micropores, a 'closest' intimacy with the zeolite acid sites, responsible for isomerization and cracking, is ensured. On the other hand, locating metal nanoparticles inside zeolite micropores can limit their accessibility for larger hydrocarbon reactants that have low diffusivity through such small pores.[10,11]

Due to the strong impact of metal nanoparticle location on the catalytic performance, various synthetic approaches were developed over the last decades to improve control over location of metal nanoparticles within (micro)porous supports.[12–14] For example, Kim et al. were able to control the location of Pt nanoparticles by using $[Pt(NH_3)_4]^{2+}$ (aq) to ion-exchange with zeolite protons to obtain Pt nanoparticles inside ZSM-5 micropores, whereas impregnation with previously synthesized colloidal particles (~1.4 nm in diameter) was used to deposit Pt nanoparticles on the outer surface of the ZSM-5 crystallites (micropore width: 0.56 nm).[15] Several papers report methods to locate metal clusters within zeolite micropores by adding stabilized metal colloids or metal complexes before complete crystallization of the zeolites.[16–19] Alternatively, applying specific thermal treatments have been used to control the distribution of metal nanoparticles in porous supports.[20]

In these and many other studies of supported metal catalysts, TEM is one of the most commonly used techniques to investigate the location of metal nanoparticles on the support.[21–24] However, the severe limitations of TEM are the low amount of catalyst that is sampled per measurement, and the projection of a catalyst's three dimensional structure in a two dimensional image. The latter issue can be overcome by the use of Electron tomography (or 3D TEM) that has been successfully applied to establish the location of metal particles within e.g. zeolite micropores.[22,24–26] Aside from TEM, several other characterization techniques have been sporadically employed to try to directly or indirectly determine the location of the metal nanoparticles on a support, including catalysis[16–19,27-29], CO infrared spectroscopy[18,30], SAXS[21], XAS[31,32] and XPS[27,28,33].

Zeolite based catalysts used in industrial processes are typically shaped as millimeter sized bodies using a porous metal oxide binder, and may consist of additional components to further improve catalyst performance.[2,3] While academic catalyst research focuses often on structurally-simple model catalysts, a number of recent publications focuses on more practical catalysts and the interplay of all the structural features that determines the catalytic performance.[34,35] In a recent study, industrially relevant zeolite Y/γ-Al_2O_3 extrudates were used as support for Pt nanoparticles, located either inside zeolite Y or on the γ-Al_2O_3 binder.[25] The resulting bifunctional catalysts were investigated by using a heavy hydrocarbon feedstock, and remarkable beneficial effects on product selectivity were observed for the catalyst with Pt nanoparticles on the γ-Al_2O_3 binder compared to the catalysts with Pt nanoparticles inside zeolite Y. TEM was used to investigate the

location of Pt nanoparticles in the zeolite Y/γ-Al_2O_3 extrudates and to overcome the challenge of overlapping features in two dimensional TEM images, authors used ultramicrotomy to section the catalysts into 70 nm thick slices. Besides that, an electron tomography study was used to study the location of Pt nanoparticles. However, both of these approaches suffer from sampling issues, with an estimated amount of sample being imaged in the order of 10^{-14} g. In studies of supported metal catalysts, synthesis-originated structural heterogeneities, such as: variation in local metal loading or metal nanoparticle size and location are regularly observed, either at the nanoscale between individual support particles[24,36] up to the microscale between individual support grains[37]. It is therefore desirable to validate results of characterization techniques, especially those that sample low amounts of catalysts per measurement, with complementary characterization techniques. In this study, the location of Pt nanoparticles in Pt/zeolite Y/γ-Al_2O_3 catalysts is assessed using a combination of commonly used laboratory techniques (quantitative XPS, CO infrared spectroscopy and catalysis) that sample significantly more catalyst than can be achieved by TEM analysis (Table 2.1, SI section 2.1, Table S2.4). The presented methods for assessment of the location of metal nanoparticles could be adopted for a wider range of catalysts, in particular catalysts with bimodal porosities, for example, to study the migration of metal nanoparticles during catalysis.[38]

Table 2.1. Employed characterization techniques and the respective amount of catalyst that is sampled per measurement, estimated using the parameters employed in this study.

Characterization technique	Amount (g)
TEM	~10^{-14}
Quantitative XPS	~10^{-9}
CO infrared spectroscopy	~10^{-2}
Catalysis	$5 \cdot 10^{-2}$

2.2. Experimental

2.2.1. Catalyst Synthesis

Cylindrical extrudates consisting of 50 wt.% of mesoporous zeolite Y (Zeolyst CBV 760) and 50 wt.% of γ-Al_2O_3 (designated as Y/A) were obtained from Shell Projects and Technology. Mesoporous zeolite Y was purchased from Zeolyst (Si/Al = 30, CBV760) and HMPA pseudo-boehmite as precursor for γ-Al_2O_3 was obtained from Shell Projects and Technology. Extrudates were crushed and sieved to particles of 0.2-0.5 mm in diameter. Textural analysis of the Y/A support, as well as γ-Al_2O_3 and zeolite Y was performed using N_2 physisorption at liquid nitrogen temperature on a Micromeritics TriStar II Plus, after drying the samples at 300 °C for 10 hours in an N_2 flow. The isotherms and textural properties can be found in Figure S2.5 and Table S2.5.

Pt-Y/A-NH_3 and Pt-Y-NH_3 catalysts

1 g of 0.2-0.5 mm Y/A particles were suspended in 300 ml Milli-Q water at room temperature and stirred for 1 hour, after which the pH of the suspension was 6.4. ~50 ml of aqueous solution containing 8.8 mg of $Pt(NH_3)_4(NO_3)_2$ (Sigma-Aldrich, 99.995% purity) was added dropwise to the suspension (aiming at nominal Pt loading of 0.5 wt.%), after which the pH dropped to 6.0. After addition of the Pt precursor, the suspension was stirred for another 3 hours, after which the

pH dropped to 5.6. The suspension was filtered and washed with Milli-Q water and dried in air overnight at 120 °C. The dried sample was calcined in a flow of 20% O_2/N_2 at 350 °C with a ramp of 0.2 °C·min^{-1} (GHSV ~16.700 h^{-1}), where after it was reduced in a flow of H_2 (GHSV ~3.300 h^{-1}) for 3 hours at 300 °C, using a ramp of 5 °C·min^{-1}. Pt-Y-NH_3 reference catalyst was prepared using the method described above, but using only zeolite Y (CBV 760) in powder form as support. Prior to the calcination/reduction the powder was pressed into a pellet, crushed and sieved into a sieve fraction of 0.2-0.5 mm in diameter, while similar GHSVs as used for the composite catalyst were used during the calcination and reduction step.

Pt-Y/A-Cl and Pt-A-Cl catalysts

A suspension containing 1 g of 0.2-0.5 mm Y/A particles in 300 ml Milli-Q water was stirred for 1 hour at room temperature, after which the pH of the suspension was lowered from 5.5 to 3.0 by adding a few drops of a 1 M HCl solution. ~50 ml of aqueous solution containing 13.5 mg of $H_2PtCl_6 \cdot 6H_2O$ (Sigma-Aldrich, ~38 wt.% Pt) was added dropwise to the suspension (aiming at nominal Pt loading of 0.5 wt. %). After 3 hours of stirring (pH increased to 3.8), the suspension was filtered and washed with Milli-Q water, and dried in air overnight at 120 °C. Dried catalyst precursor was reduced in a flow of H_2 for 3 hours at 500 °C, with a ramp of 5 °C·min^{-1} (GHSV ~3300 h^{-1}). Pt-A-Cl reference catalyst was prepared using the method described above, but using γ-Al_2O_3 in powder form as support. The γ-Al_2O_3 was obtained by calcination of HMPA pseudo-boehmite at 550 °C for 2 hours, using a ramp of 5 °C/min. Prior to the reduction the powder was pressed into a pellet, crushed and sieved into a sieve fraction of 0.2-0.5 mm in diameter, while a similar GHSV as used for the composite catalyst was used during the reduction step.

2.2.2. Elemental analysis

Pt elemental analysis was performed at Kolbe Mikroanalytisches Laboratorium, Oberhausen using an ICP-optical emission spectrometer (Perkin Elmer) after sample dissolution according to standard in-house procedures.

2.2.3. Transmission Electron Microscopy

High-Angle Annular Dark-Field Scanning Transmission Electron Microscopy (HAADF-STEM) imaging was performed on an FEI Talos F200X transmission electron microscope, equipped with a high-brightness field emission gun (X-FEG) and operated at 200 kV. For these analyses, catalysts were embedded in Epofix resin, left to cure in air overnight at 60 °C, and cut to 70 nm sections using a Reichert-Jung Ultracut E ultramicrotome with Diatome Ultra 35° diamond knife. Sections were deposited on carbon-coated copper TEM grids.

2.2.4. X-ray Photoelectron Spectroscopy

XPS was performed using a Thermo Scientific K-Alpha spectrometer equipped with a monochromated Al Kα ($h\nu$ = 1486.6 eV) X-ray source. The peak binding energies (BE) were calibrated against the sp^3 C 1s peak of adventitious carbon at 284.8 eV. Sample charging was compensated by low energy e' and Ar^+ ion flooding during measurements. Quantitative analysis of XPS data was performed using Casa XPS software based on high resolution regional spectra covering the Al 2s, Si 2p, Al 2p and Pt 4f core levels in the BE range of 60-130 eV. The ratio between

the Al 2p peak and Al 2s peak was obtained from a reference Al_2O_3 sample and used during the fitting of the Pt containing samples to determine the area of the Al 2p in the overlapping Pt 4f / Al 2p region. The remaining area was then fitted to two components with asymmetric (metallic) line shape for Pt $4f_{5/2}$ and Pt $4f_{7/2}$ core levels, whereas the line shape and the FWHM (Full width at half maximum) were kept identical for both peaks of the spin-orbit split doublet (splitting was fixed to 3.35 eV). Atomic ratios were computed using atomic sensitivity factors. Values were averaged for two locations of the sample using a spot size of 400 μm. More information about the fitting of XPS spectra can be found in SI section 1.2.

2.2.5. CO infrared spectroscopy

CO infrared spectroscopy experiments were performed on a Perkin Elmer 2000 FTIR using a transmission in-situ cell with CaF_2 windows. Spectra were recorded with a resolution of 4 cm^{-1} by coaddition of 25 scans. For each measurement, a self-supporting pellet was made of ~10 mg of sample. The pellet was dried overnight at 120 °C ($p < 10^{-5}$ mbar). Thereafter, the sample was reduced in a flow of H_2 (Linde Gas, quality 5.0) at ~1 bar whilst heating up to 300 °C (1 h, 5 °C/min) followed by evacuation of the cell for 1 h. Then, the temperature was lowered to 50 °C and a reference spectrum was measured in vacuum ($p < 10^{-5}$ mbar). A 10% CO/He gas mixture (Linde Gas, 99.998 % purity) of 200 mbar was introduced in the cell for 30 min followed by evacuation for 30 min. After evacuation of gaseous CO ($p < 10^{-5}$ mbar), a spectrum was measured of the sample with remaining chemisorbed CO. The final spectra were obtained by subtraction of the reference spectrum from the spectrum of the sample with chemisorbed CO.

2.2.6. Catalytic experiments

Hydrogenation of β-phenylcinnamaldehyde (BPCMA, Sigma-Aldrich) was performed in stainless steel autoclaves with a total volume of 15 ml. 50 mg of Pt-Y/A catalysts (or 25 mg of Pt-A-Cl or Pt-Y-NH_3 reference catalysts) with a sieve fraction of 0.2-0.5 mm, was suspended in 7 ml of 2-propanol (Merck, ≥99.5%) containing 200 mg of dissolved BPCMA and 100 μl of *n*-tetradecane (Sigma-Aldrich, 99%) as internal standard. Reactors were heated to 70 °C and continuously stirred at 500 rpm before starting the reaction by pressurizing the reactor to 20 bar with H_2 (Linde Gas, quality 6.0). Samples were taken from the reaction mixture, diluted with 2-propanol and analyzed on a VARIAN GC (Agilent VF-5 column, FID detector). First order k values normalized to reactor volume and the amount of Pt present were obtained by fitting $\ln([BPCMA]_t/[BPCMA]_{t=0})$ versus time (0-20 h).

2.3. Results and Discussion

2.3.1. Synthesis

Pt/zeolite Y/γ-Al_2O_3 catalysts were prepared with the aim to generate Pt nanoparticles onto either the zeolite Y or the γ-Al_2O_3 component of a zeolite Y/γ-Al_2O_3 composite support (50/50 wt.), using a previously reported methodology.[25] $H_2PtCl_6 \cdot 6H_2O$ or $Pt(NH_3)_4(NO_3)_2$ precursors dissolved in water yield the anionic $[PtCl_6]^{2-}$ (aq) complex or the cationic $[Pt(NH_3)_4]^{2+}$ (aq) complex, respectively, whereafter these solutions were added to an aqueous suspension of the zeolite Y/γ-Al_2O_3 composite support. In acidic conditions (pH ~3.0), $[PtCl_6]^{2-}$ (aq) adsorbs on the positively charged γ-Al_2O_3 surface (PZC ~8.5) support due to electrostatic attraction, while interactions with the zeolite Y component are minimal.[39,40] On the other hand, the $[Pt(NH_3)_4]^{2+}$ (aq)

complex ion-exchanges with protons of the zeolite Y component, which is rather independent of pH.[40] The ion-exchange was performed at mildly acidic conditions (pH ~5.0) whereby γ-Al_2O_3 is slightly positively charged to restrict adsorption of the cationic Pt complex. After Pt deposition, samples were dried and calcined/reduced to convert the adsorbed Pt complexes into Pt nanoparticles of 1-2 nm in diameter. The properties of the prepared catalysts are provided in Table 2.2.

Table 2.2. Properties of the catalysts used for XPS and HAADF-STEM measurements. Pt weight loadings were determined by ICP whereas Pt nanoparticle sizes were determined from HAADF-STEM images.

Sample	Pt precursor	Pt adsorption mechanism	Pt wt. loading (%)	Pt nanoparticle size (nm)
Pt-Y/A-NH_3	$Pt(NH_3)_4(NO_3)_2$	Ion-exchange	0.5[a]	1.4 ± 0.4
Pt-Y/A-Cl	$H_2PtCl_6 \cdot 6H_2O$	Strong electrostatic adsorption	0.5[a]	1.8 ± 0.4

a) Pt wt. loading indicated corresponds to catalysts characterized with HAADF-STEM and quantitative XPS. Catalysts wt. loadings used for CO infrared spectroscopy and catalysis are between 0.3-0.4 wt.% Pt.

2.3.2. HAADF-STEM

High-Angle Annular Dark Field Scanning Transmission Electron Microscopy (HAADF-STEM) analysis of 70 nm thick microtomed sections of the samples provided local information about the size and location of Pt nanoparticles. It was observed that in the Pt-Y/A-Cl catalyst Pt nanoparticles were mostly present on γ-Al_2O_3 (Figure 2.1a), whose highly irregular porous structure of aggregated ~10 nm long platelets can be easily distinguished from large (200-1000 nm) mesoporous zeolite crystals. In Pt-Y/A-NH_3 (Figure 2.1b), Pt nanoparticles were almost exclusively present in the zeolite Y component. Previous research using electron tomography has

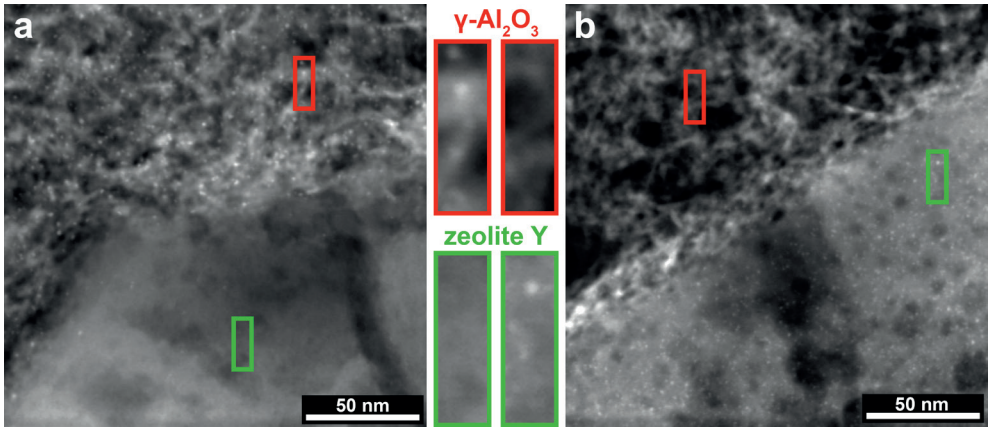

Figure 2.1. HAADF-STEM images of microtomed sections of Pt-Y/A-Cl (a) and Pt-Y/A-NH_3 (b). The γ-Al_2O_3 and zeolite Y components of the samples can be identified by their different morphology and are indicated in the images with red and green, respectively. 1-2 nm Pt nanoparticles can be identified as bright white dots, almost exclusively present in the γ-Al_2O_3 for Pt-Y/A-Cl and almost exclusively present in zeolite Y for Pt-Y/A-NH_3.

shown that Pt nanoparticles in zeolite Y are located inside zeolite crystalline domains even though their size exceeds that of the zeolite micropores.[24] To further aid distinguishing the zeolite Y from the γ-Al_2O_3, HAADF-STEM was combined with EDX elemental mapping as can be observed in Figure S2.6. In both composite catalysts, a small number of Pt nanoparticles close to the interface between γ-Al_2O_3 and zeolite Y appeared to be located on the 'opposite' component, as can be evidenced in Figure S2.7. In such cases, electron tomography could be used to determine the exact location of individual Pt nanoparticles. However, considering the low amount of catalyst sampled in a TEM measurement, it is desirable to investigate the severity of these heterogeneities (Pt nanoparticles located on the 'opposite' component) within larger amounts of the Pt/zeolite Y/γ-Al_2O_3 composite catalysts.

2.3.3 Quantitative XPS

XPS can provide quantitative information about atomic composition of the outer few nanometers of solid samples. It has been used by Wang et al. to determine if Pd nanoparticles were successfully encapsulated by a crystalline silica shell (silicalite-1)[27], whereas it was used by Winter et al. to determine if metal particles were located in the inner core or on the external surface of carbon nanofibers.[33] Here XPS was used to determine the location of Pt nanoparticles in Pt/zeolite Y/γ-Al_2O_3 composite catalysts, by relying on the probability of which part of the sample is studied in an XPS measurement. The sampling depth for XPS is only a few nanometres due to the low photoelectron escape depth (electron mean free path, EMFP), that is a function of the kinetic energy of the photoelectrons and the matrix material.[41] For the γ-Al_2O_3 platelets or nanometer-sized zeolite crystallites, it can be reasonably assumed that every orientation angle of

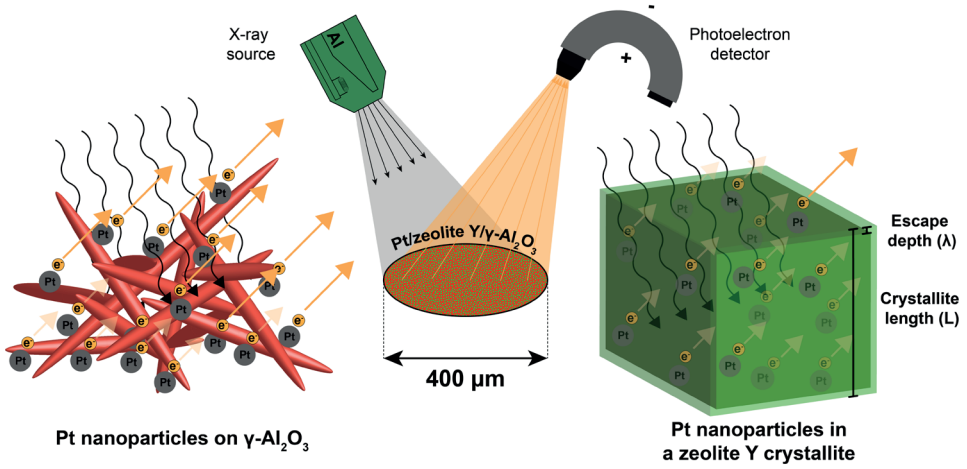

Figure 2.2. Scheme illustrating an XPS measurement of Pt/zeolite Y/γ-Al_2O_3, either with Pt nanoparticles supported on γ-Al_2O_3 (left) or Pt nanoparticles located in a zeolite Y crystallite (right). For Pt nanoparticles on γ-Al_2O_3, the signal of Pt 4f photoelectrons (kinetic energy: 1410-1415 eV) consists of contributions from Pt nanoparticles located on the external surfaces of γ-Al_2O_3 platelets. In zeolite Y crystallites, here schematically depicted as a cube with side length L, photoelectrons from Pt can only escape from the outer layer (thickness: λ) of the crystallite while the volume 'below' this layer cannot be assessed with XPS. The resulting XPS signal thus only consists of contributions of this outer layer of the zeolite Y crystals, while for γ-Al_2O_3 every part of the sample has equal probability of being sampled.

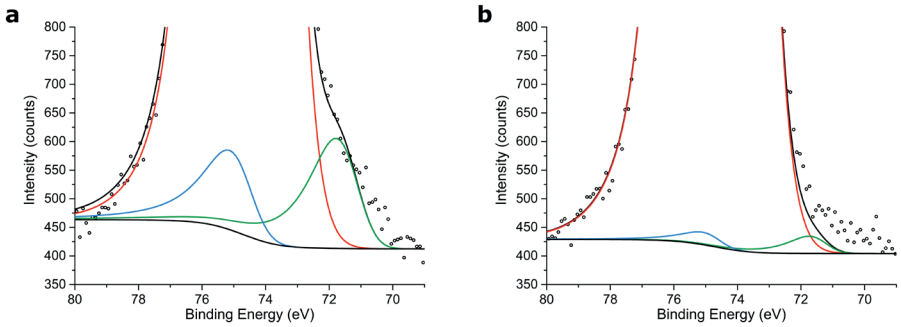

Figure 2.3. High resolution regional XPS spectra of Pt-Y/A-Cl (a) and Pt-Y/A-NH_3 (b) showing different Pt signal intensities depending on the location of the Pt nanoparticles. A Shirley background is applied to remove the contribution of the inelastically scattered electrons. Color scheme: Pt $4f_{5/2}$ (light blue), Pt $4f_{7/2}$ (dark green), Al 2p (red), Shirley background and overall fit (black).

these components within the X-ray beam (ø = 400 µm) is of equal probability and all orientations are present within the irradiated area (Figure 2.2). Therefore, in both cases, the resulting XPS signal will be an average of the of the outer surface of the sample.[42]

Because the thickness of the γ-Al_2O_3 platelets is similar to the EMFP in Al_2O_3 (kinetic energy: 1410-1415 eV), this implies that every part of the sample has equal probability of being sampled and thus, for 1-2 nm sized Pt nanoparticles supported on γ-Al_2O_3 the XPS signal is an average of the entire sample.[43] The zeolite Y crystallites are between 200 and 1000 nm in size while the EMFP for zeolite Y is approximately 4 nm (kinetic energy: 1410-1415 eV). As a consequence, only the outer layer of zeolite Y crystallites is studied, with a thickness determined by the EMFP, whereas the part below this layer does not contribute to the XPS signal. For more details about the XPS measurements and the approximation of EMFP in the samples, we refer to SI section 2.2. To assess the location of Pt nanoparticles in Pt-Y/A-Cl and Pt-Y/A-NH_3, samples were used with similar Pt weight loading and Pt particle size (Table 2.2). XPS spectra of the fitted Pt 4f core lines can be observed in Figure 2.3, while for the full regional spectra we refer to Figure S2.9.

Table 2.3 shows the surface atomic ratios obtained by XPS, obtained after correction with atomic sensitivity factors, while bulk atomic ratios based on ICP analysis for Pt and manufacturers specifications for Si and Al. Furthermore, physical mixtures of Pt-Y-NH_3 with γ-Al_2O_3 (Pt-Y-NH_3 +

Table 2.3. Bulk and surface elemental composition of the Pt/zeolite Y/γ-Al_2O_3 catalysts and physical mixtures with similar bulk composition. Bulk atomic ratios were calculated based on ICP measurements for Pt and specifications from manufacturer for Si and Al, whereas the surface atomic ratios were obtained by XPS.

Sample	Bulk		Surface (XPS)	
	Si/Al (at/at)	Pt/Al (at/at)	Si/Al (at/at)	Pt/Al (at/at)
Pt-Y/A-NH_3	0.80	0.0024	0.18	0.0003
Pt-Y/A-Cl	0.80	0.0025	0.18	0.0021
Pt-Y-NH_3 + A	0.78	0.0024	0.79	0.0001
Pt-A-Cl + Y	0.69	0.0025	0.83	0.0009

A) and Pt-A-Cl with zeolite Y (Pt-A-Cl + Y) were measured, that have similar bulk composition to the studied Pt/zeolite Y/γ-Al_2O_3 catalysts. For other relevant reference samples that were used for the fitting and standard deviations in the XPS measurements, we refer to Table S2.6.

The Si/Al surface ratios obtained by XPS were lower for the Pt/zeolite Y/γ-Al_2O_3 composite catalysts (Pt-Y/A-Cl and Pt-Y/A-NH_3) than their bulk Si/Al ratios, that can be attributed to coating of zeolite Y crystallites by γ-Al_2O_3 platelets thus attenuating the XPS signal of Si, as was also evidenced by TEM imaging (Figure S2.10).[25,44] Another factor that could contribute to the higher aluminum concentration as observed by XPS, is the preferential breaking at void-rich γ-Al_2O_3 domains during the grinding prior XPS measurements, whereas the more dense zeolite Y crystals stay intact.

The surface Pt/Al ratio reported in Table 2.3 for Pt-Y/A-Cl is by a factor 7 higher than for Pt-Y/A-NH_3, while a similar difference in Pt/Al ratio is observed for physical mixtures. For Pt-Y/A-NH_3 and Pt-Y-NH_3, we expect that the majority of Pt nanoparticles was located in zeolite Y 'underneath' the outer surface layer invisible to the XPS signal, while for Pt-Y/A-Cl and Pt-A-Cl the Pt nanoparticles are located on the γ-Al_2O_3 component where they can contribute to the XPS signal. When the zeolite Y crystallites are approximated as cubes with side length L (Figure 2.2), we anticipate that the difference in the XPS Pt/Al ratio depending on Pt nanoparticle location inside versus outside the zeolite crystals can be described by:

$$\left(\frac{I_{Pt}}{I_{Al}}\right)_{Pt\ in\ zeolite\ Y} = \left(\frac{I_{Pt}}{I_{Al}}\right)_{Pt\ on\ zeolite\ Y} \cdot \left(1 - \left(1 - \frac{2\lambda_{zeolite\ Y}}{L}\right)^3\right)$$

Wherein I_{Pt} and I_{Al} correspond to the Pt and Al peak areas, respectively, after correction for atomic sensitivity factors. $\lambda_{zeolite\ Y}$ is the EMFP of Pt 4f/Al 2p photoelectrons in zeolite Y. Assuming a uniform distribution of crystallites between 200-1000 nm and an EMFP of 4 nm, this should correspond to a difference of a factor ~50, that is a significantly larger difference than is observed here. A complicating factor for the studied composite catalysts, is that Pt nanoparticles outside zeolite Y are located on the γ-Al_2O_3 binder, with a significantly higher specific surface area of 314 m^2/g compared to the external surface of zeolite Y crystallites of ~8 m^2/g[45] leading to a lower surface coverage of Pt nanoparticles. This results in a lower Pt/Al surface ratio as observed by XPS and, consequently, a smaller difference between the Pt/zeolite Y/γ-Al_2O_3 composite catalysts based on the location of Pt nanoparticles.[43] Due to the structural complexity of the composite catalysts, the differences in XPS Pt/Al ratio cannot be accurately described by the 'Pt nanoparticle inside versus outside zeolite Y' approximation.

The quantification of the spectra of the Pt/zeolite Y/γ-Al_2O_3 composite catalysts was challenging, due to the low intensity of the Pt 4f signals and overlap in the Pt 4f and Al 2p core levels, while the isolated Pt 4d core levels could not be used because of a too low signal/noise ratio. Nevertheless, regarding the standard deviations in Pt/Al ratios indicated in Table S2.6, there is a significant difference in the XPS Pt/Al ratio between Pt-Y/A-NH_3 and Pt-Y/A-Cl, that is also observed for the physical mixture reference samples. The uncertainties in the measurements as a consequence of low Pt weight loading and the overlap in Al 2p and Pt 4f do therefore not affect the outcome of this study.

The accurate quantification of XPS spectra, proved to be a useful tool that is able to differentiate the

location of Pt nanoparticles in Pt/zeolite Y/γ-Al_2O_3 composite catalysts. A further quantification of XPS signals calls for a more elaborate study (i.e. the intensity of the Pt 4f signal could be significantly enhanced in resonant photoemission experiments at a synchrotron) and modelling efforts. Alternatively, another metal could be used that does not overlap strongly with core lines of the support.

2.3.4 CO infrared spectroscopy

Fourier-transform infrared spectroscopy (FTIR), transmission IR spectra combined with CO chemisorption can provide information on the electronic properties of Pt nanoparticles. Typically, uniformly sized supported Pt particles, results in a CO absorption band between 2100-2000 cm^{-1}.[46] Due to metal-support interactions, the electronic properties of Pt particles (1-2 nm) are affected by the support and therefore CO infrared spectroscopy can be used to determine Pt nanoparticle location.[47,48] Stakheev et al. previously studied metal-support interactions using CO-FTIR to determine the location of Pt metal clusters in K-L zeolite and were able to distinct between Pt particles inside or outside zeolite crystallites, whereas Liu et al. were able to describe differences in electronic properties between Pt/MCM-22 catalysts with different Pt dispersion and Pt nanoparticle location.[18,29] Here we have used samples with 1-2 nm Pt nanoparticles on a composite support and used references with Pt nanoparticles supported on either γ-Al_2O_3 (Pt-A-Cl) or zeolite Y (Pt-Y-NH_3) to obtain the CO band maximum corresponding to Pt nanoparticles on these supports. The CO surface coverage of Pt nanoparticles and temperature influences the degree of dipolar coupling between CO molecules.[46,49] All samples had similar Pt nanoparticle sizes that resulted in a similar CO coverage, although Pt nanoparticles located inside zeolite micropores could suffer from geometrical constraints making it more difficult for CO molecules to access the Pt sites. Figure 2.4 shows the FT-IR spectra of chemisorbed CO on the samples after subtraction of a background spectrum taken prior to CO adsorption. Both the Pt-Y/A-Cl and Pt-A-Cl samples, displayed in red in Figure 2.4 have a band maximum around ~2060 cm^{-1} that has been reported for CO coordinated to Pt particles that do not have extended crystal faces on Pt/Al_2O_3 at room temperature.[50]

This is a clear indication that for Pt-Y/A-Cl monodisperse Pt nanoparticles are located on the γ-Al_2O_3 binder. The band maximum of linearly coordinated CO on Pt-Y-NH_3 is present at 2077 cm^{-1}

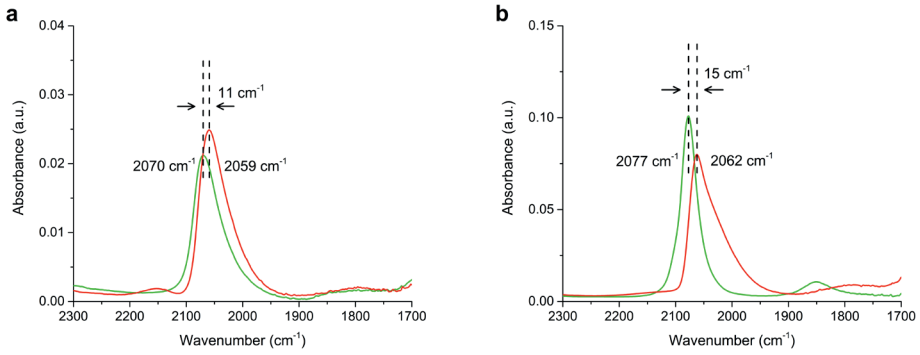

Figure 2.4. CO-FTIR of Pt-Y/A-NH_3 (a, green) and Pt-Y/A-Cl (a, red) showing a shift in band maximum likely as a results of metal-support interaction indicating a different Pt nanoparticle location. Pt-Y-NH_3 (b, green) and Pt-A-Cl (b, red) are provided as references.

shown in green in Figure 2.4b, in accordance with earlier studies reporting band maxima of 2083 cm^{-1} for Pt nanoparticles of ≤ 1 nm supported on H-Y zeolite.[51] The band maximum of Pt-Y/A-NH_3 is present at 2070 cm^{-1}, that is lower than for Pt-Y-NH_3 but significantly higher than for Pt-A-Cl. This could indicate that Pt nanoparticles could be mainly located in the zeolite Y component with a small fraction located on the γ-Al_2O_3 and the CO band maximum forms therefore an average of these populations of Pt nanoparticles. The downside of CO infrared spectroscopy is that differences between band maxima were small and a large overlap existed between relatively broad peaks. Overall, CO infrared spectroscopy data indicates Pt nanoparticles were located on γ-Al_2O_3 for Pt-Y/A-Cl and predominantly located inside zeolite Y micropores for Pt-Y/A-NH_3.

2.3.5 Catalysis

In a model reaction using 50 mg of catalyst, the catalytic activity of Pt/zeolite Y/γ-Al_2O_3 composite catalysts is determined for hydrogenation of β-phenylcinnamaldehyde (BPCMA, 0.81×1.0 nm)[28]. Due to its relatively large size, it has low diffusivity in zeolite Y micropores (0.74×0.74 nm)[52] and therefore can hardly reach Pt nanoparticles located inside the zeolite Y. If Pt nanoparticles are located on 'accessible' locations such as the zeolite Y mesopores or the external surface or the γ-Al_2O_3 binder, this would lead to fast conversion of the reactant. Similar approaches have been reported, either based on gas phase or liquid phase reactions, to determine the location of metal nanoparticles in microporous catalysts.[17–19,27,28]

Catalytic experiments were performed in a batch reactor loaded with equal amounts of BPCMA and catalyst. Figure 2.5 shows rate constants calculated from concentration profiles obtained by GC analysis of samples taken during the catalytic experiments. The references are used to study the catalytic activity of catalysts for which the location of Pt nanoparticles is known. For the concentration profiles that were used to calculate rate constants by fitting, we refer to Figure S2.11 and Table S2.8 and for product identification we refer to Figure S2.12 and S2.13.

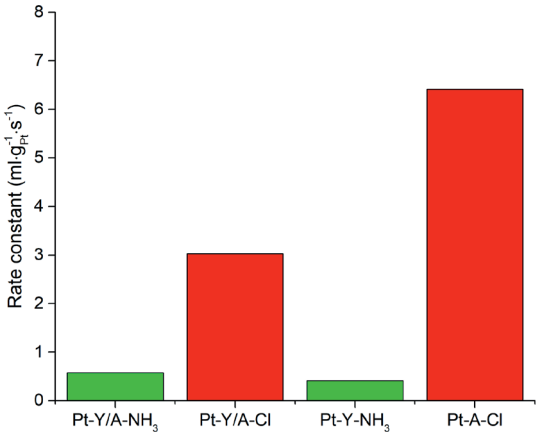

Figure 2.5. Catalytic activity of the different catalysts in the hydrogenation of β-phenylcinnamaldehyde (BPCMA). First order rate constants were obtained by fitting the reaction profiles with first order kinetic over 20 h of reaction. The composite catalysts have a Pt weight loading of 0.3-0.5 wt.%, whilst Pt-A-Cl and Pt-Y-NH_3 have weight loadings of 0.7-0.8 wt.%. Conditions: 135 mmol BPCMA/l, BPCMA/Pt (mol/mol) = 950, *i*-pro 6 ml, H_2O 1 ml, H_2 20 bar, 70 °C, 500 rpm.

The catalytic activity of Pt-Y/A-NH_3 and Pt-Y-NH_3 in this reaction was low, as could be expected for catalysts with Pt nanoparticles located inside zeolite micropores. Pt-Y/A-NH_3 had a factor 1.5 higher activity with respect to Pt-Y-NH_3 that can be contributed to a small fraction of Pt nanoparticles that are located on the γ-Al_2O_3 binder. Pt-Y/A-Cl on the other hand, had a factor 5 higher catalytic activity compared to Pt-Y/A-NH_3 that forms a strong indication that Pt nanoparticles are located on the γ-Al_2O_3 component for the former sample. The catalytic activity of Pt-A-Cl in the same reaction was also studied and was, as the activity of Pt-Y/A-Cl, significantly higher than Pt-Y/A-NH_3 and Pt-Y-NH_3. The difference in activity between Pt-Y/A-Cl and Pt-A-Cl could be attributed to Pt nanoparticles located in the zeolite, but more likely it is caused by undesired side reactions due to the reactivity of BPCMA on Brønsted acid sites. In the supporting information data is provided of a catalytic test performed with a mixture of Pt-A-Cl and zeolite Y powder, having a catalytic activity very similar to Pt-Y/A-NH_3. Overall, the catalytic experiments performed here proved to be a very useful tool in assessment of the Pt nanoparticle location in the Pt/zeolite Y/γ-Al_2O_3 composite catalysts.

2.4 Conclusions

The location of metal nanoparticles may have great impact on the performance of supported metal catalysts, but for structurally complex, practical catalysts used in industrial processes and consisting of multiple components, assessment of the location of metal particles presents great challenges.[25,53,54]

TEM has proven to be an accurate technique for determining the size and the location of metal nanoparticles in such catalysts, but a limitation is the amount of catalyst that can be sampled per measurement. In this work we explored quantitative XPS, CO infrared spectroscopy and catalysis as techniques that can offer information on metal location, while being able to sample larger amounts of catalysts. Quantitative XPS analysis of catalysts with equal Pt loading, equally sized Pt nanoparticles, but with Pt nanoparticles located either inside zeolite Y crystals or on the γ-Al_2O_3 binder of Pt/zeolite Y/γ-Al_2O_3 catalysts, lead to a significant differences in Pt/Al atomic ratios as a consequence of a different Pt nanoparticle location. By using CO infrared spectroscopy, a systematic shift in CO band maximum between catalysts was observed depending on the location of Pt nanoparticles, while by performing model reactions using a reactant molecule with low diffusivity in zeolite Y, large differences in activity were observed between catalysts with Pt nanoparticle located either inside zeolite Y or on the more accessible γ-Al_2O_3 binder. Therefore, the results of this study show that Pt/zeolite Y/γ-Al_2O_3 composite catalysts can be prepared with great control over Pt nanoparticle location and without significant variations within samples, simply by using either CPA or PTA as Pt precursor during catalyst synthesis.

Considering the techniques used in this study (quantitative XPS, CO infrared spectroscopy, catalysis) are more common laboratory techniques compared to TEM, the methods used in this study, and combinations thereof, can be a valuable asset in screening practical catalysts. Furthermore, they can be used to ensure that the results obtained from TEM imaging are not compromised by local variations in structure.

Acknowledgements

Mark Meijerink and Lars van der Wal (both UU) are acknowledged for TEM analysis of the microtomed samples. Nikos Nikolopoulos (UU) is acknowledged for performing N_2 physisorption measurements. Fouad Soulimani (UU) is acknowledged for providing the training for CO infrared spectroscopy measurements and Pascal Wijten (UU) is acknowledged for the training for the autoclave setup and GC. Shell Projects and Technology is acknowledged for supplying Zeolite Y/γ-Al_2O_3 extrudates and HMPA pseudo-boehmite.

References

[1] P. Munnik, P. E. de Jongh, K. P. de Jong, Chem. Rev. 2015, 115, 6687–6718.

[2] D. Y. Murzin, Catal. Letters 2017, 147, 613–621.

[3] S. Mitchell, N. L. Michels, J. Pérez-Ramírez, Chem. Soc. Rev. 2013, 42, 6094-6112.

[4] J. A. Martens, D. Verboekend, K. Thomas, G. Vanbutsele, J. P. Gilson, J. Pérez-Ramírez, ChemSusChem 2013, 6, 421–425.

[5] J. Weitkamp, ChemCatChem 2012, 4, 292–306.

[6] B. Peng, Y. Yao, C. Zhao, J. A. Lercher, Angew. Chemie Int. Ed. 2012, 51, 2072–2075.

[7] P. B. Weisz, Adv. Catal. 1962, 13, 137–190.

[8] N. Batalha, L. Pinard, C. Bouchy, E. Guillon, M. Guisnet, J. Catal. 2013, 307, 122–131.

[9] J. Francis, E. Guillon, N. Bats, C. Pichon, A. Corma, L. J. Simon, Appl. Catal. A Gen. 2011, 409–410, 140–147.

[10] B. D. Vandegehuchte, J. W. Thybaut, G. B. Marin, Ind. Eng. Chem. Res. 2014, 53, 15333–15347.

[11] A. Poursaeidesfahani, M. F. de Lange, F. Khodadadian, D. Dubbeldam, M. Rigutto, N. Nair, T. J. H. Vlugt, J. Catal. 2017, 353, 54–62.

[12] W. M. H. Sachtler, Z. Zhang, Adv. Catal. 1993, 39, 129–220.

[13] N. Wang, Q. Sun, J. Yu, Adv. Mater. 2018, 31, 1803966.

[14] N. Kosinov, C. Liu, E. J. M. Hensen, E. A. Pidko, Chem. Mater. 2018, 30, 3177–3198.

[15] J. Kim, W. Kim, Y. Seo, J. C. Kim, R. Ryoo, J. Catal. 2013, 301, 187–197.

[16] S. Altwasser, R. Gläser, A. S. Lo, P. H. Liu, K. J. Chao, J. Weitkamp, Microporous Mesoporous Mater. 2006, 89, 109–122.

[17] S. Goel, Z. Wu, S. I. Zones, E. Iglesia, J. Am. Chem. Soc. 2012, 134, 17688–17695.

[18] L. Liu, U. Díaz, R. Arenal, G. Agostini, P. Concepción, A. Corma, Nat. Mater. 2017, 16, 132–138.

[19] M. Moliner, J. E. Gabay, C. E. Kliewer, R. T. Carr, J. Guzman, G. L. Casty, P. Serna, A. Corma, J. Am. Chem. Soc. 2016, 138, 15743–15750.

[20] G. Prieto, J. Zečević, H. Friedrich, K. P. de Jong, P. E. de Jongh, Nat. Mater. 2012, 12, 34–39.

[21] C. J. Gommes, G. Prieto, J. Zečević, M. Vanhalle, B. Goderis, K. P. de Jong, P. E. de Jongh, Angew. Chemie - Int. Ed. 2015, 127, 11970–11974.

[22] O. Ben Moussa, L. Tinat, X. Jin, W. Baaziz, O. Durupthy, C. Sayag, J. Blanchard, ACS Catal. 2018, 8, 6071–6078.

[23] P. S. F. Mendes, A. L. Taleb, A. S. Gay, A. Daudin, C. Bouchy, J. M. Silva, M. F. Ribeiro, J. Mater. Chem. A 2017, 5, 16822-16833.

[24] J. Zečević, A. M. J. van der Eerden, H. Friedrich, P. E. de Jongh, K. P. de Jong, ACS Nano 2013, 7, 3698–3705.

[25] J. Zečević, G. Vanbutsele, K. P. de Jong, J. A. Martens, Nature 2015, 528, 245–248.

[26] A. J. Koster, U. Ziese, A. J. Verkleij, A. H. Janssen, K. P. de Jong, J. Phys. Chem. B 2000, 104, 9368–9370.

[27] N. Wang, Q. Sun, R. Bai, X. Li, G. Guo, J. Yu, J. Am. Chem. Soc. 2016, 138, 7484–7487.

[28] C. Liu, J. Liu, S. Yang, C. Cao, W. Song, ChemCatChem 2016, 8, 1279–1282.

[29] H. J. Cho, D. Kim, J. Li, D. Su, B. Xu, J. Am. Chem. Soc. 2018, 140, 13514-13520.

[30] A. Y. Stakheev, E. S. Shpiro, N. I. Jaeger, G. Schulz-Ekloff, Catal. Letters 1995, 32, 147–158.

[31] J. Guzman, B. C. Gates, Dalt. Trans. 2003, 3303-3318.

[32] A. Kulkarni, R. J. Lobo-Lapidus, B. C. Gates, Chem. Commun. 2010, 46, 5997–6015.

[33] F. Winter, G. L. Bezemer, C. van der Spek, J. D. Meeldijk, A. J. van Dillen, J. W. Geus, K. P. de Jong, Carbon 2005, 43, 327–332.

[34] G. T. Whiting, N. Nikolopoulos, I. Nikolopoulos, A. D. Chowdhury, B. M. Weckhuysen, Nat. Chem. 2019, 11, 23–31.

[35] N. L. Michels, S. Mitchell, J. Pérez-Ramírez, ACS Catal. 2014, 4, 2409–2417.

[36] L. I. van der Wal, K. P. de Jong, J. Zečević, ChemCatChem 2019.

[37] E. Plessers, J. E. van den Reijen, P. E. de Jongh, K. P. de Jong, M. B. J. Roeffaers, ChemCatChem 2017, 9, 4562–4569.

[38] P. Munnik, P.E. de Jongh, K.P. de Jong, J. Am. Chem. Soc. 2014, 136, 7333-7340.

[39] X. Hao, W. A. Spieker, J. R. Regalbuto, J. Colloid Interface Sci. 2003, 267, 259–264.

[40] M. Schreier, S. Teren, L. Belcher, J. R. Regalbuto, J. T. Miller, Nanotechnology 2005, 16, S582-S591.

[41] M. P. Seah, W. A. Dench, Surf. Interface Anal. 1979, 1, 2–11.

[42] H. P. C. E. Kuipers, Solid State Ionics 1985, 16, 15–22.

[43] F. P. J. M. Kerkhof, J. A. Moulijn, J. Phys. Chem. 1979, 83, 1612–1619.

[44] G. T. Whiting, S. Chung, D. Stosic, A. D. Chowdhury, L. I. van der Wal, D. Fu, J. Zečević, A. Travert, K. Houben, M. Baldus, et al., ACS Catal. 2019, 4792–4803.

[45] A. H. Janssen, A. J. Koster, K. P. de Jong, Angew. Chemie Int. Ed. 2001, 40, 1102–1104.

[46] F. Thibault-Starzyk, F. Maugé, in Charact. Solid Mater. Heterog. Catal. From Struct. to Surf. React. (Eds.: M. Che, J. Vedrine), 2012, pp. 1–48.

[47] A. I. Frenkel, M. W. Small, J. G. Smith, R. G. Nuzzo, K. O. Kvashnina, M. Tromp, J. Phys. Chem. C 2013, 117, 23286-23294.

[48] A. Elsen, U. Jung, F. Vila, Y. Li, O. V. Safonova, R. Thomas, M. Tromp, J. J. Rehr, R. G. Nuzzo, A. I. Frenkel, J. Phys. Chem. C 2015, 119, 25615–25627.

[49] D. C. Koningsberger, D. E. Ramaker, J. T. Miller, J. de Graaf, B. L. Mojet, Top. Catal. 2001, 15, 35–42.

[50] R. Barth, R. Pitchai, R. L. Anderson, X. E. Verykios, J. Catal. 1989, 116, 61–70.

[51] T. Visser, T. A. Nijhuis, A. M. J. Van Der Eerden, K. Jenken, Y. Ji, W. Bras, S. Nikitenko, Y. Ikeda, M. Lepage, B. M. Weckhuysen, J. Phys. Chem. B 2005, 109, 3822–3831.

[52] C. Baerlocher, L. B. McCusker, W. M. Meier, D. H. Olson, "Database of Zeolite Structures," can be found under http://www.iza-structure.org/databases, 2019.

[53] F. Meirer, S. Kalirai, D. Morris, S. Soparawalla, Y. Liu, G. Mesu, J. C. Andrews, B. M. Weckhuysen, Sci. Adv. 2015, 1, 1–12.

[54] F. Meirer, D. T. Morris, S. Kalirai, Y. Liu, J. C. Andrews, B. M. Weckhuysen, J. Am. Chem. Soc. 2015, 137, 102–105.

Supporting information

Table S2.4. Employed characterization techniques with the investigated area, corresponding studied volume and the mass of the material studied.

Technique	Sampled area	Sampling depth	Total studied sample volume (m^3)	Total studied sample mass (g)
TEM	Field of view: 200 nm × 200 nm	Sample thickness: 70 nm	$2.8 \cdot 10^{-21}$	$\sim 10^{-14}$
Quantitative XPS	X-ray spot size: 400 µm ø	EMFP: 1-5 nm	10^{-16}-10^{-15}	$\sim 10^{-9}$
CO infrared spectroscopy	Weight of pellet determined on an analytical balance			$\sim 10^{-2}$
Catalysis	Weight of catalyst determined on an analytical balance			$5 \cdot 10^{-2}$

Supporting Information 2.1

TEM

The field of view of a typical high magnification TEM image is 200 x 200 nm and the microtomed samples have a thickness of 70 nm. We assume that the field of view of the TEM is completely filled with sample and therefore the studied volume of sample per image corresponds to $2.8 \cdot 10^{-21}$ m^3. The highly porous metal oxide supports used in this study have a density in the order of 10^6 $g \cdot m^{-3}$, and thus the amount of material studied is in the range of 10^{-15}-10^{-14} g per TEM image. For TEM measurements commonly multiple TEM images are made of different areas of the sample, increasing the total amount of studied material by 1, or maximally 2 orders of magnitude.

Quantitative XPS

For the XPS measurements, a monochromatic Al Kα source of hν = 1486.6 eV was used and therefore the kinetic energy of Pt 4f photoelectrons will be in the range of 1410-1415 eV, while kinetic energies for Al 2s, Al 2p, Si 2p core levels will be between 1360-1415 eV. The escape depth of photoelectrons (with a kinetic energy in the range of 1360-1415 eV) for metal oxide supports is between 1-5 nm (see SI section 1.2).[1,2] For the XPS measurements a spot size of 400 µm diameter was used corresponding to an X-ray irradiated area of $1.3 \cdot 10^{-7}$ m^2 and therefore the sampled volume is in the order of 10^{-16}-10^{-15} m^3 per measurement. Assuming a typical porous metal oxide density in the order of 10^6 $g \cdot m^{-3}$ will give a sampled amount of material in the range of 10^{-10}-10^{-9} g, which is multiple orders of magnitude more than what is sampled in a typical TEM experiment. Performing multiple measurements at different locations on the sample can further increase the amount of sampled material (for this study 2 locations were measured).

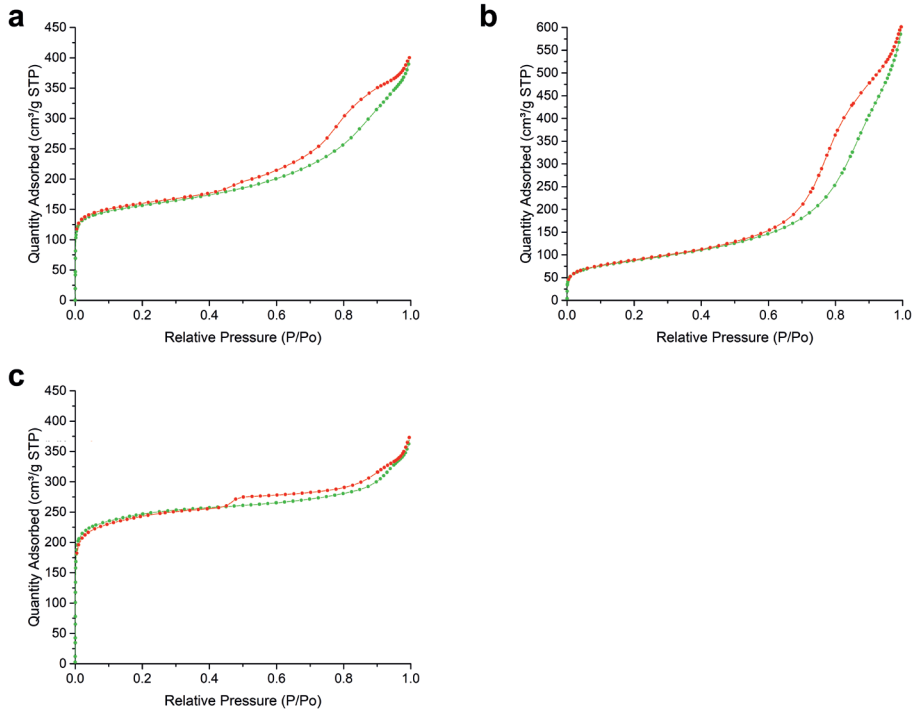

Figure S2.5. N_2 physisorption isotherms of the Y/A (zeolite Y/γ-Al_2O_3) composite support (a), the bare A (γ-Al_2O_3) binder (b), zeolite Y (Zeolyst CBV760) (c). The γ-Al_2O_3 was prepared by calcination of pseudo-boehmite at 550 °C (2 h, 5 °C/min).

Table S2.5. Results of textural analysis of the Y/A composite support and single components.

	BET surface area (m^2/g)	BJH pore volume (cm^3/g)	t-plot micropore volume (cm^3/g)	t-plot external surface area (m^2/g)
Y/A	-	0.44	0.15	209
A (γ-Al_2O_3)	314	0.89	0.02	294
Y (zeolite Y)	-	0.24	0.28	231

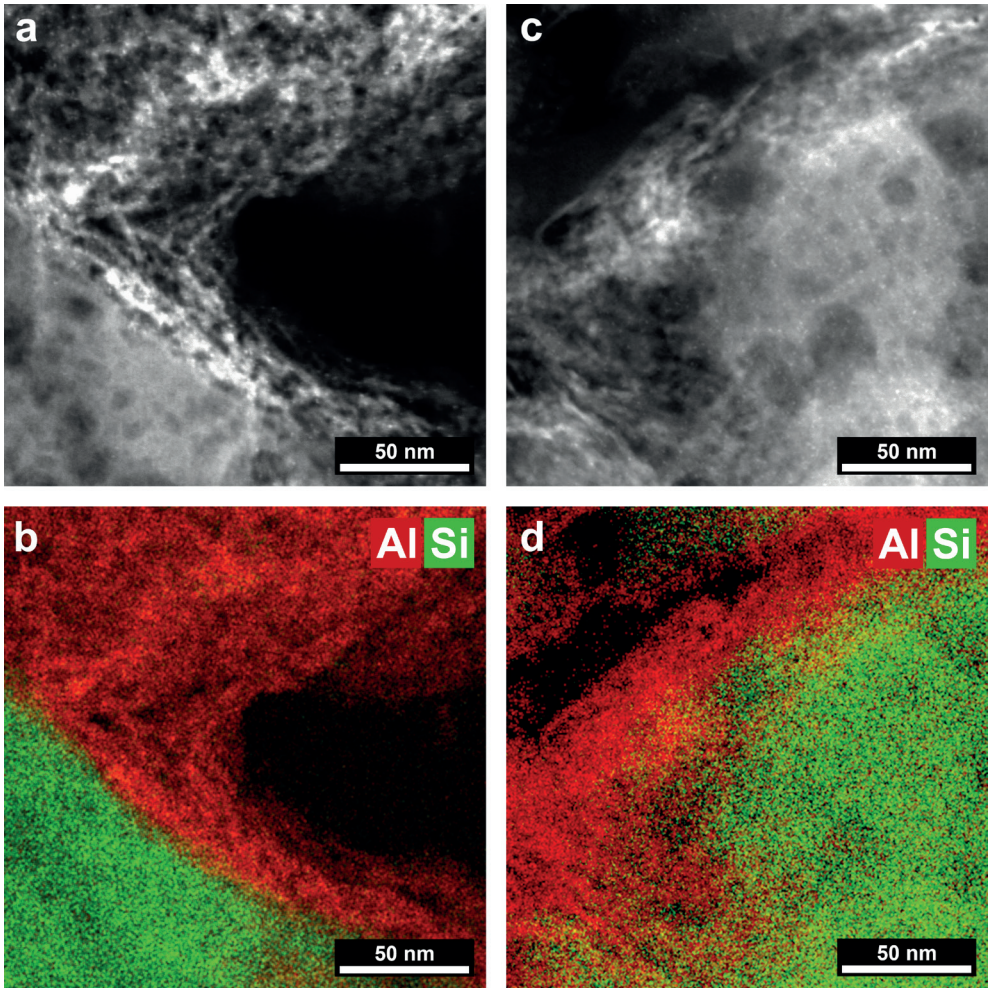

Figure S2.6. HAADF-STEM images of microtomed sections of Pt-Y/A-Cl (a) where Pt nanoparticles (apparent as bright white spots) are located on the γ-Al_2O_3 component, corresponding to the red region in the EDX elemental map (b) of the same area. HAADF-STEM images of microtomed sections of Pt-Y/A-NH_3 (c) with Pt nanoparticles located in the zeolite Y that can be identified as the green region in the EDX elemental map (d) of the same area.

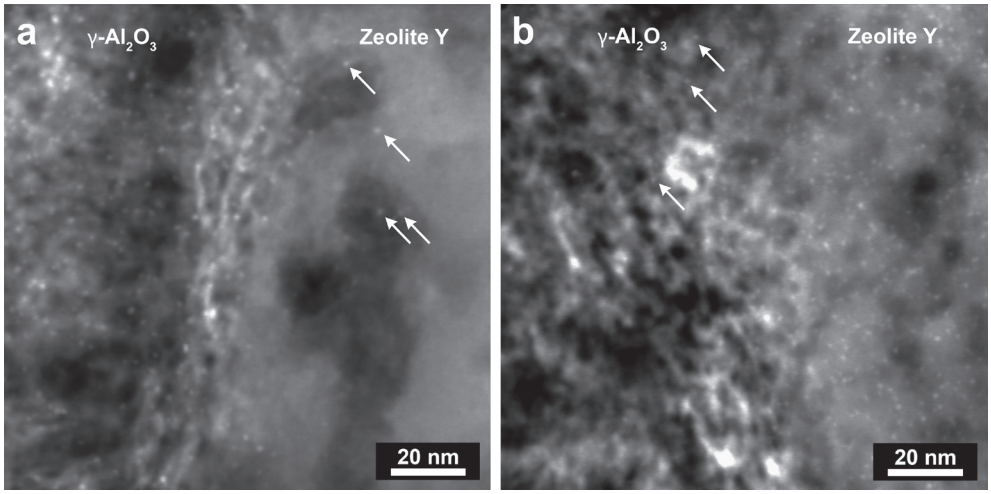

Figure S2.7. HAADF-STEM images of microtomed sections of Pt-Y/A-Cl (a) and Pt-Y/A-NH_3 (b) with the zeolite Y and γ-Al_2O_3 components indicated in the figure. The ~1.5 nm Pt nanoparticles can be identified as white dots, almost exclusively present in the γ-Al_2O_3 for Pt-Y/A-Cl (a) and almost exclusively present in zeolite Y for Pt-Y/A-NH_3 (b). White arrows indicate Pt nanoparticles that are located close to the interface of zeolite Y and γ-Al_2O_3 and that could be located on the 'opposite' component but difficult to determine unequivocally.

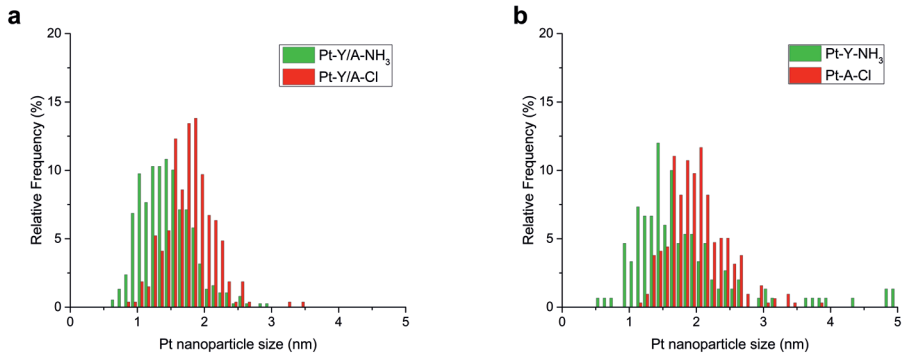

Figure S2.8. Histogram showing the size distribution of Pt nanoparticles of Pt-Y/A-Cl and Pt-Y/A-NH_3 as obtained from measuring individual particles on HAADF-STEM images. For Pt-Y/A-Cl 268 particles were counted, for Pt-Y/A-NH_3 379 particles (a). The size distribution of Pt nanoparticles of Pt-A-Cl and Pt-Y-NH_3. For Pt-A-Cl 317 particles were counted, for Pt-Y/A-NH_3 162 particles (b).

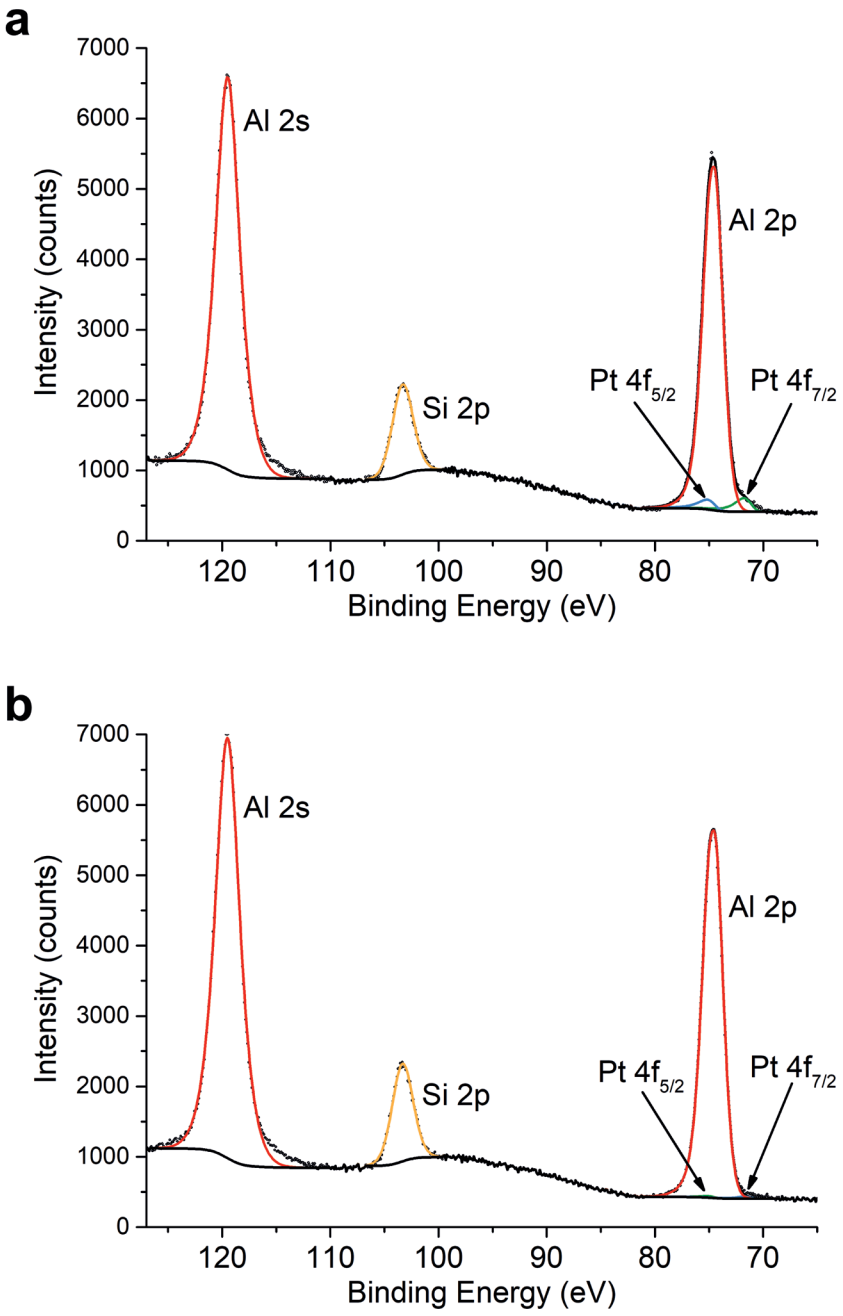

Figure S2.9. The high resolution XPS regional spectra showing the Al 2s. Si 2p, Al 2p, and Pt 4f core levels of Pt-Y/A-Cl (a) and Pt-Y/A-NH_3 (b). XPS data is depicted with small black circles. Color scheme: Pt $4f_{5/2}$ (light blue), Pt $4f_{7/2}$ (dark green), Al 2p and Al 2s (red), Si 2p (orange), Shirley background and overall fit (black).

Table S2.6. Summary of XPS results of measurements on catalyst samples and reference measurements used for spectra quantification, combined with Pt wt.%, bulk atomic ratios for Pt from ICP and manufacturers specification for Si and Al. Pt particle size was obtained from TEM analysis. Standard deviation for Pt nanoparticle sizes was based on the deviation in measuring 162-379 Pt nanoparticles from TEM images. The standard deviation in XPS measurements indicated here was based on results of two measurements on different spots on the sample. The bulk atomic ratio for physical mixtures are based on the amount of each compound used for the physical mixture, determined by weighing the powders on an analytical balance.

Sample	Pt wt.%	d_{Pt} (nm)	Bulk (at/at)		Surface (at/at)	
			Si/Al	Pt/Al	Si/Al	Pt/Al
Composite catalyst						
Pt-Y/A-NH_3	0.47	1.4 ± 0.4	0.80	0.0024	0.176 ± 0.001	0.0003 ± 0.0001
Pt-Y/A-Cl	0.48	1.8 ± 0.4	0.80	0.0025	0.182 ± 0.009	0.0021 ± 0.0003
Physical mixtures						
Pt-Y-NH_3 + A	0.47	2.2 ± 1.6	0.78	0.0024	0.79 ± 0.01	0.00015 ± 0.00003
Pt-A-Cl + Y	0.52	1.5 ± 0.3	0.69	0.0025	0.827 ± 0.004	0.0009 ± 0.0002
Pt on single component supports						
Pt-Y-NH_3	0.95	2.2 ± 1.6	30	0.0911	17 ± 3	0.0034 ± 0.0002
Pt-A-Cl	0.97	1.5 ± 0.3	-	0.0026	-	0.0023 ± 0.0001
Supports						
Y/A	-	-	0.80	-	0.199 ± 0.005	-
Y (Zeolite Y)	-	-	30	-	21 ± 6	-
A (γ-Al_2O_3)	-	-	-	-	-	-

Supporting Information 2.2

Experimental details XPS measurements

Prior to the XPS measurements, the catalysts grains were mortared to a fine powder to increase the surface to volume ratio of the sample. In all samples elements C, O, Al, Si, Pt are present. Some samples contain small amounts of Cl. Two spots per sample have been measured. Binding energy calibration was done by setting the C 1s binding energy of the adventitious carbon CC/CH (sp^3) peak to 284.8 eV. The presence of Pt next to Al complicates analysis due to the overlapping main core levels Al 2p and Pt 4f. From survey spectra, a quantitative analysis is thus not possible. Region scans have been taken for all samples covering the core levels Pt 4f / Al 2p, Si 2p and Al 2s. The area of the Al 2p peak was put into ratio with the area of the Al 2s for a reference pure Al_2O_3 sample. The same ratio has been applied to the Pt/zeolite Y/γ-Al_2O_3 samples and reference samples provided in Table S2.6, to determine the area of the Al 2p in the overlapping Pt 4f / Al 2p region based on the fitting of the isolated Al 2s peak. The remaining area was then fitted to two components with asymmetric (metallic) line shape for Pt $4f_{5/2}$ and Pt $4f_{7/2}$ core levels, whereas the line shape function, the FWHM were kept identical for both peaks of the spin-orbit split doublet and the S-O splitting was fixed to 3.35 eV. The BE of Pt $4f_{7/2}$ ranges between 71.1-71.5 eV, indicating metallic Pt. The isolated Pt 4d core level is much weaker and could not be used for quantification due to the low amounts of Pt present in the samples.

The intensities of Pt 4f core levels for Pt-Y/A-NH_3 and Pt-Y-NH_3 + A are close to the detection limit that results in a large relative error in Pt/Al ratio. By manually altering the constraints used during the fitting of the spectra, changes of +/- 100% in the fitted Pt 4f area of Pt-Y/A-NH_3 and Pt-Y-NH_3 + A could be introduced. For Pt-Y/A-Cl and Pt-A-Cl + Y, samples with higher Pt/Al ratio's, such variations were not observed upon altering the constraints.

Electron Mean Free Path (EMFP) in γ-Al_2O_3

Table S2.7. Literature data of Al_2O_3 and SiO_2.

	Solid density (g/cm³), Ref:[3]	EMPF (nm) in bulk solids E_{kin} = 1415 eV, Ref:[2]
Al_2O_3	3.65	1.8
SiO_2	2.196[a]	2.6

a) Density of fused silica.

In this case, Pt 4f, Al 2p and Si 2p photoelectrons are studied with a kinetic energy of 1380-1420 eV that need to emit from samples that consist of zeolite Y and γ-Al_2O_3 that have very different morphology and composition. γ-Al_2O_3 consists of an irregular platelet like structure with high surface to volume ratio that can be approximated as infinite sheets as has been proposed by Kerkhof et al.[4]

$$t_s = \frac{2}{\rho_s \cdot \sigma_s} = \frac{2}{314\ m^2 \cdot g^{-1} \cdot 3.65 \cdot 10^6\ g \cdot m^{-3}} = 1.8\ nm$$

The approximated γ-Al_2O_3 sheet thickness is similar to the EMFP in bulk Al_2O_3 (Table S2.7) and therefore the Pt XPS signal of Pt nanoparticles located on γ-Al_2O_3 will mainly consist of

contributions of Pt nanoparticles located on the surface of externally oriented γ-Al_2O_3 platelets, with minor contributions from Pt nanoparticles underneath the γ-Al_2O_3 surface layer.

Electron Mean Free Path (EMFP) in zeolite Y

The zeolite Y crystallites of the zeolite Y/γ-Al_2O_3 composite support are a steamed and acid leached derivative of Na-zeolite Y (Zeolyst CBV100) that consists of large crystallites of 200-1000 nm in size and a corresponding small external surface area of ~8 m^2/g.[5] In order to correct for the effect of zeolite microporosity on the EMFP, the void fraction in zeolite Y is determined by using the zeolite Y micropore volume from N_2 physisorption using the t-plot method. The void fraction of zeolite Y is given by:

$$\phi_{\text{zeolite Y}} = \frac{\rho_{SiO_2} \cdot V_{\text{zeolite Y}}}{1 + \rho_{SiO_2} \cdot V_{\text{zeolite Y}}} = \frac{2.20\,\text{g}\cdot\text{cm}^{-3} \cdot 0.28\,\text{cm}^{-3}\cdot\text{g}^{-1}}{1 + 2.20\,\text{g}\cdot\text{cm}^{-3} \cdot 0.28\,\text{cm}^{-3}\cdot\text{g}^{-1}} = 0.38$$

Using the EMFP of silica (Table S2.7), the electron mean free path in zeolite Y is then given by:

$$\text{EMFP}_{\text{zeolite Y}} = \frac{\text{EMFP}_{SiO_2}}{1-\phi} = \frac{2.6\,\text{nm}}{1-0.38} \approx 4\,\text{nm}$$

Stakheev et al. have previously reported a void fraction of 0.47, based on the water content of hydrated faujasite, resulting in an apparent EMFP of ~5 nm, which corresponds to the first two or three unit cells (2.5 nm) of zeolite Y subjacent to the external surface.[6,7]

References

[1] M. P. Seah, W. A. Dench, Surf. Interface Anal. 1979, 1, 2–11.
[2] T. Reich, V. G. Yarzhemski, V. I. Nefedov, J. Electron Spectros. Relat. Phenomena 1988, 46, 255–267.
[3] J. Rumble, Ed. , Handbook of Chemistry and Physics, CRC Press/Taylor & Francis, Boca Raton, FL., 2018.
[4] F. P. J. M. Kerkhof, J. A. Moulijn, J. Phys. Chem. 1979, 83, 1612–1619.
[5] A. H. Janssen, A. J. Koster, K. P. de Jong, Angew. Chemie Int. Ed. 2001, 40, 1102–1104.
[6] A. Y. Stakheev, W. M. H. Sachtler, J. Chem. Soc. Faraday Trans. 1991, 87, 3703–3708.
[7] T. L. Barr, M. A. Lishka, J. Am. Chem. Soc. 1986, 108, 3178–3186.

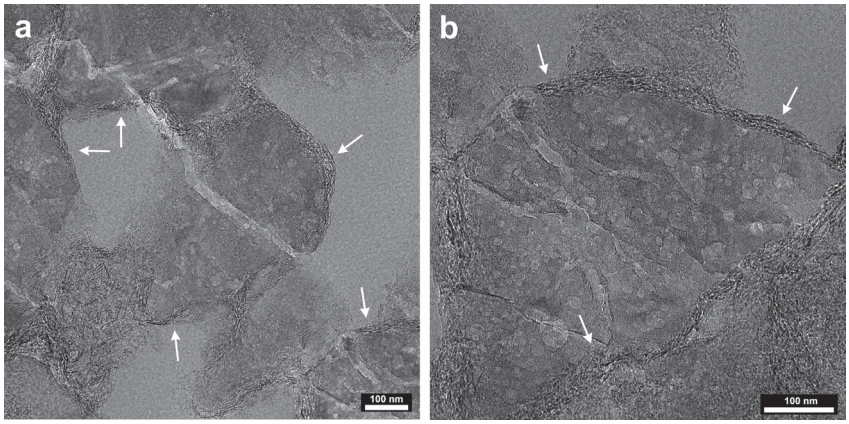

Figure S2.10. Bright-field TEM images (a,b) of ~70 nm microtome-cut sections at different magnifications showing the Y/A support. Zeolite Y crystals are coated with a layer of γ-Al_2O_3, as indicated by arrows. The γ-Al_2O_3 can be identified by the typical acicular (needle-like) morphology while zeolite Y consists of mesoporous crystallites between 200-1000 nm in size.

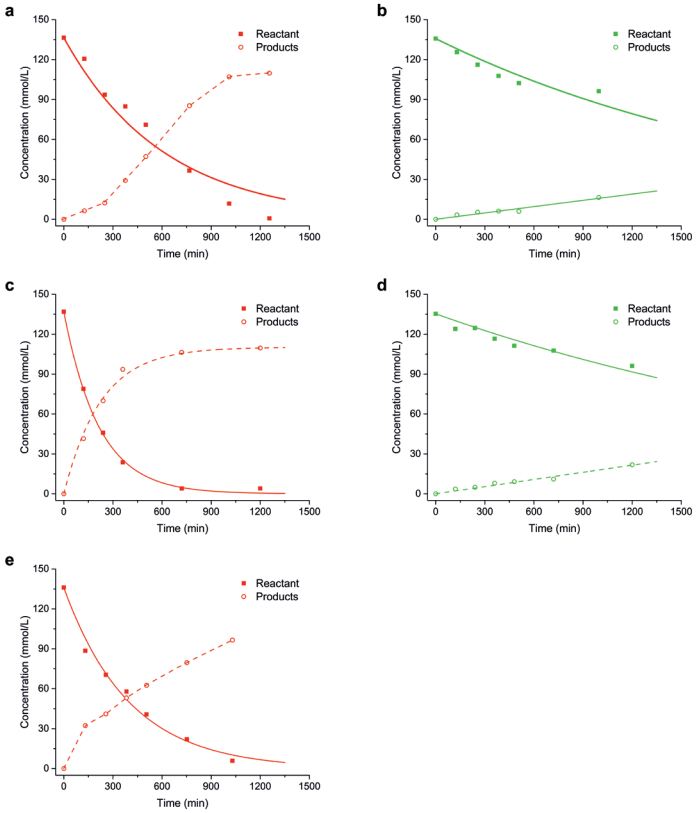

Figure S2.11. Reaction profiles showing concentrations of BPCMA (filled symbols) and Products (open symbols) as a function of time. Solid lines are first order kinetic fits of BPCMA as reactant concentration, dotted lines indicate the concentration of products and are added to guide the eye. Catalysts: Pt-Y/A-Cl (a), Pt-Y/A-NH_3 (b), Pt-A-Cl (c). Pt-Y-NH_3 (d) and Pt-A-Cl + Y (e).

Table S2.8. The weight based rate constant was obtained by fitting the concentration profiles to first-order kinetics (normalized to the amount of Pt per unit volume in the reactor), using close to identical initial concentrations of BPCMA. The Pt loading of the catalysts was determined by ICP, whereas the initial concentration of BPCMA was obtained by weighing the reactant on an analytical balance. The mass balance of the reaction (sum of products and reactants divided by amount of reactant at t = 0) as obtained by GC analysis is also reported.

	Pt. loading (wt.%)	$C_{t=0}$ (mmol/l)	k_w (ml·g_{Pt}^{-1}·s^{-1})	Mass balance (%)
Pt-Y/A-Cl	0.3	136	3.0	81
Pt-Y/A-NH_3	0.4	136	0.6	83
Pt-A-Cl	0.7	137	6.4	83
Pt-Y-NH_3	0.8	135	0.4	87
Pt-A-Cl + Y	0.4	137	3.5	81

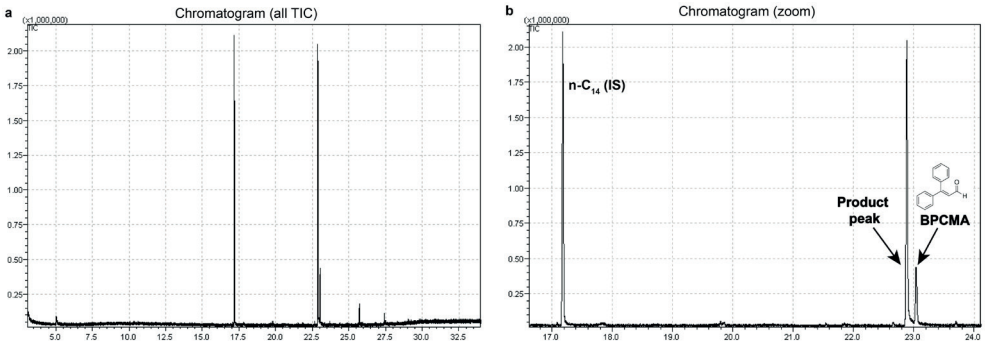

Figure S2.12. The full (a) or zoomed (b) GC-MS chromatogram of a sample taken from reaction mixture after 360 minutes with the Pt-A-Cl catalyst. Chromatograms show separate peaks for BPCMA and the formed product.

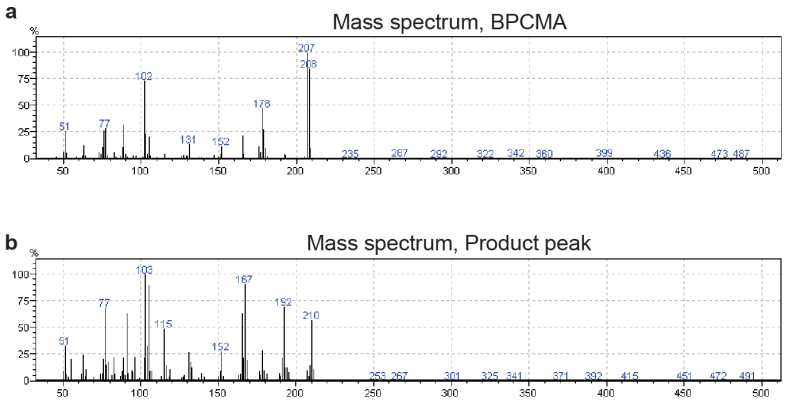

Figure S2.13. Mass spectra with peaks corresponding to BPCMA (a) and the mass spectra corresponding to the product peak (b). BPCMA and the formed products are not available in the NIST database. From the fragmentation in the MS spectrum it is apparent that the predominant product is an alcohol derivative of BPCMA, whereby the carbonyl group is converted into a hydroxyl group.

Chapter 3

Influence of Nanoscale Intimacy and Zeolite Micropore Size on the Performance of Bifunctional Catalysts for *n*-Heptane Hydroisomerization

This chapter is based on: J. Oenema, J. Harmel, R. Pérez Vélez, M.J. Meijerink, W. Eijsvogel, A. Poursaeidesfahani, T.J.H. Vlugt, J. Zečević, K.P. de Jong, ACS Catalysis 10 (2020) 13, 14245-14257.

Abstract

In this study, Pt nanoparticles on zeolite/γ-Al_2O_3 composites (50/50 wt.) were located either in the zeolite or on the γ-Al_2O_3 binder, hereby varying the average distance (intimacy) between zeolite acid sites and metal sites from 'closest' to 'nanoscale'. The catalytic performance of these catalysts was compared to physical mixtures of zeolite and Pt/γ-Al_2O_3 powders, that provide a 'microscale' distance between sites. Several beneficial effects on catalytic activity and selectivity for *n*-heptane hydroisomerization were observed when Pt nanoparticles are located on the γ-Al_2O_3 binder in nanoscale proximity with zeolite acid sites, as opposed to Pt nanoparticles located inside zeolite crystals. On ZSM-5 based catalysts mostly monobranched isomers were produced, and the isomer selectivity of these catalysts was almost unaffected with an intimacy ranging from closest to microscale, that can be attributed to the high diffusional barriers of branched isomers within ZSM-5 micropores. For composite catalysts based on large pore zeolites (zeolite Beta and zeolite Y), the activity and selectivity benefitted from the nanoscale intimacy with Pt, compared to both the closest and microscale intimacies. Intracrystalline gradients of heptenes as reaction intermediate are likely contributors to differences in activity and selectivity. This chapter aims to provide insights on the influence of the metal-acid intimacy in bifunctional catalysts based on zeolites with different framework topology.

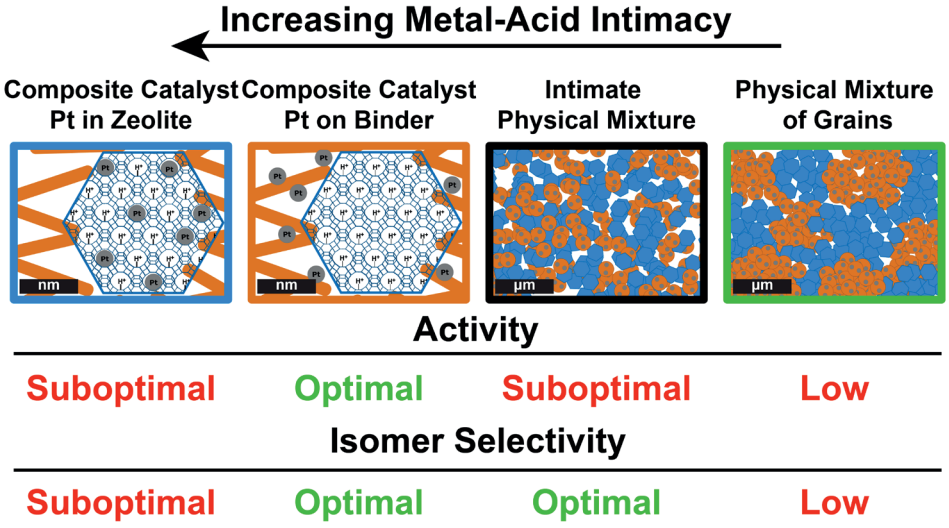

3.1. Introduction

Solid bifunctional catalysts, that combine two independent catalytic functions within one catalyst particle, are a popular class of catalysts, which typically have unique properties that cannot be obtained by the use of monofunctional catalysts.[1–5] For example, bifunctional metal-acid catalysts find application as highly stable catalysts in large scale hydrocracking and hydroisomerization processes in oil refineries for the production of transportation fuels and chemicals.[6] Bifunctional catalysts are also investigated for the hydrodeoxygenation and subsequent hydrocracking of biomass derived feedstock towards hydrocarbons.[7,8] Other investigated applications are in the hydrogenation of CO or CO_2 where beneficial effects on product selectivity towards lower alkenes (C_2-C_4) and aromatics are reported for bifunctional catalysts.[2–4,9]

Bifunctional catalysts, used for the conversion of hydrocarbons, consist of a metal function catalyzing (de)hydrogenation, which can be highly active noble metals like platinum or palladium, or more abundant but less active metal sulfides such as nickel and nickel-molybdenum sulfide or cobalt-molybdenum sulfide. The acid function for industrial catalysts is commonly obtained by using halogenated alumina, zeolites or amorphous silica-alumina, and is responsible for alkene protonation and subsequent isomerization and cracking.[10] Catalysts for industrial hydroisomerization processes are based on either Pt supported on chlorinated Al_2O_3 (6-7 wt.% Cl), or Pt supported on Mordenite zeolite. The latter catalyst operates at higher temperatures that is unfavorable in view of the thermodynamic equilibrium of the isomerization reaction[11], but with the advantage of being less sensitive to sulfur and water.

Zeolites are crystalline aluminosilicate materials possessing a regular structure of micropores (<2 nm in diameter) that are of a similar size as hydrocarbon molecules, and when the kinetic diameter of a molecule approaches the size of a micropore, their diffusivity may vary greatly.[12,13] Hampered intracrystalline diffusion in micropores may lead to concentration gradients within zeolite crystals, compromising catalytic activity and/or selectivity, e.g. by promoting undesired secondary cracking reactions.[14–16] Several studies report methods to overcome intracrystalline diffusion limitations in zeolites, e.g. by shortening the average micropore length by using nanocrystalline zeolites[17] or by using post-synthesis treatments to create mesopores in zeolite crystals that act as highways of diffusion[18–21].

A zeolite possesses shape selective properties when the fitting of a hydrocarbon molecule in a zeolite pore directly influences its conversion.[22] For example, in hydroisomerization of *n*-hexane or *n*-heptane over medium pore ZSM-5 based catalysts, the terminally monobranched isomers (e.g. 2-methylpentane) are preferentially formed over the internally monobranched isomers, which is attributed to the faster diffusion in ZSM-5 micropores of the former (i.e. product shape selectivity).[23] Bulky dibranched hexanes and heptanes are formed to a limited extent over these catalysts, due to steric constraints and fast cracking of these molecules in ZSM-5 micropores.[23,24] Large pore (12 membered ring) zeolites such as, zeolite Beta and zeolite Y impose much less steric constraints on branched isomers of hexane and heptane, and are therefore often considered to be 'non-shape selective' zeolites for these processes, with an isomer product distribution that is close to thermodynamic equilibrium.[24,25]

Hydrocarbon adsorption and diffusion in zeolites has been studied by a variety of experimental techniques: Pulsed Field Gradient Nuclear Magnetic Resonance[26], Uptake rate measurements

(e.g. combined with a Tapered Element Oscillating Microbalance)[27,28] and also Single-molecule Fluorescence Microscopy has been employed to determine the diffusion coefficient of a fluorescent hydrocarbon probe in a zeolite matrix.[29] Theoretical studies have also often focused on hydrocarbon diffusion, either by establishment of a Microkinetic-Model of a catalytic process[14,23], or by Molecular Modeling using: (dynamically corrected) Transition State Theory[30], Monte Carlo simulations[24,31,32] or Molecular Dynamics[33].

For bifunctional metal-acid catalysts, the diffusivity of the alkene intermediates between metal and acid sites determines the maximum distance between these sites before the activity or selectivity is affected by diffusion limitations.[34,35] Microporous all-silica materials have been used to study alkene adsorption and diffusion, where the alkene properties are very similar to their alkane equivalents.[36] However, the strong adsorption and high reactivity of alkenes on protonic sites hinders such studies in H-zeolites, often used for catalysis, but a significantly lower diffusivity of alkenes versus the alkane equivalent is to be expected.[37] Another factor that may contribute to this difference in diffusivity are dipole-dipole interactions between a polar aluminum-rich zeolite and the C=C bond of alkenes, causing the alkene to interact more strongly than the alkane equivalent.[38,39]

Noh et al. have recently studied different ZSM-5 crystal sizes in *n*-heptane hydroisomerization, whereby the metal function was provided by physical mixing with Pt/SiO_2, and was thus located outside the zeolite crystals.[15] For a range of differently sized ZSM-5 crystals, a constant turnover frequency per acid site was obtained, but use of the largest ZSM-5 crystals led to a lower turnover frequency, that was attributed to the limited diffusion of heptenes between extracrystalline regions and the intracrystalline zeolite acid sites. A number of examples have also indicated that for large pore zeolites, hampered diffusion of alkenes may also impact selectivity, as was inferred by Zečević et al. using a zeolite $Y/\gamma\text{-}Al_2O_3$ composite (50/50 wt.) as support for Pt nanoparticles, that were either located in zeolite Y or on the $\gamma\text{-}Al_2O_3$ binder, closely outside (i.e. within nanoscale proximity) the zeolite Y crystals.[40] In the conversion of *n*-C_{10} and *n*-C_{19}, both catalysts had a similar catalytic activity indicating the rate of the reaction was not limited by intracrystalline diffusion limitations of linear alkenes, but favorable effects on isomer selectivity were reported for the catalyst with Pt nanoparticles located on the $\gamma\text{-}Al_2O_3$ binder. It was suggested that the formation of branched alkene intermediates, formed on Pt nanoparticles inside the zeolite crystals, led to higher concentrations in the zeolite resulting in enhanced cracking. Whenever Pt nanoparticles are located on the $\gamma\text{-}Al_2O_3$ binder, alkene intermediates coming from 'outside' may react in the outer layers of the zeolite crystals and branched alkenes may quickly diffuse out. Similar favorable effects on selectivity were reported in the conversion of *n*-heptane, a hydrocarbon with relatively high diffusivity, when Pt nanoparticles were located closely outside zeolite Beta crystals on a zeolite $Beta/Al_2O_3$ composite[41], and for one-dimensional ZSM-22 and Mordenite zeolites[42], but not for ZSM-5 over a range of crystallite sizes[17].

A number of recent studies have reported innovative approaches to prepare bifunctional catalysts with varying levels of metal-acid intimacy at the nanometer length scale, such as preferential adsorption of a Pt complex on a composite support[40–44] or impregnation of previously synthesized Pt colloids to locate the metal function outside zeolite crystals[17]. Easy-to-prepare physical mixtures of a supported metal catalyst and zeolite are a more "traditional" method to

vary the metal-acid intimacy at the micrometer or millimeter length scale, that are be applied in the form of fine powders, grains or stacked beds.[15,16,45–47] This approach is only suitable to obtain catalysts with a metal-acid intimacy at the micrometer length scale and often leads to suboptimal catalytic performance.[45,46] Locating the metal function in the zeolite crystallite[17,40,48,49] provides a very close metal-acid intimacy, but for catalysts with high metal loadings, this could affect the acid function of the zeolite, that compromises a direct comparison with catalysts with the metal function outside the zeolite.[50,51]

In this study, we evaluated the effects of intimacy between metal and acid sites for zeolite based catalyst in *n*-heptane hydroisomerization, using commercially available zeolites (ZSM-5, zeolite Beta and zeolite Y) that have three-dimensional pore structures and different micropore sizes. Pt/γ-Al_2O_3/zeolite composite catalysts with a 50/50 wt. ratio between the zeolite and γ-Al_2O_3 component were used, while the location of Pt nanoparticles was varied from inside the zeolite crystals (closest intimacy) to on the γ-Al_2O_3 binder and thereby providing an intimacy in the range of 5-500 nm (nanoscale). These catalysts were compared to physical mixtures with similar bulk composition: an intimate physical mixture of Pt/γ-Al_2O_3 and zeolite prepared by mixing in a mortar followed by pelletizing (pressure: 650 kg·cm^{-2}), or a physical mixture of grains (75-212 μm) (Figure 3.1). Furthermore, using molecular simulations, diffusion coefficients of mono- and dibranched heptane isomers in the straight channels of the ZSM-5 zeolite were computed, that shows to be a determining factor in the isomer product distribution of this zeolite. The results of this study provide new insights in factors, viz. zeolite acidity, micropore size, shape selectivity and metal-acid intimacy, that determine the catalyst performance, and are of great relevance for the preparation of zeolite based metal-acid catalysts.

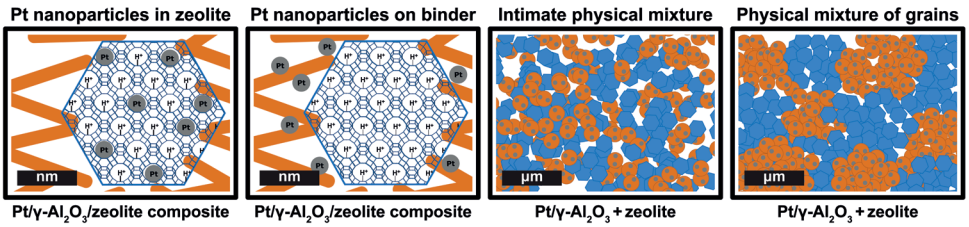

Figure 3.1. Schematic representation of the investigated samples. Pt/γ-Al_2O_3/zeolite composite catalysts with Pt nanoparticles located in the zeolite provides a 'closest' intimacy between metal sites, while catalysts with Pt nanoparticles located on the γ-Al_2O_3 binder provides a 'nanoscale' intimacy. In this case, by placing Pt nanoparticles closely outside zeolite crystals, an intimacy between metal and acid sites between 5-500 nm is created. As comparison, an intimate physical mixture and a physical mixture of grains are prepared that provide a 'microscale' metal-acid intimacy. The alumina component is indicated in orange, zeolite in blue and Pt nanoparticles are grey.

3.2. Experimental methods

3.2.1. Composite preparation

H-ZSM-5/γ-Al_2O_3 and H-zeolite Beta/γ-Al_2O_3 composites were prepared by adding 50 wt.% of ZSM-5 zeolite powder (Zeolyst CBV3024E, Si/Al = 15 at/at, particle size ~20-200 nm) or Zeolite Beta powder (Zeolyst CBV814E, Si/Al = 12.5 at/at, particle size ~20-50 nm) with 50 wt.% of Pseudo-boehmite (HMPA, Shell) in a mortar. Additional properties of the zeolites are reported in Table S3.4. Then, 2 wt.% (based on the total mass of the solid components) of acetic acid (Alfa Aesar, glacial, 99+%), and distilled water were added and mixed for ~5 minutes, resulting in a homogenous and viscous paste. Acetic acid was added as a peptizing agent for the boehmite particles, to aid in mixing and adhesion with the zeolite particles.[52] The mixture was dried overnight at 120 °C in static air followed by calcination at 550 °C for 2 h with a ramp of 5 °C·min^{-1}. Afterwards, the product was crushed and sieved to obtain grains of 212-500 μm diameter. The zeolite Y/γ-Al_2O_3 composite (based on Zeolyst CBV760, Si/Al = 30 at/at, particle size ~200-1000) was obtained from Shell technology center in the form of extrudates. The extrudates were crushed and sieved towards a fraction of 212-500 μm and used as such for Pt deposition.

3.2.2. Catalysts synthesis

Pt/γ-Al_2O_3/Zeolite catalyst with Pt nanoparticles located inside zeolite crystals

1 g Zeolite/γ-Al_2O_3 particles were suspended in 300 ml Milli-Q water at room temperature and stirred for 1 hour (~500 rpm). 40 mL of aqueous solution containing 10.2 mg of $Pt(NH_3)_4(NO_3)_2$ (Sigma-Aldrich, 99.995% purity) was added dropwise to the suspension (intake 0.5 wt.% Pt). After 3 hours of stirring, the suspension was filtered and washed with 150 mL Milli-Q water and dried in static air overnight at 120 °C. The dried catalyst was calcined in a flow of 20% O_2/N_2 (GHSV~8500 h^{-1}) at 350 °C with a ramp of 0.2 °C·min^{-1}, a procedure based on Graaf et al. for the preparation of highly dispersed Pt nanoparticles.[53] Afterwards, the catalyst was reduced in a flow of H_2 (GHSV~3300 h^{-1}) for 3 h at 600 °C, using a ramp of 5 °C·min^{-1}.

Pt/γ-Al_2O_3/Zeolite catalyst with Pt nanoparticles located on the γ-Al_2O_3 binder

1 g of Zeolite/γ-Al_2O_3 particles were suspended in 300 ml Milli-Q water at room temperature and stirred for 1 h (~500 rpm). 40 mL of aqueous solution containing 12.5 mg of $H_2PtCl_6 \cdot 6H_2O$ (Merck, ~40 wt.% Pt) was added dropwise to the suspension (intake 0.5 wt.% Pt). After 3 hours of stirring, the suspension was filtered and washed with 150 mL Milli-Q water and dried in static air overnight at 120 °C. The dried catalyst was reduced in a flow of H_2 (GHSV~3300 h^{-1}) for 3 hours at 600 °C with a ramp of 5 °C·min^{-1}. When preparing smaller amounts of catalysts, the volume of Milli-Q water in the suspension was proportionally decreased, while using similar GHSV's.

Pt/γ-Al_2O_3 + zeolite physical mixtures

Physical mixtures were prepared by using γ-Al_2O_3 in powder form as support using the Pt deposition procedure as described above for locating Pt nanoparticles on γ-Al_2O_3. After Pt deposition, the support was pressed and sieved into a sieve fraction of 212-500 μm in diameter and reduced in H_2 (GHSV~3300 h^{-1}) for 3 hours at 500 °C, with a ramp of 5 °C·min^{-1}. To produce H-ZSM-5 and H-Beta for physical mixtures, the parent zeolites in ammonium form were calcined in static air at 550 °C for 2 h. Intimate physical mixtures were prepared by mixing the Pt/γ-Al_2O_3

powder (0.8 wt.% Pt) with the zeolites in 50/50 wt. ratio in a mortar, resulting in an overall Pt loading of 0.4 wt.%. The resulting mixture was then pelletized (pressure: 650 $kg \cdot cm^{-2}$) and crushed and sieved into a fraction of 75-212 μm to be used for catalytic testing. For a physical mixture of grains, Pt/γ-Al_2O_3 powder and zeolite powder were separately pressed and sieved into a fraction of 75-212 μm and were carefully mixed with a spatula before loading the reactors.

3.2.3. Characterization

Elemental analysis of Pt was performed at Kolbe Mikroanalytisches Laboratorium using an Inductively Coupled Plasma - Optical Emission Spectrometer (ICP-OES, Perkin Elmer) after sample dissolution according to standard in-house procedures. N_2 physisorption measurements of the supports were conducted on a Micromeritics TriStar 3000 at liquid nitrogen temperature. The samples were dried overnight at 300 °C in N_2 flow before measurements. Ammonia Temperature Programmed Desorption (NH_3-TPD) was performed on a Micromeritics AutoChem II equipped with a Thermal Conductivity Detector (TCD) calibrated for ammonia. 80-100 mg of catalyst was dried in a He flow for 1 hour at 600 °C (10 $°C \cdot min^{-1}$). The temperature was then decreased to 100 °C and ammonia (10 vol% in He) was adsorbed in a pulse-wise manner until oversaturation. The physisorbed ammonia was removed by flowing He for 2 h at 100 °C, after which the ammonia desorption was monitored until 600 °C with a ramp of 10 $°C \cdot min^{-1}$. Quantification of ammonia desorption was performed by deconvolution of the TCD signals with three Gaussian functions. HAADF-STEM imaging was performed on an FEI Talos F200X transmission electron microscope, equipped with a high-brightness field emission gun (X-FEG). For these analyses, catalysts were embedded in Epofix resin, left to cure in air overnight at 60 °C, and cut to 70 nm sections using a Reichert-Jung Ultracut E ultramicrotome with Diatome Ultra 35° diamond knife. Sections were deposited on carbon/Formvar-coated copper TEM grids.

3.2.4. *n*-Heptane hydroisomerization

Catalytic experiments were conducted in an Avantium Flowrence 16 parallel fixed bed reactor setup. Stainless steel reactors (internal diameter = 2 mm) were loaded with 25 mg of catalyst in a sieve fraction of 75-212 μm. The product stream coming from the reactors was analyzed using an online GC (Agilent 7890A or Agilent 7890B) where the hydrocarbon products were analyzed on an Agilent J&W PoraBOND Q or HP-PONA column, respectively, connected to an FID. Before catalytic tests, catalysts were reduced at 300 °C (2 h; 5 $°C \cdot min^{-1}$) in a 25% H_2/He flow. *n*-Heptane hydroisomerization tests were performed with the following conditions: a $mol_{H2} \cdot mol_{n\text{-}C7}^{-1}$ ratio of 9, a feedrate of 2.6 $g_{n\text{-}C7} \cdot g_{cat}^{-1} \cdot h^{-1}$ and a total pressure of 10 bar. *n*-Heptane was obtained from Acros Organics (99+%,pure). He 5.0, N2 5.0, H2 6.0 gases were obtained from Linde gas. Results from catalytic tests were obtained by taking the average of two GC measurement performed at identical conditions. No catalyst deactivation was observed in the described experiments. The definitions for *n*-heptane conversion, product yield and selectivity are provided in Supporting information 3.1.

3.2.5. Molecular modelling

The free energy profiles and diffusion coefficients of different heptane isomers along the straight channels of ZSM-5 zeolite at zero loading are computed from Monte Carlo simulations in the canonical ensemble. The RASPA software package is used for the simulations.[32,33] Heptane

isomers are modeled using the TraPPE force field. Interactions between heptane isomers and the zeolites are described by Lennard-Jones interactions, which are truncated and shifted at 12 Å. No tail corrections are applied. The simulation box consists of 2×2×2 unit cells with periodic boundary conditions. The zeolite structure was taken from the IZA database.[54] The zeolite is modelled as a rigid structure. Simulations are performed at 207 °C, 255 °C, 294 °C, 387 °C. The length of the channels is divided into 1000 bins and the probability that a heptane isomer is in each of these slices is calculated. To compute the free energy profiles along a channel, the possible positions for the molecule are restricted to a single channel and trial moves attempting to move the molecule outside the channel are automatically rejected. The free energy of the molecule at each slice is given by:

$$F_i = -k_B T \ln(p_i)$$

where T is absolute the temperature, k_B is the Boltzmann factor, and F_i and p_i are the Landau free energy at slice i and the probability of a molecule being in slice i, respectively. Transition State Theory is used to calculate the upper bound for the diffusion coefficient of each of the heptane isomers. A molecule at top of the free energy barrier is in equilibrium with the surrounding, therefore, the velocity distribution is according to the Maxwell distribution in that temperature. It is assumed that half of the molecules that reach the top of the barrier pass. Consequently, the hopping rate is given by:

$$k^{TST} = \sqrt{\frac{k_B T}{2\pi m}} p(q^*)$$

where m is the mass of the molecule, p(q*) is the probability of being on top of the free energy barrier, and q* is the reaction coordinate at top of the free energy barrier. Upper estimates for diffusion coefficients follow then from:

$$D^{TST} = \lambda^2 k^{TST}$$

where λ is the distance between two free energy barriers. More details regarding the simulations techniques can be found elsewhere.[30,55]

3.3. Results and Discussion

3.3.1. Acidity and Pt nanoparticle location of zeolite composite catalysts

The prepared Pt/γ-Al_2O_3/zeolite catalysts (survey including designations shown in Table 3.1) were based on three commercially available zeolites whose properties (product code, Si/Al ratio, ring size, pore diameter and pore tortuosity, particle size) are indicated in Table S3.4 and the structural properties obtained from N_2 physisorption are provided in Figure S3.7 and Table S3.5. The zeolite Beta and Y used in this study possessed intercrystalline and intracrystalline mesoporosity, respectively, as evident from the hysteresis loop and pore size distribution whereas the ZSM-5 crystals were almost exclusively microporous. When the parent zeolites were transformed into zeolite/γ-Al_2O_3 composites, a bimodal porosity was obtained in all cases, displaying both zeolite microporosity and mesoporosity which is mostly attributed to the γ-Al_2O_3 binder.

After the preparation of the composite supports, the location of Pt nanoparticles could be controlled by using a previously reported methodology.[40] Pt was selectively deposited inside zeolite crystals by ion-exchange of $[Pt(NH_3)_4]^{2+}$ (aq) with zeolite protons (pH ~5), while strong electrostatic adsorption at pH ~3 of the $[PtCl_6]^{2-}$ (aq) complex was used to selectively deposit Pt on the γ-Al_2O_3 binder. Considering the range in zeolite particle sizes (Table S3.4), locating Pt nanoparticles on the γ-Al_2O_3 binder results in a bifunctional intimacy between 5 and 500 nm. Although in earlier work[56] it has been suggested that Pt particles may end up at the external surface of zeolite crystals when $[Pt(NH_3)_4]^{2+}$ (aq) is used as precursor, we have taken great care during ion-exchange and thermal pretreatments in combination with extensive characterization of the location of the Pt nanoparticles[57] to assure that they predominantly reside inside the zeolite crystals of the zeolite/γ-Al_2O_3 composites. To prevent overlap of the zeolite and γ-Al_2O_3 components in HAADF-STEM images, the Pt/γ-Al_2O_3/zeolite catalyst were ultra-microtomed into 70 nm sections before analysis.

Table 3.1. Properties of the prepared composite catalysts with their sample designation. Location and size of Pt nanoparticles was determined by HAADF-STEM analysis while the Pt weight loading was determined by ICP after sample destruction. Total acidity was determined by NH_3-TPD in the range of 100-600 °C.

Sample designation	Pt nanoparticle location (TEM)	Pt nanoparticle size (nm)	Pt weight loading (wt.%)	Total acidity ($mmol_{NH3} \cdot g_{cat}^{-1}$)
Pt-Z/A	ZSM-5 zeolite	1.8 ± 0.8	0.4	0.76
Pt-A/Z	γ-Al_2O_3 binder	1.1 ± 0.2	0.4	0.80
Pt-B/A	Zeolite Beta	1.4 ± 0.3	0.4	0.73
Pt-A/B	γ-Al_2O_3 binder	1.0 ± 0.3	0.4	0.75
Pt-Y/A	Zeolite Y	1.2 ± 0.2	0.2	0.51
Pt-A/Y	γ-Al_2O_3 binder	1.1 ± 0.2	0.2	0.54

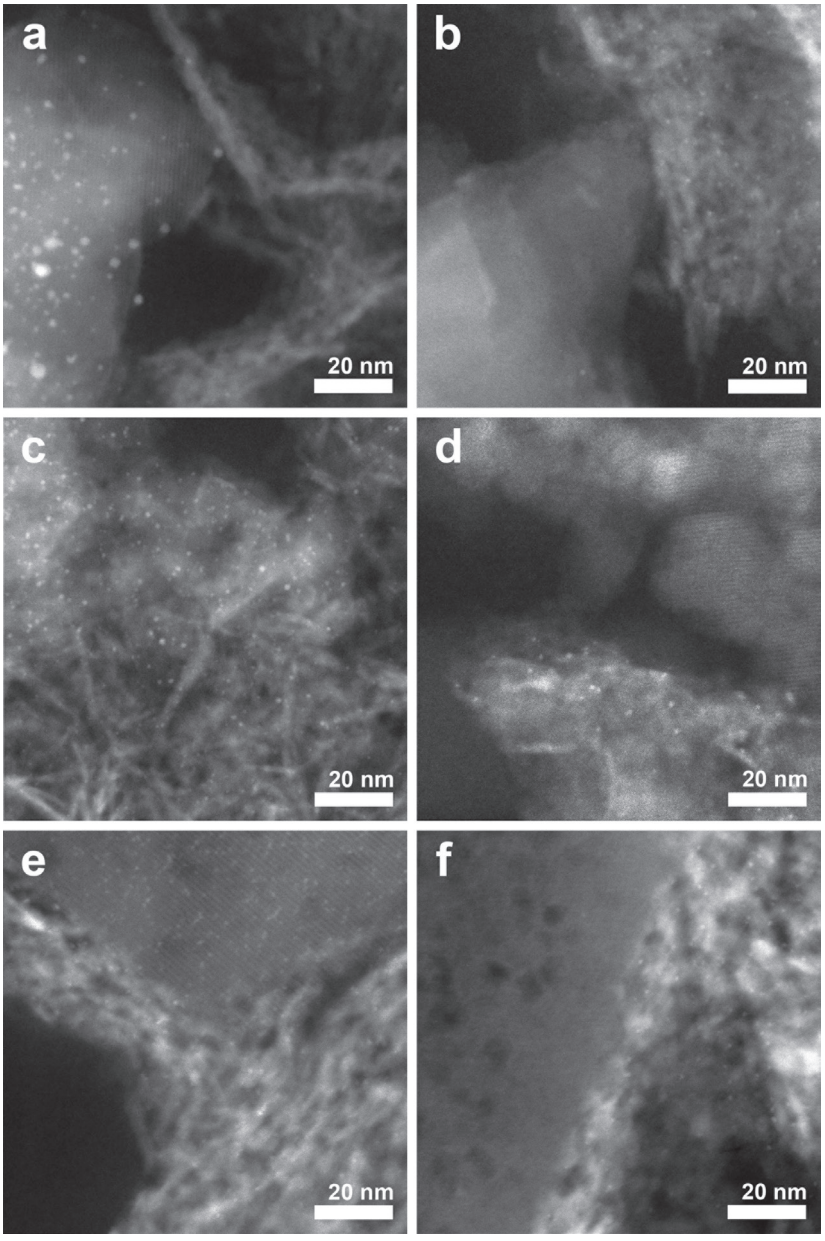

Figure 3.2. HAADF-STEM images of 70 nm-thick microtome cut sections of the Pt/γ-Al_2O_3/zeolite composite catalysts. Catalysts with the Pt nanoparticles located in the zeolite: Pt-Z/A, ZSM-5 (a); Pt-B/A, zeolite Beta (c); Pt-Y/A, zeolite Y (e). Catalysts with Pt nanoparticles located on the γ-Al_2O_3 binder: Pt-A/Z, ZSM-5 (b); Pt-A/B, zeolite Beta (d); Pt-A/Y, zeolite Y (f). Pt nanoparticles appear as bright white dots, while γ-Al_2O_3 has a needle-like structure and zeolite crystals have a more uniform contrast. The ZSM-5 crystals were relatively large with a rectangular shape (a,b), while zeolite Beta crystals were smaller and spherical (c,d). Zeolite Y had large mesopores (>5 nm) that are clearly visible within the zeolite Y component in images e,f.

In Figure 3.2, the HAADF-STEM images of the composite catalyst are provided, and point out that Pt nanoparticles were predominantly located in the zeolite component for the catalyst prepared with $[Pt(NH_3)_4]^{2+}$ (aq), or on the γ-Al_2O_3 binder for the catalyst prepared with $[PtCl_6]^{2-}$ (aq). The relatively large white areas present the γ-Al_2O_3 component of Figure 3.2e are caused by overlapping γ-Al_2O_3 needles that result in a strong contrast with respect to the dark background. The prepared catalyst exhibited a Pt nanoparticle size of 1-2 nm with narrow size distributions (Table 3.1), while previous studies have shown that such HAADF-STEM Pt particle sizes show good agreement with bulk techniques such as EXAFS.[53,58]

The Pt loadings were between 0.2-0.4 wt.% Pt and discrepancies in Pt weight loading between the composite catalysts can be attributed to variations of the uptake of the Pt precursor during the catalyst preparation. Despite differences in Pt weight loading between catalysts based on different zeolites, earlier research on the effect of Pt to acid site ratio on Al-rich zeolites (Si/Al = 3 at/at) has pointed out that with a Pt loading of ≥0.2 wt.% Pt, the rate of the reaction on the metal sites is not rate limiting and the performance is not affected.[59,60] Furthermore, the high hydrogen pressures applied in the catalytic experiments will further advance establishment of a quasi-equilibrium between alkanes and alkenes.[61] In Table 3.1, the total acidity of the catalysts is provided which was obtained from NH_3-TPD over a temperature range of 100-600 °C. In the Supporting Information, the desorption profiles of the Pt/γ-Al_2O_3/Zeolite catalyst and composite supports are provided, that were however too ill-defined to distinguish individual contributions (Figure S3.8, Table S3.6). Besides the composites, the single components (parent zeolites, γ-Al_2O_3) were also studied with NH_3-TPD, and the desorption profiles of the zeolites could be deconvoluted revealing the presence of a low and high temperature band (Figure S3.9, Table S3.7). The high temperature band (300-400 °C) is commonly assigned to ammonia desorption from Brønsted acid sites, and shows a correlation with the Si/Al ratio.[62] The band maximum of the high temperature NH_3 desorption is at a higher temperature for ZSM-5 (Figure S3.9a) than for zeolite Beta and zeolite Y (Figure S3.9b and S3.9c), which is indicative of slower transport of ammonia out of the smaller micropores of the relatively large ZSM-5 particles (Table S3.7). A number of recent studies have pointed out that such differences in desorption maxima of NH_3 cannot be related to acid site strength, and the acid strengths of Brønsted acid sites in ZSM-5, zeolite Beta and Y are very similar.[63,64] The desorption of ammonia at lower temperatures can be attributed to weakly adsorbed ammonia on Lewis acid sites or weakly acidic hydroxyl groups such as those observed on the γ-Al_2O_3 binder (Figure S3.9d-e). More detailed studies on the acidities of the different components of composite catalysts can be found in literature.[65,66]

When comparing the total acidities of the Pt/γ-Al_2O_3/zeolite composite catalysts, prepared with either $[PtCl_6]^{2-}$ (aq) or $[Pt(NH_3)_4]^{2+}$ (aq), a slight but systematic higher total acidity is observed for the former (Table 3.1). The use of $[Pt(NH_3)_4]^{2+}$ (aq) yields catalysts with Pt nanoparticles inside the zeolite crystals, but the three dimensional pore structures of the zeolites combined with low Pt weight loadings (<0.4 wt.% Pt), cannot explain alterations in the zeolite acid function, e.g. pore blockage by Pt nanoparticles. Rather, the higher NH_3 uptake for catalyst prepared with $[PtCl_6]^{2-}$ (aq) is pointing towards a partial chlorination of the surface of the γ-Al_2O_3 binder enhancing its acidity. In a recent paper on Pt/γ-Al_2O_3/zeolite composite catalysts, the effect of residual chlorine from the Pt precursor was studied in detail using (pyridine) FTIR and NH_3-TPD, revealing that acidity from residual chlorine had no consequences for catalysis.[67] For ZSM-5, Zeolite Beta and

Zeolite Y numerous acidity studies are available in literature, using NMR[68] or FTIR with basic probe molecules (e.g. CO, pyridines and acetonitrile)[69,70] sometimes in conjunction with catalytic tests[71], to describe the various acidic sites of these zeolites. There is general agreement that the strong Brønsted acid sites resulting from a bridging hydroxyl group of a charge-balancing tetrahedrally-coordinated aluminium atoms (Al^{3+}) with a silicon atom (Al-OH-Si), are the active sites for isomerization and cracking reactions of hydrocarbons. Recent computational studies have suggested that the acid strength of these sites on high-silica zeolites (Si/Al > 10 at/at), such as those used in this study, is independent of framework or the location of the acid site within the framework.[63,64,72]

3.3.2. Catalytic activity and isomer vs. cracking selectivity in *n*-heptane isomerization

The *n*-heptane hydroisomerization experiments of the Pt/γ-Al_2O_3/zeolite composite catalysts and physical mixtures of the parent zeolites and Pt/γ-Al_2O_3, were performed at a feedrate of 2.6 $g_{n\text{-}C7} \cdot g_{cat}^{-1} \cdot h^{-1}$, a total pressure of 10 bar and 9 $mol_{H2}/mol_{n\text{-}C7}$. As is apparent from Figure 3.3a, the catalytic activity of composite catalysts followed a trend of ZSM-5 based catalysts as most active, followed by zeolite Beta and zeolite Y. As stated in the introduction, the activity of zeolite based catalysts is highly dependent on its accessibility which is determined by e.g.: the porosity and zeolite crystal size.

The lower relative activity of the zeolite Y based catalysts can be attributed to the lower number of acid sites on this zeolite due to the relatively high Si/Al ratio. However, for the hydroisomerization of light *n*-alkanes, a high relative activity for ZSM-5 with smaller micropores, followed by zeolite Beta and zeolite Y is more often observed, and the origin has been debated.[11,15,73] Noh et al., have attributed the higher reactivity for zeolites with smaller micropores, to stronger van der Waals interactions between the carbocation and the zeolite framework, leading to a more stable transition state.[15] In other studies the trend in activity is attributed to the stronger adsorption (a more negative enthalpy of adsorption) of *n*-hydrocarbons on zeolites with smaller micropores, which lowers the net activation energy.[73,74] Denayer et al. have reported adsorption enthalpies of *n*-heptane at zero coverage: -79.6 $kJ \cdot mol^{-1}$ for ZSM-5, -72.6 $kJ \cdot mol^{-1}$ for zeolite Beta and -50.1 $kJ \cdot mol^{-1}$ for USY zeolite.[75,76] However, from the apparent activation energies that were calculated from the catalytic data (Figure S3.10, Table S3.8), we do not find that the adsorption enthalpy only can explain the trends in activity of the zeolites.[73,77] Furthermore, composite catalysts with Pt nanoparticles located on the γ-Al_2O_3 binder displayed in all cases a higher catalytic activity than the catalysts with Pt nanoparticles located inside the zeolite crystals (Figure 3.3a), while apparent activation energies were similar between the composite catalysts based on the same zeolite (Table S3.8). We postulate that these differences in catalytic activity are caused by intracrystalline concentration gradients in heptenes, as a result of the different location of Pt nanoparticles which will be discussed in more detail in section 4.

In Figures 3.3b-d, the yields towards monobranched, dibranched isomers and cracking products (propane and butanes) are plotted as function of conversion for the composite catalysts, that were observed to be the main reaction products for all catalysts, indicative of the predominance of acid catalyzed isomerization and cracking (Figure S3.11).[10,35] Earlier research has pointed out that for hydroisomerization of *n*-alkanes on zeolite based bifunctional catalysts, such isomer/cracking yield curves are unique functions of conversion over a broad range of reaction temperatures,

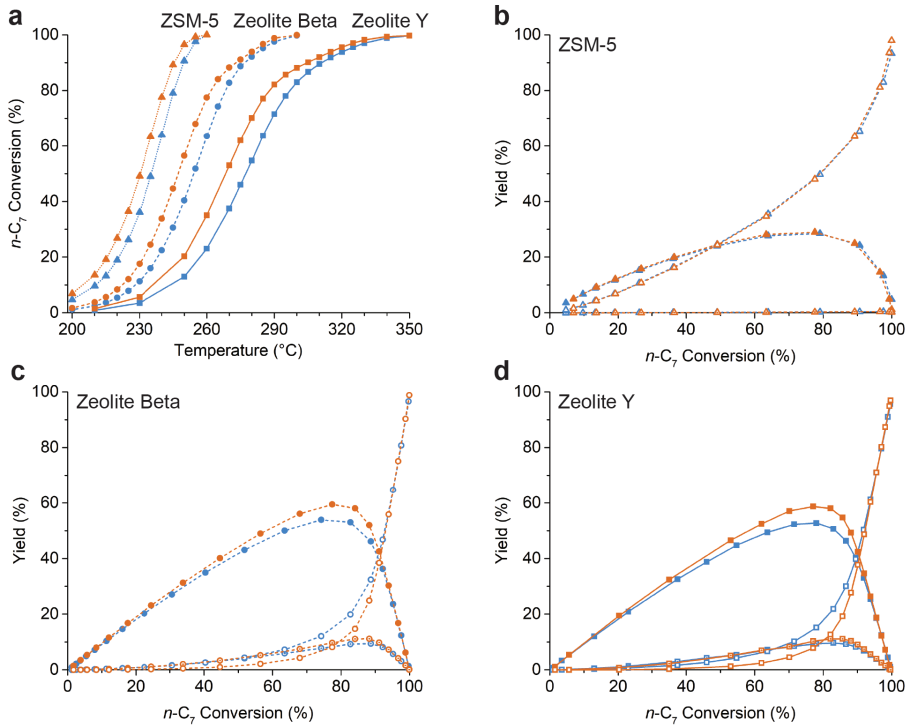

Figure 3.3. Catalytic activity of the Pt/γ-Al_2O_3/zeolite composite catalysts (a), *n*-heptane conversion as a function of temperature, at a feedrate of 2.6 $g_{n\text{-}C7} \cdot g_{cat}^{-1} \cdot h^{-1}$, a total pressure of 10 bar and 9 $mol_{H2} \cdot mol_{n\text{-}C7}^{-1}$. Weight-based product yields towards monobranched isomers (closed symbols), dibranched isomers (asterikses) and C_3, C_4 cracking products (open symbols) as function of conversion for ZSM-5 based catalyst (b), zeolite Beta based catalyst (c) and zeolite Y based catalyst (d). Catalysts with Pt nanoparticles located in the zeolite are indicated in blue, while catalysts with Pt nanoparticles located on the γ-Al_2O_3 binder indicated in orange. The differences in temperature of samples based on the same zeolite are within a margin of 5-10 °C, while differences between catalysts based on ZSM-5 and Zeolite Y are ~50 °C.

since the overall isomerization and cracking rates increase simultaneously upon an increase in temperature.[61,78] From Figure 3.3b and Table 3.2 can be observed that both ZSM-5 based catalysts had a virtually identical selectivity towards monobranched isomers and cracked products, while only a limited amount of dibranched isomers were formed.

Table 3.2. Maximum yield (%) of mono- and dibranched heptane isomers obtained over Pt/γ-Al_2O_3/zeolite ('X') catalysts at a feedrate of 2.6 $g_{n\text{-}C7} \cdot g_{cat}^{-1} \cdot h^{-1}$, a total pressure of 10 bar and 9 $mol_{H2}/mol_{n\text{-}C7}$.

	Pt-'zeolite'/A		Pt-A/'zeolite'	
	Mono (%)	**Di (%)**	**Mono (%)**	**Di (%)**
ZSM-5	28.5	0.4	28.9	0.4
Zeolite Beta	53.9	9.4	59.4	11.1
Zeolite Y	52.7	9.6	58.7	11.1

Similar findings for ZSM-5 have been reported before in literature, more specifically, Kim et al. have observed that the location of Pt nanoparticles for ZSM-5 based catalysts (inside or outside zeolite crystals) did not impact the isomer selectivity below a zeolite crystallite size of 300 nm (this study: 20-200 nm), while the zeolite porosity, Si/Al ratio and zeolite particle size did show to influence the total isomer yield that could be obtained.[17,42]

For the large pore zeolite Beta and zeolite Y (Figure 3.3 c,d), locating Pt nanoparticles on the γ-Al_2O_3 binder had a beneficial effect on isomer selectivity, both to mono- and dibranched isomers. Considering the maximum isomer yields of these catalysts (Table 3.2), zeolite Beta and zeolite Y perform similarly, despite the significant structural differences such as micropore size, zeolite particle size, porosity, Si/Al ratio between the zeolites. Earlier research has pointed out that there are no great differences in diffusivity of skeletal heptane isomers in the micropores of these 12 membered ring zeolites.[24] Zeolite Y based catalysts were studied before using a *n*-C_{19} feed, resulting in a larger enhancement in isomer selectivity (~50 %) by locating Pt nanoparticles outside zeolite Y than observed here for *n*-heptane.[40] The relatively high diffusivity of the branched heptane isomers allows relatively quick diffusion the zeolite, and therefore catalysts with Pt nanoparticles located in the zeolite also have a high isomer yield.

3.3.3. Isomer product distribution of composite ZSM-5 zeolite based catalysts

The formation of isomers of heptene is commonly attributed by the Protonated cyclopropyl mechanism (PCP), which consists of relatively fast reaction steps for the formation and shift of methyl groups.[35] In large pore zeolites, the reaction is non-selective with respect to the isomer formed and therefore, in principle, the distribution between either monobranched or dibranched isomers is dictated by the thermodynamic equilibrium.[24] The isomer product distribution on medium pore ZSM-5 catalysts is subject to shape-selectivity, which has been studied in various previous studies.[23,24] The isomer product distribution for Pt-Z/A and Pt-A/Z, catalysts with the Pt nanoparticles in ZSM-5 or on the γ-Al_2O_3 binder respectively, is provided in Figure 3.4 showing that the catalysts had a high selectivity towards 2 and 3-methylhexanes and minute amounts of 2,3 and 2,4-dimethylpentane were formed. Meanwhile, on zeolite Beta and zeolite Y catalysts, both mono- and di-, as well as tribranched isomers were formed (Figure S3.12). The ratio between the

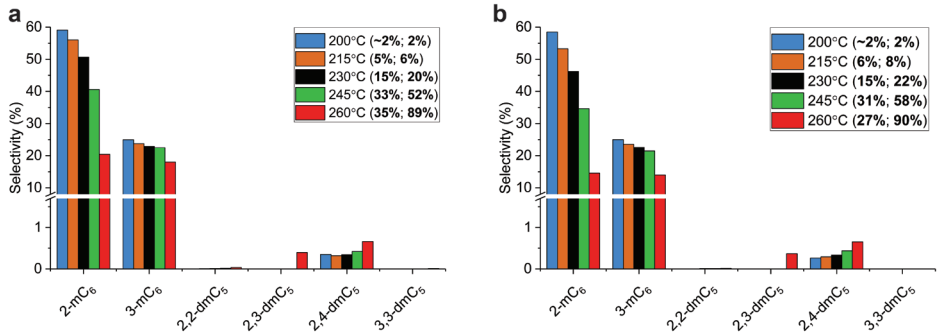

Figure 3.4. Isomer product distribution for Pt/γ-Al_2O_3/ZSM-5 catalyst: Pt-Z/A (a) and Pt-A/Z (b). The Y axis denotes the selectivity, i.e. the fraction of the total products formed at a certain conversion level. Data between brackets are the total isomer yield and total *n*-heptane conversion at the indicated temperature, respectively.

Table 3.3. The upper bounds of diffusion coefficients of the heptane isomers in the straight channels of ZSM-5 zeolite, computed with transition state theory.

Heptane isomer	Diffusion coefficients ($m^2 \cdot s^{-1}$)			
	207 °C	255 °C	294 °C	387 °C
n-heptane	$4.3 \cdot 10^{-8}$	$4.2 \cdot 10^{-8}$	$4.2 \cdot 10^{-8}$	$4.1 \cdot 10^{-8}$
2-methylhexane	$1.1 \cdot 10^{-10}$	$2.0 \cdot 10^{-10}$	$3.1 \cdot 10^{-10}$	$6.1 \cdot 10^{-10}$
3-methylhexane	$1.8 \cdot 10^{-11}$	$3.0 \cdot 10^{-11}$	$4.9 \cdot 10^{-11}$	$9.7 \cdot 10^{-11}$
2,2-dimethylpentane	$1.1 \cdot 10^{-17}$	$9.4 \cdot 10^{-17}$	$4.5 \cdot 10^{-16}$	$3.9 \cdot 10^{-15}$
2,3-dimethylpentane	$1.3 \cdot 10^{-14}$	$4.1 \cdot 10^{-14}$	$8.2 \cdot 10^{-14}$	$3.3 \cdot 10^{-13}$
2,4-dimethylpentane	$5.0 \cdot 10^{-12}$	$1.0 \cdot 10^{-11}$	$1.9 \cdot 10^{-11}$	$4.4 \cdot 10^{-11}$
3,3-dimethylpentane	$3.5 \cdot 10^{-18}$	$1.8 \cdot 10^{-17}$	$9.8 \cdot 10^{-17}$	$9.5 \cdot 10^{-16}$

2-methylhexane and 3-methylhexane was ~0.7, in good agreement with the ratio predicted by the thermodynamic equilibrium (Figure S3.13).

The results of the ZSM-5 catalysts show clear evidence of shape-selectivity in *n*-heptane hydroisomerization, resulting in a very low selectivity to di- and tribranched isomers and a 2-methylhexane/3-methylhexane ratio that is deviating from the equilibrium value.[23] Previous research has pointed out the that the isomer product distribution of ZSM-5 is mainly governed by the free energy barriers for diffusion of different heptane isomers within micropores, i.e. product shape selectivity.[24] The isomers formed within the zeolite with a high free energy barrier for diffusion, are more likely to undergo cracking and leave the zeolite as fast diffusing propane and *i*-butane. The extent to which the slower diffusing isomers are formed with respect to the faster diffusing isomers is known to change as a function of zeolite crystallite size.[14,17,24] Based on the free energy barriers, upper limits of the diffusion coefficients for different heptane isomers were computed at different temperatures, and are provided in Table 3.3. One methyl side group in heptane caused the diffusion coefficient in the straight channels of ZSM-5 to drop by approximately 2-3 orders of magnitude. The data confirms that the internally branched 3-methylhexane is slower diffusing than the terminally branched 2-methylhexane, leading to a deviation in the ratio between the two, that changes as a function of crystallite size.[14] Dibranched isomers with geminal methyl groups (2,2 and 3,3-dimethylpentane) have very low diffusion coefficients. For isomers with vicinal methyl groups (2,3-dimethylpentane), the diffusion coefficient is higher and increases further for the isomer with more isolated methyl groups (2,4-dimethylpentane). These trends are reflected by the isomer selectivities of the ZSM-5 catalysts in Figure 3.4, showing small amounts of the 2,3 and 2,4-dimethylpentane were formed, whereas no 2,2 and 3,3-dimethylpentane were observed. Furthermore, the 2-methylhexane/3-methylhexane ratio does not differ between Pt-Z/A and Pt-A/Z catalysts (Figure S3.13). These observations are therefore indicative of the large diffusional differences between skeletal isomers of heptane in ZSM-5 that determine the isomer product distribution.[14,23,24] The results also show that the product distribution is not affected by the location of Pt nanoparticles in composite supports.[79]

3.3.4. Cracking product distribution of composite zeolite based catalysts

Due to their high octane number, dibranched heptane isomers are more desired products than monobranched isomers for heptane hydroisomerization. However, neighboring methyl groups enable energetically favorable (β-scission, type B) cracking reactions[10] and their slow micropore diffusivity further increases the probability of cracking[15,24] and consequently, they are only formed to a limited extent. To get more insight in the cracking behavior of the composite catalysts, the dimethylpentanes/*i*-butane ratio is plotted, which scales the amount of dimethylpentanes that are able to leave the zeolite micropores relative to those being cracked on acid sites, towards propane and *i*-butane (Figure 3.5a). For ZSM-5 based catalysts, almost no dibranched products were observed (section 3.3.3) and therefore the ratio is close to zero for the entire conversion range. For the large pore (Beta, Y) zeolites, placing Pt nanoparticles on the γ-Al_2O_3 binder significantly suppresses the cracking of dibranched isomers, i.e. by a factor 2-3, over a broad conversion range. Furthermore, the plot shows that below a conversion level of ~80%, for both zeolite Y based catalysts, less dibranched isomers are cracked than on the zeolite Beta catalyst. Poursaidesfahani et al. have shown that such a difference in isomerization versus cracking tendency depends on the height of the free energy barriers of diffusion and/or the micropore length as determined by zeolite crystal size.[24] Here, both zeolite Beta and Y possess significant mesoporosity, while zeolite Beta consists of smaller zeolite particles than zeolite Y that, in principle, should lead to a lower cracking tendency.[17] The higher cracking tendency of zeolite Beta with respect to zeolite Y is therefore expected to be caused by a combination of micropore size and higher acid site density. In Figure 3.5b the ratio between *n*-butane and *i*-butane is plotted as a function of cracking conversion, i.e. the amount of heptane that is cracked towards propane and butanes. This ratio can be used as an indication of the cracking of monobranched versus dibranched isomers: *i*-butane and propane are formed from cracking (β-scission, type B) of all dibranched isomers, except 2,3-dimethylpentane, while *n*-butane is either formed by the cracking of monobranched isomers or 2,3-dimethylpentane (β-scission, type C), or hydrogenolysis

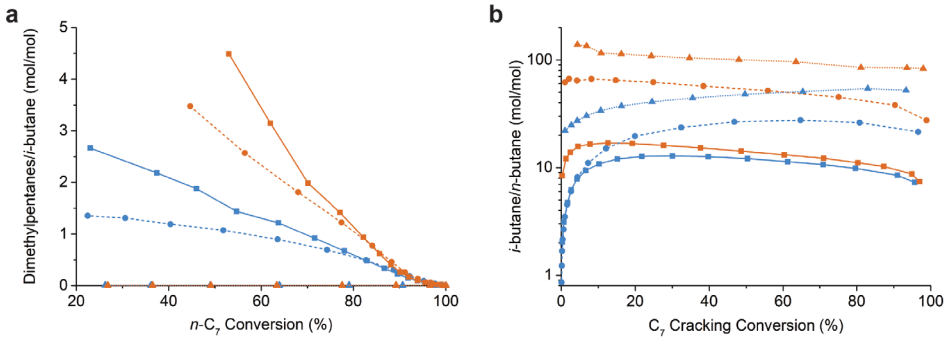

Figure 3.5. The ratio of dimethylheptanes over *i*-butane as function of *n*-heptane conversion (a) and the ratio between *i*-butane and *n*-butane as a function of heptane cracking conversion (b). Composite catalyst with Pt nanoparticles located in the zeolite are indicated in blue, catalyst with Pt nanoparticles located on the γ-Al_2O_3 binder indicated in orange, ZSM-5 based catalysts are indicated as triangles, zeolite Beta (circles), zeolite Y (squares). Different *n*-heptane conversion or heptane cracking conversion levels were obtained by changing the temperature of the reactor between 200-350 °C. Differences in temperature in between catalysts based on the same zeolite are within 10 °C difference at iso-conversion.

(metal catalyzed cracking).[80] The higher relative *i*-butane production for the ZSM-5 catalysts compared to zeolite Beta and zeolite Y, may be explained by the preferential formation of geminal dibranched isomers, especially 2,2-dimethylpentane, that is unique for the ZSM-5 framework.[24,79] Due to the high free energy barrier of diffusion of geminal dibranched isomers in ZSM-5, they are subsequently cracked towards *i*-butane and propane. The large pore zeolite Beta and Y do not possess such shape-selectivity, which might therefore result in slightly more contributions of Type C β-scission reactions of 2,3-dimethylpentane yielding *n*-butane. For all studied catalysts with Pt nanoparticles located on the γ-Al_2O_3 binder, it is apparent that more *i*-butanes are formed over *n*-butanes compared to catalysts with Pt nanoparticles in the zeolite. A similar difference has been observed for ZSM-22 catalysts, and shows to be more subtle for the zeolites with a three dimensional pore structure and larger micropores.[42] These observations point out that when Pt nanoparticles are located in the zeolite, the acid cracking reactions are prone to more pronounced confinement effects (shape-selectivity) within the zeolite micropores, leading to the formation of *n*-butane. To assess if the isomerization of the *i*- and *n*-butanes influences the *i*-butane/*n*-butane ratio, the ratios from Figure 3.5b were compared to the equilibrium ratio (Figure S3.14), that should be approached upon secondary isomerization. Previous studies have confirmed that shape selectivity is absent for butanes in ZSM-5, zeolite Beta or zeolite Y due to the relatively small size of the C_4 hydrocarbons.[81] The *i*-butane/*n*-butane ratios obtained in the catalytic experiments were significantly higher than the equilibrium value, while the slight downward trend at higher cracking conversions might be attributed to conversion of *i*-butane towards *n*-butane. Nevertheless, the systematically high *i*-butane/*n*-butane ratio over a broad cracking conversion range confirms the relative inertness of butanes under the conditions of *n*-heptane hydroisomerization. Furthermore, from the product distributions it is apparent that to a limited extent so-called bimolecular reactions took place for zeolite Beta and Y based catalysts (Figures S3.11, S3.12) resulting in formation of 3-ethylpentane and C_5-C_6 cracking products, while hardly any of these product were observed for ZSM-5.[80,82]

3.3.5. Catalytic performance of composite catalysts and physical mixtures

In Figure 3.6, trends in activity (a) and maximum heptane isomer selectivity (b) are shown for the different catalysts over a broad intimacy range, and in the Supporting Information, the cracking product distribution (Figure S3.11) and more detailed catalytic data (Figure S3.15) are provided. When comparing catalytic activity of the physical mixtures to the composite catalysts, it is apparent that a close metal-acid intimacy is crucial for all catalysts, and catalysts with Pt nanoparticles on the γ-Al_2O_3 binder, with a metal-acid intimacy at the nanoscale, were optimal for catalytic activity. Interestingly, the catalytic activity for the intimate physical mixture of Pt/γ-Al_2O_3 and ZSM-5 was higher than for the ZSM-5 composite catalyst with Pt nanoparticles located inside the zeolite crystal, while for the other zeolites a worse performance of the physical mixtures was observed. The apparent activation energies for the intimate physical mixtures with respect to the composite catalysts, were similar (ZSM-5, zeolite Beta) or slightly higher for the zeolite Y based physical mixtures (Figure S3.10, Table S3.8). The physical mixtures of grains had a significantly lower catalytic activity than the composite catalysts and intimate physical mixtures and all displayed a lower apparent activation energy, that can be attributed to diffusion limitations as a result of the large distance between metal and acid sites.[34] The intimate physical mixtures appeared to be in a transition zone between the composite catalysts and the physical mixtures

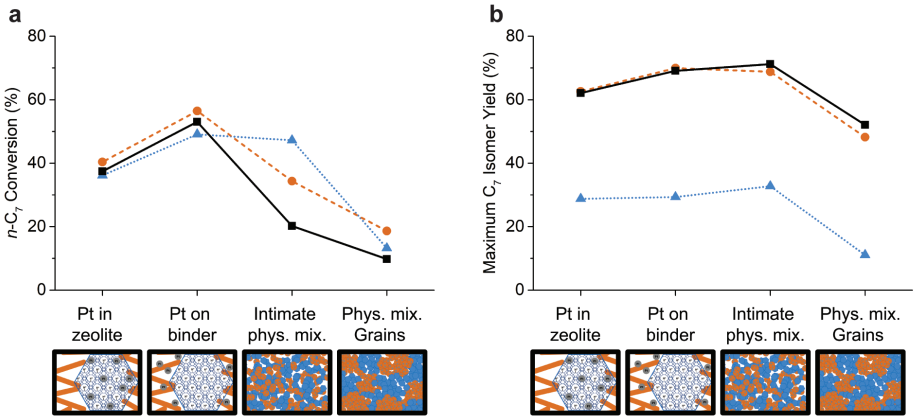

Figure 3.6. Conversion for each zeolite at a fixed temperature (ZSM-5, 230 °C; zeolite Beta, 250 °C; zeolite Y, 270 °C) (a) and maximum heptane isomer yield (b) with metal-acid intimacy ranging from closest to microscale. ZSM-5 based catalysts are indicated as blue triangles, zeolite Beta based catalyst as orange circles and zeolite Y based catalysts as black squares.

of grains: the apparent activation energies were not directly affected by diffusion limitations, but the greater average distance between metal and acid sites compared to the composite catalysts negatively affects the catalytic activity. The maxima in isomer yield for the composite catalysts and physical mixtures are provided in Figure 3.6b and show that the selectivity of the ZSM-5 based catalyst was rather constant over the intimacy range from Pt nanoparticles in ZSM-5 zeolites to intimate physical mixtures of Pt/γ-Al_2O_3 and ZSM-5 zeolite. For zeolite Beta and zeolite Y, the intimate physical mixtures have similar selectivity towards isomers as catalysts with Pt nanoparticles located on the γ-Al_2O_3 binder, although higher temperatures are required to obtain the optimum isomer yield. The isomer yield for the physical mixtures of grains was worse for all zeolites. Considering both catalytic activity and isomer selectivity, catalysts with Pt nanoparticles located outside the zeolite, but in close (nanoscale) vicinity to zeolite acid sites are optimal for catalytic performance.

3.4. General discussion

In the foregoing sections, we have discussed the effect of the metal-acid intimacy in zeolite based bifunctional catalysts (composite catalysts and physical mixtures based on ZSM-5, zeolite Beta and zeolite Y) on differences in the performance in *n*-heptane hydroisomerization. We observed that the metal-acid intimacy, altered by varying the location of Pt nanoparticles, for zeolite based catalysts plays its role for catalyst activity and selectivity. Of all catalysts based on the same zeolite, the composite catalysts with Pt nanoparticles on the γ-Al_2O_3 binder had the highest catalytic activity and optimal isomer selectivity. For large pore zeolite Beta and zeolite Y, locating Pt nanoparticles in the zeolite was detrimental for isomer yield, whereas for the ZSM-5 based catalysts, the isomer yield was rather constant ranging from closest intimacy to the microscale of the intimate physical mixture. Finally, for all composite catalysts, locating Pt nanoparticles in the zeolite increased the amount of *n*-butanes formed over *i*-butanes.

To explain the enhancement in activity and isomer selectivity, we argue that the average reactant diffusion pathway and related reaction events on the composite catalysts with Pt nanoparticles

on the γ-Al_2O_3 binder are different with respect to catalysts with Pt nanoparticles located in the zeolite. The heptenes formed on Pt nanoparticles outside the zeolite upon entering the zeolite may adsorb and react on the first Brønsted acid site they encounter, while still being close to the zeolite outer surface. After conversion to a methyl branched heptene, we propose that it is 'easier' for the isomer to diffuse out than to diffuse into the zeolite crystal, i.e. there is an anisotropy in the diffusion coefficient based on direction, as was earlier proposed for a Pt/γ-Al_2O_3/ZSM-22 catalysts.[42] This implies that the heptene isomers in the outer surface layer should 'remember' the zeolite pore entrance to rapidly diffuse out and subsequently be hydrogenated on Pt nanoparticles on the γ-Al_2O_3 binder. This mechanism effectively decreases the average residence time in the zeolite micropores of heptenes formed outside the zeolite, with respect to heptenes formed on Pt nanoparticles inside the zeolite, that has shown to be a determining factor in the catalysts selectivity.[15] We anticipate that, on average, heptenes formed inside the zeolite, are located deeper in the zeolite with lower diffusion coefficients resulting in cracking reactions, producing quickly diffusing butenes and propene. This reaction mechanism is beneficial for the catalyst activity, and for the large pore zeolite Beta and zeolite Y, also for the selectivity towards branched isomers.

For ZSM-5, the 10 membered ring pores of the zeolite imposes such strict confinement on heptene intermediates that the yield and product distribution of isomers remains unaffected for the catalysts with a different Pt nanoparticle location (inside or outside the zeolite). This behavior can be attributed to the presence of a three dimensional micropore network and intersections that facilitate isomerization and cracking and erase the 'memory effect' mentioned above and is therefore fundamentally different from one-dimensional 10 membered ring zeolites such as ZSM-22 that have generally high selectivities towards branched isomers.[16,42] Other evidence of the impact of concentration gradients in heptenes in the zeolites being affected by Pt location, is the higher *i*-butane/*n*-butane ratio when Pt nanoparticles are placed outside the zeolite, with respect to inside, that was observed for all composite catalysts.[42]

For the physical mixtures, the greater distance between metal and acid sites may lead to concentration gradients of heptenes.[46] Nevertheless, optimal isomer selectivity could also be obtained using intimate physical mixtures, that can be attributed to a similar transport of alkenes with the zeolite as for the composite catalysts with Pt nanoparticles on the γ-Al_2O_3 binder. The large metal-acid distances present in the physical mixtures of grains negatively affected both the activity and isomer selectivity for all catalysts.

The results of this study are therefore in general agreement with previously reported results where beneficial effects have been reported when Pt nanoparticles located are outside zeolite crystals and in nanoscale intimacy with a zeolite acid sites.[40–42]

3.5. Conclusions

In this study, beneficial effects on activity for *n*-heptane hydroisomerization were observed when Pt nanoparticles are placed on the γ-Al_2O_3 binder of zeolite/γ-Al_2O_3 composite supports as opposed to Pt located inside zeolite crystals. The activity of the ZSM-5 based catalyst appeared to be rather unsensitive for Pt nanoparticle location within the nanoscale to microscale range, while the catalytic activity of large pore zeolites benefitted from a nanoscale metal-acid intimacy.

For both zeolite Beta and zeolite Y based catalyst, beneficial effects on isomer selectivity were observed while cracking was suppressed when Pt nanoparticles were placed on the γ-Al_2O_3 binder. The enhanced selectivity of large pore zeolites towards isomers is ascribed to the shorter residence time of intermediates in zeolite micropores as a consequence of concentration gradients of heptenes. For ZSM-5 no significant differences in selectivity were observed between catalysts over a range of metal-acid intimacies, that can be explained by the large diffusional barriers of heptane/heptene isomers in the ZSM-5 zeolite that dictate the product distribution. In general, it is concluded that the catalytic performance of zeolite based bifunctional catalyst for the conversion of hydrocarbons is affected by pore-mouth mechanisms and intracrystalline diffusion of reaction intermediates in zeolite crystals.

Acknowledgements

We acknowledge the European Research Council, EU FP7 ERC Advanced Grant no. 338846 for support. T.J.H.V. acknowledges NWO-CW for a VICI grant. Remco Dalebout, Laura Barberis and Nikos Nikolopoulos (UU) are acknowledged for performing N_2 physisorption measurements. Shell Projects and Technology is acknowledged for supplying the Zeolite Y/γ-Al_2O_3 extrudates and HMPA pseudo-boehmite.

References

[1] H. L. Coonradt, W. E. Garwood, Ind. Eng. Chem. Process Des. Dev. 1964, 3, 38–45.

[2] J. L. Weber, I. Dugulan, P. E. de Jongh, K. P. de Jong, ChemCatChem 2018, 10, 1107–1112.

[3] K. Cheng, B. Gu, X. Liu, J. Kang, Q. Zhang, Y. Wang, Angew. Chemie Int. Ed. 2016, 55, 4725–4728.

[4] F. Jiao, J. Li, X. Pan, J. Xiao, H. Li, H. Ma, M. Wei, Y. Pan, Z. Zhou, M. Li, et al., Science. 2016, 351, 1065–1068.

[5] S. Sartipi, K. Parashar, M. Makkee, J. Gascon, F. Kapteijn, Catal. Sci. Technol. 2013, 3, 572–575.

[6] J. W. Thybaut, G. B. Marin, in Adv. Catal., Elsevier Inc., 2016, pp. 109–238.

[7] B. Peng, Y. Yao, C. Zhao, J. A. Lercher, Angew. Chemie - Int. Ed. 2012, 51, 2072–2075.

[8] J. A. Martens, D. Verboekend, K. Thomas, G. Vanbutsele, J. P. Gilson, J. Pérez-Ramírez, ChemSusChem 2013, 6, 421–425.

[9] P. Gao, S. Li, X. Bu, S. Dang, Z. Liu, H. Wang, L. Zhong, M. Qiu, C. Yang, J. Cai, et al., Nat. Chem. 2017, 9, 1019–1024.

[10] J. Weitkamp, ChemCatChem 2012, 4, 292–306.

[11] A. Chica, A. Corma, J. Catal. 1999, 187, 167–176.

[12] D. M. Ruthven, M. F. M. Post, in Stud. Surf. Sci. Catal. 137 (Eds.: H. Van Bekkum, J.C. Jansen, P.A.Jacobs, E.M. Flanigen), Elsevier Science B.V., 2001, pp. 525–577.

[13] J. Kärger, D. M. Ruthven, D. N. Theodorou, in Diffus. Nanoporous Mater., Wiley-VCH Verlag GmbH & Co. KGaA, Weinheim, Germany, 2012, pp. 653–728.

[14] B. D. Vandegehuchte, I. R. Choudhury, J. W. Thybaut, J. A. Martens, G. B. Marin, J. Phys. Chem. C 2014, 118, 22053–22068.

[15] G. Noh, Z. Shi, S. I. Zones, E. Iglesia, J. Catal. 2018, 368, 389–410.

[16] G. Noh, S. I. Zones, E. Iglesia, J. Catal. 2019, 377, 255–270.

[17] J. Kim, W. Kim, Y. Seo, J.-C. Kim, R. Ryoo, J. Catal. 2013, 301, 187–197.

[18] M. Tromp, J. A. van Bokhoven, M. T. Garriga Oostenbrink, J. H. Bitter, K. P. de Jong, D. C. Koningsberger, J. Catal. 2000, 190, 209–214.

[19] K. P. de Jong, J. Zečević, H. Friedrich, P. E. de Jongh, M. Bulut, S. van Donk, R. Kenmogne, A. Finiels, V. Hulea, F. Fajula, Angew. Chemie Int. Ed. 2010, 49, 10074–10078.

[20] S. Ban, A. N. C. Van Laak, J. Landers, A. V. Neimark, P. E. De Jongh, K. P. De Jong, T. J. H. Vlugt, J. Phys. Chem. C 2010, 114, 2056–2065.

[21] G. Wang, E. Johannessen, C. R. Kleijn, S. W. de Leeuw, M. O. Coppens, Chem. Eng. Sci. 2007, 62, 5110–5116.

[22] B. Smit, T. L. M. Maesen, Nature 2008, 451, 671–678.

[23] B. D. Vandegehuchte, J. W. Thybaut, G. B. Marin, Ind. Eng. Chem. Res. 2014, 53, 15333–15347.

[24] A. Poursaeidesfahani, M. F. de Lange, F. Khodadadian, D. Dubbeldam, M. Rigutto, N. Nair, T. J. H. Vlugt, J. Catal. 2017, 353, 54–62.

[25] J. W. Thybaut, G. B. Marin, G. V. Baron, P. A. Jacobs, J. A. Martens, J. Catal. 2001, 202, 324–339.

[26] J. Kärger, in Mol. Sieves - Sci. Technol., Springer-Verlag Berlin Heidelberg, Berlin, Heidelberg, 2008, pp. 85–133.

[27] S. Van Donk, A. Broersma, O. L. J. Gijzeman, J. A. Van Bokhoven, J. H. Bitter, K. P. De Jong, J. Catal. 2001, 204, 272–280.

[28] W. Zhu, F. Kapteijn, J. . Moulijn, Microporous Mesoporous Mater. 2001, 47, 157–171.

[29] F. C. Hendriks, F. Meirer, A. V. Kubarev, Z. Ristanović, M. B. J. Roeffaers, E. T. C. Vogt, P. C. A. Bruijnincx, B. M. Weckhuysen, J. Am. Chem. Soc. 2017, 139, 13632–13635.

[30] D. Dubbeldam, E. Beerdsen, T. J. H. Vlugt, B. Smit, J. Chem. Phys. 2005, 122.

[31] T. L. M. Maesen, M. Schenk, T. J. H. Vlugt, J. P. De Jonge, B. Smit, J. Catal. 1999, 188, 403–412.

[32] D. Dubbeldam, A. Torres-Knoop, K. S. Walton, Mol. Simul. 2013, 39, 1253–1292.

[33] D. Dubbeldam, S. Calero, D. E. Ellis, R. Q. Snurr, Mol. Simul. 2016, 42, 81–101.

[34] P. B. Weisz, Adv. Catal. 1962, 13, 137–190.

[35] J. A. Martens, P. A. Jacobs, in Stud. Surf. Sci. Catal., 2001, pp. 633–671.

[36] N. Dvoyashkina, D. Freude, A. G. Stepanov, W. Böhlmann, R. Krishna, J. Kärger, J. Haase, Microporous Mesoporous Mater. 2018, 257, 128–134.

[37] V. B. Kazansky, Catal. Today 1999, 51, 419–434.

[38] D. M. Ruthven, S. C. Reyes, Microporous Mesoporous Mater. 2007, 104, 59–66.

[39] M. Hartmann, S. Kunz, D. Himsl, O. Tangermann, S. Ernst, A. Wagener, Langmuir 2008, 24, 8634–8642.

[40] J. Zečević, G. Vanbutsele, K. P. De Jong, J. A. Martens, Nature 2015, 528, 245–254.

[41] O. Ben Moussa, L. Tinat, X. Jin, W. Baaziz, O. Durupthy, C. Sayag, J. Blanchard, ACS Catal. 2018, 8, 6071–6078.

[42] K. Cheng, L. I. Wal, H. Yoshida, J. Oenema, J. Harmel, Z. Zhang, G. Sunley, J. Zečević, K. P. Jong, Angew. Chemie Int. Ed. 2020, 59, 3592–3600.

[43] J. Harmel, L. I. van der Wal, J. Zečević, P. E. de Jongh, K. P. de Jong, Catal. Sci. Technol. 2020, 10, 2111–2119.

[44] J. E. Samad, J. Blanchard, C. Sayag, C. Louis, J. R. Regalbuto, J. Catal. 2016, 342, 213–225.

[45] N. Batalha, L. Pinard, Y. Pouilloux, M. Guisnet, Catal. Letters 2013, 143, 587–591.

[46] H. Y. Chu, M. P. Rosynek, J. H. Lunsford, J. Catal. 1998, 178, 352–362.

[47] J. L. Weber, N. A. Krans, J. P. Hofmann, E. J. M. Hensen, J. Zecevic, P. E. de Jongh, K. P. de Jong, Catal. Today 2020, 342, 161–166.

[48] E. J. Creyghton, A. C. T. Van Duin, J. C. Jansen, P. J. Kooyman, H. W. Zandbergen, H. Van Bekkum, J. Chem. Soc. - Faraday Trans. 1996, 92, 4637–4642.

[49] T. Iida, D. Zanchet, K. Ohara, T. Wakihara, Y. Román-Leshkov, Angew. Chemie - Int. Ed. 2018, 57, 6454–6458.

[50] M. A. Camblor, A. Corma, A. Martínez, V. Martínez-Soria, S. Valencia, J. Catal. 1998, 179, 537–547.

[51] J. Francis, E. Guillon, N. Bats, C. Pichon, A. Corma, L. J. Simon, Appl. Catal. A Gen. 2011, 409–410, 140–147.

[52] G. T. Whiting, S. H. Chung, D. Stosic, A. D. Chowdhury, L. I. Van Der Wal, D. Fu, J. Zecevic, A. Travert, K. Houben, M. Baldus, et al., ACS Catal. 2019, 9, 4792–4803.

[53] J. De Graaf, A. J. Van Dillen, K. P. De Jong, D. C. Koningsberger, J. Catal. 2001, 203, 307–321.

[54] C. Baerlocher, L. B. McCusker, "Database of Zeolite Structures," 2014.

[55] T. J. H. Vlugt, R. Krishna, B. Smit, J. Phys. Chem. B 1999, 103, 1102–1118.

[56] H. J. Cho, D. Kim, J. Li, D. Su, B. Xu, J. Am. Chem. Soc. 2018, 140, 13514–13520.

[57] J. Oenema, J. P. Hofmann, E. J. M. Hensen, J. Zečević, K. P. de Jong, ChemCatChem 2020, 12, 615–622.
[58] J. Zečević, A. M. J. Van Der Eerden, H. Friedrich, P. E. De Jongh, K. P. De Jong, ACS Nano 2013, 7, 3698–3705.
[59] M. Guisnet, F. Alvarez, G. Giannetto, G. Perot, Catal. Today 1987, 1, 415–433.
[60] F. Alvarez, F. R. Ribeiro, G. Perot, C. Thomazeau, M. Guisnet, J. Catal. 1996, 162, 179–189.
[61] J. W. Thybaut, C. S. Laxmi Narasimhan, J. F. Denayer, G. V. Baron, P. A. Jacobs, J. A. Martens, G. B. Marin, Ind. Eng. Chem. Res. 2005, 44, 5159–5169.
[62] L. Rodríguez-González, F. Hermes, M. Bertmer, E. Rodríguez-Castellón, A. Jiménez-López, U. Simon, Appl. Catal. A Gen. 2007, 328, 174–182.
[63] A. J. Jones, E. Iglesia, ACS Catal. 2015, 5, 5741–5755.
[64] M. Rybicki, J. Sauer, Catal. Today 2019, 323, 86–93.
[65] M. E. Z. Velthoen, A. Lucini Paioni, I. E. Teune, M. Baldus, B. M. Weckhuysen, Chem. - A Eur. J. 2020, 26, 11995–12009.
[66] G. T. Whiting, A. D. Chowdhury, R. Oord, P. Paalanen, B. M. Weckhuysen, Faraday Discuss. 2016, 188, 369–386.
[67] J. Oenema, R. A. van Alst, M. J. Meijerink, J. Zečević, K. P. de Jong, Appl. Catal. A Gen. 2020, 117815.
[68] M. Hunger, in Handb. Heterog. Catal. (Eds.: G. Ertl, H. Knozinger, F. Schuth, J. Weitkamp), Wiley-VCH Verlag GmbH& Co. KGaA, 2008, pp. 1163–1178.
[69] H. Knozinger, in Handb. Heterog. Catal. (Eds.: G. Ertl, H. Knozinger, F. Schüth, J. Weitkamp), Wiley-VCH Verlag GmbH& Co. KGaA, 2008, pp. 1135–1163.
[70] W. Daniell, N. Y. Topsøe, H. Knözinger, Langmuir 2001, 17, 6233–6239.
[71] S. Kotrel, J. H. Lunsford, H. Knözinger, J. Phys. Chem. B 2001, 105, 3917–3921.
[72] M. Boronat, A. Corma, ACS Catal. 2019, 9, 1539–1548.
[73] A. Van De Runstraat, J. A. Kamp, P. J. Stobbelaar, J. Van Grondelle, S. Krijnen, R. A. Van Santen, J. Catal. 1997, 171, 77–84.
[74] J. A. van Bokhoven, M. Tromp, D. . C. Koningsberger, J. . T. Miller, J. A. . A. Z. Pieterse, J. A. Lercher, B. A. Williams, H. . H. Kung, J. Catal. 2001, 202, 129–140.
[75] J. F. Denayer, W. Souverijns, P. A. Jacobs, J. A. Martens, G. V. Baron, J. Phys. Chem. B 1998, 102, 4588–4597.
[76] J. F. Denayer, G. V. Baron, J. A. Martens, P. A. Jacobs, J. Phys. Chem. B 1998, 102, 3077–3081.
[77] M. Guisnet, V. Fouche, M. Belloum, J. P. Bournonville, C. Travers, Appl. Catal. 1991, 71, 295–306.
[78] G. F. Froment, Catal. Today 1987, 1, 455–473.
[79] T. L. . Maesen, M. Schenk, T. J. . Vlugt, B. Smit, J. Catal. 2001, 203, 281–291.
[80] J. A. Martens, M. Tielen, P. A. Jacobs, Catal. Today 1987, 1, 435–453.
[81] J. Houžvička, S. Hansildaar, V. Ponec, J. Catal. 1997, 167, 273–278.
[82] E. Blomsma, J. A. Martens, P. A. Jacobs, J. Catal. 1996, 159, 323–331.

Supporting Information

Supporting Information 3.1

n-heptane conversion ($X_{n\text{-}C7}$) is calculated by:

$$X_{n\text{-}C_7} = \left(1 - \frac{F_{C\,wt.\,n\text{-}C_7,\,out}}{F_{C\,wt.\,n\text{-}C_7,\,in}}\right)\cdot 100\%$$

Wherein $F_{C\,wt.\,n\text{-}C7,out}$ and $F_{C\,wt.\,n\text{-}C7,in}$ are the flows, based on weight of carbon, of *n*-heptane going out or into the reactor, respectively. Heptane isomer yield ($Y_{i\text{-}C7}$) is calculated by:

$$Y_{i\text{-}C_7} = \left(\frac{F_{C\,wt.\,i\text{-}C_7,\,out}}{F_{C\,wt.\,n\text{-}C_7,\,in}}\right)\cdot 100\%$$

The yield of cracked products (Y_{C3+C4}) is calculated by:

$$Y_{C_3+C_4} = \left(\frac{F_{C\,wt.\,C_3,\,out} + F_{C\,wt.\,C_4,\,out}}{F_{C\,wt.\,n\text{-}C_7,\,in}}\right)\cdot 100\%$$

Wherein $F_{C\ wt.\ i\text{-}C7,\ out}$ and $F_{C\ wt.\ Cm,\ out}$ are the flows, based on weight of carbon, of i-C_7 or cracked products C_m (m = 1-6), respectively, going out of the reactor. The i-C_7 isomer selectivity ($S_{i\text{-}C7}$) is determined as follows:

$$S_{i\text{-}C_7} = \left(\frac{F_{C\,wt.\,i\text{-}C_7,\,out}}{F_{C\,wt.\,n\text{-}C_7,\,in} - F_{C\,wt.\,n\text{-}C_7,\,out}}\right)\cdot 100\%$$

The selectivity towards cracked products (S_{Cm}) is determined as follows:

$$S_{C_m} = \left(\frac{F_{C\,wt.\,C_m,\,out}}{F_{C\,wt.\,n\text{-}C_7,\,in} - F_{C\,wt.\,n\text{-}C_7,\,out}}\right)\cdot 100\%$$

Table S3.4. Details of the parent zeolites.

	Zeolite Code[a]	Si/Al Zeolite[a] (at·at^{-1})	Ring size[b]	Micropore size (nm)[b]	Micropore tortuosity[b]	Estimated crystal size (nm)[c]
ZSM-5	CBV3024E	15	10	0.55×0.51 + 0.56×0.53	Straight + sinusoidal	20-200
Zeolite Beta	CP814E	12.5	12	0.66×0.67 + 0.56×0.56	Straight pores	20-50
Zeolite Y	CBV760	30	12	0.74×0.74	Straight pores + cages	200-1000

a) Manufacturers specification, Zeolyst.
b) International Zeolite Association (Ch. Baerlocher, L.B. McCusker; Database of Zeolite Structures)
c) Obtained from TEM analysis

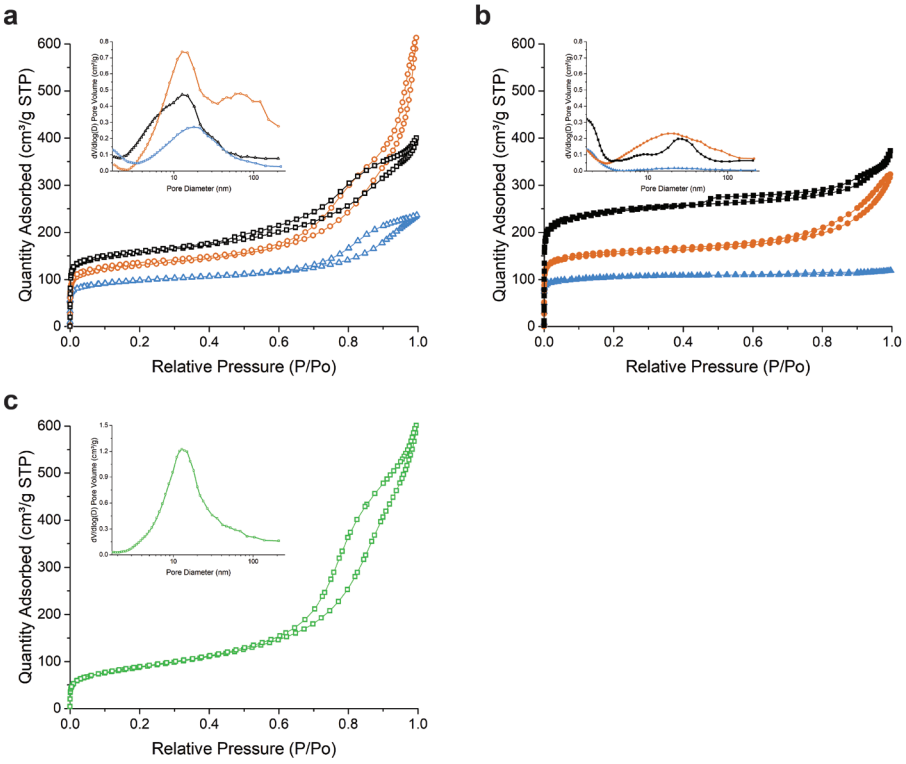

Figure S3.7. N_2 physisorption isotherms of the Zeolite/γ-Al_2O_3 (50/50 wt.) composites, with the BJH pore size distributions derived from the adsorption branch as insert (a): ZSM-5/γ-Al_2O_3 composite (blue), Zeolite Beta/γ-Al_2O_3 composite (orange) and Zeolite Y/γ-Al_2O_3 (black). Parent zeolites (b): ZSM-5 (blue), Zeolite Beta (orange) and Zeolite Y (black) and the γ-Al_2O_3 binder (c).

Table S3.5. Quantitative information derived from N_2 physisorption measurements.

Sample	BET surface area ($m^2 \cdot g^{-1}$)	t-plot external surface area ($m^2 \cdot g^{-1}$)	t-plot micropore volume ($cm^3 \cdot g^{-1}$)	BJH mesopore volume ($cm^3 \cdot g^{-1}$)
ZSM-5/γ-Al_2O_3	-	135	0.09	0.26
Zeolite Beta/γ-Al_2O_3	-	187	0.12	0.80
Zeolite Y/γ-Al_2O_3	-	209	0.15	0.47
ZSM-5	-	77	0.13	0.04
Zeolite Beta	-	135	0.18	0.30
Zeolite Y	-	231	0.28	0.24
γ-Al_2O_3	314	-	-	0.89

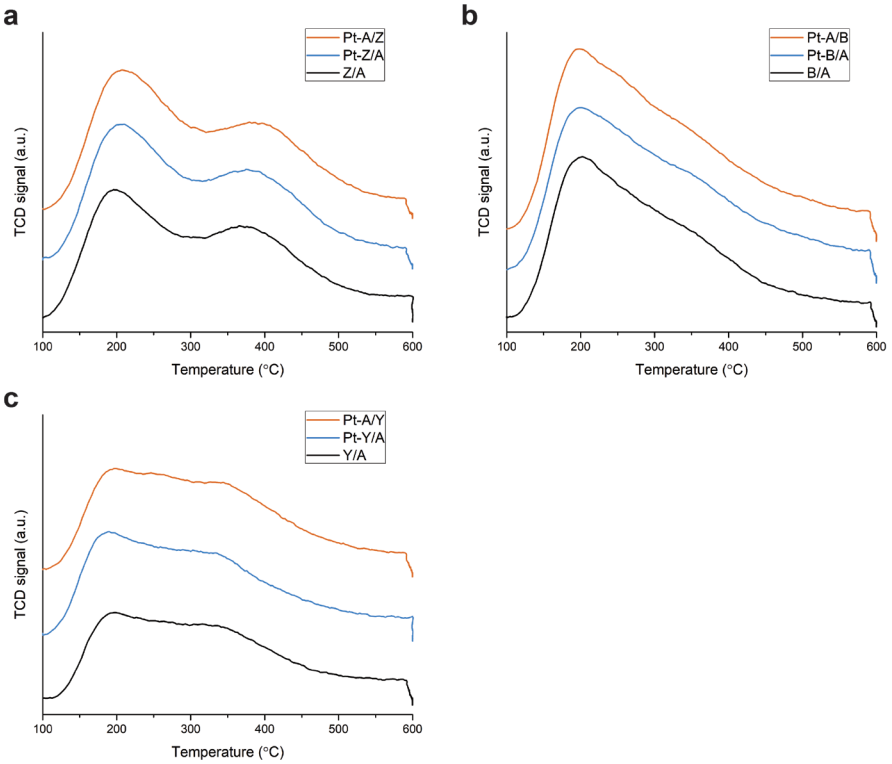

Figure S3.8. NH_3-TPD profiles of the Pt/γ-Al_2O_3/zeolite composite catalysts and the zeolite/γ-Al_2O_3 composite support. Catalysts or supports are based on ZSM-5 (a), zeolite Beta (b), and Zeolite Y (c).

Table S3.6. Total acidity of Pt/γ-Al_2O_3/zeolite composite catalysts and zeolite/γ-Al_2O_3 composite supports as obtained by NH_3-TPD.

Sample	Total NH_3 desorped (mmol·g^{-1})
Pt-A/Z	0.79
Pt-Z/A	0.75
Z/A (ZSM-5/γ-Al_2O_3)	0.70
Pt-A/B	0.75
Pt-B/A	0.72
B/A (Zeolite Beta/γ-Al_2O_3)	0.64
Pt-A/Y	0.54
Pt-Y/A	0.51
Y/A (Zeolite Y/γ-Al_2O_3)	0.41

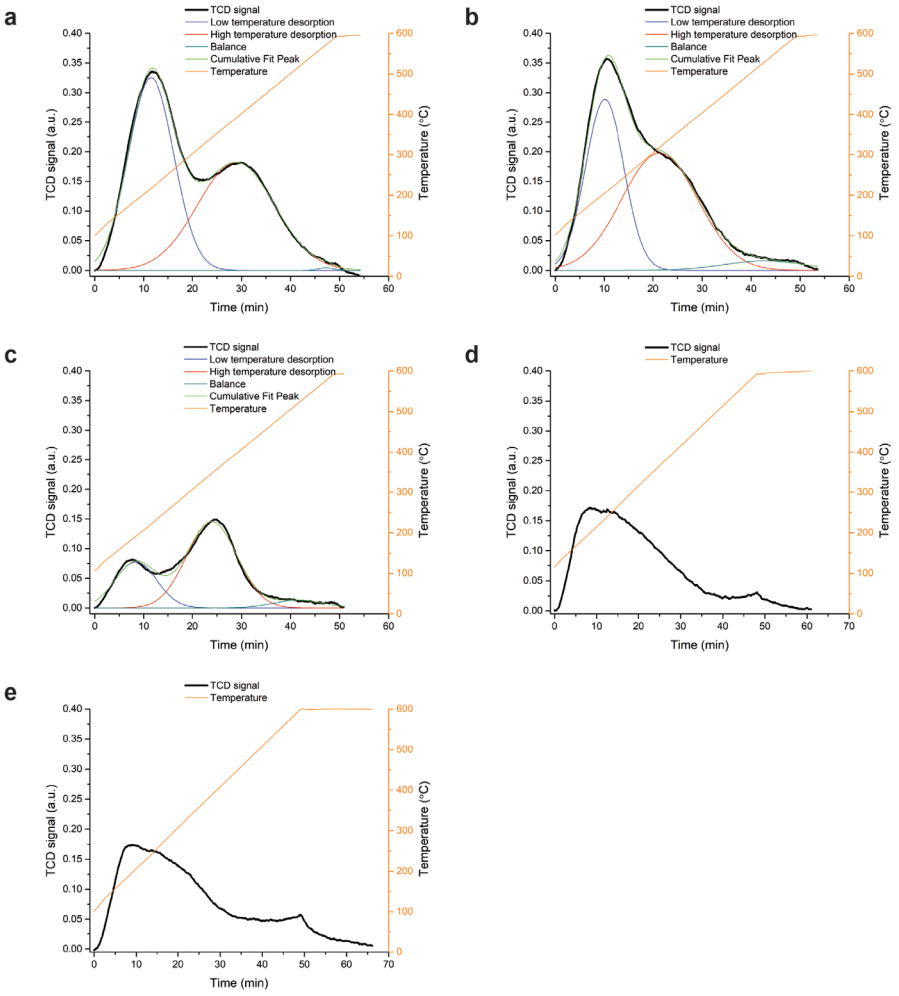

Figure S3.9. NH_3-TPD profiles of parent ZSM-5 (a), zeolite Beta (b), zeolite Y (c) γ-Al_2O_3 (d) and γ-Al_2O_3 that was peptized with acetic acid prior to calcination (e).

Table S3.7. Results of deconvolution low temperature and high temperature desorption of the NH_3-TPD signal of parent zeolites. The total acidity is calculated by integration of the TCD signal over the temperature range of 100-600 °C.

	Si/Al Zeolite	NH_3 desorbed Low T ($mmol_{NH3} \cdot g_{cat}^{-1}$)	NH_3 desorbed High T ($mmol_{NH3} \cdot g_{cat}^{-1}$)	Total NH_3 desorbed ($mmol_{NH3} \cdot g_{cat}^{-1}$)
ZSM-5	15	0.42	0.40	0.82
Zeolite Beta	12.5	0.31	0.42	0.73
Zeolite Y	30	0.09	0.21	0.32
γ-Al_2O_3	-	-	-	0.49
γ-Al_2O_3 (peptized)	-	-	-	0.56

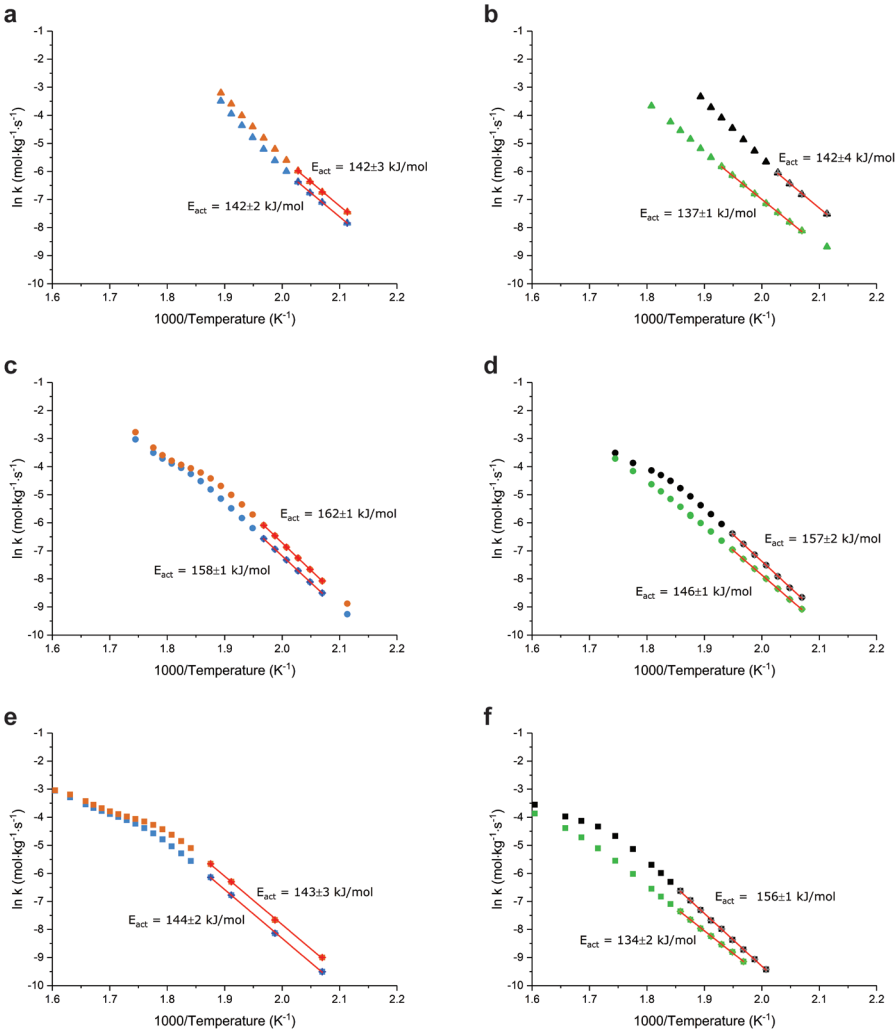

Figure S3.10. Arrhenius plots for ZSM-5 (a, b), Zeolite Beta (c, d) and Zeolite Y (e, f) based catalysts, at a feedrate of 2.6 $g_{n\text{-}C7} \cdot g_{cat}^{-1} \cdot h^{-1}$, 10 bar of total pressure and 9 $mol_{H2}/mol_{n\text{-}C7}$. Catalyst with closest intimacy between Pt sites and zeolite sites are indicated in blue, catalyst with a nanoscale intimacy are indicated in orange, intimate physical mixtures are indicated in black while physical mixtures of grains are indicated in green. The indicated errors of the apparent activation energies denote the standard error of the fit. The first order rate constant was obtained from ln(k) = ln(-(ln(1-X)/(W/F)) wherein X is the *n*-heptane conversion, W the catalyst mass (kg) and F the molar flow of *n*-heptane ($mol \cdot s^{-1}$). Datapoints at relatively low conversion levels were fitted to a straight line, and the slope of this line was then multiplied by -R (gasconstant, R = 8.314 $J \cdot mol^{-1} \cdot K^{-1}$) to obtain the apparent activation energy. Previous kinetic studies by Guisnet et al. (Appl. Catal. 71 (1991) 295–306) and Van de Runstraat et al. (J. Catal.171 (1997) 77–84) have confirmed that a first order dependence of relatively light hydrocarbons in hydroisomerization is a valid assumption.

Table S3.8. Pre-exponential factors and apparent activation energies of Pt/γ-Al_2O_3/zeolite composite catalysts and physical mixtures. The indicated errors of the activation energy denote the standard error of the fit.

	Pre-exponential factor ($mol \cdot kg^{-1} \cdot s^{-1}$)	**Apparent activation energy ($kJ \cdot mol^{-1}$)**
Pt-Z/A	$1.7 \cdot 10^{12}$	142 ± 2
Pt-A/Z	$2.7 \cdot 10^{12}$	142 ± 3
Intimate phys. mix. (ZSM-5)	$2.6 \cdot 10^{12}$	142 ± 4
Phys. mix. grains (ZSM-5)	$2.0 \cdot 10^{11}$	137 ± 1
Pt-B/A	$2.6 \cdot 10^{13}$	158 ± 1
Pt-A/B	$1.1 \cdot 10^{14}$	162 ± 1
Intimate phys. mix. (Zeolite Beta)	$1.7 \cdot 10^{13}$	157 ± 2
Phys. mix. grains (Zeolite Beta)	$7.7 \cdot 10^{11}$	146 ± 1
Pt-Y/A	$2.9 \cdot 10^{11}$	144 ± 2
Pt-A/Y	$3.8 \cdot 10^{11}$	143 ± 3
Intimate phys. mix. (Zeolite Y)	$1.8 \cdot 10^{12}$	156 ± 1
Phys. mix. grains (Zeolite Y)	$5.9 \cdot 10^{9}$	134 ± 2

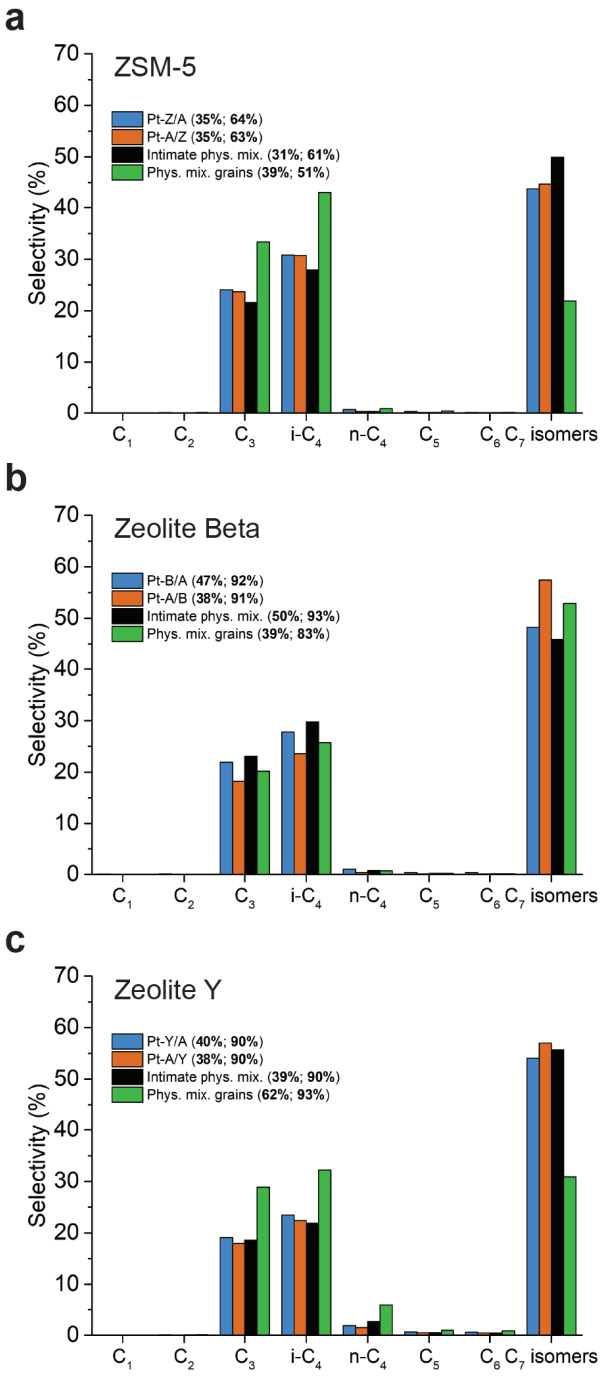

Figure S3.11. The cracking products distribution pattern for the ZSM-5 based catalysts (a), zeolite Beta based catalysts (b) and zeolite Y based catalyst (c). Data between brackets denote: cracking conversion; total *n*-heptane conversion, respectively.

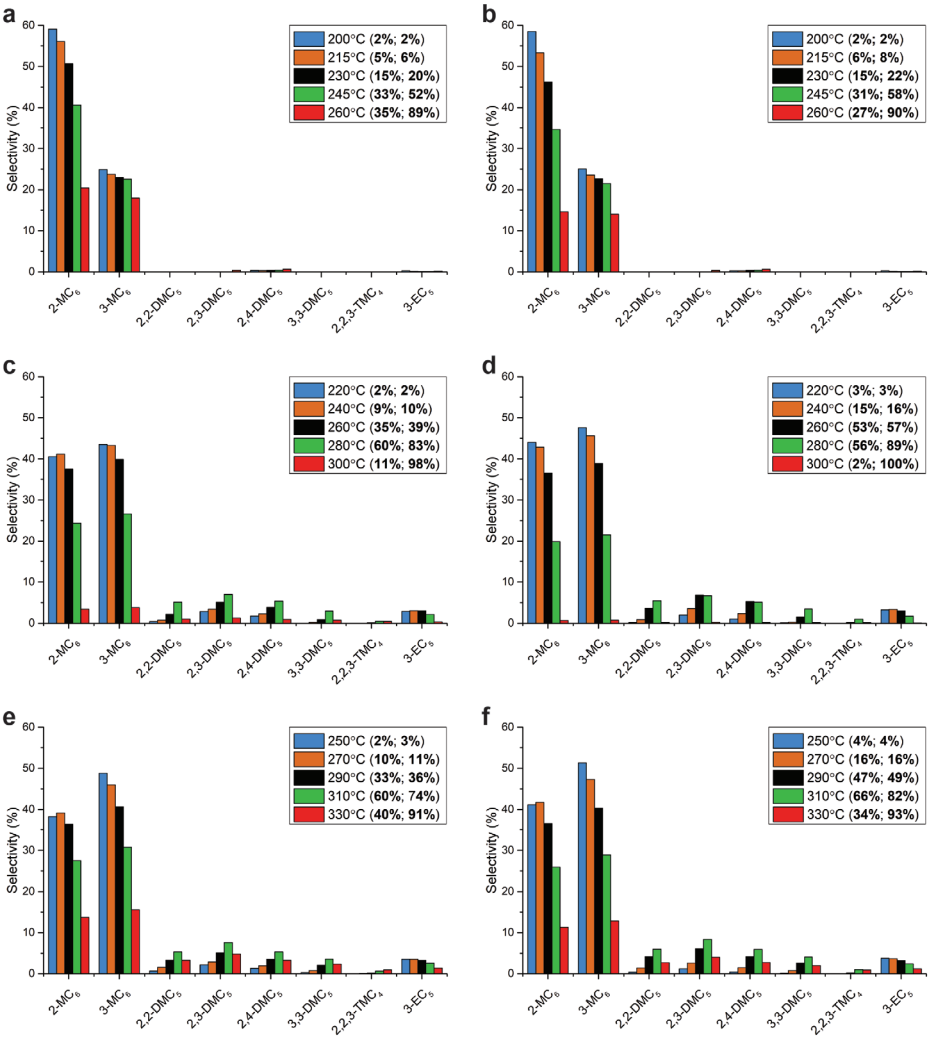

Figure S3.12. Isomer product distribution ZSM-5 (a,b), Zeolite Beta (c,d) and Zeolite Y (e,f) at a feedrate of 2.6 $g_{n\text{-}C7} \cdot g_{cat}^{-1} \cdot h^{-1}$ and 10 bar of total pressure. Data between brackets denote: isomer yield; total *n*-heptane conversion, respectively.

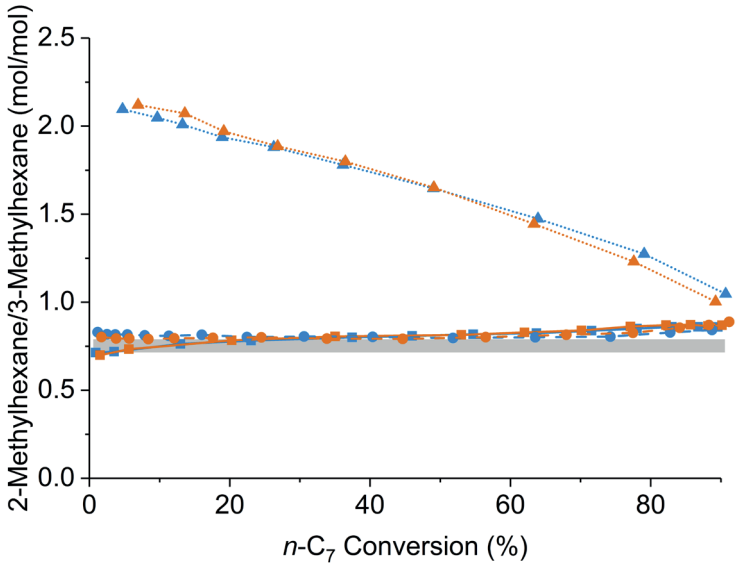

Figure S3.13. Ratio between 2-Methylhexane and 3-Methylhexane as a function of conversion for ZSM-5 (triangles), zeolite Beta (circles) and zeolite Y (squares). Catalyst with Pt nanoparticles located in the zeolite are indicated in blue, while catalyst with Pt nanoparticles located on the γ-Al_2O_3 binder indicated in orange. The grey rectangle indicates the value (2-Methylhexane/[(R)-3-Methylhexane+(S)-3-Methylhexane]) at thermodynamic equilibrium between 200-300 °C as was computed with Outotec HSC Chemistry software, v9.

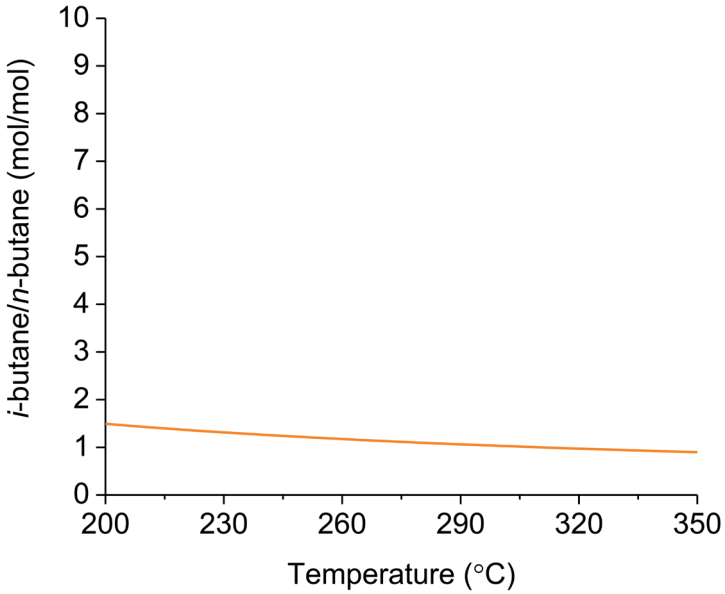

Figure S3.14. Ratio between *i*-butane and *n*-butane (mol/mol) at thermodynamic equilibrium between 200 and 350 °C. The value was computed with Outotec HSC Chemistry software, v9.

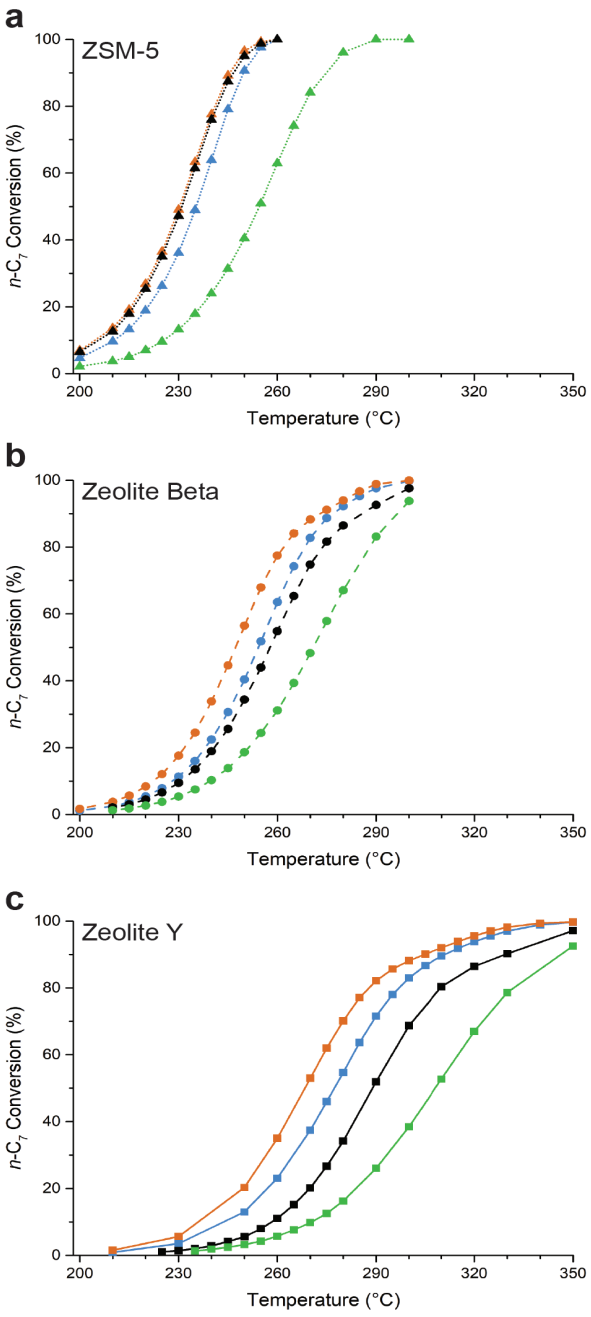

Figure S3.15. Conversion of *n*-heptane as a function of temperature of ZSM-5 (a), Zeolite Beta (b) and Zeolite Y (c) at a feedrate of 2.6 $g_{n\text{-}C7} \cdot g_{cat}^{-1} \cdot h^{-1}$ at 10 bar of total pressure and 9 $mol_{H2} \cdot mol_{n\text{-}C7}^{-1}$. Catalyst with closest intimacy between Pt sites and zeolite sites are indicated in blue, catalyst with a nanoscale intimacy are indicated in orange, intimate physical mixtures are indicated in black while physical mixtures of grains are indicated in green.

Chapter 4

The Influence of Residual Chlorine on Pt/Zeolite Y/γ-Al_2O_3 Composite Catalysts: Acidity and Performance

This chapter is based on: J. Oenema, R.A. van Alst, M.J. Meijerink, J. Zečević, K.P. de Jong, Applied Catalysis A, General 605, 2020, 117815.

Abstract

In previous studies $H_2PtCl_6 \cdot 6H_2O$ or $Pt(NH_3)_4(NO_3)_2$ were used to control the location of Pt nanoparticles in Zeolite/γ-Al_2O_3 composites for the synthesis of metal-acid bifunctional catalysts. Use of $H_2PtCl_6 \cdot 6H_2O$ led to Pt nanoparticles located on the γ-Al_2O_3 binder, in a 'nanoscale' intimacy with zeolite acid sites being beneficial for performance in the conversion of hydrocarbons, compared to catalysts with Pt nanoparticles located in zeolite Y ('closest' metal-acid intimacy) obtained by use of $Pt(NH_3)_4(NO_3)_2$. A side effect of using $H_2PtCl_6 \cdot 6H_2O$ was a higher NH_3 uptake in NH_3-TPD experiments, that suggested a higher acidity possibly affecting catalysis. In this study the effect of residual chlorine on Pt/Zeolite Y/γ-Al_2O_3 catalysts (0.1-0.6 wt.% Cl) was investigated by (pyridine) FTIR, NH_3-TPD and *n*-alkane hydroisomerization. The coordination of chlorine to γ-Al_2O_3 was observed and led to a higher NH_3 uptake, but no effect of chlorine on the catalytic performance of the catalysts was detected.

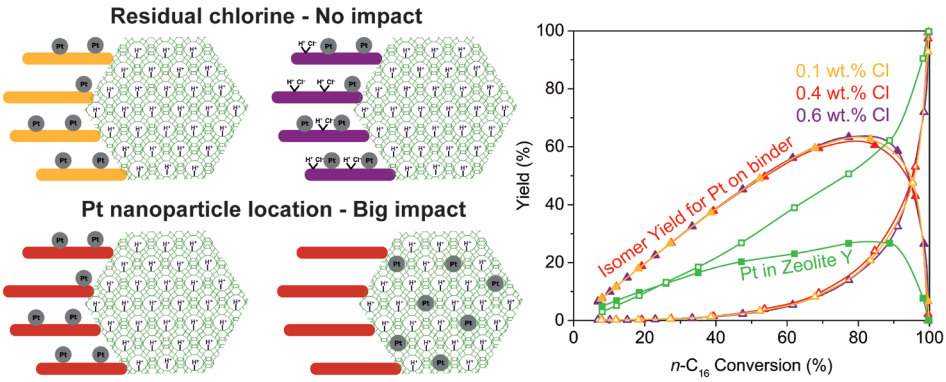

4.1 Introduction

Bifunctional catalysts based on metal (oxides, sulfides) in combination with zeolites find application in large-scale hydroisomerization and hydrocracking processes in oil refineries for the production of transportation fuels and chemicals.[1,2] Besides industrial use, they are also studied for the conversion of biomass feedstocks[3,4], waste plastics[5] and for the hydrogenation of CO or CO_2 towards lower alkenes (C_2-C_4)[6,7], light alkanes[8,9] and aromatics[10,11]. The bifunctional catalysts employed for the conversion of hydrocarbons, consist of a (de)hydrogenation function and a Brønsted acid function. The (de)hydrogenation function can be performed by highly active noble metals like platinum or palladium, or more abundant, less active metal (sulfides), such as nickel, nickel-molybdenum sulfide or cobalt-molybdenum sulfide. The acid function, responsible for alkene protonation and subsequent isomerization and/or cracking, is commonly obtained by using an halogenated alumina, a zeolite or an amorphous silica-alumina support.[1,2]

Zeolite based industrial hydroisomerization processes for light alkanes are mostly performed using Pt/Mordenite as catalyst and operate at temperatures of 230-280 °C.[12] The catalysts typically have good long-term stability under reaction conditions, but have the downside that hampered hydrocarbon diffusion through zeolite micropores may lead to undesired cracking reactions. Alternatively, Pt/Cl-Al_2O_3 catalysts with relatively high chlorine loadings of 6-8 wt.% are used, that are active at relatively low operating temperatures (100-200 °C), which is favorable in view of the thermodynamic equilibrium of the isomerization reaction.[12] The downside of these catalysts is that they are highly sensitive towards sulfur and water traces in the feed and require a continuous spiking of the feed with chlorinating agents to retain catalytic activity. These chlorinating agents are converted to HCl, which leads to corrosion problems and requires to be extracted from the product stream.[13,14] Other applications of Pt/Cl-Al_2O_3 catalysts are in the catalytic reforming of naphtha, that takes place at operating temperatures between 425 and 525 °C.[12] Such reforming catalysts commonly also contain secondary/other metals such as Re or Sn, and have chlorine contents in the range of 0.3-1.0 wt.% Cl, yielding much less acidic catalysts than those used for hydroisomerization processes.[12,15]

According to the classical bifunctional mechanism, carbenium ions are formed by adsorption on Brønsted acid sites, that are relatively well described for zeolites, i.e. a bridged hydroxyl group between a framework silicon and a framework aluminum atom.[12] Most high surface area aluminas and silicas possess a large number of hydroxyl groups, but they have generally too weak acidity to act as Brønsted acid sites under 'mild' catalytic conditions (e.g. used for hydroisomerization).[16,17] The substitution of surface hydroxyl groups for chlorine may enhance the acidity of the neighboring hydroxyl groups on oxidic supports, and is accomplished at elevated temperatures by exposure to HCl, or chlorinating agents to be converted to HCl (Figure 4.1, reaction I).[14,18] The high electronegativity of chlorine weakens the chemical bond between H and O of the hydroxyl neighbor, increasing the tendency for proton transfer and thus increase Brønsted acidity. In case of harsh chlorination of alumina, up to a chlorine loading of 6-8 wt.%, an $AlCl_3$ phase is obtained at the surface, which is a strong Lewis acid. However, in conjunction with HCl an $AlCl_3$/HCl phase may be obtained, that has strong Brønsted acid sites able to catalyze hydrocarbon isomerization reactions at low temperatures.[19] Ducourty et al. have described strong Brønsted acid sites on chlorinated alumina as dissociatively adsorbed HCl on an Al site, coordinated to two Cl atoms (Figure 4.1, reaction II).[20] Supposedly, this configuration provides

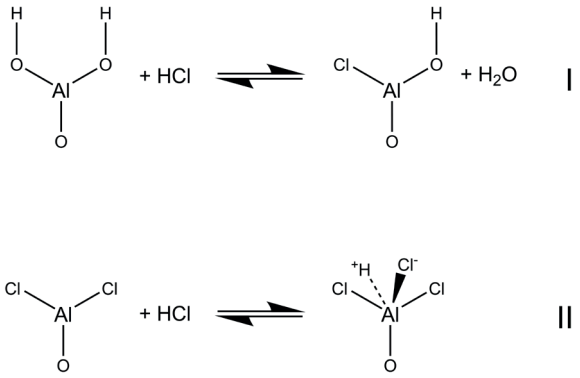

Figure 4.1. Reactions leading to chlorine coordination to the surface of γ-Al_2O_3, resulting in (enhanced) Brønsted acidity. Formula I represents the substitution of surface hydroxyl groups, resulting in enhanced Brønsted acidity of neighboring hydroxyl groups.[18] Formula II represents the dissociative chemisorption of HCl on a chlorinated γ-Al_2O_3 surface, leading to strong Brønsted acidity.[20]

the acid function of the low temperature Pt/Cl-Al_2O_3 hydroisomerization processes. For the synthesis of supported metal catalysts, metal precursors (mostly inorganic metal salts) are used, that are decomposed in subsequent heat treatments, to obtain metallic or oxidic nanoparticles.[21] In an earlier study, $Pt(NH_3)_4(NO_3)_2$ and $H_2PtCl_6{\cdot}6H_2O$ were used as Pt precursors, to control the location of Pt nanoparticles on a Zeolite Y/γ-Al_2O_3 (50/50 wt.) composite support.[22] Pt could be selectively deposited inside zeolite crystals by ion-exchange (pH ~5) of $[Pt(NH_3)_4]^{2+}$ (aq), whereas adsorption (pH ~3) of $[PtCl_6]^{2-}$ (aq) was used to deposit Pt on the γ-Al_2O_3 binder. After Pt deposition, catalysts were heat treated at 600 °C to decompose the metal complexes and generate Pt nanoparticles. Interestingly, the catalysts with Pt nanoparticles located on the γ-Al_2O_3 binder displayed a higher isomer selectivity in the conversion of heavy *n*-alkanes than catalysts with Pt nanoparticles located inside zeolite Y, despite the larger distance between metal and acid sites. Later, this approach was adopted for zeolite/γ-Al_2O_3 composites based on 1 dimensional zeolites (MOR and ZSM-22) and used for conversion of *n*-heptane, a relatively light feedstock, also resulting in beneficial effects for catalysts with Pt nanoparticles on the γ-Al_2O_3 binder, prepared with $H_2PtCl_6{\cdot}6H_2O$.[23] Selective deposition of Pt has also been studied on several mesoporous composite supports, and it was typically found that the performance of resulting catalysts largely depends on the nature of the acid function, while it is not very sensitive towards the location of Pt nanoparticles, provided the intimacy criterion for bifunctional catalysts is fulfilled.[24,25] However, NH_3-TPD measurements in the aforementioned studies on nanoscale intimacy suggest subtle increased acidities for catalysts prepared with $H_2PtCl_6{\cdot}6H_2O$, compared to catalysts prepared with $Pt(NH_3)_4(NO_3)_2$, which is induced by traces of chlorine.[22,23,26] In this study, the effect of residual ex-precursor chlorine is studied by assessing its impact on the acidity and catalytic performance of the catalysts. The chlorine content of catalysts was systematically controlled by using different reduction temperatures and applying steam treatments. This was followed by characterization using (pyridine) FTIR, NH_3-TPD and catalytic experiments under industrially relevant conditions.

4.2. Experimental

4.2.1. Composite preparation

Zeolite Y/γ-Al_2O_3 composites were prepared by adding of 15 g of zeolite powder (Zeolyst CBV760) with 15 g of Pseudo-boehmite (PURAL SB, Sasol) to a mortar. Then, 2 wt.% (based on dry mass of the supports) of Acetic acid (Alfa Aesar, glacial, 99+%) and distilled water were added and components were mixed with a pestle for ~5 minutes until a viscous, homogeneous paste was obtained. Acetic acid was added as a peptizing agent for the boehmite particles, to aid in mixing and adhesion at the nanoscale with the zeolite crystallites.[27] The mixture was dried overnight at 120 °C in static air followed by calcination at 550 °C for 2 h, 5 °C·min^{-1}. Afterwards, the product was crushed and sieved to obtain grains of 212-500 μm diameter and used as such for Pt deposition. γ-Al_2O_3 as support for Pt nanoparticles was obtained by calcination of Pseudo-boehmite (PURAL SB, Sasol) at 550 °C for 2 h, 5 °C·min^{-1}.

4.2.2. Catalyst synthesis

Pt/Zeolite Y/γ-Al_2O_3 catalysts with Pt nanoparticles located inside the zeolite (Pt-Y/A-NH_3)

1.01 g of Zeolite Y/γ-Al_2O_3 particles were suspended in 300 mL Milli-Q water at room temperature and stirred for 1 hour (~500 rpm). 50 mL of aqueous solution containing 10.42 mg of $Pt(NH_3)_4(NO_3)_2$ (Sigma-Aldrich, 99.995% purity) was added dropwise to the suspension. After 3 hours of stirring (500 rpm), the suspension was filtered and washed with 150 mL Milli-Q water and dried in static air overnight at 120 °C. The dried sample was reduced in a flow of 'dry' H_2 (GHSV~3300 h^{-1}) for 3 hours at 600 °C, using a ramp of 5 °C·min^{-1}.

Pt/Zeolite Y/γ-Al_2O_3 catalyst with Pt nanoparticles located on the γ-Al_2O_3 binder (Pt-Y/A-Cl)

4.00 g of Zeolite Y/γ-Al_2O_3 particles were suspended in 1200 mL Milli-Q water at room temperature and stirred for 1 h (~500 rpm). The suspension was acidified by adding a 1 M HCl solution dropwise until a pH of 2.7 was obtained. 50 mL of aqueous solution containing 99.5 mg of $H_2PtCl_6{\cdot}6H_2O$ (Merck, ~40 wt.% Pt) was added dropwise to the suspension. After 3 hours of stirring (500 rpm), the suspension was filtered and washed with 400 mL Milli-Q water and dried in static air overnight at 120 °C. The dried sample was divided into fractions of 500-600 mg, and reduced at temperatures between 300 °C and 600 °C in a flow of 'dry' H_2 (GHSV~3300 h^{-1}) for 2 hours with a ramp of 5 °C·min^{-1}. After reduction at 600 °C, two fractions were submitted to an additional 'steam treatment' to remove residual chlorine. A flow of H_2 saturated with water (P_{H2O} = 0.03 atm) was obtained by flowing H_2 as carrier gas through a saturator containing water at 20 °C. Subsequently the gas was flowed over the catalysts (GHSV~3300 h^{-1}) in a plug flow reactor, for 3 or 12 hours at a temperature of 530 °C (5 °C·min^{-1}), which was shown to be an optimal temperature for the (endothermic) substitution of chlorine for hydroxyl groups.[14]

Pt/γ-Al_2O_3 catalysts (Pt-A-Cl) were prepared by adsorption of $H_2PtCl_6{\cdot}6H_2O$ on 1.00 g γ-Al_2O_3 (PURAL SB pseudo-boehmite calcined for 2 hours at 550 °C), using the same procedure as for the Zeolite Y/γ-Al_2O_3 composite support, followed by drying in static air overnight at 120 °C, followed by reduction in 'dry' hydrogen at temperatures of 400 °C or 600 °C (GHSV~3300 h^{-1}).

4.2.3. Characterization

Elemental analysis of Pt and Cl was performed at Kolbe Mikroanalytisches Laboratorium using

an Inductively Coupled Plasma - Optical Emission Spectrometer (ICP-OES, Perkin Elmer) for platinum and Ion Chromatography for chlorine, after sample dissolution according to standard in-house procedures.

N_2 physisorption measurements of the supports were conducted on a Micromeritics TriStar 3000 at liquid nitrogen temperature. The samples were dried overnight at 300 °C in a N_2 flow before measurements.

X-ray diffraction (XRD) measurements of the catalysts were performed using a Bruker D2 PHASER, equipped with Co Kα radiation (λ = 1.789 Å). Diffractograms were measured from 5° to 80° 2θ with 0.05° increments and a scan rate of 0.1 second per step.

Ammonia Temperature Programmed Desorption (NH_3-TPD) was performed on a Micromeritics AutoChem II equipped with a Thermal Conductivity Detector (TCD) calibrated for ammonia. 100 mg of catalyst was dried in a He flow for 1 hour at 600 °C (10 °C·min^{-1}). The temperature was then decreased to 100 °C and ammonia (10 vol% in He) was adsorbed in a pulsewise manner until oversaturation. The physisorbed ammonia was removed by flowing He for 2 h at 100 °C, whereafter the ammonia desorption was monitored until 600 °C with a ramp of 10 °C·min^{-1}. Quantification of ammonia desorption was performed by integration of the TCD signal.

HAADF-STEM imaging was performed on an FEI Talos F200X transmission electron microscope, equipped with a high-brightness field emission gun (X-FEG), operated at 200 keV. For these analyses, catalysts were embedded in Epofix resin, left to cure in air overnight at 60 °C, and cut to 70 nm sections using a Reichert-Jung Ultracut E ultramicrotome with Diatome Ultra 35° diamond knife. For analysis, the sections were deposited on carbon-coated copper TEM grids.

FTIR (infrared spectroscopy) experiments were performed on a Thermo Scientific Nicolet iS5 FTIR spectrometer (32 scans, 4 cm^{-1} resolution, DTGS detector) using a transmission in situ cell with CaF_2 windows. For each measurement, a self-supporting pellet was made of ~13 mg of sample. The pellet was dried for 2 hours at 500 °C (10 °C·min^{-1}) in vacuum. After drying, the pellet was cooled down to 50 °C and a vacuum was obtained of $<7 \cdot 10^{-5}$ mbar, whereafter a spectrum was measured. Following the drying procedure, pyridine (redistilled, 99.9 %, Sigma-Aldrich) was introduced as vapor at a pressure of ~17 mbar, and was adsorbed for 30 min subsequent by 30 min of evacuation whereafter a spectrum was measured.

4.2.4. Hydroisomerization experiments

Catalytic experiments were conducted in an Avantium Flowrence 16 parallel fixed bed reactor setup.

n-Heptane hydroisomerization experiments were performed in stainless steel reactors (internal diameter = 2 mm) and were loaded with 25 mg of Pt/Zeolite Y/γ-Al_2O_3 catalyst or 12.5 mg of Pt/γ-Al_2O_3 catalysts, both in a sieve fraction of 75-212 μm. The product stream coming from the reactors was analyzed using an online GC (Agilent 7890A) were the hydrocarbon products were analyzed on an Agilent J&W PoraBOND Q column, connected to an FID. Catalysts were reduced at 300 °C (2 h; 5 °C·min^{-1}) in a 25 % H_2/He flow prior to catalytic testing. For *n*-heptane hydroisomerization the following conditions were used: a feed rate of 2.6 $g_{n\text{-}C7} \cdot g_{cat}^{-1} \cdot h^{-1}$, a total pressure of 10 bar and 9 $mol_{H2} \cdot mol_{n\text{-}C7}^{-1}$

n-Hexadecane hydroisomerization experiments were performed in stainless steel reactors (internal diameter = 2 mm) and were loaded with 50 mg of Pt/Zeolite Y/γ-Al_2O_3 catalyst or 25 mg of Pt/γ-Al_2O_3 catalysts, both in a sieve fraction of 75-212 μm. The product stream coming from the reactors was analyzed using an online GC (Agilent 7890B) were the hydrocarbon products were analyzed on an Agilent J&W HP-PONA column, connected to an FID. Before catalytic tests, catalysts were reduced at 300 °C (2 h; 5 °C·min^{-1}) in an H_2 flow. For *n*-hexadecane hydroisomerization the following conditions were used: a feed rate of 1.7 $g_{n\text{-}C16}\cdot g_{cat}^{-1}\cdot h^{-1}$, a total pressure of 4.7 bar and 10 $mol_{H2}\cdot mol_{n\text{-}C16}^{-1}$.

n-Heptane (99+%, pure) and *n*-Hexadecane (99%, pure) were obtained from Acros Organics, He 5.0, N2 5.0, H2 6.0 gasses were obtained from Linde gas. Results from catalytic tests were obtained by taking the average of two GC measurement performed at identical conditions.

The calculations to compute the *n*-alkane conversion, product yield and selectivity are provided in the Supplementary information 3.1 for *n*-heptane and in 4.1 for *n*-hexadecane.

4.3. Results and Discussion

4.3.1 Regulation of the chlorine content

Structural information on the porosity of the catalysts supports was obtained from N2 physisorption and is provided in the supplementary information (Figure S4.6, Table S4.1). To control the chlorine loadings of the Pt/Zeolite Y/γ-Al_2O_3 catalysts (0.9-1.0 wt.% Pt) prepared with $H_2PtCl_6\cdot 6H_2O$, a series of reduction temperatures and subsequent steam treatments were used. In Figure 4.2 an overview is provided of the chlorine loading of the samples after their respective thermal treatment. Based on the stoichiometry between Pt and Cl in $H_2PtCl_6\cdot 6H_2O$ and the respective atomic weights, a chlorine loading of approximately 1 wt.% is expected for 1 wt.% Pt catalysts, assuming no loss of chlorine during the synthesis and washing steps. From the measured chlorine contents in Figure 4.2, it is apparent that this estimate is close to the chlorine loading obtained after drying. By reducing the dried sample using H_2, chlorine was partially removed from the catalyst surface, and especially when higher reduction temperatures were used, the amount of chlorine of the catalysts decreased gradually.[28] However, to be able to completely remove chlorine from the catalysts, steam treatments at elevated temperatures were required in line with literature.[18] Removal of chlorine by steam can be explained by chlorine coordinated to the γ-Al_2O_3 surface by a covalent bond, that is exchanged for a OH group, i.e. the reverse of the reaction shown in Figure 4.1,I.[14] This method was successfully applied to remove almost all chlorine from the catalyst.

From here on, the catalysts prepared with $H_2PtCl_6\cdot 6H_2O$ will be referred to as Pt-Y/A-(X)Cl, where the '(X)' indicates the chlorine loading in weight percentage. The characterization is focused on the composite catalysts reduced in H_2 at 400 °C and 600 °C (Pt-Y/A-0.6Cl and Pt-Y/A-0.4Cl, respectively) and the catalysts that was steam treated for 12 hours (Pt-Y/A-0.1Cl). This catalysts has a 'baseline' chlorine content of 0.1 wt.% that is similar to the chlorine content of the Y/A parent composite support. Chlorine loadings of 0.6, 0.4 and 0.1 wt.% correspond to surface coverages of 0.9, 0.6 and 0.2 Cl atoms·nm^{-2} on γ-Al_2O_3, respectively. In the supplementary information Table S4.2, more details are provided on the platinum and chlorine contents of the catalysts used for this study. In order to disentangle the effect of location of Pt nanoparticles from the chlorine content,

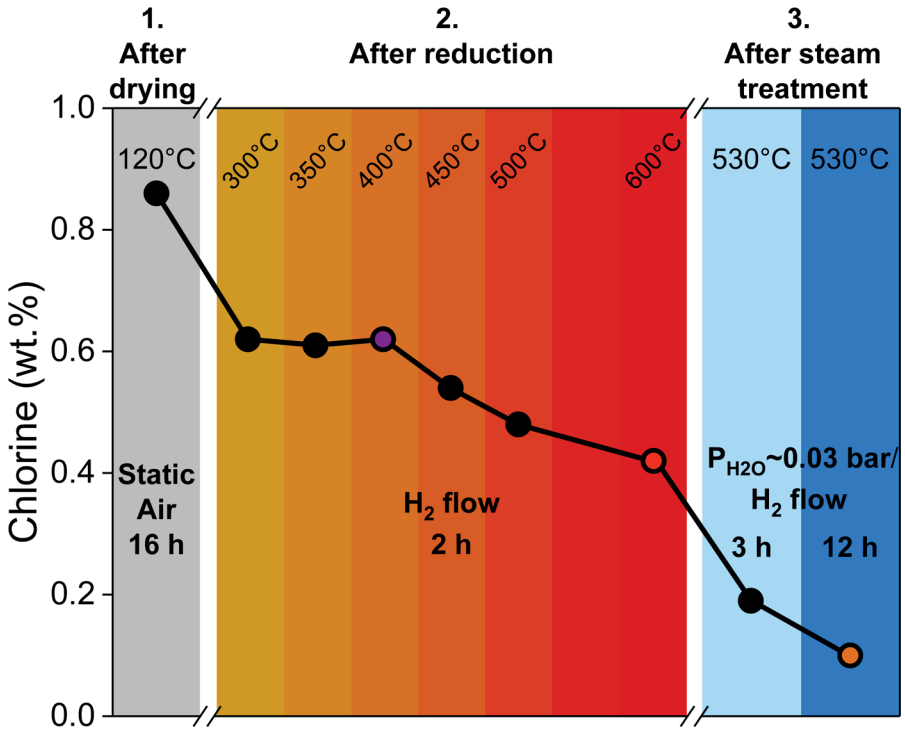

Figure 4.2. Chlorine content of Pt-Y/A-Cl catalysts (0.9-1.0 wt.% Pt), prepared with $H_2PtCl_6{\cdot}6H_2O$, after different stages of the catalyst preparation. The chlorine contents of the samples were determined with Ion-chromatography after sample destruction.

a Pt/Zeolite Y/γ-Al_2O_3 catalyst was prepared using $Pt(NH_3)_4(NO_3)_2$ with a Pt loading of 0.3 wt.%, which will be referred to as Pt-Y/A-NH_3. Furthermore Pt/γ-Al_2O_3 catalysts were prepared to study the catalytic performance of catalyst without the acid function of the zeolite and will be indicated as Pt-A-(X)Cl. The obtained composite catalyst were extensively characterized to ensure that the structural properties of the catalysts remained intact after the various thermal treatments. In the supplementary information (Figure S4.7), XRD diffractograms are provided of the steam treated Pt-Y/A-Cl catalysts and are compared to the parent Y/A composite support. It shows sharp diffraction peaks of Zeolite Y for all samples, indicating that zeolite crystallinity was not affected by the steam treatments. Characterization methods such as pyridine FTIR and NH_3-TPD require preconditioning of the catalysts at elevated temperatures. In this case, this might influence the amount of chlorine on the catalysts and therefore, the catalysts reduced at 400 °C were not studied with these techniques, but were only tested in catalytic experiments.

4.3.2 HAADF-STEM images

In Figure 4.3, HAADF-STEM images of 70 nm thick sections are provided, confirming that the location of Pt nanoparticles was controlled by using either $H_2PtCl_6{\cdot}6H_2O$ or $Pt(NH_3)_4(NO_3)_2$ as precursor, according to a previously reported method.[22] The control on location of Pt nanoparticles by using this method has been studied before, using techniques that sample relatively large amounts of catalysts per measurement.[29] Histograms showing the Pt particle

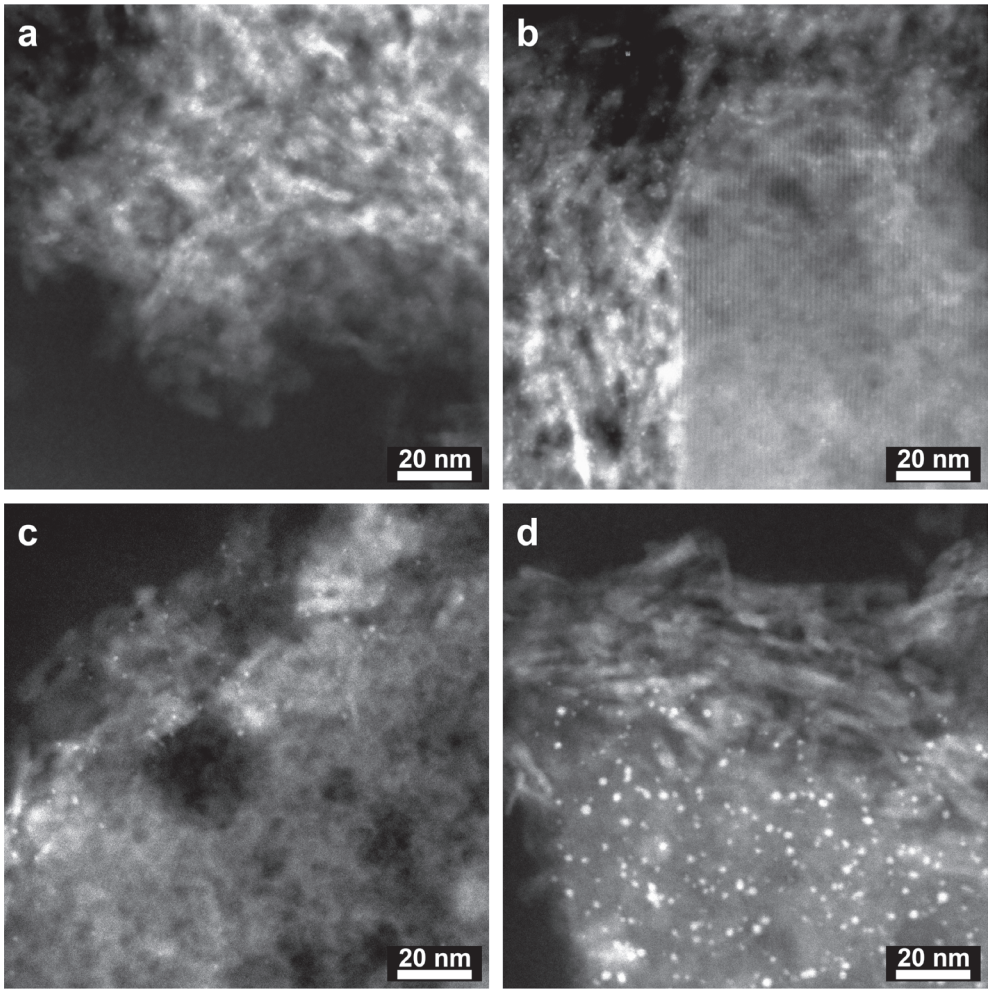

Figure 4.3. HAADF-STEM images of the Pt-Y/A-0.6Cl (a), Pt-Y/A-0.4Cl (b) and Pt-Y/A-0.1Cl (c) catalysts, prepared with $H_2PtCl_6 \cdot 6H_2O$, with Pt nanoparticles located on the γ-Al_2O_3 binder, and the Pt-Y/A-NH_3 catalyst (d) prepared with $Pt(NH_3)_4(NO_3)_2$, with Pt nanoparticles located in the zeolite component.

size distribution are provided in the supplementary information (Figure S4.8), and show that Pt particle sizes are relatively narrow for samples prepared with $H_2PtCl_6 \cdot 6H_2O$ despite the different heat treatments with and without steam, while use of $Pt(NH_3)_4(NO_3)_2$ and direct reduction led to an higher average particle size and a slightly broader size distribution.

4.3.3. Characterization by (pyridine) FTIR and NH_3-TPD

In Figure 4.4, transmission FTIR spectra of the hydroxyl region of γ-Al_2O_3, Pt/γ-Al_2O_3 and Pt/Zeolite Y/γ-Al_2O_3 samples are provided. In a number of recent computational publications, Digne et al. were able to assign many γ-Al_2O_3 hydroxyl vibrations located on different crystallographic planes.[30,31] More 'acidic' hydroxyl groups, with a relatively labile H-O bond, are found at lower wavenumbers, while the isolated hydroxyl groups with more rigid H-O bonds, but relatively

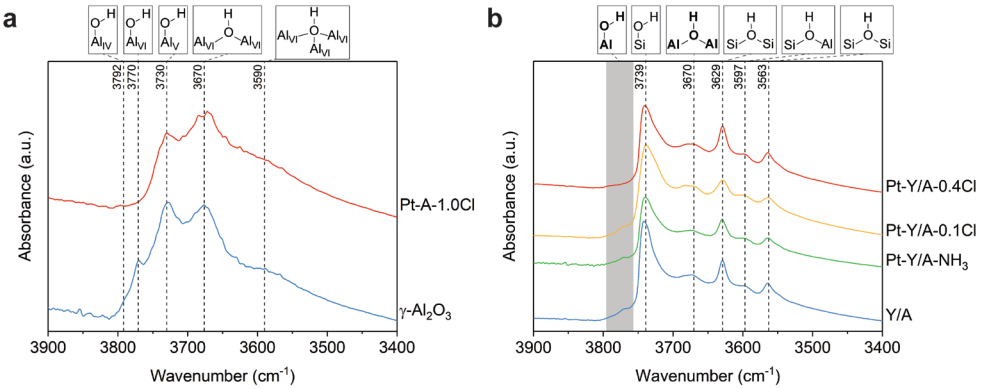

Figure 4.4. Transmission FTIR spectra of the hydroxyl region of γ-Al_2O_3 and Pt-A-1.0Cl, with the absorption bands of the different types of hydroxyl groups indicated (a).[30,31] The Al coordination of the hydroxyl O atom (isolated, bridged, tribridged) is indicated per band, whereas the subscript of Al indicates the O coordination number of the Al atom. For Pt-A-1.0Cl, absorption bands at higher wavenumbers disappear with respect to those of γ-Al_2O_3. The transmission FTIR spectra of the hydroxyl region of the Pt/Zeolite Y/γ-Al_2O_3 catalysts and the Zeolite Y/γ-Al_2O_3 composite support are provided in (b).[30–32] The region of the absorption bands of isolated alumina hydroxyl groups are indicated in grey, and could not be assigned individually due to overlap with the band from isolated silanol groups from zeolite Y. Nevertheless, a negative correlation is observed between the intensity of the isolated Al_2O_3 hydroxyl groups with respect to the chlorine loading of the catalysts, confirming the coordination of chlorine to the γ-Al_2O_3 component in Pt-Y/A-0.4Cl.

labile O-Al bonds, are observed at higher wavenumbers. Because the isolated hydroxyl groups are removed firstly during calcination treatments and are most easily substituted for Cl, they are considered as 'basic' hydroxyl groups.[16,32] From Figure 4.4a it is indeed observed that some of these isolated hydroxyl groups have disappeared for the Pt-A-1.0Cl catalysts with respect to γ-Al_2O_3, that can be attributed to substitution with Cl. Furthermore, the H-O bonds neighboring the chlorine atoms will become more labile, and thus shift to lower wavenumbers in the IR spectrum, which might explain the flatness of the spectrum of Pt-A-1.0Cl around 3650 cm^{-1} compared to γ-Al_2O_3. A similar trend can be observed for the Pt/Zeolite Y/γ-Al_2O_3 catalysts (Figure 4.4b), where the vibrations for isolated γ-Al_2O_3 hydroxyl groups dissapear with increasing chlorine loading. The spectra of the Pt/Zeolite Y/γ-Al_2O_3 catalysts are less conclusive due to the overlap with silanol vibrations from zeolite Y, but the trend can still be observed. Another indication for the increased acidity for catalysts with higher chlorine content can be obtained from NH_3-TPD, where higher NH_3 uptakes for chlorine modified γ-Al_2O_3 compared to unmodified γ-Al_2O_3 are typically found.[33] For the Pt/Zeolite Y/γ-Al_2O_3 catalysts in the temperature range of 100-600 °C, the amount of desorbed NH_3 was higher for Pt-Y/A-0.4Cl than for Pt-Y/A-0.1Cl (Figure S4.9, Table S4.3). The difference between Pt-Y/A-0.4Cl and Pt-Y/A-0.1Cl corresponds approximately to the difference that was previously observed for Pt-Y/A-0.4Cl and Pt-Y/A-NH_3 catalysts.[22] While NH_3-TPD is a useful technique providing a quantitative information on acidity, the 'classical' method for a qualitive distinction between Brønsted or Lewis acidity is adsorption-desorption of pyridine in combination with spectroscopy.[34–37] By protonation of pyridine on a Brønsted acid site, a pyridinium ion is created, that appears as an isolated absorption band in FTIR spectra. Several studies have used pyridine FTIR to study (modified) aluminas, but have generally only

observed evidence for Lewis acidity.[16,34–36] The only cases pyridinium ions were observed was for fluorinated aluminas (2-4 wt.% F)[38] or in presence of HCl.[39] In the supplementary information pyridine FTIR spectra are provided of γ-Al_2O_3, Pt-A-1.0Cl and Pt-Y/A-0.4Cl, that shows that only pyridinium ions were formed on Pt-Y/A-0.4Cl, that can be attributed to adsorption on zeolite Brønsted acid sites (Figure S4.10).

4.3.4 Catalytic performance in the hydroisomerization of *n*-heptane and *n*-hexadecane

In Figure 4.5, the results of the hydroisomerization experiments are provided of hydrocarbons with different molecular weight for the catalysts with varying chlorine loading. The catalysts possess Pt weight loadings of 0.3-1.0 wt.% and a sub 2-nm Pt particle size as evidenced from HAADF-STEM. Earlier research has pointed out that on such catalysts, the rate of the reaction on the metal sites is not rate limiting.[40,41] The high hydrogen pressures applied in catalytic experiments will further benefit establishment of an equilibrium between alkanes and alkenes[42],

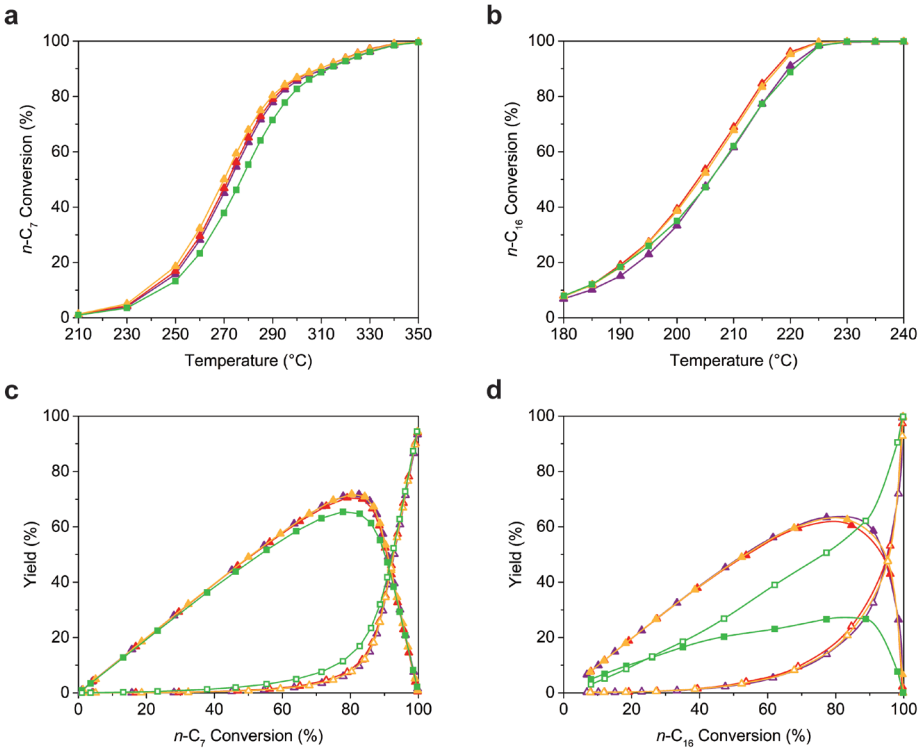

Figure 4.5. Results of hydroisomerization experiments showing the effect of chlorine loading and location of Pt nanoparticles on activity (a) and isomer yield (c) for the conversion of *n*-Heptane, and activity (b) and isomer yield (d) for the conversion of *n*-Hexadecane. Pt-Y/A-Cl catalysts (0.9-1.0 wt.% Pt) are indicated by triangles: Pt-Y/A-0.6Cl (purple), Pt-Y/A-0.4Cl (red) and Pt-Y/A-0.1Cl (yellow), while the Pt-Y/A-NH_3 catalyst (0.3 wt.% Pt) is indicated by green squares. In c and d, closed symbols denote isomer yield while open symbols denote cracking yield. Experimental conditions for the conversion of *n*-heptane were a feed rate of 2.6 $g_{n\text{-}C7}\cdot g_{cat}^{-1}\cdot h^{-1}$, a total pressure of 10 bar and 9 $mol_{H2}\cdot mol_{n\text{-}C7}^{-1}$, while for the conversion of *n*-hexadecane a feed rate of 1.7 $g_{n\text{-}C16}\cdot g_{cat}^{-1}\cdot h^{-1}$, a total pressure of 4.7 bar and 10 $mol_{H2}\cdot mol_{n\text{-}C16}^{-1}$ were used.

which is further confirmed by a close-to-identical activity for the Pt-Y/A-NH_3 and Pt-Y/A-Cl catalysts. The data of *n*-heptane and *n*-hexadecane hydroisomerization in Figure 4.5, show good reproducibility with previous studies where Pt nanoparticles located inside zeolite crystallites had a slight negative effect on catalytic activity and was detrimental for isomer selectivity, especially for linear feedstocks of high molecular weight.[22,23] Strikingly, there appear to be no effects of the chlorine loading of Pt-Y/A-Cl catalysts on their catalytic performance: in Figure 4.5c and 4.5d, the isomer yield curves are overlapping. The cracking product distribution, provided in the supplementary information (Figure S4.11) shows the tendency of the Pt-Y/A-NH_3 catalysts for secondary cracking for feedstocks of high molecular weight, while for the Pt-Y/A-Cl catalysts an identical bell-shaped curve is observed.[22] Chlorine contents of the catalysts after the n-hexadecane hydroisomerization experiments are provided in Table S4.3, and show that a limited loss of chlorine (20-30%) occurred during a test of 8 days at temperatures between 180 °C and 300 °C. As a reference experiment, the catalytic performance of the Pt-A-1.0Cl and Pt-A-2.0Cl catalysts was investigated over a broad temperature range (Figure S4.12). As can be inferred from Table S4.4, the cracking products observed on the Pt-Al-Cl reference catalysts are not those typically observed from cracking on acid sites, but are mostly linear cracking products, pointing towards cracking on Pt sites via hydrogenolysis reactions. Further evidence for a distinct reaction mechanism on Pt-Al-Cl catalysts is obtained from the apparent activation energies, revealing similar activation energies for the zeolite based composites, but a distinct lower value for the Pt-A-Cl catalysts (Table S4.5). From these results it is evident that such a catalysts has no significant activity at the catalytic conditions of hydroisomerization applied for zeolite based catalysts.

4.4. Conclusions

In this study the effect of residual chlorine from the $H_2PtCl_6{\cdot}6H_2O$ precursor on Pt/Zeolite Y/γ-Al_2O_3 composite catalyst was investigated. It was found that a significant amount of chlorine remained on the catalysts after reduction in H_2, of up to 0.6 wt.% Cl for a 1 wt.% Pt catalysts. Characterization with FTIR revealed the coordination of Cl to the γ-Al_2O_3 surface while NH_3-TPD revealed a higher NH_3 uptake for the catalyst with higher chlorine loadings. Therefore, subtle differences in NH_3 uptake between catalysts prepared with $H_2PtCl_6{\cdot}6H_2O$ or $Pt(NH_3)_4(NO_3)_2$ observed here and previous studies, are therefore rightfully attributed to the presence of chlorine. *n*-Heptane and *n*-hexadecane hydroisomerization experiments on Pt/Zeolite Y/γ-Al_2O_3 composite catalysts, with Pt nanoparticles located on the γ-Al_2O_3 binder and chlorine loadings in a range of 0.6-0.1 wt.%, revealed that residual chlorine had no impact on the catalytic performance of these catalysts. The coordination of chlorine on Pt/Cl-Al_2O_3 catalysts (0.8-1.5 Cl atoms·nm^{-2}), did neither lead to strong Brønsted acid sites that could be detected by pyridine FTIR, nor provided measurable catalytic activity in *n*-heptane and *n*-hexadecane hydroisomerization experiments. However, the presence of chlorine on catalysts in the range of 0-2 wt.% Cl, as observed by. Hydroisomerization experiments with a *n*-heptane and *n*-hexadecane feedstock did result in significant differences as a result of the location of Pt nanoparticles, while no differences were observed depending on the chlorine loading of the catalysts.

Acknowledgements

We acknowledge the European Research Council, EU FP7 ERC Advanced Grant no. 338846

for financial support. Nikos Nikopoulos and Remco Dalebout (both UU) are acknowledged for performing N_2 physisorption measurements. Sasol Germany GmbH is acknowledged for supplying the Pural SB, pseudo-boehmite support. We thank Prof. Gary Haller (Yale University) for raising the issue of possible effects of chlorine in our earlier studies on nanoscale intimacy in bifunctional catalyst.

References

[1] E. T. C. Vogt, G. T. Whiting, A. Dutta Chowdhury, B. M. Weckhuysen, Zeolites and Zeotypes for Oil and Gas Conversion, Elsevier Inc., 2015.

[2] J. W. Thybaut, G. B. Marin, in Adv. Catal., Elsevier Inc., 2016, pp. 109–238.

[3] B. Peng, Y. Yao, C. Zhao, J. A. Lercher, Angew. Chemie - Int. Ed. 2012, 51, 2072–2075.

[4] G. W. Huber, J. N. Chheda, C. J. Barrett, J. A. Dumesic, Science. 2005, 308, 1446–1450.

[5] D. Munir, M. F. Irfan, M. R. Usman, Renew. Sustain. Energy Rev. 2018, 90, 490–515.

[6] F. Jiao, J. Li, X. Pan, J. Xiao, H. Li, H. Ma, M. Wei, Y. Pan, Z. Zhou, M. Li, et al., Science. 2016, 351, 1065–1068.

[7] K. Cheng, B. Gu, X. Liu, J. Kang, Q. Zhang, Y. Wang, Angew. Chemie Int. Ed. 2016, 55, 4725–4728.

[8] P. Gao, S. Li, X. Bu, S. Dang, Z. Liu, H. Wang, L. Zhong, M. Qiu, C. Yang, J. Cai, et al., Nat. Chem. 2017, 9, 1019–1024.

[9] S. Sartipi, M. Makkee, F. Kapteijn, J. Gascon, Catal. Sci. Technol. 2014, 4, 893–907.

[10] J. L. Weber, I. Dugulan, P. E. de Jongh, K. P. de Jong, ChemCatChem 2018, 10, 1107–1112.

[11] S. Kasipandi, J. W. Bae, Adv. Mater. 2019, 31, 1–18.

[12] A. Corma, A. Martinez, in Handb. Porous Solids (Eds.: F. Schüth, K.S.W. Sing, J. Weitkamp), Wiley-VCH Verlag GmbH & Co. KGaA, 2002, pp. 2825–2922.

[13] V. M. Akhmedov, S. H. Al-Khowaiter, Catal. Rev. 2007, 49, 33–139.

[14] M. Digne, P. Raybaud, P. Sautet, D. Guillaume, H. Toulhoat, J. Am. Chem. Soc. 2008, 130, 11030–11039.

[15] R. J. Verderone, C. L. Pieck, M. R. Sad, J. M. Parera, Appl. Catal. 1986, 21, 239–250.

[16] C. Morterra, G. Magnacca, Catal. Today 1996, 27, 497–532.

[17] X. Liu, R. E. Truitt, J. Am. Chem. Soc. 1997, 119, 9856–9860.

[18] A. A. Castro, O. A. Scelza, E. R. Benvenuto, G. T. Baronetti, J. M. Parera, J. Catal. 1981, 69, 222–226.

[19] V. N. Ipatieff, L. Schmerling, Ind. Eng. Chem. 1948, 40, 2354–2360.

[20] B. Ducourty, G. Szabo, J. P. Dath, J. P. Gilson, J. M. Goupil, D. Cornet, Appl. Catal. A Gen. 2004, 269, 203–214.

[21] P. Munnik, P. E. De Jongh, K. P. De Jong, Chem. Rev. 2015, 115, 6687–6718.

[22] J. Zečević, G. Vanbutsele, K. P. De Jong, J. A. Martens, Nature 2015, 528, 245–254.

[23] K. Cheng, L. I. Wal, H. Yoshida, J. Oenema, J. Harmel, Z. Zhang, G. Sunley, J. Zečević, K. P. Jong, Angew. Chemie Int. Ed. 2020, 59, 3592–3600.

[24] J. E. Samad, J. Blanchard, C. Sayag, C. Louis, J. R. Regalbuto, J. Catal. 2016, 342, 203–212.

[25] J. Harmel, L. I. van der Wal, J. Zečević, P. E. de Jongh, K. P. de Jong, Catal. Sci. Technol. 2020, 10, 2111–2119.

[26] J. E. Samad, J. Blanchard, C. Sayag, C. Louis, J. R. Regalbuto, J. Catal. 2016, 342, 213–225.

[27] G. T. Whiting, S. H. Chung, D. Stosic, A. D. Chowdhury, L. I. Van Der Wal, D. Fu, J. Zecevic, A. Travert, K. Houben, M. Baldus, et al., ACS Catal. 2019, 9, 4792–4803.

[28] A. Kytökivi, M. Lindblad, A. Root, J. Chem. Soc. Faraday Trans. 1995, 91, 941–948.

[29] J. Oenema, J. P. Hofmann, E. J. M. Hensen, J. Zečević, K. P. de Jong, ChemCatChem 2020, 12, 615–622.

[30] M. Digne, P. Sautet, P. Raybaud, P. Euzen, H. Toulhoat, J. Catal. 2002, 211, 1–5.

[31] M. Digne, P. Sautet, P. Raybaud, P. Euzen, H. Toulhoat, J. Catal. 2004, 226, 54–68.

[32] F. Thibault-Starzyk, F. Maugé, Characterization of Solid Materials and Heterogeneous Catalysts, Wiley-VCH Verlag GmbH & Co. KGaA, Weinheim, Germany, 2012.

[33] P. Berteau, B. Delmon, Catal. Today 1989, 5, 121–137.

[34] J. A. Ripmeester, J. Am. Chem. Soc. 1983, 105, 2925–2927.
[35] S. M. Riseman, F. E. Massoth, G. M. Dhar, E. M. Eyring, J. Phys. Chem. 1982, 86, 1760–1763.
[36] E. P. Parry, J. Catal. 1963, 2, 371–379.
[37] M. E. Z. Velthoen, S. Nab, B. M. Weckhuysen, Phys. Chem. Chem. Phys. 2018, 20, 21647–21659.
[38] A. Corma, V. Fornes, E. Ortega, J. Catal. 1985, 92, 284–290.
[39] G. Clet, J.-M. Goupil, D. Cornet, Bull. Soc. Chim. Fr. 1997, 134, 223–233.
[40] F. Alvarez, F. R. Ribeiro, G. Perot, C. Thomazeau, M. Guisnet, J. Catal. 1996, 162, 179–189.
[41] M. Guisnet, F. Alvarez, G. Giannetto, G. Perot, Catal. Today 1987, 1, 415–433.
[42] J. W. Thybaut, C. S. Laxmi Narasimhan, J. F. Denayer, G. V. Baron, P. A. Jacobs, J. A. Martens, G. B. Marin, Ind. Eng. Chem. Res. 2005, 44, 5159–5169.

Supporting Information

Supporting Information 4.1

The conversion of the *n*-hexadecane feedstock ($X_{n\text{-}C16}$) was calculated by:

$$X_{n\text{-}C_{16}} = \left(1 - \frac{F_{C\,wt.\,n\text{-}C_{16},\,out}}{F_{C\,wt.\,n\text{-}C_{16},\,in}}\right) \cdot 100\%$$

Wherein $F_{C\,wt.\,n\text{-}C16,\,out}$ and $F_{C\,wt.\,n\text{-}C16,\,in}$ are the flows, based on weight of carbon, of the *n*-hexadecane feedstock going out or into the reactor, respectively.

The hydrocarbon isomer yield ($Y_{i\text{-}C16}$) was calculated by:

$$Y_{i\text{-}C_{16}} = \left(\frac{F_{C\,wt.\,i\text{-}C_{16},\,out}}{F_{C\,wt.\,n\text{-}C_{16},\,in}}\right) \cdot 100\%$$

The yield of cracked products ($Y_{C1\text{-}14}$) for *n*-hexadecane was calculated by:

$$Y_{C_{1\text{-}14}} = \left(\frac{F_{C\,wt.\,C_{1\text{-}14},\,out}}{F_{C\,wt.\,n\text{-}C_{16},\,in}}\right) \cdot 100\%$$

Wherein $F_{C\,wt.\,C1\text{-}14,\,out}$ are the flows, based on weight of carbon, of $C_{1\text{-}14}$ cracked products, respectively, going out of the reactor. For the cracking product distribution patterns of *n*-hexadecane hydroisomerization, the yield of individual cracked products in mol% (Y_{Cm}; m = 1-14), was calculated by:

$$Y_{C_m} = \left(\frac{F_{C\,wt.\,C_m,\,out}}{F_{C\,wt.\,n\text{-}C_{16},\,in}}\right) \cdot \left(\frac{16}{m}\right) \cdot 100\%$$

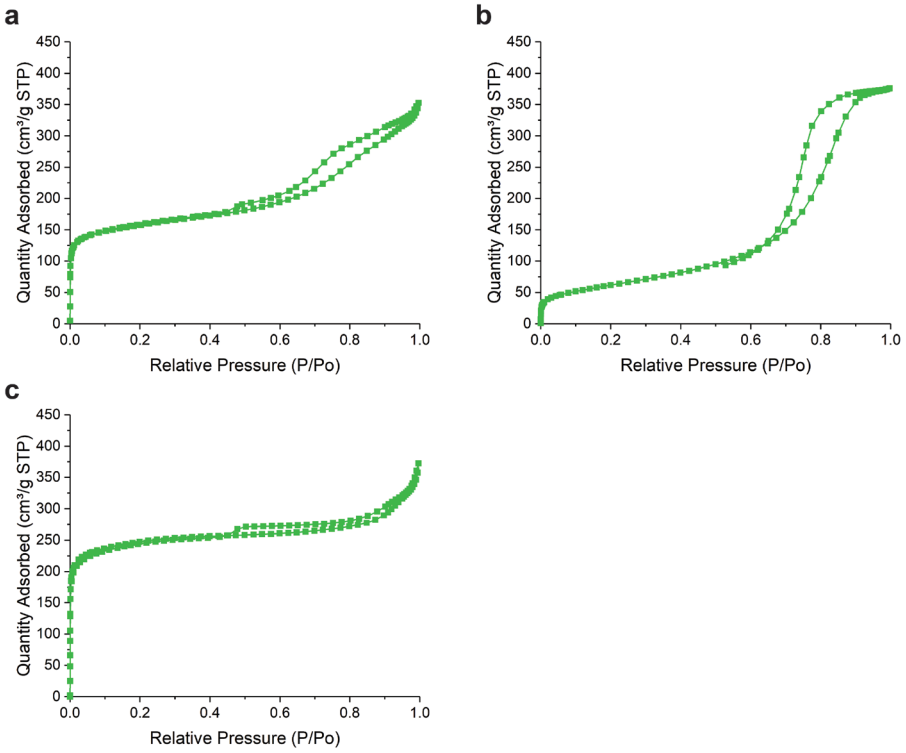

Figure S4.6. N_2 physisorption isotherms of the Zeolite Y/γ-Al_2O_3 composite support (a), the γ-Al_2O_3 support (b) and parent zeolite Y (c).

Table S4.1. Properties and results of textural analysis by N_2 physisorption of the Zeolite Y/γ-Al_2O_3 composite support and the single components.

	Product code	Si/Al ratio ($at \cdot at^{-1}$)	BET surface area ($m^2 \cdot g^{-1}$)	BJH pore volume ($cm^3 \cdot g^{-1}$)	t-plot micropore volume ($cm^3 \cdot g^{-1}$)	t-plot external surface area ($m^2 \cdot g^{-1}$)
Y/A	-	-	-	0.37	0.15	214
A (γ-Al_2O_3)	Sasol Pural SB (calcined)	-	224	0.59	-	-
Y (zeolite Y)	Zeolyst CBV760	30	-	0.23	0.29	203

Table S4.2. Results of elemental analysis by Inductively Coupled Plasma-Atomic Emission Spectroscopy for platinum and Ion Chromatography for chlorine. Prior to analysis, samples have been dried at 120 °C for 16 hours in vacuum (<5 mbar). Chlorine loadings after catalysis have been obtained after an *n*-hexadecane hydroisomerization run at reactor temperatures between 180-300 °C that lasted 8 days in total.

Sample Code	Sample description	Pt loading (wt.% Pt)	Cl loading (wt.% Cl)	Cl surface coverage* (Cl atoms ·nm^{-2})	Cl loading after catalysis (wt.% Cl)	Cl surface coverage* after catalysis (Cl atoms ·nm^{-2})
Composite catalysts prepared with $H_2PtCl_6 \cdot H_2O$						
Pt-Y/A-Cl	After drying (120 °C), before reduction	0.9(3)	0.8(6)	1.3(0)	-	-
Pt-Y/A-Cl	After reduction (300 °C)	0.9(3)	0.6(2)	0.9(4)	-	-
Pt-Y/A-Cl	After reduction (350 °C)	0.9(3)	0.6(1)	0.9(3)	-	-
Pt-Y/A-0.6Cl	After reduction (400 °C)	0.9(3)	0.6(2)	0.9(4)	0.4(6)	0.7(0)
Pt-Y/A-Cl	After reduction (450 °C)	0.9(3)	0.5(4)	0.8(2)	-	-
Pt-Y/A-Cl	After reduction (500 °C)	0.9(3)	0.4(8)	0.7(3)	-	-
Pt-Y/A-0.4Cl	After reduction (600 °C)	0.9(3)	0.4(2)	0.6(4)	0.3(5)	0.5(3)
Pt-Y/A-Cl	After reduction (600 °C), followed by steam treatment for 3 h (530 °C)	1.0(0)	0.1(9)	0.2(9)	-	-
Pt-Y/A-0.1Cl	After reduction (600 °C), followed by steam treatment for 12 h (530 °C)	1.0(0)	0.1(0)	0.1(5)	<0.01	<0.0(2)
Composite catalysts prepared with $Pt(NH_3)_4(NO_3)_2$						
Pt-Y/A-NH_3	After reduction (600 °C)	0.2(9)	0.1(2)	0.1(8)	<0.01	<0.0(2)
Pt/γ-Al_2O_3 catalysts prepared with $H_2PtCl_6 \cdot H_2O$						
Pt-A-2.0Cl	After reduction (400 °C)	1.4(9)	2.0(2)	1.5(3)	0.9(3)	0.7(1)
Pt-A-1.0Cl	After reduction (600 °C)	1.4(9)	1.0(1)	0.7(7)	1.1(7)	0.8(9)
Catalyst supports						
Y/A	Bare composite support	-	0.1(1)	0.1(7)	-	-
Y (Zeolite Y)	Zeolyst CBV760	-	0.0(5)	-	-	-
A (γ-Al_2O_3)	Sasol Pural SB (calcined)	-	0.2(6)	0.2(0)	-	-

*) Values for Cl surface coverage on γ-Al_2O_3 are based on the specific surface area (BET) of γ-Al_2O_3. For the Zeolite Y/γ-Al_2O_3 composite supports, it is assumed that all chlorine is present on the γ-Al_2O_3 component, and the BET surface area of γ-Al_2O_3 is assumed to be the same as the specific surface area of the γ-Al_2O_3 component in the composite supports.

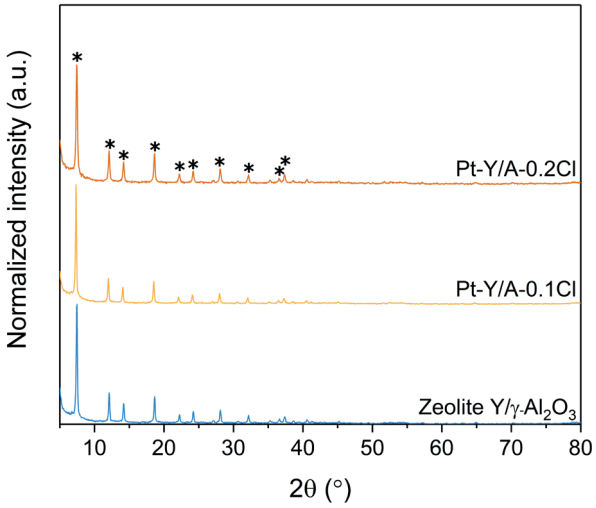

Figure S4.7. XRD diffraction patterns of Pt-Y/A-Cl catalysts steamed for 3 hours (Pt-Y/A-0.2Cl) or for 12 hours (Pt-Y/A-0.1Cl), showing no observable loss of crystallinity with respect to the Zeolite Y/γ-Al_2O_3 composite support of the catalysts after the steam treatments. Choice of step size (0.05° 2θ) and scan rate (0.1 sec per step) were optimized for Zeolite Y and consequently, no peaks corresponding to γ-Al_2O_3 were detected. Peaks corresponding to zeolite Y are indicated with an asterisk (*).

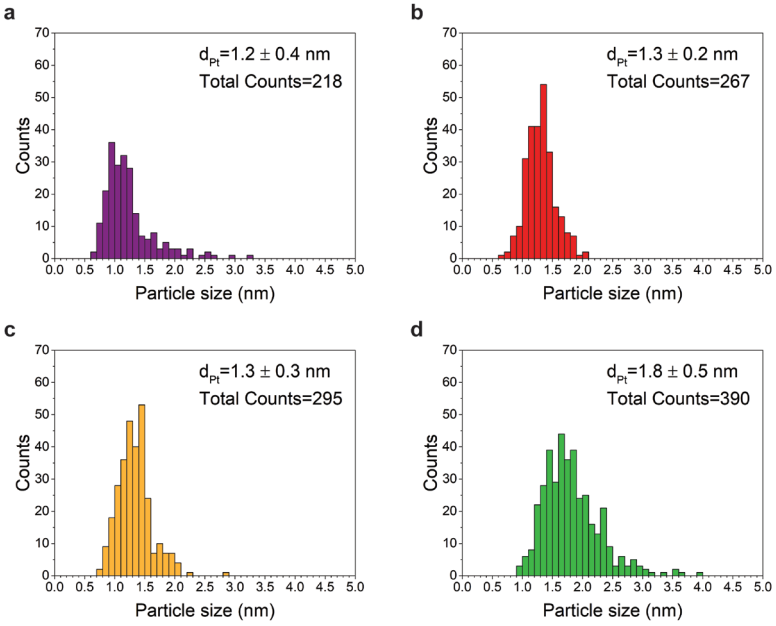

Figure S4.8. Pt particle size distribution from counting single Pt particles on HAADF-STEM images. The average Pt particle size, standard deviation in Pt particle size and number of Pt particles counted are indicated. Pt-Y/A-0.6Cl (a), Pt-Y/A-0.4Cl (b), Pt-Y/A-0.1Cl (c), Pt-Y/A-NH_3 (d).

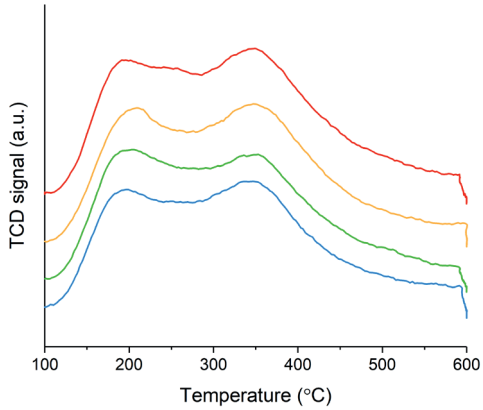

Figure S4.9. NH_3-TPD profiles of Pt-Y/A-0.4Cl (red), Pt-Y/A-0.1Cl (orange), Pt-Y/A-NH_3 (green) and Zeolite Y/γ-Al_2O_3 composite support (blue).

Table S4.3. Total acidity of Pt/Zeolite Y/γ-Al_2O_3 composite catalysts and Zeolite Y/γ-Al_2O_3 composite support as obtained by integration of the NH_3-TPD signal.

Sample	Total NH_3 desorbed ($mmol_{NH3} \cdot g^{-1}$)
Pt-Y/A-0.4Cl	0.59
Pt-Y/A-0.1Cl	0.51
Pt-Y/A-NH_3	0.52
Zeolite Y/γ-Al_2O_3	0.49

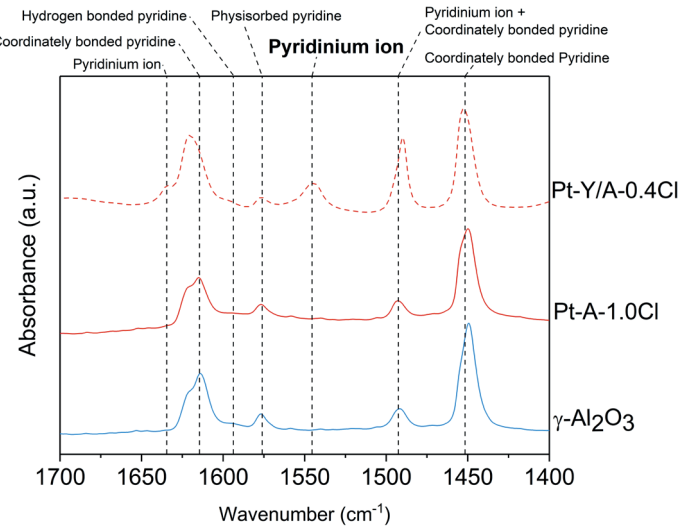

Figure S4.10. Pyridine FTIR spectra of γ-Al_2O_3, Pt-A-1.0Cl and the Pt-Y/A-0.4Cl catalysts measured in vacuum (<10^{-5} mbar) at 50 °C. Spectra show coordinately bonded pyridine for all samples, indicating the presence of Lewis sites. However, the pyridinium ion is not observed on γ-Al_2O_3 and Pt-A-1.0Cl, while for the Pt-Y/A-0.4Cl composite catalysts, its formation can be attributed to the adsorption on zeolite Brønsted acid sites. Band identification was obtained from: [12].

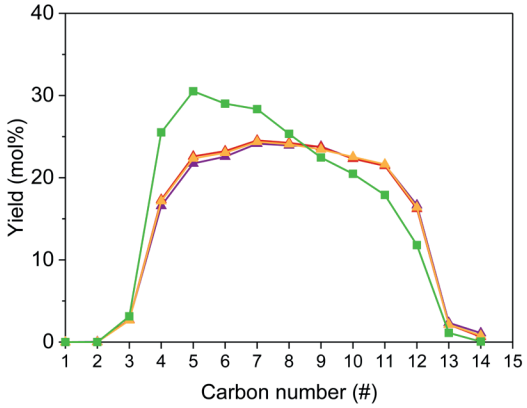

Figure S4.11. Cracking product distribution pattern at a cracking conversion of hexadecane between 30-50%. The Pt-Y/A-Cl catalysts are indicated by triangles: Pt-Y/A-0.6Cl (purple), Pt-Y/A-0.4Cl (red), Pt-Y/A-0.1Cl (yellow), while Pt-Y/A-NH_3 is indicated by green squares. Conditions for *n*-hexadecane hydroisomerization: feed rate of 1.7 $g_{n\text{-}C16} \cdot g_{cat}^{-1} \cdot h^{-1}$, a total pressure of 4.7 bar and 10 $mol_{H2} \cdot mol_{n\text{-}C16}^{-1}$.

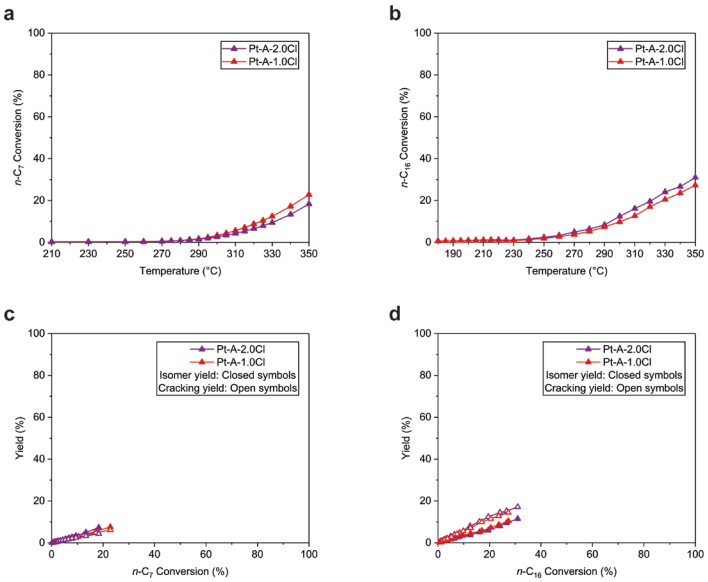

Figure S4.12. Results of hydroisomerization tests showing the activity (a) and isomer vs. cracking yield (c) of the Pt-A-2.0Cl (purple) and Pt-A-1.0Cl (red) catalysts for the conversion of *n*-heptane. The reactors were loaded with half the amount (in weight) of catalyst as used for the Pt/Zeolite Y/γ-Al_2O_3 composite catalysts, to mimic the performance of the γ-Al_2O_3 binder in the composite catalysts. This resulted in a feed rate of 5.2 $g_{n\text{-}C7} \cdot g_{cat}^{-1} \cdot h^{-1}$, while a total pressure of 10 bar and 9 $mol_{H2} \cdot mol_{n\text{-}C7}^{-1}$ were used. In (b) and (d) the activity and isomer vs. cracking yield of the the Pt-A-2.0Cl (purple) and Pt-A-1.0Cl (red) catalysts are provided for the conversion of *n*-hexadecane, at a feed rate of 3.5 $g_{n\text{-}C16} \cdot g_{cat}^{-1} \cdot h^{-1}$, a total pressure of 4.7 bar and 10 $mol_{H2} \cdot mol_{n\text{-}C16}^{-1}$. In c and d, closed symbols denote isomer yield while open symbols denote cracking yield.

Table S4.4. Ratio between branched and linear cracking products for *n*-heptane and *n*-hexadecane hydroisomerization at the cracking conversion (i.e. cracking yield) level indicated.

Sample	*n*-C_7 Cracking conversion (%)	*i*-C_4/*n*-C_4	*n*-C_{16} Cracking conversion (%)	*i*-C_8/*n*-C_8
Pt-Y/A-0.6Cl	39	8.1	32	7.7
Pt-Y/A-0.4Cl	35	8.8	53	8.1
Pt-Y/A-0.1Cl	40	9.0	47	8.0
Pt-Y/A-NH_3	42	9.0	51	13.8
Pt-A-2.0Cl	9	0.1	14	0.1
Pt-A-1.0Cl	11	0.0	17	0.1

Table S4.5. Apparent activation energies that were determined based on the activities of the catalysts in *n*-heptane and *n*-hexadecane hydroisomerization within the temperature range indicated. Reported apparent activation energies were based on first order kinetics. Errors indicate the error in the fit of the selected data points.

Sample	Temperature range *n*-C_7 (°C)	Apparent E_{act} *n*-C_7 (kJ·mol^{-1})	Temperature range *n*-C_{16} (°C)	Apparent E_{act} *n*-C_{16} (kJ·mol^{-1})
Pt-Y/A-0.6Cl	210-250	149 ± 2	180-200	156 ± 3
Pt-Y/A-0.4Cl	210-250	142 ± 4	180-200	161 ± 3
Pt-Y/A-0.1Cl	210-250	144 ± 2	180-200	161 ± 1
Pt-Y/A-NH_3	210-250	141 ± 2	180-200	147 ± 3
Pt-A-2.0Cl	315-350	113 ± 1	260-310	84 ± 1
Pt-A-1.0Cl	315-350	109 ± 2	260-310	85 ± 3

Chapter 5

Kinetic Analysis of the Conversion of *n*-Alkanes on Pt/Zeolite Y/γ-Al_2O_3 Catalysts: Effect of Catalyst Grain Size and Pt Nanoparticle Location

Abstract

A kinetic study was performed of Pt/Zeolite Y/γ-Al_2O_3 composite catalysts for *n*-decane and *n*-heptane hydroisomerization, wherein the effects of catalysts grain size (dp = 25-75 μm, 75-150 μm and 150-212 μm), the location of Pt nanoparticles within the composite catalyst, contact time, pressure and temperature were studied. The experiments were conducted in a high-throughput reactor system consisting of 16 parallel fixed-bed reactors over a temperature range of 170-300 °C, contact times of $W/F_{n\text{-}C(7,10)}$ = 53-587 kg·s·mol^{-1}, pressures of 5, 10 or 20 bar (for *n*-heptane only 5 bar), while the ratio between hydrogen and *n*-alkane was varied in the range of 1.5-10.8 mol_{H2}·$mol_{n\text{-}C10}^{-1}$ and 0.9-10.8 mol_{H2}·$mol_{n\text{-}C7}^{-1}$. All catalysts with Pt nanoparticles in the zeolite displayed a lower catalytic activity compared to catalysts with Pt nanoparticles on the γ-Al_2O_3 binder. As predicted by the Wheeler-Weisz modulus, similar catalytic activities were observed for all grain sizes within one family (Pt inside or outside the zeolite) of catalysts. However, for catalysts with Pt nanoparticles in zeolite Y, the isomer yield decreased upon an increase in catalyst grain size, while for catalyst with Pt nanoparticles on the γ-Al_2O_3 binder an 'optimal' isomer yield was obtained for all grain sizes. An increased branched/linear ratio of cracking products for the larger catalyst grains of the former catalysts, indicated progressive secondary reactions on acid sites of branched decane isomers. The smallest catalyst grains (d_p = 25-75 μm) displayed an optimal isomer yield, irrespective of Pt nanoparticle location. Reaction orders in hydrogen and *n*-decane were obtained in the range of -0.8 to -0.2 and 0.1 to 0.9, respectively. A relatively strong dependence of temperature on the reaction orders for the conversion of *n*-decane was observed, that is attributed to strong adsorption of *n*-decane on zeolite Y, moreover since weaker temperature dependences were observed for *n*-heptane. No significant effect of the location of Pt nanoparticles on reaction orders was observed.

5.1 Introduction

According to the classical bifunctional mechanism, alkanes are dehydrogenated on the metal function, followed by isomerization or cracking of alkene intermediates on the Brønsted acid function, and lastly hydrogenation towards alkanes on the metal function.[1] In an 'ideal' process, the dehydrogenation-hydrogenation reactions on the metal function are quasi-equilibriated which is characterized by high flexibility in product selectivity towards either isomers or cracking products that can be altered by changing the reaction temperature or contact time.[2] In principle, no catalyst deactivation is encountered in ideal processes, while for nonideal processes catalyst deactivation may be encountered through the formation of coke, especially for heavier aromatic feedstocks. The effects of conditions on the ideality of the process were investigated in a study by Thybaut et al., using a Zeolite Y/Al_2O_3 catalyst (65/35 wt.) with 0.5 wt.% of platinum, and thus a given ratio of metal to acid sites.[3] It was found that a decreasing total pressure, an increasing temperature and an increase in feedstock carbon number eventually lead to nonideality. Below hydrogen/*n*-alkane ratios of 10 mol/mol, an increase in this ratio would favor ideality, whereas for a further increase in the hydrogen/*n*-alkane ratio up to 300, a deviation from ideal behavior was expected based on a microkinetic model.

Studies by Froment et al. have pointed out that for zeolite Y based catalysts, isomer yield is a 'unique' curve as a function of *n*-alkane conversion, which is a consequence of similar activation energies for the main cracking and isomerization reactions.[4,5] The *n*-alkane conversion level is usually increased by increasing the reaction temperature, but also a lower total pressure or a change in partial pressures of *n*-alkane or hydrogen may change the conversion level. In later studies detailed micro-kinetic models were proposed for the isomerization and cracking of *n*-alkanes on zeolite catalysts.[6,7] In these studies activation energies for isomerization and cracking reactions are reported that where not necessarily the same for the various reaction types. However, the values for the most energetically favorable cracking reaction (from tertiary carbenium ions towards tertiary carbenium ions) by β-scission, are similar to the main PCP (Protonated CycloPropane mechanism) isomerization reactions.[3] For less favorable cracking reactions (involving primary or secondary carbenium ions), higher activation energies were reported, but these reactions are supposed to be rather insignificant for zeolite Y under ideal conditions.

For relatively light alkanes, such as *n*-hexane and *n*-heptane, the reactant coverage of the catalysts surface is proportional to the partial pressure in the gasphase.[8,9] For heavier alkanes (*n*-C_{10} and *n*-C_{12}) on zeolites, this is no longer valid due to strong adsorption within zeolite micropores. Denayer et al. determined Henry coefficients of *n*-alkanes on a number of zeolites at low partial pressures, and found that these values increase exponentially with increasing carbon number.[10] Strong adsorption of *n*-alkanes leads to high surface coverages and should, in principle, result in a zero-order dependence of the partial pressure on the rate of reaction.[4,5] Steijns and Froment, have proposed a modified version of the classical bifunctional mechanism where adsorption and desorption are included as separate steps, which is provided in Table 5.1.[4] Hydroisomerization of *n*-decane was fitted to a rate equation that included a Langmuir-type isotherm to describe *n*-alkane adsorption.[4,5,11] More recent kinetic studies have led to the development of 'Single-Event' Microkinetic Modelling (SEMK) wherein all elementary reaction steps are incorporated in a model, thereby obtaining fundamental information on each step of the catalytic reaction.[5,7,13]

Table 5.1. The modified classical bifunctional mechanism, including an adsorption and desorption step, as proposed by Hosten and Froment et al.[4,11,12]

	Reaction step			Active site
1.	*n*-alkane (g)	↔	*n*-alkane (ads)	
2.	*n*-alkane (ads)	↔	*n*-alkene (ads) + H_2	metal
3a.	*n*-alkene (ads) + H^+	↔	*n*-carbenium ion$^+$	acid site
3b.	*n*-carbenium ion$^+$	↔	*i*-carbenium ion$^+$	acid site
3c.	*i*-carbenium ion$^+$	↔	*i*-alkene (ads) + H^+	acid site
4.	*i*-alkene (ads) + H_2	↔	*i*-alkane (ads)	metal
5.	*i*-alkane (ads)	↔	*i*-alkane (g)	

Such information may then be used, for example, as input for catalyst synthesis leading to a more rational design of improved catalysts.[14] In literature SEMK models are presented for the conversion of a single *n*-alkane feed in vapor phase[6,15], or much more complex alkane mixtures in liquid phase to mimic industrial conditions.[16,17] The disadvantage of using alkane mixtures, is that not all feed compounds and reaction products can be identified and require to be lumped, making the model less specific and possibly loosing fundamental information on the course of the reaction.

For laboratory studies on *n*-alkane conversion, vapor phase conditions are often preferred, due to easier setup construction and analytics.[6,15] However, industrial hydrocracking processes usually convert hydrocarbon feedstocks of high molecular weight at high pressures, and thus operate predominantly in liquid phase, i.e. in trickle-bed operation. A comparative study of vapor phase and liquid phase processes has pointed out that for vapor phase physisorption effects may affect the reaction, which is not the case for liquid phase processes.[16] When mixtures of alkanes of different length are used as feedstock, differences in adsorption behavior might lead to a differences in the ratio of activity when transferring from vapor phase to liquid phase or vice versa.[18] Another difference that might be encountered, in case of full catalysts wetting, is that the rate of reaction is no longer affected by the molar inlet hydrogen flow, but by the hydrogen concentration in the liquid feed which depends on the hydrogen solubility that is affected by the hydrogen pressure and temperature.[16]

In this study, a kinetic study is presented on the conversion of *n*-decane and *n*-heptane on the Pt/Zeolite Y/γ-Al_2O_3 composite catalysts (0.5-0.7 wt.% Pt), with Pt nanoparticles located either in the zeolite or on the γ-Al_2O_3 binder. A number of recent studies on zeolite based composite catalysts have indicated that the location of metal nanoparticles with respect to the acid function of the zeolite may have a impact on both activity and selectivity in the conversion of *n*-alkanes.[19–22] In a study by Zečević et al., a Zeolite Y/γ-Al_2O_3 composite (50/50 wt.) was used as support for Pt nanoparticles, that were either located inside zeolite Y (providing a "closest" intimacy) or on the γ-Al_2O_3 binder, closely outside the Zeolite Y crystals (within "nanoscale" proximity).[19] In the conversion of *n*-C_{10} and *n*-C_{19} favorable effects on isomer selectivity were reported for the catalyst with Pt nanoparticles located on the γ-Al_2O_3 binder compared to catalysts with Pt nanoparticles located inside the zeolite. Similar beneficial effects were reported for the conversion of *n*-heptane, an alkane with relatively high diffusivity, when Pt nanoparticles were located closely outside zeolite Beta or zeolite Y[21,22], and for one-dimensional ZSM-22 and Mordenite zeolites.[20]

In this study, a preliminary kinetic study is performed studying both the effect of Pt nanoparticle location and catalyst grain size. A high-throughput reactor system was used consisting of 16 parallel fixed-bed reactors combined with online gas chromatography for analysis of the reactor product stream. The experiments were performed over a temperature range of 170-300 °C and contact times of: $W/F_{n\text{-}C(7,10)}$ = 53-587 kg·s·mol^{-1}. The reaction was studied at total pressures of 5, 10 or 20 bar, while the ratio between hydrogen and *n*-alkane was varied in ranges of 1.5-10.8 $mol_{H2}{\cdot}mol_{n\text{-}C10}^{-1}$ and 0.9-10.8 $mol_{H2}{\cdot}mol_{n\text{-}C7}^{-1}$. Furthermore, catalyst grain sizes were studied in three size ranges: d_p = 25-75 µm, 75-150 µm and 150-212 µm.

5.2 Experimental methods

5.2.1 Catalysts synthesis

Pt/Zeolite Y/γ-Al_2O_3 catalyst with Pt nanoparticles located inside zeolite crystallites

2.00 gram of Zeolite Y/γ-Al_2O_3 grains (212-500 µm) were suspended in 600 mL Milli-Q water at room temperature and stirred for 1 hour (~500 rpm). 50 mL of aqueous solution containing 38.35 mg of $Pt(NH_3)_4(NO_3)_2$ (Sigma-Aldrich, 99.995% purity) was added dropwise to the suspension (intake 1.0 wt.% Pt). After 3 hours of stirring, the suspension was filtered and washed with 150 mL Milli-Q water and dried in static air overnight at 120 °C. The dried catalyst was calcined in a flow of 20% O_2/N_2 (GHSV~8500 $mL_{gas}{\cdot}mL_{cat}^{-1}{\cdot}h^{-1}$) at 350 °C with a ramp of 0.2 °C·min^{-1}, a procedure based on Graaf et al. for the preparation of highly dispersed Pt nanoparticles. Afterwards, the catalyst was reduced in a flow of hydrogen (GHSV~3300 $mL_{gas}{\cdot}mL_{cat}^{-1}{\cdot}h^{-1}$) for 3 hours at 600 °C, using a ramp of 5 °C·min^{-1}. Hereafter, this catalyst will be referred to as Pt-Y/A-NH_3.

Pt/Zeolite Y/γ-Al_2O_3 catalyst with Pt nanoparticles located on the γ-Al_2O_3 binder

2.00 g of Zeolite Y/γ-Al_2O_3 grains were suspended in 300 mL Milli-Q water at room temperature and stirred for 1 hour (~500 rpm). 50 mL of aqueous solution containing 24.5 mg of $H_2PtCl_6{\cdot}6H_2O$ (Merck, ~40 wt.% Pt) was added dropwise to the suspension (intake 0.5 wt.% Pt). After 3 hours of stirring, the suspension was filtered and washed with 150 mL Milli-Q water and dried in static air overnight at 120 °C. The dried catalyst was reduced in a flow of hydrogen (GHSV ~3300 $mL_{gas}{\cdot}mL_{cat}^{-1}{\cdot}h^{-1}$) for 3 hours at 600 °C with a ramp of 5 °C·min^{-1}. Hereafter, this catalyst will be referred to as Pt-Y/A-Cl.

After reduction, both Pt-Y/A-NH_3 and Pt-Y/A-Cl were made into different grain sizes by gently crushing the samples in a mortar using a pestle followed by sieving using a number of stacked sieves with openings of different sizes.

5.2.2 Characterization

Elemental analysis of Pt was performed at Kolbe Mikroanalytisches Laboratorium using an Inductively Coupled Plasma - Optical Emission Spectrometer (ICP-OES, Perkin Elmer) after sample dissolution according to standard in-house procedures.

Nitrogen physisorption measurements of the supports were conducted on a Micromeritics TriStar 3000 at liquid nitrogen temperature. The samples were dried overnight at 300 °C in nitrogen flow before measurements.

X-ray diffraction (XRD) measurements of the catalysts were performed using a Bruker D2

PHASER, equipped with Cobalt Kα radiation (λ = 1.789 Å). Diffractograms were measured from 5° to 80° 2θ with 0.05° increments and a scan rate of 0.1 second per step.

Ammonia Temperature Programmed Desorption (NH_3-TPD) was performed on a Micromeritics AutoChem II equipped with a Thermal Conductivity Detector (TCD) calibrated for ammonia. 100 mg of catalyst was dried in a He flow for 1 hour at 600 °C (10 °C·min^{-1}). The temperature was then decreased to 100 °C and ammonia (10 vol% in He) was adsorbed in a pulse-wise manner until oversaturation. The physisorbed ammonia was removed by flowing helium for 2 hours at 100 °C, after which the ammonia desorption was monitored until 600 °C with a ramp of 10 °C·min^{-1}.

HAADF-STEM imaging was performed on a FEI Talos F200X transmission electron microscope, equipped with a high-brightness field emission gun (X-FEG). For these analyses, catalysts were embedded in Epofix resin, left to cure in air overnight at 60 °C, and cut to 70 nm sections using a Reichert-Jung Ultracut E ultramicrotome with Diatome Ultra 35° diamond knife. Sections were deposited on carbon/Formvar-coated copper TEM grids.

5.2.3. Catalytic testing

5.2.3.1 Reactor setup

The catalytic experiments were conducted in a Flowrence 16 parallel fixed-bed reactor setup, supplied by Avantium N.V. The reactor set up consists of several mass flow controllers and a high pressure liquid pump to allow accurate control of gasses and liquids, respectively, through small-scale (<1 mL) parallel reactors. The 16 reactors are divided over 4 heatingblocks that each have 4 reactor positions and individual temperature control. The product stream coming from the reactors was analyzed using an online GC (Agilent 7890B GC system) where the hydrocarbon products were analyzed on a HP-PONA column connected to a FID, while permanent gasses (H_2, He, N_2) were analyzed on a Hayesep Q column connected to a TCD. *n*-Decane (99+%) and *n*-Heptane (99+%) were obtained from Acros Organics. He 5.0, N_2 5.0, H_2 6.0 gases were obtained from Linde gas. Further details about the Avantium Flowrence setups are available elsewhere in literature and online.[24–26]

5.2.3.2 Reactor loading

Stainless steel reactor tubes with an inner diameter (d_t) of 2.0 mm were used that had a total length of 155 mm, including a 2 mm thick stainless steel frit (ø = 20 μm) at the bottom of the reactor. Empty reactor tubes were filled with a 20-25 mm layer of SiC (d_p = 212-425 μm) as filling material. Catalysts in the form of powders were weighed on an analytical balance and loaded on top of the layer of SiC, followed by careful tapping of the reactor. The amounts and catalyst grain sizes that were loaded in each of the 16 reactors are indicated in Table 5.2. Before and after filling of reactors with catalyst grains, the catalysts bed length was measured.

The variation in catalyst bed length (L_b) was between 12-54 mm and the catalyst bed volumes were between 0.04 and 0.17 mL. On top of the catalysts bed, a layer of SiC was added to aid the gradual evaporation of *n*-decane or *n*-heptane resulting in a stable flow of *n*-alkane vapor. On top of the layers of SiC and catalyst, a fiberglass thread was used to prevent formation of droplets from the inlet of the liquid feed. The reactor loading is schematically depicted in Figure 5.1. Measurements performed with an external thermocouple before the catalytic experiments

Table 5.2. Overview of the reactor loading of the Pt-Y/A-NH_3 and Pt-Y/A-Cl catalyst. The availability of 16 reactors allowed simultaneous variation of the amount of catalysts and the catalysts grain size, while 'identical reactors' were used for triplicate (Pt-Y/A-NH_3) and quadruplicate measurements (Pt-Y/A-Cl).

Block	#	Sample code	d_p (µm)	Amount of catalyst (mg)
1	1	Pt-Y/A-NH_3	75-150	50
	2	Pt-Y/A-Cl	75-150	50
	3	Pt-Y/A-Cl	75-150	50
	4	Reference (SiC)	212-425	
2	5	Pt-Y/A-NH_3	75-150	25
	6	Pt-Y/A-Cl	75-150	25
	7	Pt-Y/A-NH_3	75-150	100
	8	Pt-Y/A-Cl	75-150	100
3	9	Pt-Y/A-NH_3	75-150	50
	10	Pt-Y/A-Cl	75-150	50
	11	Pt-Y/A-NH_3	25-75	50
	12	Pt-Y/A-Cl	25-75	50
4	13	Pt-Y/A-NH_3	75-150	50
	14	Pt-Y/A-Cl	75-150	50
	15	Pt-Y/A-NH_3	150-212	50
	16	Pt-Y/A-Cl	150-212	50

pointed out that the isothermal zone in the reactorblocks was positioned from the bottom of the reactors up to ≥80 mm in height. During the loading of the reactors, care was taken for the bottom layer of SiC + catalyst bed (height: 33-78 mm) not to exceed this level. The total bed height (catalyst + 2 SiC layers) varied between 102-130 mm.

When analyzing the catalysts after the experiment, it was noticed that for the smallest catalysts grains of 25-75 µm, some of the catalyst (e.g. 20-30 %) was mixed with the bottom layer of SiC, having a grain size of 212-425 µm, as a consequence of the large difference in grain size. In this study, we did not find evidence that results were affected by mixing of the catalyst and SiC layers.

To assure that the reactors closely mimic the behavior of an ideal plug flow reactor, i.e. with a flat velocity profile and a negligible axial dispersion, the a number of criteria from literature were regarded in the design of the reactor loading.[27–29] Indicated below are the lowest values obtained after assessment of all reactors. The criteria from literature are indicated in italics.

The difference between the packing density of catalyst grains in the interior of the reactor and near the wall may cause a deviation from ideal plug flow. A lower packing density near the reactor wall causes a higher local velocity, resulting in a non-flat radial velocity profile, and possibly also bypassing of gas along the wall.

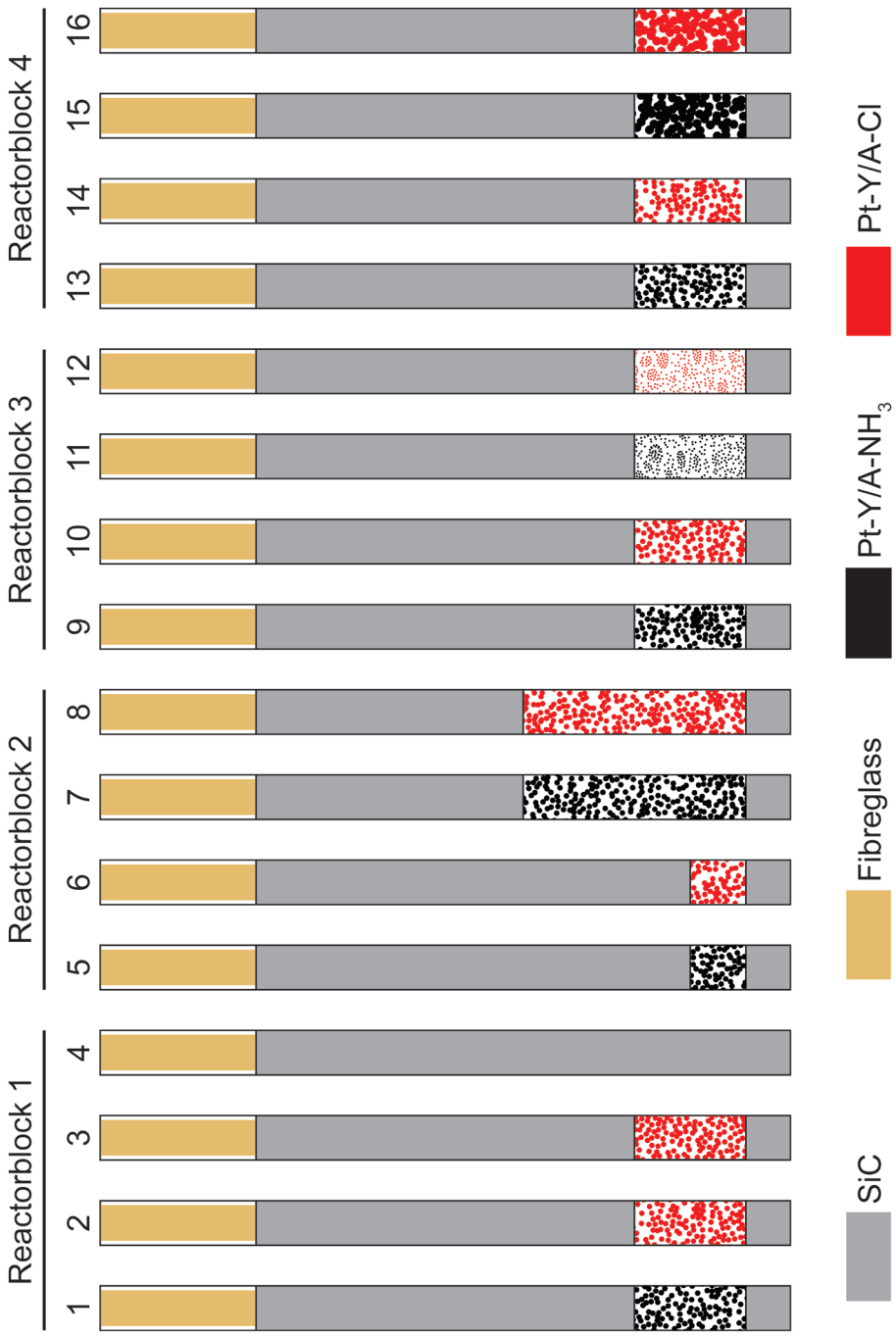

Figure 5.1. Schematic representation of the reactor loading used in the hydroisomerization tests, wherein both the amount of catalyst per reactor and the catalysts grain size were varied. The reactors were made from stainless steel and had a total length of 155 mm, while the isothermal bed height was ≥80 mm measured from the bottom of the reactors.

The lowest value of the ratio between reactor diameter d_t (m) and maximum grain diameter d_p (m) is compared to the criterion from literature which is of similar value.[27–29]

$$d_t/d_p \geq 9.4 \cong 10$$

A more stringent criterion for d_t/d_p, that also takes into account the conversion level is:

$$d_t/d_p > 35 \cdot X$$

Wherein X is the *n*-decane conversion (%) divided by 100. According to this criterion, wall effects might become non-negligible at a conversion levels of 27, 38 or 76 % *n*-decane conversion for grains with diameters of 212, 150 and 75 μm, respectively.

To assess the effect of axial dispersion under the conditions applied in the catalytic experiments, the lowest ratio between the catalyst bed length L_b (m) and the catalysts grain size d_p (m) of all 16 reactors was compared to the criterion, which is of a lower value.[27–29]

$$L_b/d_p \geq 80 > 50$$

A more stringent criterion for the ratio between the (minimum) catalyst bed length and the catalysts grain size, that takes into account the conversion level and the flow properties is:

$$\frac{L_b}{d_p} > \frac{8n}{Pe_p} ln\left(\frac{1}{1-X}\right)$$

Wherein n is the order of reaction (-) and Pe_p is the Péclet particle number (-), which is determined by the Reynolds particle number. The Reynolds particle number (Re_p) for grains of 212 μm in the applied mixture of *n*-decane, hydrogen and helium was determined to be 1.3; a relatively low value typical for laboratory reactors with low fluid velocities.[28] (approximate gas phase density = 7 $kg \cdot m^{-3}$, fluid velocity = $1.8 \cdot 10^{-2}$ $m \cdot s^{-1}$, approximate gas phase viscosity = $2 \cdot 10^{-5}$ $kg \cdot m^{-1} \cdot s^{-1}$). For low Reynolds particle numbers, the Péclet particle number is between 0.3-0.7 for gas phase processes.[28] By assuming a Péclet particle number of 0.5 for gas phase reaction and a reaction order of n = 1, the criterion was always below a L_b/d_p ratio of 80 up to *n*-decane conversion levels of 99 %. However, when a Péclet particle number of 0.05 is used, typical for trickle bed operation the criterion is no longer met above 40 % *n*-decane conversion.

5.2.3.3 Procedure of catalytic experiments

For the data summarized in this chapter, a total of three experiments were performed (two with *n*-decane, one with *n*-heptane) using the same loading scheme (Figure 5.1). For all three experiments, pristine fractions of the prepared catalysts were used, i.e. before every test the reactors were loaded with 'fresh' catalyst grains.

Catalysts were pretreated by drying in a He flow at 150 °C for 5 hours, with a ramp of 10 $°C \cdot min^{-1}$, followed by reduction in a hydrogen flow at 400 °C for 2 hours and a ramp of 5 $°C \cdot min^{-1}$. Thereafter the reactors were cooled down to 170 °C (*n*-decane) or 200 °C (*n*-heptane), followed by pressurization to 5 bar and starting the flow of *n*-decane or *n*-heptane to the reactors, followed by a stabilization time of 10 hours.

The three experiments that were performed consisted of two consecutive stages. In the first stage

the temperature was varied at fixed flows of hydrogen and *n*-alkane, while in the second stage the flows of either hydrogen or the *n*-alkane were varied to study their respective influence on the reaction.

Temperature profiles for *n*-decane and *n*-heptane

For *n*-decane, a temperature profile was measured by stepwise increasing the reactor temperatures from 170 °C to 280 °C (10 °C interval), while analyzing all 16 reactors at each step. This procedure was performed, at a total pressure of 5 bar followed by cooling down and then at 10 and subsequently at 20 bar. When a new temperature was reached after having changed the setpoint of the reactor temperature, ≥15 minutes stabilization time was regarded before starting analysis of the reactor product streams. When a new total pressure was reached after having changed the set point, ≥1 hour stabilization time was regarded before starting analysis of the reactor product streams. The ratio between hydrogen and *n*-alkane was kept constant at 10.8 $mol_{H2} \cdot mol_{n\text{-}C10}^{-1}$. Their respective partial pressures are indicated as red symbols in Figure 5.2 at 5 bar (circles), 10 bar (up triangle) and 20 bar (down triangle). For *n*-heptane the reactor temperatures were stepwise increased from 200 to 300 °C (10 °C interval) at a total pressure of 5 bar and 10.8 $mol_{H2} \cdot mol_{n\text{-}C7}^{-1}$.

After measurement of a temperature profile, from low to high, a reference measurement ('back-check') was performed at 230 °C for *n*-decane or 250 °C for *n*-heptane to examine the catalyst activity over time. For *n*-decane, it was observed that the maximum deviation in conversion level of these reference measurements was +/-3.3 %, while for *n*-heptane, the maximum deviation in

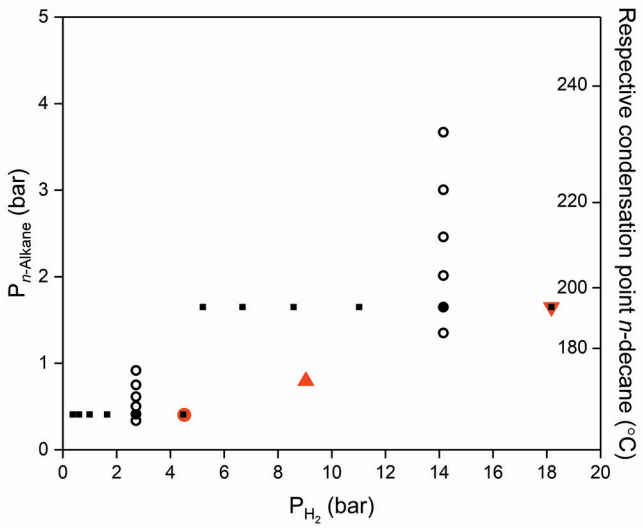

Figure 5.2. Grid of the partial pressures of hydrogen (x-axis) or *n*-alkane (y-axis) that were investigated. The red symbols indicate the partial pressures used for the measurement of the temperature profiles at 5 bar (circles), 10 bar (up triangle) and 20 bar (down triangle). The black symbols indicate the partial pressures used for the variation of the hydrogen and *n*-alkane partial pressure. The right y-axis indicates the condensation temperatures of *n*-decane at the respective partial pressures indicated on the left y-axis.[30,31]

conversion level of the back-check measurements was +/-1.8 %. Since both deviations towards higher and lower conversion levels were obtained and deviations were relatively small, it was concluded that any conceivable catalyst deactivation was within the experimental error and moreover, deemed unlikely regarding the conditions that favor and 'ideal' operation.[3]

Variation of the hydrogen and *n*-alkane partial pressures

Partial pressures of *n*-alkane or hydrogen were varied by flowing different amounts of either to the reactors. By exchanging the *n*-alkane or hydrogen for helium, the total flow through the reactor was kept constant (assuming vapor phase conditions). For *n*-decane, partial pressures were varied at total pressures of 5 and 20 bar in two different experiments (Figure 5.2). For *n*-heptane one experiment was conducted at a total pressure of 5 bar. At a total pressure of 20 bar *n*-decane condenses below 200 °C, resulting in trickle bed operation. Regarding the relatively low partial pressures of the *n*-alkane with respect to hydrogen or helium, this results in minor changes in total flow. However, liquid phase conditions might require longer stabilization times as well as require full catalyst wetting and sufficient hydrogen solubility.[16]

***n*-Decane conversion at 5 bar total pressure**

Following a program wherein temperatures were varied between 170-300 °C (5 bar, 10.8 $mol_{H2} \cdot mol_{n\text{-}C10}^{-1}$, no catalyst deactivation) the hydrogen partial pressure was systematically varied followed by variation of the *n*-alkane partial pressure. The hydrogen partial pressure was decreased in five steps between 4.5 to 0.6 bar, as indicated in Figure 5.2, followed by a back-check at 4.5 bar. After having changed the hydrogen and helium flow, 1 hour stabilization time was regarded before starting analysis of the reactor product streams. In a first cycle, the rate of reaction was determined for the identical reactors (1&2, 9&10, 13&14) at temperatures of 180 and 190 °C. During the back-check experiments, the initial *n*-decane conversion level could always be reproduced within 0.4 % *n*-decane conversion. Afterwards, a second cycle was performed at 200 °C and 210 °C. In this case the *n*-decane conversion was at most 1.1 % lower (back-check at 200 °C,), while at 210 °C it was 5.2 % lower. This observation points to catalyst deactivation for higher temperatures at relatively low partial pressures of hydrogen.[3]

Thereafter, the *n*-decane partial pressure was lowered from 0.4 to 0.3 bar, and then stepwise increased up to 0.9 bar followed by a back-check at 0.4 bar (6 steps in total). After having changed the *n*-decane flow, ≥5 hours stabilization time was regarded before starting analysis of the reactor product streams. Due to the longer stabilization times of the liquid feed, the product stream was analyzed using two different temperatures per heating block (≥15 minutes stabilization time in between). The limited stability of the system after changing the hydrocarbon flow made it difficult to distinct between experimental error and (further) deactivation. Any conceivable deactivation at (210 °C) not exceed 2.9 % *n*-decane conversion.

***n*-Decane conversion at 20 bar total pressure**

Following a temperature profile at 5, 10 and 20 bar as described above, at first the *n*-alkane partial pressure was varied followed by variation of the hydrogen partial pressure. The same procedure, temperatures and stabilization times were applied as for the experiment conducted at 5 bar. The *n*-decane partial pressure was decreased from 1.7 to 1.3 bar and then stepwise increased to 3.7 bar (6 steps in total, as indicated in Figure 5.2), followed by a back-check at

1.7 bar. In these back-check experiments, the initial *n*-decane conversion level (180-210 °C) could always reproduced within +/-1.0 % *n*-decane conversion. Thereafter, the hydrogen partial pressure was stepwise decreased from 18.2 to 5.2 bar in 6 steps followed by a back-check at 18.2 bar. The initial *n*-decane conversion level (180-210 °C) could always reproduced within +/-0.7 % *n*-decane conversion.

***n*-Heptane conversion at 5 bar total pressure**

Following a temperature profile at 5 bar as described above, the partial pressure of hydrogen was lowered stepwise from 4.5 to 0.4 bar (Figure 5.2) followed by a back-check at 4.5 bar. After changing the hydrogen flow, 1 hour stabilization time was regarded before starting analysis of the reactor product streams. The rate of reaction was determined at 200, 210, 220 °C (cycle 1) and 230, 250, 270 °C (cycle 2). The initial *n*-heptane conversion level between 200-220 °C could always reproduced within +/-0.6 %. For the measurements at higher temperatures, the *n*-heptane conversion level measured at the back-check was significantly lower. At 230 °C, the *n*-heptane conversion level was 7.1 % lower than the initial value, at 250 °C 30.6 % lower and at 270 °C 48.5 % lower.

5.2.3.6 Assessment of mass transport limitations and intimacy criteria

In kinetic studies of catalyzed reactions, special care has to be taken to avoid interference of physical transport phenomena, e.g. heat and mass transfer from the gas phase to the catalysts grain (external transport) and within the grains (internal transport) to affect catalysts performance. From Figure 5.2, it can be inferred that reactors were operated in vapor phase conditions during all experiments, except for those at 20 bar total pressure below 200 °C. From literature, a number of criteria were used to calculate whether the rate data is influenced by less than 5 % by transport limitations.[27] On basis of the highest activities (100 % conversion), partial pressures at 20 bar, and considering the full range of catalyst grain sizes and catalysts bed lengths, the following maxima were obtained and are compared with criteria from literature, provided in italics. Values for *n*-decane at lower total pressures or *n*-heptane will be lower than the maxima computed for *n*-decane at 20 bar total pressure, due to lower partial pressures of *n*-alkane and higher diffusivities of *n*-heptane.

Carberry number for extraparticle mass transfer limitations was calculated by assuming an extraparticle diffusion coefficient of *n*-decane (in a hydrogen/helium gas mixture) of $1.0 \cdot 10^{-5}$ $m^2 \cdot s^{-1}$ and a film thickness of $1.5 \cdot 10^{-5}$ m:

$$Ca = 3 \cdot 10^{-6} << 0.05$$

Wheeler-Weisz modulus to assess intraparticle diffusion limitations was based on an intraparticle diffusion coefficient for *n*-decane of $1.0 \cdot 10^{-6}$ $m^2 \cdot s^{-1}$, a value that is typical for Knudsen diffusion e.g. *n*-decane diffusing in mesopores of γ-Al_2O_3. For the largest grains used in this study (d_p = 212 µm), the Wheeler-Weisz modulus is:

$$\eta\phi^2 = 6 \cdot 10^{-5} << 0.15$$

For bifunctional catalyst, the Weisz intimacy criterion indicates the maximum distance between two types of sites for maximal catalytic activity, and is related to the Wheeler-Weisz modulus for intraparticle diffusion.[32,33] By assuming an intraparticle (mesopore) diffusion coefficient of

$1.0 \cdot 10^{-6}$ $m^2 \cdot s^{-1}$ for *n*-decane and using the highest activities, the maximum distance between sites is:

$$2R = 6 \cdot 10^{-3} \text{ m}$$

If an approximate micropore diffusion coefficient of $1.0 \cdot 10^{-9}$ $m^2 \cdot s^{-1}$ for zeolite Y[33] is used while other parameters are kept constant, the maximum distance between sites decreases to:

$$2R = 2 \cdot 10^{-4} \text{ m}$$

In both cases, the maximum proximity limit from the intimacy criterion is significantly higher than the typical metal-acid distances of the catalysts used in this study, which is estimated at $\leq 5 \cdot 10^{-7}$ m for Pt-Y/A-Cl and $\leq 5 \cdot 10^{-9}$ m for the Pt-Y/A-NH_3 catalysts.[19]

5.3 Results and discussion

5.3.1 Results of catalyst synthesis

The prepared Zeolite Y/γ-Al_2O_3 composite support was based on a commercially available ultra-stabilized zeolite Y (CBV 760, Si/Al = 30 at/at). In Figure 5.3 HAADF-STEM and EDX images are presented of this support, showing the γ-Al_2O_3 component to be well mixed with the zeolite Y crystallites.[34] This support was then used as support for Pt nanoparticles, wherein the location of Pt nanoparticles was controlled by using a previously reported methodology.[19] Pt was selectively deposited inside zeolite crystals by ion-exchange of $[Pt(NH_3)_4]^{2+}$ (aq) with zeolite protons (pH ~5), while strong electrostatic adsorption at pH ~3 of the $[PtCl_6]^{2-}$ (aq) complex was used to selectively deposit Pt on the γ-Al_2O_3 binder. Considering the variation in zeolite crystal sizes (200-1000 nm), locating Pt nanoparticles on the γ-Al_2O_3 binder results in an approximate distance of 500 nm between metal and acid sites.[19]

The location of the Pt nanoparticles was studied with HAADF-STEM (Figure 5.4) and to prevent overlap of the zeolite and γ-Al_2O_3 components in HAADF-STEM images, the Pt/Zeolite Y/γ-Al_2O_3

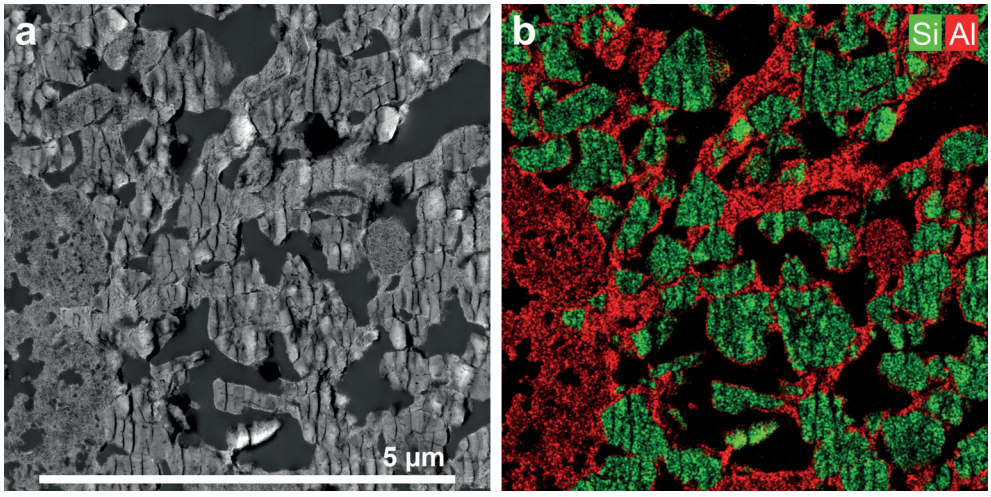

Figure 5.3. HAADF-STEM image (a) and an EDX map (b) of the ultra-microtomed Zeolite Y/γ-Al_2O_3 composite support. The zeolite Y crystallites appear in green (silicon) in the EDX map and are covered by a layer of γ-Al_2O_3 that appears as red (aluminum).

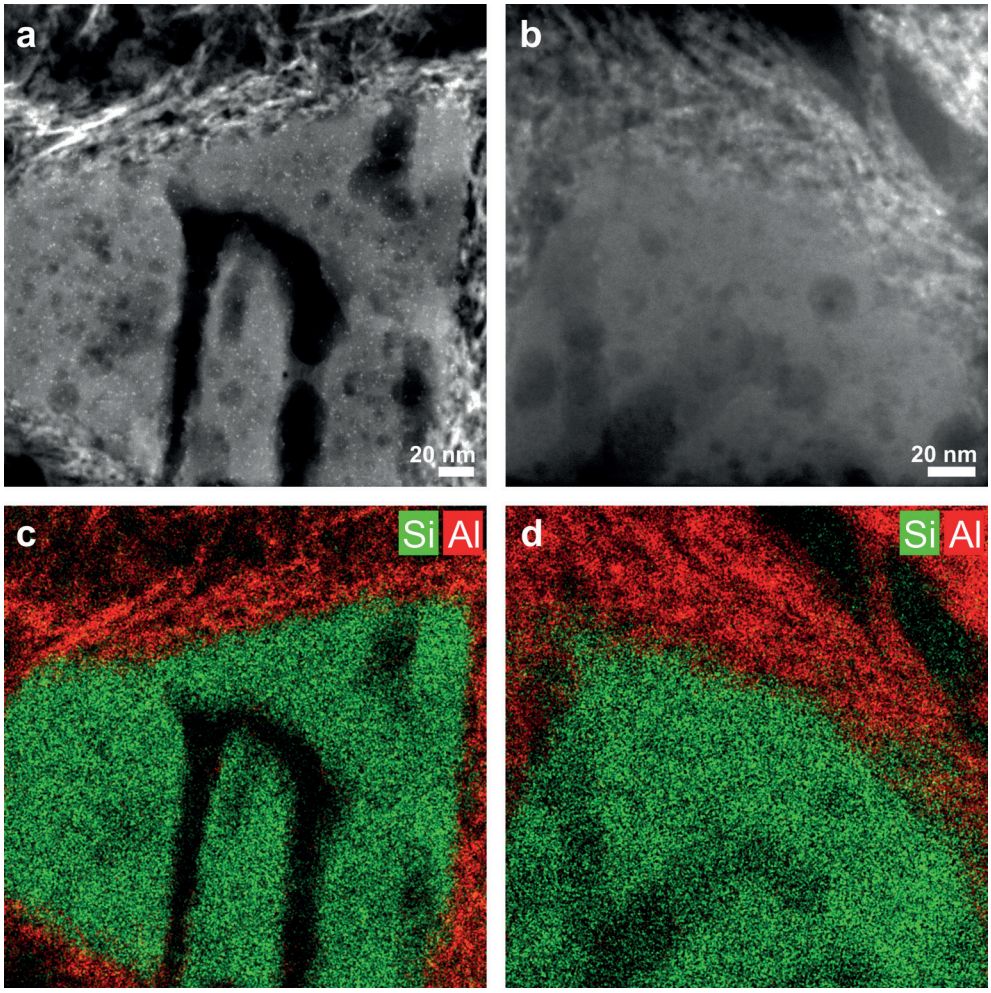

Figure 5.4. TEM imaging of ultra-microtomed sections (70 nm thickness) of the Pt/Zeolite Y/γ-Al_2O_3 composite catalysts. An HAADF-STEM image of the Pt-Y/A-NH_3 catalysts is provided in (a), wherein Pt nanoparticles can be identified as bright white dots, being located in the zeolite component. An HAADF-STEM image of the Pt-Y/A-Cl catalysts is provided in b, with Pt nanoparticles located on the γ-Al_2O_3 binder. In the HAADF-STEM images γ-Al_2O_3 has an amorphous needle-like structure, while zeolite crystallites have a more uniform contrast. EDX elemental maps of the Pt-Y/A-NH_3 and the Pt-Y/A-Cl catalysts are provided in c and d, showing Si signals in green and Al signals in red.

Table 5.3. Properties of the prepared composite catalysts. Pt weight loading was determined by ICP after sample destruction, while the size of Pt nanoparticles and the standard distribution therein was determined by manually counting Pt particles on HAADF-STEM images. Total acidity was determined by NH_3-TPD in the range of 100-600 °C and d_p = 212-500 µm.

Catalyst	Pt precursor	Pt loading (wt.%)	Pt particle size (nm)	Total acidity ($mmol_{NH3} \cdot g^{-1}$)
Pt-Y/A-NH_3	$Pt(NH_3)_4(NO_3)_2$	0.56	1.3 ± 0.2	0.50
Pt-Y/A-Cl	$H_2PtCl_6 \cdot 6H_2O$	0.71	1.4 ± 0.3	0.56

catalyst were ultra-microtomed into 70 nm thick sections before analysis. The selective deposition of Pt has been confirmed by previous research, using characterization techniques that sample large amount of catalysts per measurement.[35] The Pt weight loading was obtained by ICP, while structural properties of the prepared composite catalysts are provided in table 5.3. It is apparent that catalyst of similar Pt weight loading and Pt particle size could be obtained. For the catalyst prepared with $H_2PtCl_6 \cdot 6H_2O$, a higher acidity was observed that can be attributed to residual chlorine, that has no consequences for catalysis.[36]

5.3.2 Experimental conditions, measurement error and reproducibility

The accuracy of catalytic data largely depends on how well experimental conditions can be controlled and maintained during catalytic tests. In this section, the accuracy and variation in pressure and temperature were assessed during the *n*-decane hydroisomerization experiment that formed the basis of the results described in this chapter. Averages and standard deviations of identical reactors are computed that provides a measure of the spread between results of these reactors. In Table 5.4 the values displayed for identical reactors loaded with the Pt-Y/A-NH_3 catalyst or the Pt-Y/A-Cl catalysts, and combined values of all 16 reactors at 5, 10 and 20 bar total pressure are displayed.

From Table 5.4, it is apparent from the average processing values that the pressure setpoints could be reached with ≤0.3 bar accuracy, while with an increase in pressure, a larger deviation from the pressure setpoint was observed. Standard deviations between reactors were ≤0.1 bar, and did not seem to be dependent on the total pressure. As a result, the relative standard deviation between reactors becomes smaller at higher pressures.

In Table 5.5 an overview is provided of average processing values of the temperatures during the experiment that are compared to results from 'external' measurements. These measurements were performed before the catalytic experiments, by inserting a thermocouple connected to a multimeter inside each reactor position. The difference between the setpoint and the measured

Table 5.4. Average processing values and standard deviations (σ) of reactor pressures operating at setpoints of 5, 10 or 20 bar, measured during a temperature profile between 170-280 °C.

Catalyst	Reactors (N)	Pressure setpoint (bar)	Average processing value (bar)	σ (bar)
Pt-Y/A-NH_3	3		5.00	0.07
Pt-Y/A-Cl	4	5.00	5.12	0.05
All reactors	16		5.07	0.07
Pt-Y/A-NH_3	3		10.08	0.08
Pt-Y/A-Cl	4	10.00	10.18	0.06
All reactors	16		10.12	0.07
Pt-Y/A-NH_3	3		20.20	0.08
Pt-Y/A-Cl	4	20.00	20.30	0.05
All reactors	16		20.23	0.09

Table 5.5. Evaluation of temperature setpoint and processing value indicated by the temperature regulator of reactors of identical reactors and the averaged temperature of all 16 reactors. The processing values were measured during the temperature profile of *n*-decane at 20 bar total pressure. Deviations from the average temperature are reported as standard deviations (σ).

Temperature Set point (°C)	Pt-Y/A-NH_3 N = 3		Pt-Y/A-Cl N = 4		All reactors N = 16		External measurement N = 16	
	Average (°C)	σ (°C)	Average (°C)	σ (°C)	Average (°C)	σ (°C)	Average (°C)	σ (°C)
150							150.88	0.21
170	169.99	0.01	170.00	0.03	169.98	0.02		
180	180.00	0.00	180.01	0.01	179.99	0.01		
190	190.01	0.02	190.00	0.02	189.99	0.02		
200	200.00	0.02	200.00	0.03	200.03	0.01	199.94	0.23
210	210.00	0.01	209.99	0.00	209.99	0.00		
220	220.01	0.02	219.99	0.00	219.99	0.00		
230	230.01	0.03	229.99	0.01	230.02	0.02		
240	240.00	0.03	239.98	0.01	240.04	0.02		
250	250.01	0.02	250.00	0.02	250.04	0.02	249.33	0.26
260	259.99	0.01	260.01	0.01	260.00	0.00		
270	270.00	0.02	270.00	0.03	269.97	0.02		
280	280.00	0.01	280.02	0.02	280.01	0.01		
300							298.77	0.31

temperature (accuracy) based on the temperature regulator of the setup was ≤0.1 °C while standard deviations in measured temperatures between reactors set at the same temperature were equally small. The values obtained during the external measurements revealed a larger standard deviation between reactors (≤0.3 °C) and lower accuracy for higher reactor temperatures (≤1.3 °C).

Another origin of measurement error are impurities in the n-alkane feed and or product stream. The encountered impurities are a combination of feedstock impurities that were used as reactants (<1 % purity), traces in the setup from previous experiments with different feedstocks and 'crosstalk' between reactors as a result of switching from reactor to reactor while using a single analysis line for the GC. By analyzing the product stream from the reactor filled with SiC (reactor 4), the concentration of other components besides *n*-decane or *n*-heptane was determined to be 1.5 %, as based on an average of GC analyses that were performed during the experiment. The encountered impurities were mostly hydrocarbon products of similar boiling point as *n*-decane or *n*-heptane.

Further errors might be introduced by slight variations in the amount of catalysts loaded per (identical) reactor. For example, for the identical reactors loaded with Pt-Y/A-NH_3 the average amount of three reactors was 50.25 mg of catalysts (aimed at 50 mg) with a standard deviation of 0.25 mg, while for the Pt-Y/A-Cl catalyst the average amount was 50.15 mg of four reactors with a standard deviation of 0.13 mg.

5.3.3. Effect of Contact time and Reproducibility between Reactors

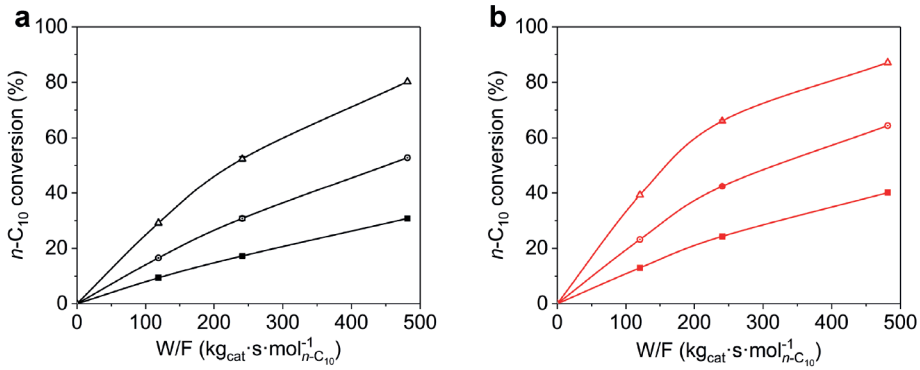

Figure 5.5. *n*-Decane conversion versus contact time of Pt-Y/A-NH_3 (a) and Pt-Y/A-Cl (b) at 230 °C (filled squares), 240 °C (dotted circles) and 250 °C (open triangles). Lines are a guide to the eye. (pressure = 20 bar, 10.8 $mol_{H2}·mol_{n\text{-}C10}^{-1}$, d_p = 75-150 μm)

In Figure 5.5 the catalytic activity of the Pt-Y/A-NH_3 (a) and Pt-Y/A-Cl (b) catalysts is provided as a function of contact time at 230 °C, 240 °C and 250 °C. At low conversion levels, an almost linear dependence of the *n*-decane conversion versus contact time is observed, while at higher conversion levels the trend deviates from linearity. This can be attributed to the depletion of *n*-decane at higher contact times, that starts to affect the rate of reaction and is indicative of a positive order in *n*-decane. Furthermore, it is apparent that the Pt-Y/A-Cl catalysts always had a higher catalytic activity than the Pt-Y/A-NH_3 catalysts, irrespective of contact time or temperature within the investigated range.

In Table 5.6, the standard deviations in *n*-decane conversion of 'identical' reactors at the same temperature are provided. The standard deviations indicate the variation within the obtained values for *n*-decane conversion on the reactors. Since every reactorblock had an independent temperature controller, a distinction is made between reactors within one reactorblock, and reactors within different blocks. Based on the data in Table 5.6, it was concluded that the 'identical' reactors showed a good reproducibility, i.e. the standard deviation in *n*-decane conversion was always below 1.1 % *n*-decane conversion. Furthermore, the results show that using reactors in different reactorblocks did not lead to large changes in the standard deviations.

In the figures in the sections 5.3.3, 5.3.4 and 5.3.5 the data from identical reactors was averaged and error bars based on standard error are included in the graphs for these data points. The standard errors indicate the typical error in the conversion, yield or reaction rate of a reactor with respect to the true mean of the population. In most cases the error bars are smaller than the symbols and not visible. The reactors located in block 2, had different amounts of catalyst, and where not measured in multitude. For the experiments wherein the partial pressures of hydrogen and *n*-decane were varied, different temperatures were used per reactorblock. Therefore this data could not be based on the average result of identical reactors, but was based on the result of a single reactor.

Table 5.6. Average *n*-decane conversion (%) of identical reactors at the same temperature and their standard deviations (σ), indicating the reactor-to-reactor reproducibility of the measured catalytic activity. To compute the averages between reactors within the same block data from reactorblock 1 was used, while for all identical reactors data from reactorblocks 1, 3 and 4 was used. ($W/F_{n\text{-}C10}$ = 244 kg·s·mol^{-1}, 10.8 mol_{H2}·$mol_{n\text{-}C10}^{-1}$, d_p = 75-150 µm)

Temperature (°C)	Reactorblock 1		Reactorblock 1, 3, 4			
	Pt-Y/A-Cl N = 2		Pt-Y/A-NH_3 N = 3		Pt-Y/A-Cl N = 4	
	Avg *n*-C_{10} conv (%)	σ (%)	Avg *n*-C_{10} conv (%)	σ (%)	Avg *n*-C_{10} conv (%)	σ (%)
170	1.35	0.08	1.31	0.54	1.55	0.21
180	2.00	0.07	1.62	0.67	2.10	0.11
190	2.59	0.08	2.44	0.29	2.78	0.20
200	3.45	0.07	3.30	0.46	3.87	0.42
210	7.08	0.15	4.97	0.71	7.15	0.13
220	12.92	0.01	8.94	0.75	13.07	0.16
230	24.11	0.06	17.23	0.39	24.30	0.20
240	42.23	0.18	30.80	0.73	42.45	0.28
250	65.84	0.33	52.38	0.81	66.05	0.35
260	87.40	0.25	79.17	1.04	87.56	0.27
270	97.93	0.20	97.79	0.30	98.14	0.26
280	99.95	0.00	99.95	0.01	99.96	0.01

5.3.4 Effect of Total pressure on Activity of *n*-Decane Conversion

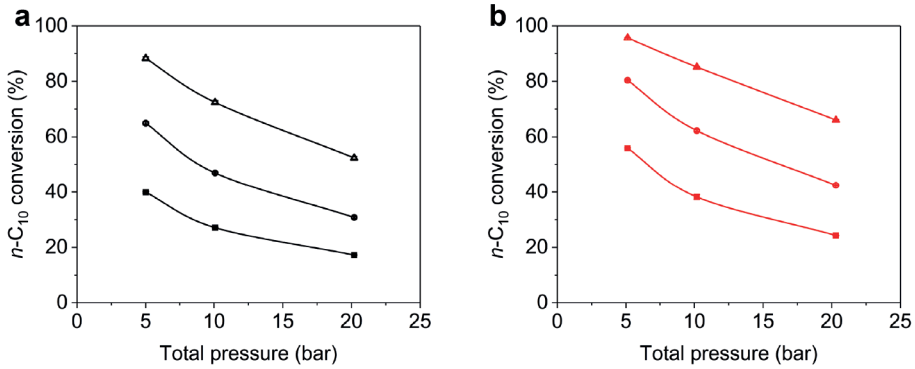

Figure 5.6. Effect of total pressure on the *n*-decane conversion of Pt-Y/A-NH_3 (a) and Pt-Y/A-Cl (b) at 230 °C (filled squares), 240 °C (dotted circles) and 250 °C (open triangles). Lines are a guide to the eye. (W/F = 244 kg·s·mol^{-1}, 10.8 mol_{H2}·$mol_{n\text{-}C10}^{-1}$, d_p = 75-150 µm)

In Figure 5.6, the *n*-decane conversion level for Pt-Y/A-NH_3 (a) and Pt-Y/A-Cl (b) is provided as a function of total pressure at 230, 240 and 250 °C. The effect of total pressure on hydroisomerization has been studied a number of times before, and may be different depending on the process conditions.[4,5] Thybaut et al. have reported that the activity goes through an optimum upon increasing the total pressure, while at the same time transitioning from a nonideal to an ideal process.[3] At low total pressures, under nonideal conditions, increasing the total pressure results in increased amounts of dehydrogenation reactions leading to higher alkene concentrations. These alkenes are subsequently converted on acid sites, resulting in a higher catalytic activity. Conversely, under ideal conditions where the dehydrogenation-hydrogenation is quasi equilibrated, further increasing the total pressure shifts the dehydrogenation-hydrogenation equilibrium (Table 5.1, step 2 and 4) towards *n*-alkanes. In turn, this leads to a lower concentration of alkenes/carbenium ions that consequently leads to a lower activity. Varying the total pressure of the reaction while monitoring the catalytic activity, can thus be used as a method to assess the ideality of a process. For the data provided in Figure 5.6, a systematic negative correlation of the catalytic activity on the total pressure is observed, which is independent of catalyst or reactor temperature. This therefore confirms that the reaction is operating under 'ideal' conditions. An alternative explanation for the effect of total pressure was provided in a study by Van de Runstraat et al., wherein the lower activity at higher total pressures was attributed to a more favorable adsorption of *n*-alkanes, that are competing with alkenes leading to lower concentrations of reactive intermediates at acid sites.[37]

5.3.5. Effect of Catalysts Grain Size on Activity and Selectivity in *n*-Decane Conversion

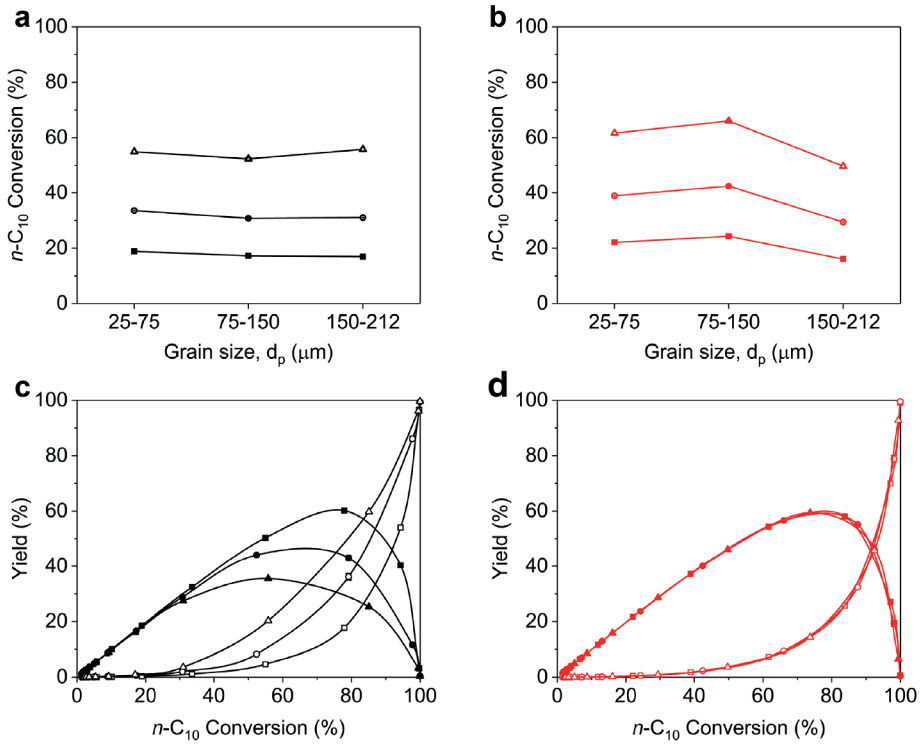

Figure 5.7. Effect of catalyst grain size on the *n*-decane conversion for Pt-Y/A-NH_3 (a) and Pt-Y/A-Cl catalysts (b) at 230 °C (filled squares), 240 °C (dotted circles) and 250 °C (open triangles). The product yields from Pt-Y/A-NH_3 (c) and Pt-Y/A-Cl (d) catalysts from isomerization (filled symbols) and cracking (open symbols) as a function of *n*-decane conversion. A range of *n*-decane conversion levels was obtained by varying the temperature between 170-280 °C. The 25-75 μm grains are indicated as squares, 75-150 μm grains are indicated as circles and 150-212 μm grains are indicated as triangles. Lines are a guide to the eye. (W/F = 244 kg·s·mol^{-1}, 10.8 mol_{H2}·$mol_{n\text{-}C10}^{-1}$, pressure = 20 bar)

A range of catalyst grain sizes of the same catalyst can be studied to experimentally verify the absence of intraparticle diffusion limitations in reactions catalyzed by porous solid catalysts.[27] The usage of relatively small reactors and the plug-flow criteria discussed earlier, implied that the catalysts grain size range is limited to values within the micrometer range. According to the Wheeler-Weisz modulus and the typical rates encountered in these *n*-decane hydroisomerization experiments, intraparticle diffusion limitations within 150-212 μm catalysts would become rate limiting at an intraparticle diffusivities of ≤10^{-10} m^2·s^{-1}. Since a mesopore diffusivity in the order of 10^{-6} m^2·s^{-1} is expected for *n*-decane within zeolite Y/γ-Al_2O_3 grains, it is improbable that the rate of the reaction is limited by diffusion limitations, and is indicated by a low value for the Wheeler-Weisz modulus. In Figure 5.7, the *n*-decane conversion level for Pt-Y/A-NH_3 (a) and Pt-Y/A-Cl (b) is plotted as a function of catalyst grain size at 230, 240 and 250 °C. Despite the same amount of catalysts (i.e. identical contact time) for each reactor, the variation within the activity was larger than observed for 'identical' reactors loaded with catalyst of the same grain size. At 250 °C,

changes of 2.2 % *n*-decane conversion for Pt-Y/A-NH_3 and 6.9 % for Pt-Y/A-Cl were determined. Given the values of the Wheeler-Weisz criterion, these variations cannot be simply attributed to intraparticle diffusion limitations, the more so since there is no consistent trend of lower activity for larger catalyst grains. Only for the Pt-Y/A-Cl catalysts with the largest grain sizes, a systematic lower activity is encountered, which is not observed for Pt-Y/A-NH_3 of the same grain size. A possible explanation is that for the reactor loaded with Pt-Y/A-Cl catalysts of the largest grain size, bypassing of the catalyst bed has occurred. This reactors is therefore operating at lower effective contact time than the other reactors. Furthermore, the Pt-Y/A-Cl catalysts with grain sizes between 25-75 µm had a systematically higher catalytic activity than the Pt-Y/A-NH_3 catalyst of the same grain sizes, similarly to what was observed for 75-150 µm catalyst grains in section 5.3.3.

From Figure 5.7 c and d can be inferred that selectivity towards decane isomers for Pt-Y/A-NH_3 was highly dependent on catalyst grain size, while no such dependence was observed for Pt-Y/A-Cl. From the temperature profiles that were obtained at 5 and 10 bar total pressure, it was concluded that these difference in isomer yield were independent of pressure (Figure S5.16). This result points to an intraparticle diffusion effect for Pt-Y/A-NH_3 catalysts that favors cracking over isomerization. Since this effect is emerging for micrometer sized catalyst grains, low diffusivities of the reaction intermediates such as those that are typical for branched isomers in zeolite micropores, form the likely contributor. As stated above, for a diffusion coefficient of $\leq 10^{-10}$ $m^2 \cdot s^{-1}$, the reaction becomes rate limiting for the larger catalyst grains, if this is the average diffusivity over the entire Zeolite Y/γ-Al_2O_3 grain, also involving mesopore diffusion. Therefore the actual diffusivity of branched isomers in zeolite Y crystals should then be lower for catalyst with Pt nanoparticles located in the zeolite, which is not likely. Moreover, this would not be affected by grain size due to negligible differences between mesopore and extra grain diffusivity. Therefore, at the current state of affairs, these observations leave us without explanation.

To gain more insights in the reactions occurring on catalysts of different grain size, Arrhenius plots of the temperature range of 170-280 °C were plotted based on reaction rates first order in hydrocarbon pressure (Figure 5.8). The apparent activation energies within the temperature range of 210-240 °C were determined at relatively low conversion levels (<40 % *n*-decane

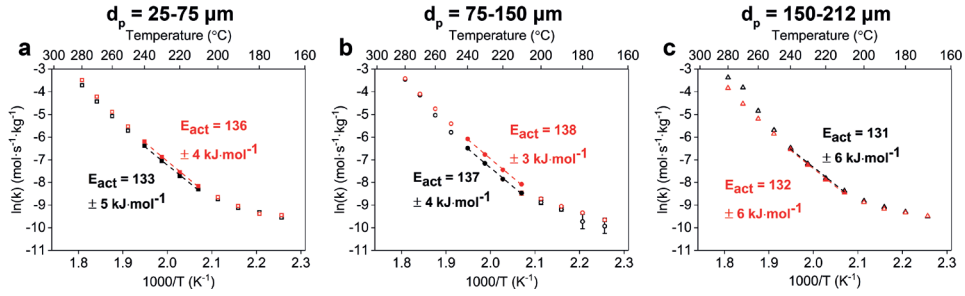

Figure 5.8. Arrhenius plots based on first order kinetics of Pt-Y/A-NH_3 (black) and Pt-Y/A-Cl catalysts (red) with different catalyst grain sizes: d_p = 25-75 µm (a), 75-150 µm (b), 150-212 µm (c). The dashed lines indicate the linear fit of datapoints within a temperature range of 210-240 °C, errors indicate error in fit. (W/F = 244 kg·s·mol^{-1}, 10.8 $mol_{H2} \cdot mol_{n\text{-}C10}^{-1}$, pressure = 20 bar)

conversion), wherein mostly decane isomers are produced on all catalysts, and thus the activation energy will mimic the activation energy of the isomerization reaction. The obtained values for the apparent activation energy are in general agreement with the value of 138.9 ± 2.5 kJ·mol^{-1}, that was reported by Froment et al. for the hydroisomerization of *n*-decane on Pt/Zeolite Y.[5] Furthermore, it was observed that for all catalysts similar activation energies were obtained (within error of fit), and thus independent of Pt nanoparticle location or grain size.

In principle, intraparticle diffusion limitations are expected to lead to a decrease in the slope of the Arrhenius plots at higher conversions (by approximately a factor 0.5), that should be more pronounced for the larger catalyst grain sizes.[38] Such a trend is not observed in the Arrhenius plots, given the similar values of the apparent activation energies for the entire range of catalyst grain sizes, while the linear fit can be extrapolated to higher conversion levels relatively well. This observation provides further indication that the rate of the reaction is not limited by intraparticle diffusion limitations within the studied range of grain sizes. Another observation from the Arrhenius plots is that for the Pt-Y/A-NH$_3$ catalysts an upward trend was observed for catalyst with increasing grain sizes at higher conversion levels (above 240 °C), which was not observed for Pt-Y/A-Cl. For the larger grains (75-150 µm and 150-212 µm) of Pt-Y/A-NH$_3$ at this conversion level, cracking is significantly favored over isomerization that might here be reflected in the Arrhenius plot.

In previous studies, the validity of first order kinetics for *n*-decane on zeolite Y was debated and reaction orders of *n*-decane close to zero were reported.[4] In Figure S5.17 Arrhenius plot are provided based on a zero order rate constant showing slightly lower values for the apparent activation energies compared to those obtained from the first order. The effect of process conditions on the orders in *n*-decane will be further discussed in section 5.3.6..

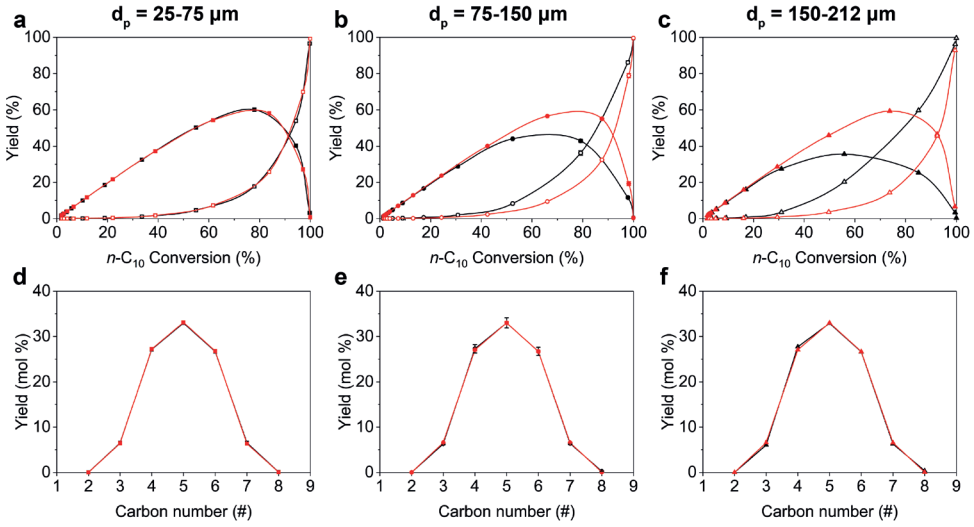

Figure 5.9. Isomer and cracking yield curves as function of *n*-decane conversion of Pt-Y/A-NH$_3$ (black) and Pt-Y/A-Cl (red) catalysts are provided in a-c, for catalysts with three different grain sizes. The corresponding cracking distribution patterns obtained at cracking conversions between 32-70 % are provided in d-f. (W/F = 244 kg·s·mol^{-1}, 10.8 mol_{H2}·$mol_{n\text{-}C10}^{-1}$, pressure = 20 bar)

In Figure 5.9 the yields towards decane isomers and cracking products and selectivity in cracking products is provided Pt-Y/A-NH_3 and Pt-Y/A-Cl catalysts of the same grain sizes. For all catalysts and grain sizes, a 'bell shaped' curved is obtained, that is typical for *n*-decane conversion on zeolite Y catalysts.[39] Froment has confirmed that the cracking product distribution in *n*-decane conversion remains symmetrical up to cracking conversions up to 90 %, proving that the decane cracking products are relatively inert under the reaction conditions.[5] This rationalizes why, while the selectivity towards the isomer versus cracking depends on catalysts grain size for Pt-Y/A-NH_3 catalyst, the distribution of cracking products is unaltered.

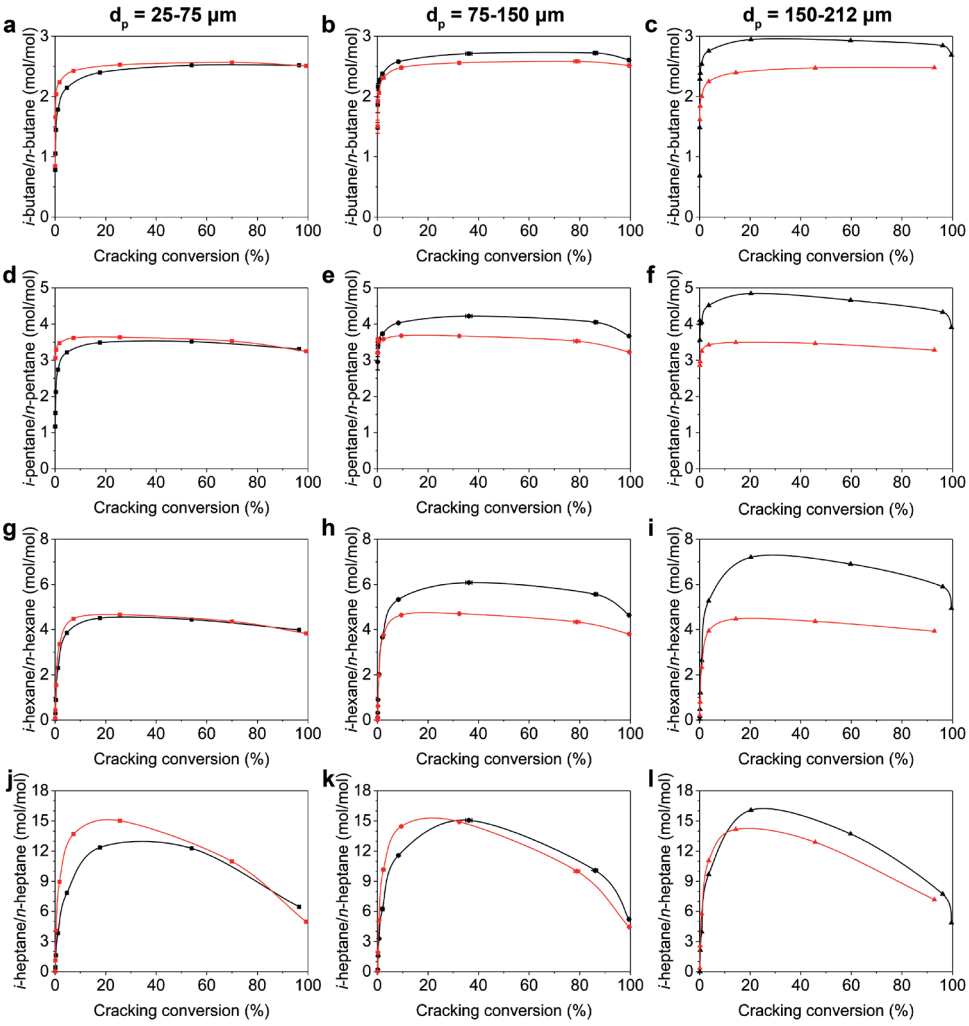

Figure 5.10. Ratio between branched and linear cracking products of butanes (a-c), pentanes (d-f), hexanes (g-i) and heptanes (j-l) of the Pt-Y/A-NH_3 (black symbols) and Pt-Y/A-Cl (red symbols) with different catalyst grain sizes indicated on top of the figure. (W/F = 244 kg·s·mol^{-1}, 10.8 mol_{H2}·$mol_{n\text{-}C10}^{-1}$, pressure = 20 bar)

Earlier studies on the isomer selectivity in hydroisomerization on large pore zeolite catalysts has pointed out that the product distributions between mono, di and tribranched isomers at medium conversion levels are determined by the thermodynamic equilibrium.[40,41] This is a consequence of the relatively fast methyl shift reactions in relation to PCP isomerization and β-scission reactions responsible for cracking. Although assignment of specific decane isomers was not possible from the obtained chromatograms due to peak overlap, an overlay of the obtained chromatograms at different temperatures (Figure S5.18) provides a qualitative confirmation that there are no significant differences in the product distributions of decane isomers between catalysts of different grain size.

In Figure 5.10, the ratio between branched and linear cracking products is provided as function of cracking conversion (i.e. cracking yield) which provides information on the type of cracking reactions that are taking place.[2] An enhanced production of branched cracking products versus linear products indicates the occurrence of energetically favorable β-scission reactions. The ratio is known to depend on crystallite size for ZSM-5 based catalysts[42] and on Pt nanoparticle location in composite zeolite based catalysts.[20,22] A lower formation of branched products was observed for larger zeolite crystals and composite catalysts with Pt nanoparticles located in the zeolite, a both phenomena were attributed to shape-selectivity effects.

In Figure 5.10 a,d,g,j the curves are provided for 25-75 μm sized catalysts grain and it is apparent that the Pt-Y/A-Cl catalyst has a higher formation of branched cracking products, which is similar as observed before for *n*-heptane conversion on zeolite Y.[22]

For larger Pt-Y/A-Cl catalyst grains, this ratio is does not change, while for the Pt-Y/A-NH_3 catalyst an upward trend is observed with respect to catalyst grain sizes. This observation points to enhanced cracking of decane isomers with multiple branches (at least dibranched) on zeolite acid sites for the latter catalysts. Other factors, besides cracking on acid sites, that could influence the branched versus linear ratio are hydrogenolysis (producing linear cracking products) and isomerization of cracking products. Hydrogenolysis of *n*-alkanes occurs on Pt nanoparticles at relatively high temperatures, for catalysts with a weak acid function and/or relatively unreactive short *n*-alkane feedstock.[15,36] Since the experiments in this study are conducted at temperatures of maximally 300 °C, and methane formation during experiments was negligible, hydrogenolysis can be excluded as relevant side reaction. In order to assess the reactivity of the cracking products under reaction conditions, possibly influencing the branched versus linear ratio between cracking products by secondary isomerization reactions, changes in the ratio between a terminally branched (2-methylhexane) and an internally branched heptane cracking product (3-methylhexane) were compared. In the hydroisomerization of *n*-hexane and *n*-heptane on zeolite Y, it is known that this ratio reaches equilibrium already at low conversion levels.[15] This is attributed to relatively fast methyl-shift reaction compared to the PCP reaction for the creation of a methyl group and β-scission cracking reactions.[43] In Figure 5.11, the ratio between 2-methylhexane and 3-methylhexane is provided as function of cracking conversion, for the composite catalysts with different grain size. The equilibrium value between 2-methylhexane and 3-methylhexane within 170-280 °C is indicated in grey. These plots indicate that under reaction conditions the equilibrium value is approached but not reached.

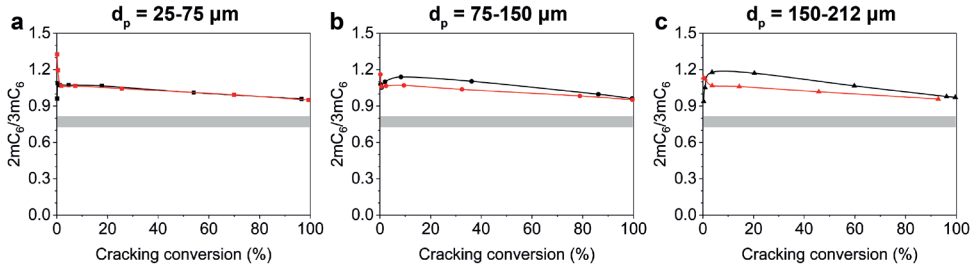

Figure 5.11. The ratio between 2-methylhexane and 3-methylhexane as heptane cracking products of *n*-decane. The equilibrium value of the ratio between 170 °C and 280 °C is indicated by the grey rectangle and was calculated with the HSC software from Outotec, v9. (W/F = 244 kg·s·mol^{-1}, 10.8 mol_{H2}·$mol_{n\text{-}C10}{}^{-1}$, pressure = 20 bar)

Considering that the methyl shifts required for the conversion of 2-methylhexane towards 3-methylhexane are fast with respect to the PCP reaction responsible for addition/removal of methyl side groups, it thus provides further evidence that heptane cracking products from decane are relatively inert under reaction conditions. Since C_4, C_5 and C_6 cracking products are less reactive than heptane cracking products, changes in the isomer/linear ratio as a consequence from PCP reactions can also be excluded for these cracking products. The differences between reactivity of *n*-heptane and *n*-decane were studied before by Steijns. et al. by using an equimolar mixture of *n*-heptane and *n*-decane.[4] They observed that the rate of *n*-decane conversion was unaffected compared to a pure *n*-decane feed, while the rate of conversion of *n*-heptane was drastically reduced with respect to a pure feed. This was attributed it to competitive physical adsorption in the zeolite pores, in which adsorption of *n*-decane is favored. In conclusion, the increasing ratio between linear and branched cracking products for Pt-Y/A-NH_3 catalysts as function of catalysts grain size (Figure 5.10), can be attributed to cracking reactions on acid sites albeit that the cracking product distribution was not affected (Figure 5.9 d-f).

To verify absence of changes on the catalysts structure as a consequence of grinding and sieving of catalyst grains, in the supplementary information characterization of spent catalysts by XRD (Figure S5.19, Table S5.12) and nitrogen physisorption (Figure S5.20, Table S5.13,) is presented. The similar FWHM evidenced by XRD and similar pore volumes from nitrogen physisorption indicate that grinding had no detrimental effect on zeolite crystallinity or catalyst grain porosity.

5.3.6. Effect of Hydrogen and *n*-Decane Partial Pressure

Based on the bifunctional mechanism, reaction orders between 0 and 1 are expected for *n*-alkanes, with lower values for n-alkanes that adsorb strongly resulting in increased surface coverages. By increasing or decreasing the partial pressure of hydrogen, the dehydrogenation-hydrogenation equilibrium is shifted, and thus the partial pressure of hydrogen determines the relative alkene concentration at the catalyst surface.[8,44] The order in hydrogen according to the bifunctional mechanism is therefore expected to be between -1 and 0, with more negative orders indicating a stronger effect of alkene concentration on the reaction rate. Earlier studies have indicated that due to strong adsorption of *n*-decane on zeolite Y, the micropores are saturated with *n*-decane, almost independent of *n*-decane partial pressure.[5] As a consequence, the rate of *n*-decane conversion was found to be nearly independent of the partial pressure of *n*-decane i.e. zero order dependence. Lighter alkanes such as *n*-octane and *n*-hexane were found to adsorb less strongly and therefore higher partial pressures were required to saturate the catalysts surface and thus transition from a first order to zero order dependence when going from low to high partial pressures.[8,45]

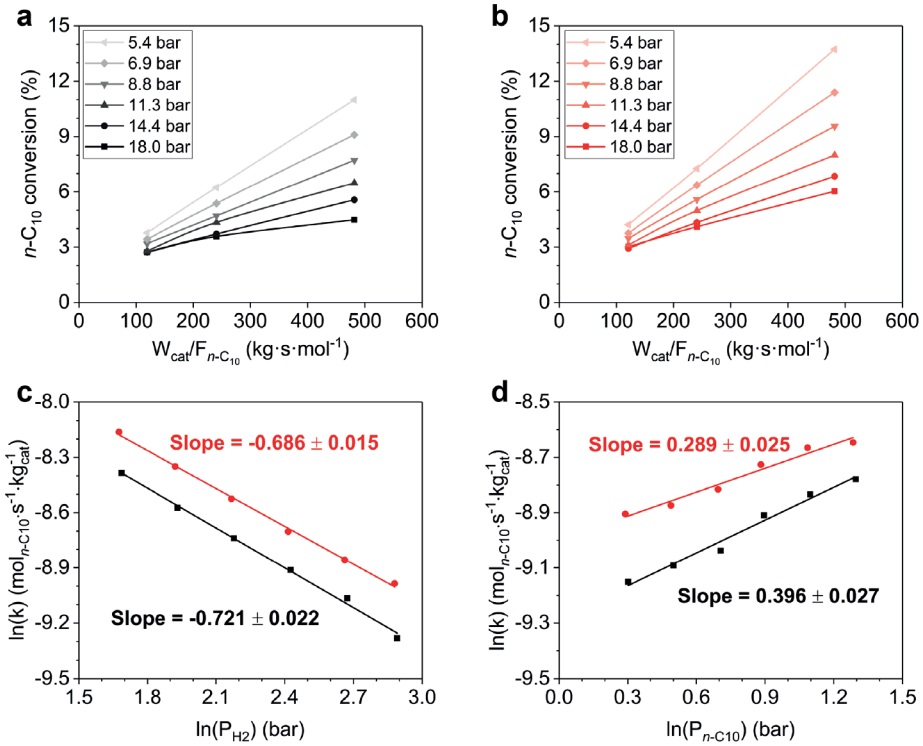

Figure 5.12. The *n*-decane conversion at 200 °C as a function of contact time at the hydrogen partial pressures indicated in the legend for the Pt-Y/A-NH_3 (a) and Pt-Y/A-Cl (b) catalysts. In (c) the natural logarithm of the rate is plotted versus the natural logarithm of the hydrogen partial pressure for the Pt-Y/A-NH_3 (black) and the Pt-Y/A-Cl (red) catalysts (W/F = 488 kg·s·mol^{-1}) with the slope of a linear fit indicated corresponding to the order in hydrogen. In (d) the natural logarithm of the rate was plotted versus the natural logarithm of the *n*-decane partial pressure, where the slope of the linear fit indicates the order in hydrogen. (200 °C, pressure = 20 bar, d_p = 75-150 µm).

In Figure 5.12, the effect of a decreasing hydrogen partial pressure is shown for the Pt-Y/A-NH_3 (a) and Pt-Y/A-Cl (b) catalysts as a function of contact time. It is apparent that the conversion increases for both catalysts at lower hydrogen partial pressures, indicative of a negative reaction order in hydrogen. Since the total conversion at 200 °C is relatively low, catalytic activities are not affected by the depletion of the *n*-decane reactant and thus linear dependencies on contact time are obtained. At relatively low conversion levels, the presence of feed impurities plays a significant role on the measured conversion levels and explains why the curves in Figure 5.12 a, b cannot be extrapolated to 0 % conversion at 0 contact time. Similar trends were obtained at a total pressure of 5 bar albeit at higher conversion levels (Figure S5.21). In Figure 5.12 c the rate constant is plotted versus partial pressure of hydrogen for the two catalysts, and the orders in hydrogen are obtained by fitting. In figure 5.12 d, the rate constant is plotted as function of *n*-decane pressure and the orders in *n*-decane were determined over a range of contact times (W/F = 216-587 kg·s·mol^{-1}). As expected a negative order in hydrogen was obtained and a positive order in *n*-decane.

In Table 5.7, the results are displayed of the order dependencies of reactors loaded with different amount of catalysts at 200 °C. It shows that more negative orders in hydrogen were obtained at higher contact times while simultaneously lower orders in n-decane were obtained. Furthermore, reaction orders in hydrogen and *n*-decane were determined at total pressures of 20 and 5 bar at different temperatures (Table 5.8, 5.9). It is observed that both the orders in hydrogen and *n*-decane are going through a minimum upon an increase in temperature in both cases. The order in hydrogen decreases upon an increase in temperature at 20 bar, whereas at 5 bar the order in hydrogen decreases from 180 to 200 °C and subsequently increases at 210 °C. For the order in *n*-decane a decreasing trend is observed upon an increase in temperature at both pressures.

At higher temperatures the decreasing trend of reaction orders in hydrogen and *n*-decane reverses, and both orders increase as a result of the depletion of n-decane. This trend is not fully reflected in the data obtained between 180-210 °C in Tables 5.8. and Table 5.9., but can be inferred from Figure 5.5, where the *n*-decane conversion is plotted as a function of contact time and deviates from the straight line going from 0 to 100 % *n*-decane conversion that is expected for a zero order dependence in *n*-decane.

Table 5.7. The reaction orders in hydrogen and *n*-decane for the catalysts determined at different contact times at 200 °C. The error's indicate the error in the fit. (pressure = 20 bar, d_p = 75-150 μm)

		$W_{cat}/F_{n\text{-}C10}$ (kg·s·mol^{-1})		
Catalyst	**Order**	**122**	**244**	**488**
Pt-YA-NH_3	H_2	-0.397 ± 0.019 (5.4-11.3 bar H_2)	-0.47 ± 0.03	-0.721 ± 0.022
Pt-AY-Cl	H_2	-0.40 ± 0.03 (5.4-11.3 bar H_2)	-0.487 ± 0.020	-0.686 ± 0.015
		53-145	107-292	216-587
Pt-YA-NH_3	*n*-C_{10}	0.71 ± 0.07	0.55 ± 0.04	0.396 ± 0.027
Pt-AY-Cl	*n*-C_{10}	0.68 ± 0.06	0.39 ± 0.03	0.289 ± 0.025

A difference between 20 and 5 bar is that for the lower *n*-decane partial pressures at 5 bar, the process operates at full vapor phase conditions, while at 180 and 190 °C at 20 bar, *n*-decane may condensate as can be inferred from Figure 5.2 (right axis). For trickle-bed operation and a completely wetted catalysts bed, Pt nanoparticles can no longer be accessed by hydrogen through the gas phase. However, due to an anticipated quick gas-liquid equilibration of hydrogen in *n*-decane, this is expected to have no significant effect on the reaction. The data obtained at 5 bar is not affected by differences in aggregation state of the *n*-alkane, but as stated in the experimental, some evidence for catalyst deactivation was encountered for measurements at higher temperatures. The fits that were performed to determine the reaction orders are provided in Figure S5.22 for 20 bar and Figure S5.23 for 5 bar total pressure.

The observation that both orders in hydrogen and *n*-decane are changing simultaneously has been observed before and indicates a shift in the rate limiting step of the reaction upon an increase in temperature.[44] This can be ascribed to a number of exothermic and endothermic steps that are involved in the formation of carbeniumions and their subsequent conversion to isomers and cracked products. Alkane adsorption and alkene protonation are exothermic steps, while the dehydrogenation of alkanes is endothermic.[46] To be able to distinguish between e.g. physisorption effects, alkene protonation, or isomerization reactions controlling the rate of reaction under given conditions, requires a more detailed kinetic modelling study which is beyond the scope of the current study.

To summarize, the activity of the catalysts is determined by a number of fundamental reaction steps that become of increasing or decreasing importance upon increasing the temperature, or the amount of catalyst. Moreover, from the data obtained in this study, no evidence was obtained for differences in reaction orders as a consequence of a different Pt nanoparticle location.

Table 5.8. Effect of temperature on reaction orders of hydrogen and *n*-decane at 20 bar. Orders in hydrogen were determined at $W_{cat}/F_{n\text{-}C10}$ = 244 kg·s·mol^{-1}, and at hydrogen partial pressures between 5.2-17.6 bar. Orders in *n*-decane were obtained between $W_{cat}/F_{n\text{-}C10}$ = 107-292 kg·s·mol^{-1} and at *n*-decane partial pressures of between 1.3-3.7 bar. (d_p = 75-150 μm)

		Temperature			
Catalyst	**Order**	**180 °C**	**190 °C**	**200 °C**	**210 °C**
Pt-Y/A-NH_3	H_2	-0.23 ± 0.03	-0.328 ± 0.018	-0.47 ± 0.03	-0.654 ± 0.016
Pt-Y/A-Cl	H_2	-0.214 ± 0.023	-0.362 ± 0.013	-0.487 ± 0.020	-0.625 ± 0.006
Pt-Y/A-NH_3	*n*-C_{10}	0.90 ± 0.07	0.744 ± 0.023	0.55 ± 0.04	0.387 ± 0.004
Pt-Y/A-Cl	*n*-C_{10}	0.88 ± 0.07	0.70 ± 0.06	0.39 ± 0.03	0.30 ± 0.04

Table 5.9. Effect of temperature on reaction orders of hydrogen and *n*-decane at 5 bar. Orders in hydrogen were determined at $W_{cat}/F_{n\text{-}C10}$ = 244 kg·s·mol^{-1} and at hydrogen partial pressures between 1.0-4.5 bar. Orders in *n*-decane were obtained between $W_{cat}/F_{n\text{-}C10}$ = 107-292 kg·s·mol^{-1} and at *n*-decane partial pressures of between 0.3-0.9 bar. (d_p = 75-150 μm)

		Temperature			
Catalyst	**Order**	**180 °C**	**190 °C**	**200 °C**	**210 °C**
Pt-Y/A-NH_3	H_2	-0.66 ± 0.03	-0.738 ± 0.015	-0.75 ± 0.04	-0.64 ± 0.04
Pt-Y/A-Cl	H_2	-0.64 ± 0.05	-0.677 ± 0.026	-0.78 ± 0.03	-0.65 ± 0.05
Pt-YA-NH_3	*n*-C_{10}	0.40 ± 0.05	0.400 ± 0.006	0.250 ± 0.013	0.21 ± 0.03
Pt-Y/A-Cl	*n*-C_{10}	0.41 ± 0.06	0.312 ± 0.006	0.078 ± 0.010	0.09 ± 0.05

5.3.7. Effect of Catalysts Grain Size and Hydrogen Pressure for *n*-Heptane Conversion

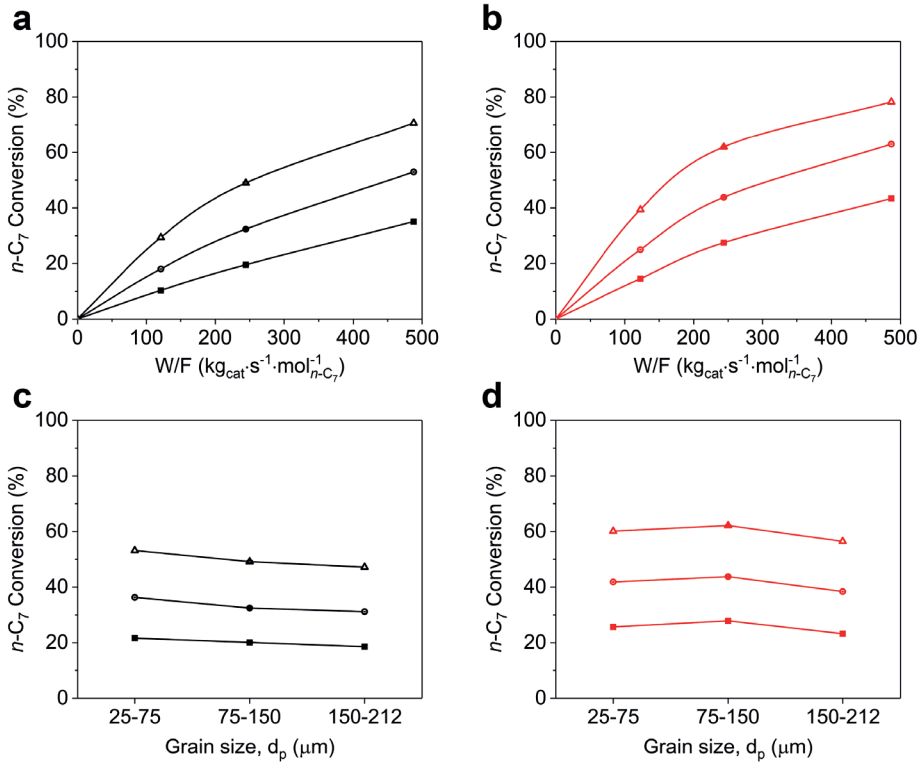

Figure 5.13. *n*-Heptane conversion versus contact time of Pt-Y/A-NH_3 (a) and Pt-Y/A-Cl (b) at 240 °C (filled squares), 250 °C (dotted circles) and 260 °C (open triangles). Effect of catalyst grain size on the *n*-heptane conversion for Pt-Y/A-NH_3 (a) and Pt-Y/A-Cl catalysts (b) at 240 °C (filled squares), 250 °C (dotted circles) and 260 °C (open triangles). Lines are a guide to the eye ($W_{cat}/F_{n\text{-}C7}$ = 244 kg·s·mol^{-1}). (pressure = 5 bar, 10.8 mol_{H2}·$mol_{n\text{-}C7}^{-1}$)

Besides *n*-decane also the hydroisomerization of *n*-heptane was studied, which has a higher diffusivity and less negative adsorption enthalpy than *n*-decane.[10] The results of experiments on the Pt-Y/A-NH_3 and Pt-Y/A-Cl composite catalysts are provided in Figure 5.13 at different contact times (a,b) and of different catalyst grain sizes (c,d). Similarly to *n*-decane, a higher activity was observed for the Pt-Y/A-Cl catalyst which did not seem to be dependent of catalyst grain size. In Figure 5.14, Arrhenius plots are provided and the apparent activation energies were determined between 210-240 °C, based on the first order rate constant. In the temperature range of the activation energies for the Pt-Y/A-NH_3 catalyst seemed to be systematically lower than for the Pt-Y/A-Cl catalyst, although differences between catalysts are small. In contrast to what was observed for *n*-decane, in the higher temperature range the slope of the Arrhenius plot decreases, which can be attributed to diffusion limitations that start to affect the rate of the reaction at higher conversion levels.

Furthermore, also a slightly lower isomer selectivity was observed for the Pt-Y/A-NH_3 catalysts of grain sizes of 75-150 and 150-212 μm (Figure 5.15 a-c), similar to what was observed for *n*-decane. No dependence on the ratio between branched and linear isomers dependent of

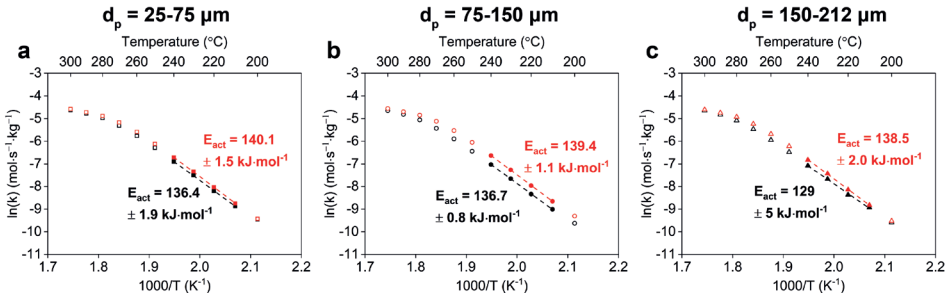

Figure 5.14. Apparent activation energies of *n*-heptane hydroisomerization based on first order kinetics on catalysts with varying catalyst grain sizes. Apparent activation energies were determined at temperatures between 210-240 °C, errors indicate error in fit. ($W_{cat}/F_{n\text{-}C7}$ = 244 kg·s·mol^{-1}, pressure = 5·bar, 10.8 mol_{H2}·$mol_{n\text{-}C7}^{-1}$)

catalyst grain size could be detected and was always higher for the Pt-Y/A-Cl catalyst (Figure 5.15 d-f). For *n*-decane, the higher branched/linear ratios of cracking products were explained by secondary reactions of branched isomers of decane. Likely, for *n*-heptane the lower isomer yield for Pt-Y/A-NH_3 of grains larger than 75 µm, the effect of the cracking of isomers within the catalyst grain is too small to result in an observable effect on the ratio of branched to linear butanes.

In Table 5.10, the orders in hydrogen obtained at different contact times for *n*-heptane are provided, whereas in Table 5.11 the orders obtained at different temperatures are displayed. It was observed that the orders in hydrogen were more negative than those observed for *n*-decane and rather independent of contact time. This is an indication that concentration of alkenes affects the rate of the reaction, while other factors such as adsorption and alkene protonation are less important. Orders in *n*-heptane were not determined during the experiments. Based on results

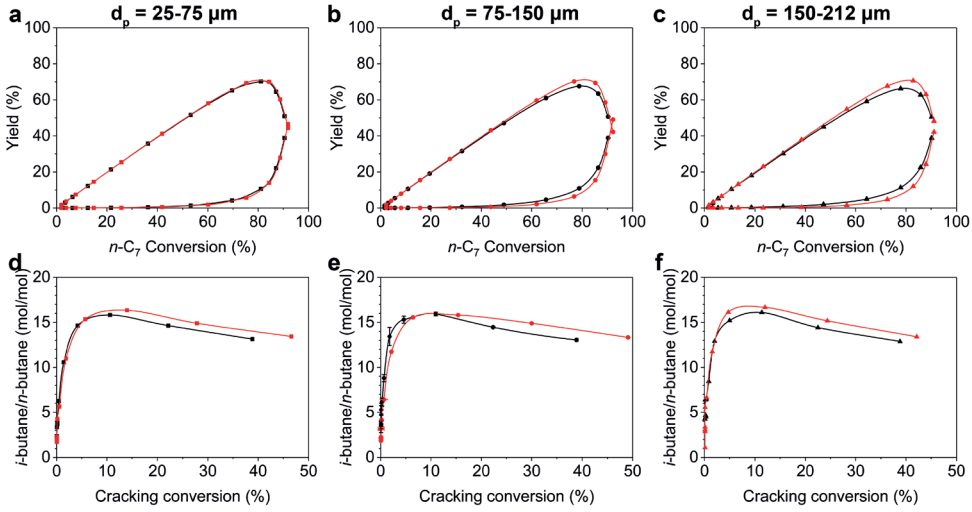

Figure 5.15. Isomer and cracking yield curves as function of *n*-decane conversion of Pt-Y/A-NH_3 (black) and Pt-Y/A-Cl (red) catalysts are provided in (a-c), for catalysts with three different grain sizes. Ratio between branched and linear cracking products of butane are indicated as a function of cracking conversion in d-f. ($W_{cat}/F_{n\text{-}C7}$ = 244 kg·s·mol^{-1}, pressure = 5 bar, 10.8 mol_{H2}·$mol_{n\text{-}C7}^{-1}$)

of Guisnet et al., reaction orders of light alkanes on zeolite Y are the mostly the opposite of the order of hydrogen, e.g. an approximate order of ~0.9 in *n*-heptane between (200-230 °C).[9] At 250 and 270 °C the order in hydrogen decreases indicating that the (de)hydrogenation function becomes a less important factor for the rate of the reaction. At such high conversion levels, the rate of reaction is mostly limited due to the depletion of *n*-heptane as reactant. As is evident from the back-check measurements that were performed at 250 and 270 °C also significant catalyst deactivation was encountered which, was unexpected in view of the lower molecular weight of the feedstock (Figure S5.24).

Table 5.10. Order in hydrogen obtained on catalysts at three different contact times at 200 °C. These values were obtained by fitting datapoints in a range of 1.0-4.2 bar hydrogen. (pressure = 5 bar, d_p = 75-150 μm)

		$W_{cat}/F_{n\text{-}C7}$ (kg·s·mol^{-1})		
Catalyst	**Order**	**122**	**244**	**488**
Pt-Y/A-NH_3	H_2	-0.847 ± 0.007	-0.869 ± 0.026	-0.885 ± 0.022
Pt-Y/A-Cl	H_2	-0.869 ± 0.015	-0.892 ± 0.018	-0.903 ± 0.012

Table 5.11. Order in hydrogen obtained on catalysts at different temperatures. These values were obtained by fitting datapoints in a range of 1.0-4.2 bar hydrogen. ($W_{cat}/F_{n\text{-}C7}$ = 244 kg·s·mol^{-1}, pressure = 5 bar, d_p = 75-150 μm)

		Temperature					
Catalyst	**Order**	**200 °C**	**210 °C**	**220 °C**	**230 °C**	**250 °C**	**270 °C**
Pt-Y/A-NH_3	H_2	-0.869 ± 0.026	-0.871 ± 0.011	-0.882 ± 0.026	-0.82 ± 0.04	-0.53 ± 0.06	-0.18 ± 0.05
Pt-Y/A-Cl	H_2	-0.892 ± 0.018	-0.889 ± 0.021	-0.885 ± 0.027	-0.80 ± 0.05	-0.42 ± 0.06	-0.11 ± 0.03

5.4 Discussion

In previous studies, effects in activity and selectivity as a consequence of Pt nanoparticle location were attributed to alkene concentration gradients within zeolite crystals. Here, results of catalyst with varying grain sizes provide evidence that concentration gradients within catalyst grains seem to play a role on the selectivity of the catalysts, if and only if, Pt nanoparticles reside within the zeolite crystals.

Previous studies on the effects of Pt nanoparticle location for composite catalysts based on zeolites were limited to grain sizes of 75-212 μm[20,22,36] or 200-500 mm[19] sized grains. Here, for the first time a range of grain sizes was studied. For the smallest catalysts grains of 25-75 μm, irrespective of the location of the Pt nanoparticles within the composite catalysts, an identical isomer yield was obtained. In a way, this is a logical outcome in view of a number of studies that point out that zeolite Y is a 'non-shape selective' catalyst for the conversion of n-alkanes.[3,15,47,48]

Diffusion limitations of reactants, intermediates or products can cause concentration gradients within catalysts grains and can lead to low (suboptimal) catalytic activities. However, in this study we did not find evidence for diffusion limitations since similar catalytic activities were obtained for catalysts of different grain size and the Wheeler-Weisz modulus was sufficiently low.

As an approximation, for the Zeolite Y/γ-Al_2O_3 support the amount of zeolite crystals in a given catalyst grain is proportional to its volume, and thus the number of zeolite crystals per catalyst grain increases with the third power upon an increase in the catalyst grain size. This results in a factor of 1-1000 larger amount of zeolite crystals per catalyst grain when comparing 25-75 μm grains towards those of 75-150 and 150-212 μm. However, no markedly different diffusion coefficients are expected for hydrocarbons within mesopores of γ-Al_2O_3 or outside a catalyst grain. Therefore, the differences in selectivity cannot be rationalized by the amount of zeolite crystals per catalysts grain. The observation that cracking is enhanced for catalyst with Pt nanoparticles residing in the zeolite of grain sizes exceeding 75 μm, leaves us without explanation at the current state of affairs.

The observation that the branched/linear ratios of cracking products can depend on the preparation method (i.e. Pt nanoparticle location) has been made before. In studies on Pt/Zeolite Y powders used for *n*-decane hydroisomerization, it was noted that the branched/linear ratio of pentane cracking products was dependent on the catalyst preparation method.[39] A catalyst prepared by an ion-exchange procedure of $[Pt(NH_3)_4^{2+}]$ (aq) displayed a higher production of branched pentane products compared to a catalyst prepared by an impregnation procedure, independent of reaction conditions.

5.5 Conclusions

A kinetic study was performed on the hydroisomerization of n-alkanes on Pt/Zeolite Y/γ-Al_2O_3 catalysts of different grain size and with different Pt nanoparticle location within the composite support. The effect of contact time, total pressure, catalysts grain size, Pt nanoparticle location and partial pressures of hydrogen and *n*-alkane were studied. Measurements at different contact time provided evidence of a positive order in *n*-alkane, for both *n*-decane and *n*-heptane. Furthermore, an increase in total pressure resulted in a decreasing catalytic activity, proving that the conditions for an ideal process were satisfied irrespective of Pt nanoparticle location. Both the grain size and the location of Pt nanoparticles proved to have a crucial impact on activity and selectivity. The activity of the Pt-Y/A-NH_3 catalyst, with Pt nanoparticle located in the zeolite, was always lower under identical conditions (grain size, contact time, pressure, temperature) compared to the activity of the Pt-Y/A-Cl catalyst. Furthermore, on Pt-Y/A-NH_3 catalysts the isomer yield seemed to depend on catalyst grain size and the smallest (d_p = 25-75 μm) catalyst grains had an 'optimal' isomer yield, identical to what was obtained for Pt-Y/A-Cl catalysts. Variation of the partial pressure of hydrogen and *n*-alkane revealed a strong effect of temperature on the orders that were obtained. Both the order in hydrogen and the *n*-alkane went through a minimum upon an increase in temperature, whereas no systematically evidence of different orders on the location of Pt nanoparticles were obtained.

Acknowledgements

Lars van der Wal is acknowledged for performing transmission electron microscopy measurements. Luc Smulders, Dennie Wezendonk and Jan Willem de Rijk are acknowledged for their efforts in the commissioning of the Flowrence setup. Suzan Schoemaker and Remco Dalebout are acknowledged for performing nitrogen physisorption measurements. Shell Projects and Technology is acknowledged for supplying Zeolite Y/γ-Al_2O_3 extrudates.

Nomenclature

Ca	Carberry number (-)
d_p	Diameter of catalyst grain (m)
d_t	Inner diameter of reactor tube (m)
E_{act}	Apparent activation energy (kJ·mol^{-1})
EDX	Energy-Dispersive X-ray spectroscopy
$F_{n\text{-alkane}}$	Molar flow rate (mol·s^{-1})
FWHM	Full Width at Half Maximum (-)
GHSV	Gas Hourly Space Velocity (mL_{gas}·mL_{cat}^{-1}·h^{-1})
HAADF-STEM	High-Angle Annular Dark-Dield Scanning Transmission Electron Microscopy
ICP-OES	Inductively Coupled Plasma-Optical Emission Spectroscopy
L_b	Length of catalyst bed (m)
NH_3-TPD	Ammonia Temperature Programmed Desorption
$P_{n\text{-C10}}$	Partial pressure of *n*-decane (bar)
$P_{n\text{-C7}}$	Partial pressure of *n*-heptane (bar)
P_{H2}	Partial pressure of hydrogen (bar)
P_{He}	Partial pressure of helium(bar)
PCP	Protonated Cyclo Propene

W	Catalyst Weight (kg)
η	Effectiveness factor of catalyst (-)
ϕ	Thiele modulus (-)
SEMK	Single Event Micro Kinetic model
XRD	X-ray Diffraction
σ	Standard deviation

References

[1] H. L. Coonradt, W. E. Garwood, Ind. Eng. Chem. Process Des. Dev. 1964, 3, 38–45.

[2] J. Weitkamp, ChemCatChem 2012, 4, 292–306.

[3] J. W. Thybaut, C. S. Laxmi Narasimhan, J. F. Denayer, G. V. Baron, P. A. Jacobs, J. A. Martens, G. B. Marin, Ind. Eng. Chem. Res. 2005, 44, 5159–5169.

[4] M. Steijns, G. F. Froment, Ind. Eng. Chem. Prod. Res. Dev. 1981, 20, 660–668.

[5] G. F. Froment, Catal. Today 1987, 1, 455–473.

[6] G. G. Martens, G. B. Marin, J. A. Martens, P. A. Jacobs, G. V. Baron, J. Catal. 2000, 195, 253–267.

[7] B. D. Vandegehuchte, J. W. Thybaut, A. Martínez, M. A. Arribas, G. B. Marin, Appl. Catal. A Gen. 2012, 441–442, 10–20.

[8] A. van de Runstraat, J. A. Kamp, P. J. Stobbelaar, J. van Grondelle, S. Krijnen, R. A. van Santen, J. Catal. 1997, 171, 77–84.

[9] M. Guisnet, V. Fouche, M. Belloum, J. P. Bournonville, C. Travers, Appl. Catal. 1991, 71, 295–306.

[10] J. F. Denayer, G. V. Baron, J. A. Martens, P. A. Jacobs, J. Phys. Chem. B 1998, 102, 3077–3081.

[11] M. A. Baltanas, H. Vansina, G. F. Froment, Ind. Eng. Chem. Prod. Res. Dev. 1983, 22, 531–539.

[12] L. H. Hosten, G. F. Froment, Ind. Eng. Chem. Process Des. Dev. 1971, 10, 280–287.

[13] J. W. Thybaut, G. B. Marin, J. Catal. 2013, 308, 352–362.

[14] J. W. Thybaut, I. R. Choudhury, J. F. Denayer, G. V. Baron, P. A. Jacobs, J. A. Martens, G. B. Marin, Top. Catal. 2009, 52, 1251–1260.

[15] J. W. Thybaut, G. B. Marin, G. V. Baron, P. A. Jacobs, J. A. Martens, J. Catal. 2001, 202, 324–339.

[16] J. W. Thybaut, C. S. Laxmi Narasimhan, G. B. Marin, Catal. Today 2006, 111, 94–102.

[17] J. A. Muñoz Arroyo, G. G. Martens, G. F. Froment, G. B. Marin, P. A. Jacobs, J. A. Martens, Appl. Catal. A Gen. 2000, 192, 9–22.

[18] J. F. M. Denayer, R. A. Ocakoglu, W. Huybrechts, B. Dejonckheere, P. Jacobs, S. Calero, R. Krishna, B. Smit, G. V. Baron, J. A. Martens, J. Catal. 2003, 220, 66–73.

[19] J. Zečević, G. Vanbutsele, K. P. De Jong, J. A. Martens, Nature 2015, 528, 245–254.

[20] K. Cheng, L. I. Wal, H. Yoshida, J. Oenema, J. Harmel, Z. Zhang, G. Sunley, J. Zečević, K. P. Jong, Angew. Chemie Int. Ed. 2020, 59, 3592–3600.

[21] O. Ben Moussa, L. Tinat, X. Jin, W. Baaziz, O. Durupthy, C. Sayag, J. Blanchard, ACS Catal. 2018, 8, 6071–6078.

[22] J. Oenema, J. Harmel, R. P. Vélez, M. J. Meijerink, W. Eijsvogel, A. Poursaeidesfahani, T. J. H. Vlugt, J. Zečević, K. P. de Jong, ACS Catal. 2020, 10, 14245–14257.

[23] J. De Graaf, A. J. Van Dillen, K. P. De Jong, D. C. Koningsberger, J. Catal. 2001, 203, 307–321.

[24] "Avantium website," can be found under: https://www.catalysis.avantium.com/flowrence-technology-platform/, 2020.

[25] R. Moonen, J. Alles, E. J. Ras, C. Harvey, J. A. Moulijn, Chem. Eng. Technol. 2017, 40, 2025–2034.

[26] J. C. van der Waal, E.-J. Ras, C. M. Lok, R. Moonen, N. van der Puil, in Mod. Appl. High Throughput R&D Heterog. Catal. (Ed.: A.H. and A.F. Volpe), Bentham Science, 2014, pp. 197–226.

[27] J. Pérez-Ramírez, R. J. Berger, G. Mul, F. Kapteijn, J. A. Moulijn, Catal. Today 2000, 60, 93–109.

[28] F. Kapteijn, J. A. Moulijn, in Handb. Heterog. Catal. (Eds.: G. Ertl, H. Knozinger, J. Weitkamp), Wiley-VCH Verlag GmbH, Weinheim, Germany, 1997, pp. 1359–1398.

[29] R. J. Berger, J. Pérez-Ramírez, F. Kapteijn, J. A. Moulijn, Appl. Catal. A Gen. 2002, 227, 321–333.

[30] R. D. Chirico, A. Nguyen, W. V. Steele, M. M. Strube, C. Tsonopoulos, J. Chem. Eng. Data 1989, 34, 149–156.

[31] G. F. Carruth, R. Kobayashi, J. Chem. Eng. Data 1973, 18, 115–126.

[32] P. B. Weisz, Adv. Catal. 1962, 13, 137–190.

[33] J. A. A. Martens, P. A. A. Jacobs, in Stud. Surf. Sci. Catal., 2001, pp. 633–671.

[34] G. T. Whiting, S. H. Chung, D. Stosic, A. D. Chowdhury, L. I. Van Der Wal, D. Fu, J. Zecevic, A. Travert, K. Houben, M. Baldus, et al., ACS Catal. 2019, 9, 4792–4803.

[35] J. Oenema, J. P. Hofmann, E. J. M. Hensen, J. Zečević, K. P. de Jong, ChemCatChem 2020, 12, 615–622.

[36] J. Oenema, R. A. van Alst, M. J. Meijerink, J. Zečević, K. P. de Jong, Appl. Catal. A Gen. 2020, 117815.

[37] A. van de Runstraat, J. van Grondelle, R. A. van Santen, Ind. Eng. Chem. Res. 1997, 36, 3116–3125.

[38] I. Chorkendorff, J. W. Niemantsverdriet, Concepts of Modern Catalysis and Kinetics, Wiley-VCH Verlag, 2017.

[39] J. A. Martens, P. A. Jacobs, Zeolites 1986, 6, 334–348.

[40] A. Poursaeidesfahani, M. F. de Lange, F. Khodadadian, D. Dubbeldam, M. Rigutto, N. Nair, T. J. H. Vlugt, J. Catal. 2017, 353, 54–62.

[41] M. Steijns, G. Froment, P. Jacobs, J. Uytterhoeven, J. Weitkamp, Ind. Eng. Chem. Prod. Res. Dev. 1981, 20, 654–660.

[42] E. Verheyen, C. Jo, M. Kurttepeli, G. Vanbutsele, E. Gobechiya, T. I. Korányi, S. Bals, G. Van Tendeloo, R. Ryoo, C. E. A. Kirschhock, et al., J. Catal. 2013, 300, 70–80.

[43] J. A. Martens, P. A. Jacobs, J. Weitkamp, Appl. Catal. 1986, 20, 283–303.

[44] A. Van De Runstraat, Adsorption Effects in Acid Catalysis by Zeolites, 1997.

[45] M. A. Baltanas, K. K. Van Raemdonck, G. F. Froment, S. R. Mohedas, Ind. Eng. Chem. Res. 1989, 28, 899–910.

[46] J. W. Thybaut, C. S. Laxmi Narasimhan, G. B. Marin, J. F. M. Denayer, G. V. Baron, P. A. Jacobs, J. A. Martens, Catal. Letters 2004, 94, 81–88.

[47] J. A. Martens, R. Parton, L. Uytterhoeven, P. A. Jacobs, G. F. Froment, Appl. Catal. 1991, 76, 95–116.

[48] J. F. Denayer, G. V. Baron, G. Vanbutsele, P. A. Jacobs, J. A. Martens, J. Catal. 2000, 190, 469–473.

Supporting information

Supporting information 5.1

The conversion of *n*-decane or *n*-heptane ($X_{n\text{-alkane}}$) is calculated by:

$$X_{n\text{-alkane}} = \left(1 - \frac{F_{C\,wt.\,n\text{-alkane, out}}}{F_{C\,wt.\,n\text{-alkane, in}}}\right) \cdot 100\%$$

Wherein $F_{C\,wt.\,n\text{-alkane, out}}$ and $F_{C\,wt.\,n\text{-alkane, in}}$ are the flows, based on weight of carbon, of *n*-alkane going out or into the reactor, respectively. The isomer yield ($Y_{i\text{-alkane}}$) is calculated by:

$$Y_{i\text{-alkane}} = \left(\frac{F_{C\,wt.\,i\text{-alkane, out}}}{F_{C\,wt.\,n\text{-alkane, in}}}\right) \cdot 100\%$$

Wherein $F_{C\,wt.\,i\text{-alkane, out}}$ is the flow going out of the reactor, based on weight of carbon of branched isomers of the *n*-alkane. For *n*-heptane hydroisomerization, the yield of cracked products ($Y_{cracked\ alkanes}$) is calculated by:

$$Y_{cracked\ alkanes} = \left(\frac{F_{C\,wt.\,C_{1\text{-}6}\text{, out}}}{F_{C\,wt.\,n\text{-}C_7\text{, in}}}\right) \cdot 100\%$$

For *n*-decane hydroisomerization, the yield of cracked products ($Y_{cracked\ alkanes}$) is calculated by:

$$Y_{cracked\ alkanes} = \left(\frac{F_{C\,wt.\,C_{1\text{-}8}\text{, out}}}{F_{C\,wt.\,n\text{-}C_{10}\text{, in}}}\right) \cdot 100\%$$

Wherein $F_{C\,wt.\,Cm\text{-}n,\,out}$ are the flows going out of the reactor, based on weight of carbon, of the sum of cracked products of carbon numbers within the range of (m-n). For the cracking product distribution patterns of *n*-decane, the yield of individual cracked products in mol% (Y_{cm}), was calculated by:

$$Y_{C_m} = \left(\frac{F_{C\,wt.\,C_m\text{, out}}}{F_{C\,wt.\,n\text{-}C_{10}\text{, in}}}\right) \cdot \left(\frac{10}{m}\right) \cdot 100\%$$

The ln of the zeroth order rate constant was calculated by:

$$\ln(k) = \ln\left(\frac{X_{n\text{-alkane}}}{W_{cat} / F_{mol,\,n\text{-alkane}}}\right)$$

The ln of the first order rate constant was calculated by:

$$\ln(k) = \ln\left(-\frac{\ln(1 - X_{n\text{-alkane}})}{W_{cat} / F_{mol,\,n\text{-alkane}}}\right)$$

Wherein $F_{mol,\,n\text{-alkane}}$ is the inlet flow of the *n*-alkane (mol·s^{-1}), and W_{cat} is the weight of catalysts (kg).

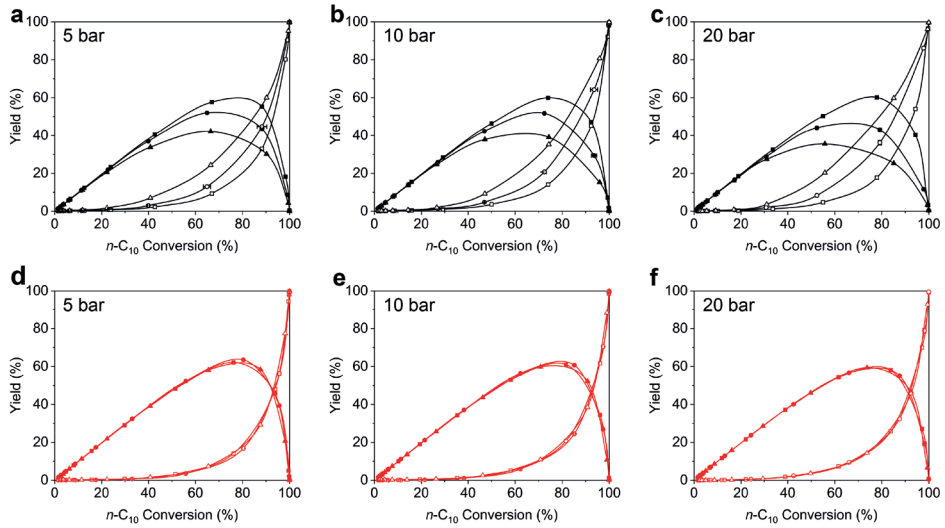

Figure S5.16. The product yields at 5, 10 and 20 bar total pressure from Pt-Y/A-NH_3 (a-c) and Pt-Y/A-Cl (d-f) catalysts as a function of *n*-decane conversion. Isomer yield is indicated as filled symbols while cracking products are indicated as open symbols. The 25-75 µm particles are indicated as squares, 75-150 µm particles are indicated as circles and 150-212 µm particles are indicated as triangles. Lines are a guide to the eye. (W/F = 244 kg·s·mol^{-1}, 10.8 mol_{H2}·$mol_{n\text{-}C10}^{-1}$)

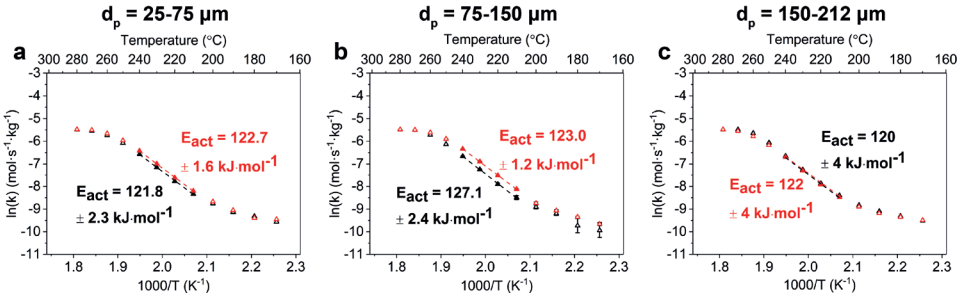

Figure S5.17. Arrhenius plots based on zero order rate constant of Pt-Y/A-NH_3 (black) and Pt-Y/A-Cl catalysts (red) with different catalyst grain sizes: d_p = 25-75 µm (a), 75-150 µm (b), 150-212 µm (c). The dashed lines indicate the linear fit of datapoints within a temperature range of 210-240 °C. (W/F = 244 kg·s·mol^{-1}, 10.8 mol_{H2}·$mol_{n\text{-}C10}^{-1}$, pressure = 20 bar)

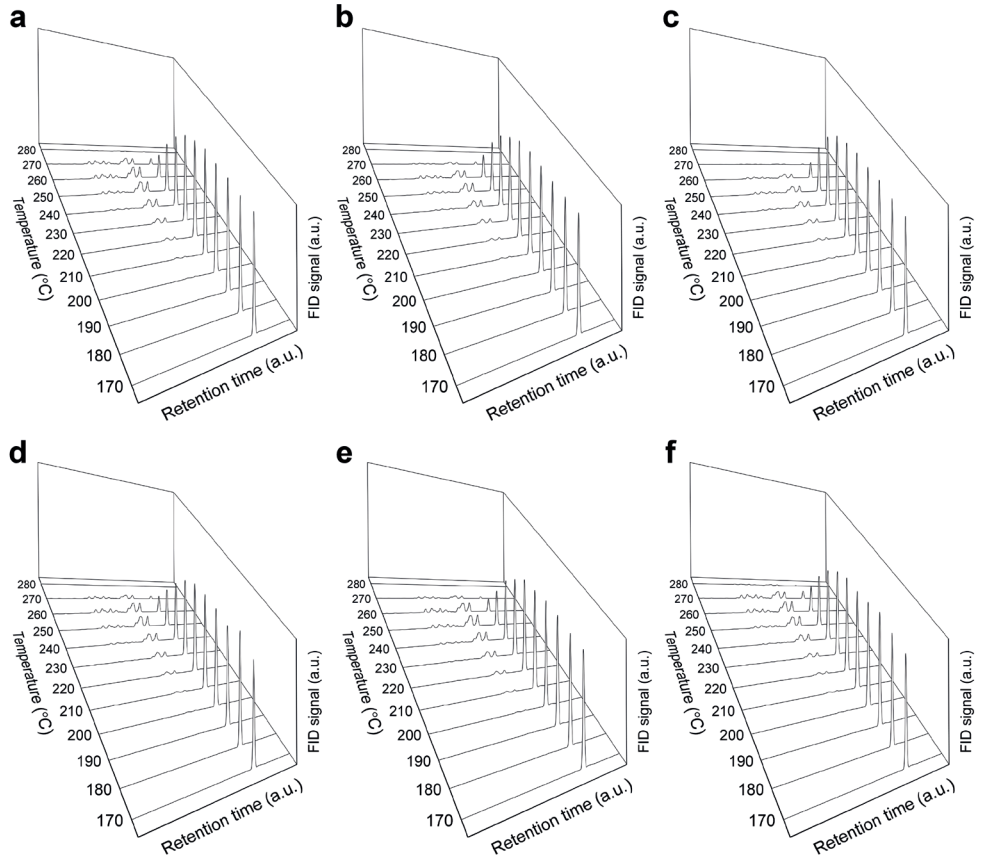

Figure S5.18. FID signals of the 'decane region' in the chromatograms of Pt-Y/A-NH_3 of d_p = 25-75 µm (a), 75-150 µm (b) and 150-212 µm (c) and Pt-Y/A-Cl of d_p = 25-75 µm (d), 75-150 µm (e) and 150-212 µm (f). The sharp peak of high intensity is identified as *n*-decane, which is converted into isomers of decane at higher temperatures, that elute from the column before *n*-decane due to their lower boiling point. Cracking products elute from the GC column before decane products and are out of the range shown in the figures. For the Pt-Y/A-NH_3 catalysts with d_p = 75-150 µm and d_p = 150-212 µm a lower intensity of the isomer peaks is observed. However, for all catalysts, the decane isomer peaks appeared at the same retention times indicative of similar isomer product distributions for all catalysts. (W/F = 244 kg·s·mol^{-1}, 10.8 mol_{H2}·$mol_{n\text{-}C10}^{-1}$, pressure = 20 bar)

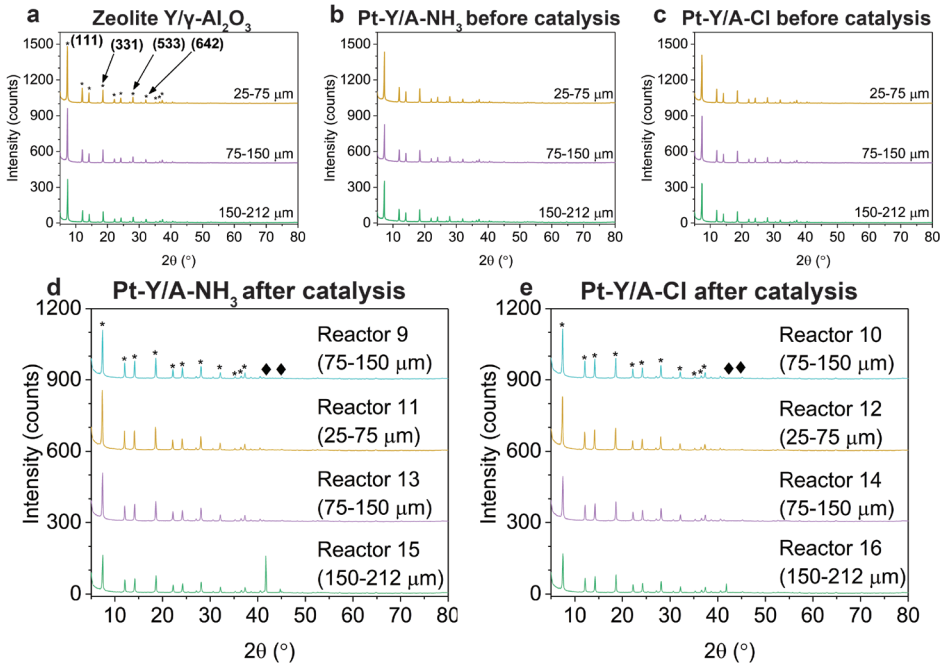

Figure S5.19. XRD patterns of different sieve fractions of the Zeolite Y/γ-Al_2O_3 support (a) and composite catalysts before catalysis (b,c). The catalysts after the hydroisomerization experiments are provided in d-e. Asterisks (*) indicate diffraction peaks from zeolite Y, diamonds (◊) indicate diffraction peaks from SiC. Diffraction patterns in a-c are stacked with 500 counts, while diffraction patterns in d-e are stacked with 300 counts. The lower absolute intensity for the measurements on catalysts after catalysis can be largely attributed to the smaller amount of catalyst used for the measurements, which was limited by the amount in the reactors.

Table S5.12. Full Width Half Maximum (FWHM) of the 111, 331, 533 and 642 diffraction peaks.

d_p (μm)	Reactor	111 (°2θ)	331 (°2θ)	533 (°2θ)	642 (°2θ)
			Zeolite Y/γ-Al_2O_3		
25-75	-	0.191	0.156	0.175	0.197
75-150	-	0.186	0.160	0.179	0.190
150-212	-	0.195	0.185	0.207	0.218
			Pt-Y/A-NH_3 (before catalysis)		
25-75	-	0.180	0.150	0.175	0.183
75-150	-	0.190	0.164	0.179	0.186
150-212	-	0.185	0.159	0.174	0.197
			Pt-Y/A-Cl (before catalysis)		
25-75	-	0.180	0.150	0.175	0.183
75-150	-	0.187	0.169	0.185	0.206
150-212	-	0.188	0.175	0.203	0.204
			Pt-Y/A-NH_3 (after catalysis)		
75-150	9	0.188	0.171	0.191	0.194
25-75	11	0.183	0.153	0.170	0.180
75-150	13	0.190	0.164	0.195	0.219
150-212	15	0.192	0.174	0.193	0.199
			Pt-Y/A-Cl (after catalysis)		
75-150	10	0.185	0.163	0.190	0.201
25-75	12	0.184	0.162	0.173	0.186
75-150	14	0.192	0.173	0.200	0.192
150-212	16	0.186	0.159	0.194	0.183

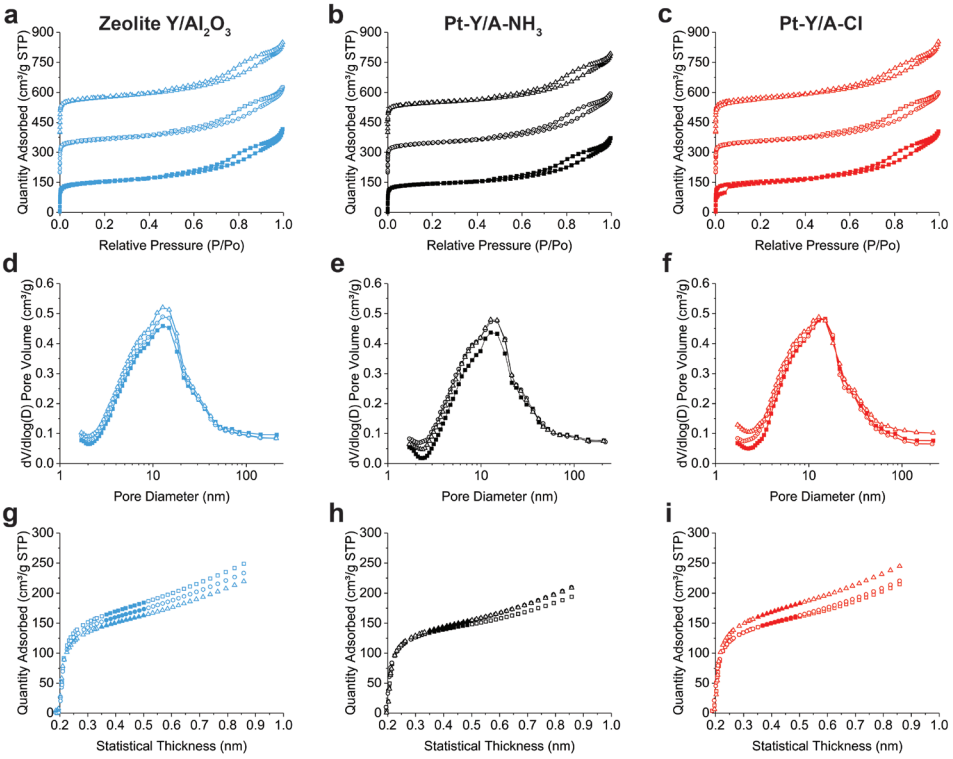

Figure S5.20. Adsorption-desorption isotherms (a-c), BJH pore size distribution (d-f) and the t-plot (g-i) from nitrogen physisorption on the Zeolite Y/γ-Al_2O_3 support (blue), Pt-Y/A-NH_3 (black) and Pt-Y/A-Cl (red) catalysts (both before catalysis) of different particle size. Data from 25-75 µm particles are displayed as filled squares, 75-150 µm are displayed as dotted circles and 150-212 µm particles are displayed as open triangles. Isotherms in a-c of different particle sizes are stacked with intervals of 200 $cm^3 \cdot g^{-1}$.

Table S5.13. Properties and results of textural analysis by nitrogen physisorption of the Zeolite Y/γ-Al_2O_3 support and the Pt-Y/A-NH_3 and Pt-Y/A-Cl catalysts of different particle size.

d_p (µm)	t-plot external surface area ($m^2 \cdot g^{-1}$)	t-plot micropore volume ($cm^3 \cdot g^{-1}$)	BJH pore volume ($cm^3 \cdot g^{-1}$)
	Zeolite Y/γ-Al_2O_3		
25-75	195	0.15	0.46
75-150	210	0.16	0.47
150-212	228	0.17	0.50
	Pt-Y/A-NH_3		
25-75	141	0.16	0.39
75-150	194	0.14	0.45
150-212	179	0.15	0.44
	Pt-Y/A-Cl		
25-75	179	0.16	0.45
75-150	200	0.15	0.45
150-212	234	0.17	0.51

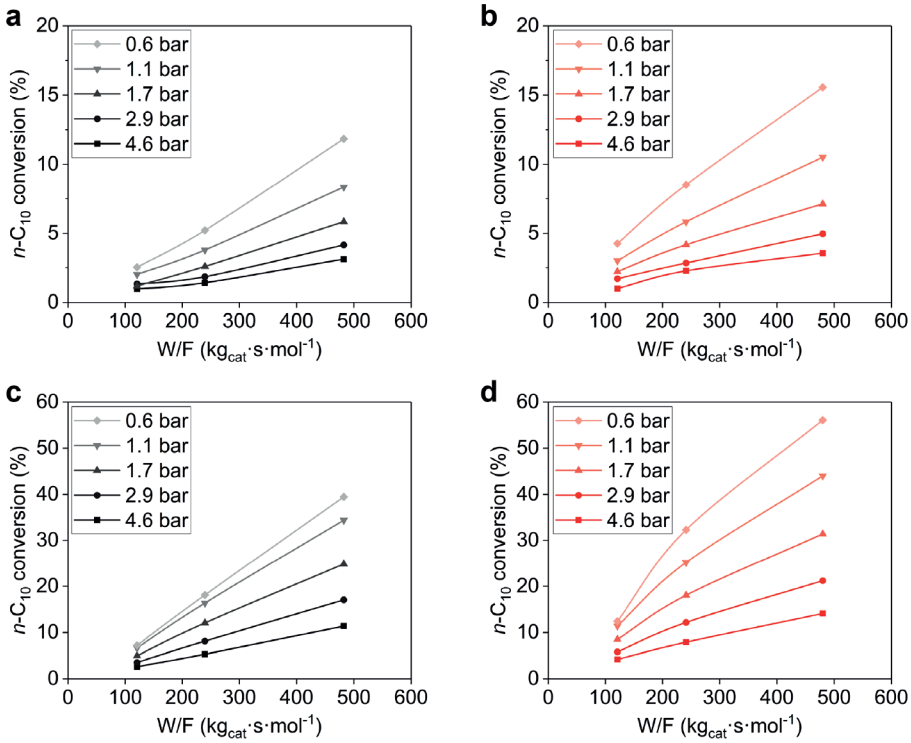

Figure S5.21. The *n*-decane conversion at 180 °C as a function of contact time at the hydrogen partial pressures indicated in the legend for the Pt-Y/A-NH_3 (a) and Pt-Y/A-Cl (b) catalysts and at 200 °C for the same catalysts (c,d). (pressure = 5 bar, d_p = 75-150 μm).

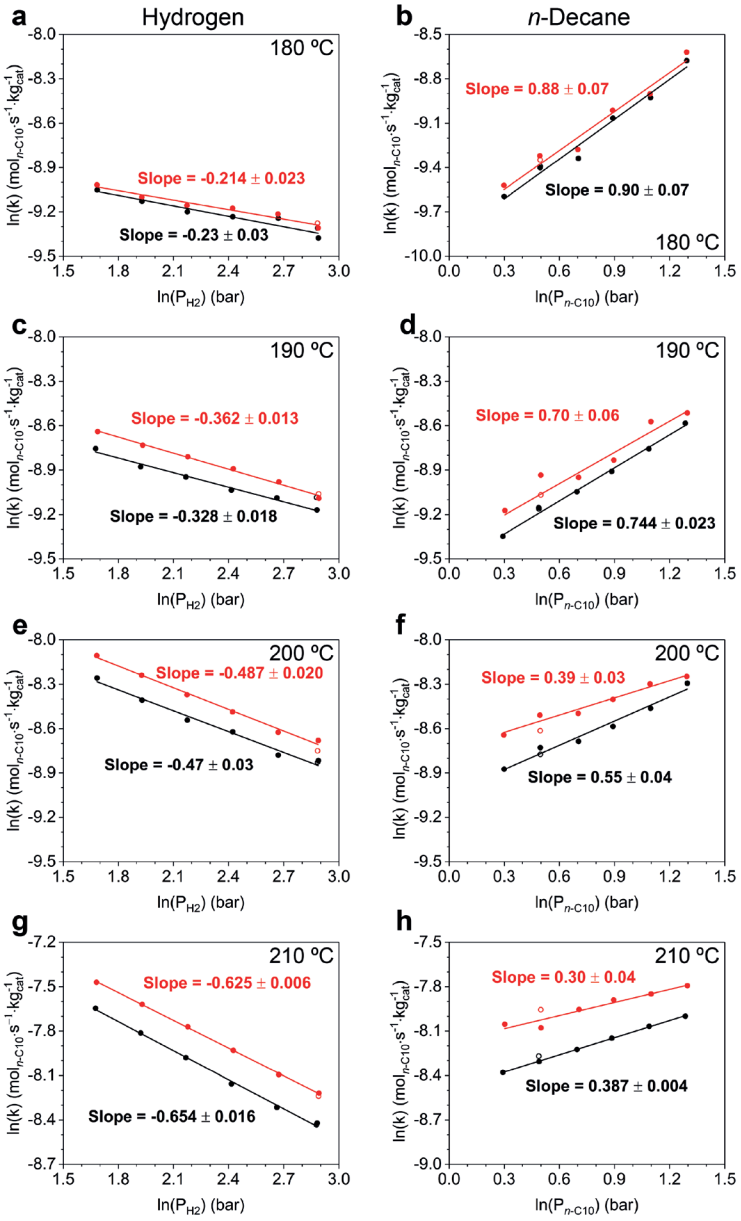

Figure S5.22. Effect of temperature on reaction orders of hydrogen and *n*-decane at 20 bar. Orders in hydrogen were determined at $W_{cat}/F_{n\text{-}C10}$ = 244 kg·s·mol^{-1}, and at hydrogen partial pressures between 5.2-17.6 bar. Orders in *n*-decane were obtained between $W_{cat}/F_{n\text{-}C10}$ = 107-292 kg·s·mol^{-1} and at *n*-decane partial pressures of between 1.3-3.7 bar. Closed symbols indicate datapoints that were used for the fit, whereas open symbols were not used. Open symbols at $\ln(p_{H2})$ = 2.9 or $\ln(p_{HC})$ = 0.5 represent the activity of the back check. While varying the hydrogen partial pressure at higher temperatures catalyst deactivation was encountered, while for experiments where the *n*-decane partial pressure was varied, fluctuations may also result from instabilities in the liquid flow. (d_p = 75-150 µm)

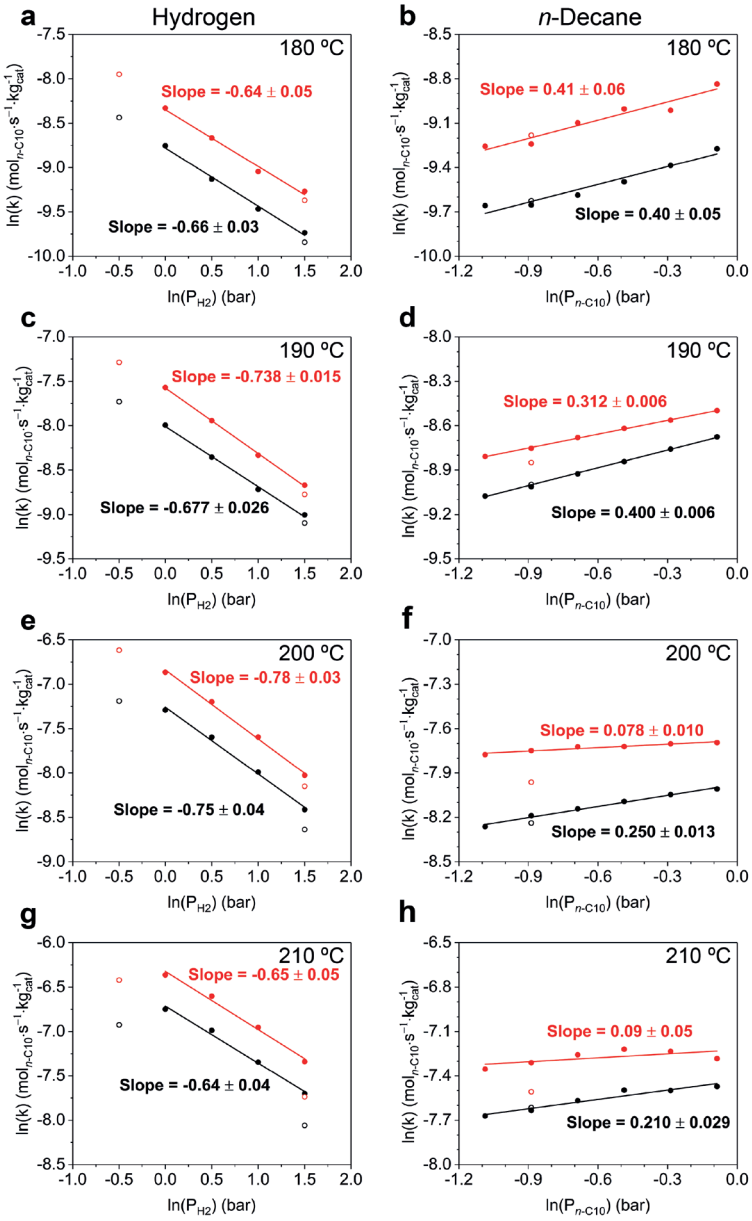

Figure S5.23. Effect of temperature on reaction orders of hydrogen and *n*-decane at 5 bar. Orders in hydrogen were determined at $W_{cat}/F_{n\text{-}C10}$ = 244 kg·s·mol^{-1} and at hydrogen partial pressures between 1.0-4.5 bar, while hydrogen pressures were varied between 0.6-4.5 bar. Orders in *n*-decane were obtained between $W_{cat}/F_{n\text{-}C10}$ = 107-292 kg·s·mol^{-1} and at *n*-decane partial pressures of between 0.3-0.9 bar. Closed symbols indicate datapoints that were used for the fit, whereas open symbols were not used. Open symbols at ln(P_{H2}) = 1.5 or ln($P_{n\text{-}C10}$) = -0.9 represent the activity of the back check. While varying the hydrogen partial pressure at higher temperatures catalyst deactivation was encountered, while for experiments where the *n*-decane partial pressure was varied, fluctuations may also result from instabilities in the liquid flow. (d_p = 75-150 µm)

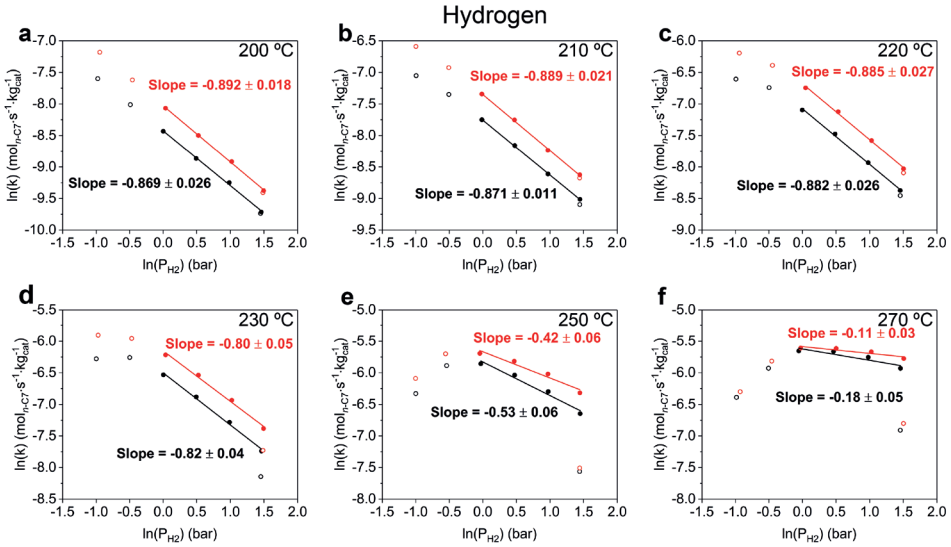

Figure S5.24. Effect of temperature on reaction orders of hydrogen at 5 bar for *n*-heptane hydroisomerization. Orders in hydrogen were determined at $W_{cat}/F_{n\text{-}C7}$ = 244 kg·s·mol^{-1} and at hydrogen partial pressures between 1.0-4.5 bar. Hydrogen pressures were varied between 0.4-4.5 bar. Closed symbols indicate datapoints that were used for the fit, whereas open symbols were not used. Open symbols at ln(p_{H2}) = 1.5 represent the activity measured during the back check. For higher temperatures catalyst deactivation was encountered. (d_p = 75-150 µm)

Chapter 6a

Summary and Outlook

Summary

The topic of this thesis are zeolite based bifunctional catalysts, used for the conversion of hydrocarbons in the presence of hydrogen. The bifunctionality stems from the fact that metal nanoparticles on the surface of the catalyst provide the metal function for (de)hydrogenation, while the zeolite provides acid sites for isomerization and cracking. These catalysts are used for the production of liquid fuels and chemicals in large-scale industrial processes such as hydrocracking and hydroisomerization. Hydrocrackers currently convert approximately 5.6 million barrels of feedstock per day and the process is performed in at least 170 oil refineries around the globe. The feedstock for these processes is mostly derived from fossil resources such as crude oil or Fischer-Tropsch products from natural gas. Bifunctional catalysts can also be applied for the conversion of more sustainable hydrocarbon feedstocks, such as biomass or waste streams. In some cases the feedstocks can be converted directly, or they need to undergo a sequence of processes involving gasification towards synthesis gas, a Fischer-Tropsch process and finally an hydrocracking process.

Zeolite-based bifunctional catalysts generally provide relatively high catalytic activities and typically the lifetime of industrial bifunctional catalysts is excellent, i.e. a batch of hydroisomerization catalyst may operate in a reactor for several years. One of the greatest challenges for zeolite-based catalysts is to optimize mass transport of reactants and products through a catalyst. Molecules reacting in a zeolite micropore may get 'trapped' in the pore structure, resulting in secondary reactions towards undesired cracking products (e.g. Liquefied Petroleum Gas, LPG) or the formation of coke. Ideally, zeolite based catalyst possess a so called hierarchical pore network, consisting of interconnected macro, meso and micropores to allow efficient transport of molecules through the catalyst.

Zeolite crystals may have sizes in the range of a few nanometers (10^{-9} m) and up to a few micrometers (10^{-6} m), and come in the form of powders that cannot be used directly in industrial processes. Zeolite crystals are therefore shaped into millimeter-sized catalyst bodies, providing mechanical strength to the catalyst, enhancing their stability, and preventing high pressure drops in fixed-bed reactors. Catalyst shaping usually also improves the mass-transfer and heat-transfer properties of a zeolite based catalyst. In Figure 6.1, a conceptual overview is provided of the different stages of the preparation of a typical industrial zeolite based bifunctional catalyst. In the first stage the zeolite powder is mixed with a binder precursor and additives (water, peptizer, etc.) followed by extrusion and calcination to obtain composite extrudates.

In the second stage the metal is deposited on the composite support, which is often performed by impregnation with an aqueous metal precursor solution, followed by a heat treatment. The exact catalyst composition and preparation method may differ per catalyst manufacturer and are often part of the intellectual property and/or kept secret.

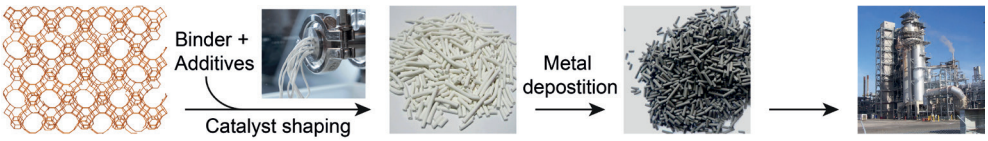

Figure 6.1. Stages in the preparation of an industrial metal-acid bifunctional catalyst.

Bifunctional catalysts (based on zeolite Y), have already been studied for several decades and many fundamental studies on these catalysts have appeared too. The reaction mechanism for the conversion of *n*-alkanes on bifunctional catalysts is considered to be well understood and usually referred to as the 'classical bifunctional mechanism'. Several studies have focused on the effect of the ratio between metal and acid sites, or the maximal distance between sites required for efficient transport of reaction intermediates between sites for optimal catalytic performance. The intimacy criterion for bifunctional catalysts, proposed by Paul B. Weisz in 1962, can be used to predict the maximal distance (often referred to as intimacy) between metal and acid sites when the reaction conditions, rate of reaction and intermediate diffusivity are known. Usually quantification of the criterium leads to distances within the micrometer length scale (1-1000 μm) and is often interpreted as 'the closer the better'. However, a number of recent studies on zeolite based bifunctional catalysts suggest that locating metal nanoparticles within a zeolite crystal, providing a very close intimacy between metal and acid sites, is detrimental for the catalytic performance.

In **Chapter 1**, a more extensive introduction to bifunctional catalysis is provided, as well as a general introduction on catalysis and zeolites.

The research described in this thesis is focused on the proximity between metal and acid sites in Pt/zeolite/γ-Al_2O_3 composite catalysts. Throughout this thesis, the metal function was provided by Pt nanoparticles, that are either located in the zeolite component or on the γ-Al_2O_3 component of zeolite/γ-Al_2O_3 composite supports. By doing so, the average distance between metal and zeolite acid sites is varied at the nanoscale rather than at the micrometer scale, as in earlier studies. Selective deposition of the metal function was obtained by using a cationic Pt complex: $[Pt(NH_3)_4]^{2+}$ (aq), to selectively deposit Pt in zeolite crystals, whereas electrostatic adsorption of an anionic Pt complex, $[PtCl_6]^{2-}$ (aq), was used to selectively deposit Pt on the γ-Al_2O_3 component.

In **Chapter 2**, a study is presented on the location of Pt nanoparticles within composite Zeolite Y-based catalysts. Results from Transmission Electron Microscopy (TEM) are compared with characterization techniques that sample multiple orders larger amounts of sample. Quantitative X-ray Photoelectron Spectroscopy (XPS), CO infrared spectroscopy and catalysis with probe molecules, were successfully employed to provide information on the location of Pt nanoparticles.

In **Chapter 3**, the effects of zeolite micropore size and metal-acid intimacy were studied by using composite supports based on zeolites of different micropore size: ZSM-5, Zeolite Beta and Zeolite Y. Besides composite supports, the effect of metal-acid intimacy was extended towards the microscale range by using physical mixtures of zeolite and Pt/γ-Al_2O_3. It was revealed that locating Pt nanoparticles on the binder for 12 membered ring zeolites (Zeolite Beta, Zeolite Y) had a positive effect on catalytic activity and isomer selectivity whereas for the 10 membered ring ZSM-5 based catalysts, it was only beneficial for catalytic activity.

In **Chapter 4**, the effect of residual chlorine from the Pt precursor $H_2PtCl_6 \cdot 6H_2O$ on zeolite Y-based composite catalysts was studied. Heat treatments at different temperatures either in a flow of 'dry' or water-rich hydrogen were successfully used to regulate the chlorine content on the catalysts. NH_3-temperature programmed desorption revealed an increased ammonia uptake for catalysts

with higher chlorine contents, while infrared spectroscopy indicated the loss of hydroxyl surface groups by the substitution of OH with Cl. However, in *n*-alkane hydroisomerization experiments no effect of the residual chlorine was observed, and therefore it was concluded that acidity as a consequence of chlorine was too weak to act as Brønsted acid site under the conditions of *n*-alkane hydroisomerization and thus chlorine had not interfered in previous proximity studies.

In **Chapter 5**, a preliminary kinetic study was performed on Pt/zeolite Y/γ-Al_2O_3 catalysts wherein the effects of contact time, temperature, pressure, orders in hydrogen and *n*-alkane, catalyst grain size and the location of Pt nanoparticles were studied for the hydroisomerization of *n*-decane and *n*-heptane. A higher total pressure led to a lower catalytic activity, that was indicative of an 'ideal' hydroisomerization process. For catalysts with Pt nanoparticles in the zeolite component, the selectivity towards isomers was dependent on catalyst grain size, whereas for catalysts with Pt nanoparticles located on the γ-Al_2O_3 component no effect of the selectivity of the catalysts was observed. Activation energies and orders in hydrogen and *n*-alkane are reported and did not strongly depend on the location of Pt nanoparticles.

In summary, the work in this thesis explores the effects of the proximity of metal and acid sites at the nanoscale for zeolite based composite catalysts. It was proven that by using either of two different Pt-precursors for catalyst synthesis, Pt could be selectively deposited on the zeolite or on the γ-Al_2O_3 component of a composite support, with limited heterogeneities within samples. A positive effect on the isomer selectivity for Pt nanoparticles located on the γ-Al_2O_3 binder could be confirmed, and was extended to other zeolites and physical mixtures. For short-chain alkanes having relatively high diffusivities, the proximity between metal and acid sites was less important than for long-chain alkanes, but still relevant. Moreover, possible side-effects of residual chlorine from the Pt-precursor on the catalytic performance could be excluded. Overall, the results point to enhanced cracking for composite catalysts based on large pore zeolites and Pt nanoparticles located in zeolite crystals. The insights from the work in this thesis provide guides to further optimize current industrial catalysts, whereas also strategies and clues for future studies are provided.

Outlook

The majority of academic studies on heterogenous catalysts is focused on nanoscale phenomena on research catalyst, that have limited similarities with catalysts used in industrial processes. Typical research catalysts studied in academia usually come in the form of fine powders and consist of a few elemental components. Industrial catalysts typically consist of several components and possess a macroscopic structure, i.e. they are usually shaped into a catalyst bodies such as extrudates. Upon studying more practical catalyst in an academic research environment, that is fully adapted to research catalysts, a number of hurdles can be encountered during catalyst preparation, characterization and catalyst testing. For example, to prepare extrudates in a lab, a laboratory mixer and extruder may be required, while metal deposition methods that are optimized for powders may not be suitable for catalyst bodies, or need to be adapted. Furthermore, catalyst bodies likely fail to meet plug flow criteria in calcination and catalytic reactors designed for powders, or depending on their size, may not even fit in millimeter-sized reactor tubes of some laboratory setups. For the work described in this thesis, these issues are largely circumvented by grinding extrudates of approximately 1 centimeter in size (Figure 6.2. a) into grains of a few hundred micrometer (Figure 6.2 b). Working with composite grains allows synthesis, characterization and catalytic testing in a similar fashion as for research catalysts, while having a closer similarity to industrial catalysts. However, grinding catalysts bodies also inevitably compromises the direct relevance of these findings for industrial catalysts. Composite catalysts in grain form can therefore be regarded as an 'hybrid' between research catalysts and industrial catalysts. Studies on catalyst bodies are relatively rare in academia, and may require some innovations in catalyst preparation and characterization. A nice solution is the possibility to study catalysts bodies in a so called "single-pellet-string reactor", wherein cylindrical catalyst bodies are stacked in the longitudinal direction in a laboratory reactor, that has a diameter of a few millimeters (Figure 6.2. c).[1] For example, the findings in Chapter 5, wherein a related effect was found between the location of Pt nanoparticles within a Zeolite Y/γ-Al_2O_3 composite support and the catalyst grain size call for further research focused on such phenomena. It is recommended

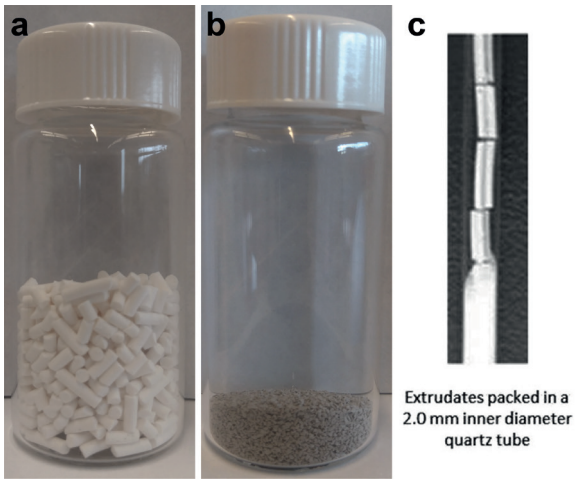

Figure 6.2. Zeolite Y/γ-Al_2O_3 composite in extrudate form (a), and Pt/Zeolite Y/γ-Al_2O_3 catalysts in grain form (b). A single-pellet-string reactor wherein cylindrical catalyst bodies are stacked in the longitudinal direction (c). The image in (c) was obtained from [1].

that in future studies also catalysts bodies are included, preferably in their 'true' industrial form.

The understanding of the effects observed in Chapter 5 could be further enhanced by development of a (micro)-kinetic model, wherein the elemental reaction steps can be unraveled causing the differences in catalytic performance. Such a modelling effort for the first time would need to include the transport of alkenes in zeolites. Transport of alkenes has been studied a lot in zeolites but alkenes are 'sticky' with respect to acid sites and diffusion models are considered to be much more complex.

In this thesis, a number of characterization methods were applied to study the location of metal nanoparticles Pt/Zeolite Y/γ-Al_2O_3 composite catalysts (Chapter 2). A drawback of this catalysts for XPS is that the Pt 4f peaks overlaps with Al 2s peak, which has an much higher intensity. This complicates quantification of the contributions of different core lines. In future studies aiming to use quantitative XPS for determining the location of metal nanoparticles in microporous supports, platinum could be replaced with another metal, such as palladium, which does not suffer from peak overlap. Another possibility is to enhance the signal intensities in resonant photoemission experiments at a synchrotron. Besides XPS, also X-ray Absorption Spectroscopy techniques such as Resonant Inelastic X-ray Spectroscopy can be applied to provide information on Pt nanoparticle location. Catalyis with probe molecules may also provide information on the location of metal nanoparticles. In Chapter 2, hydrogenation of β-phenylcinnamaldehyde was used and it was observed that β-phenylcinnamaldehyde may undergo side reactions on zeolite acid sites. For future studies, finding probe reactions with reactants that are inert to acid sites are therefore preferred but are somewhat scarce. An overview of probe reactions that can be used to determine the location of metal nanoparticles in microporous supports, used in recent literature was published by Cho et al..[2]

The catalysts prepared in this thesis, were prepared with ion adsorption/exchange synthesis techniques, enabling control over the location of metal nanoparticles and generally good metal dispersions. The downside of these synthesis techniques is that it provides a limited control over the final metal loading, which may be limited by the uptake capacity of the catalysts support. For this thesis, platinum weight loadings were determined by ICP measurements after sample destruction. Destruction of silicate materials typically involves treatments with hydrofluoric acid and due to the risks involved and the specialized nature of the analysis, these measurements where outsourced to a commercial analytical laboratory. Besides ICP, alternative methods to determine the metal loading were explored, that were based on determining the concentration of Pt precursor in the filtrate after ion exchange and washing procedures. When the total volume of the filtrate is known, the intake of Pt precursor can be corrected for the Pt concentration of the filtrate. Figure 6.3, shows an example of a relatively simple test that can be performed by UV-VIS spectroscopy, using the absorption maximum at 198.5 nm of $[Pt(NH_3)_4]^{2+}$ (aq). The platinumtetraamine concentrations used for ion-exchange procedures fell within the linear range of the calibration curve. The $[PtCl_6]^{2-}$ (aq) complex absorbs less strongly in the UV-VIS range and this method is not suitable for this complex, while quantification is further complicated by the limited stability of this complex in water. AAS or ICP could be used as alternative methods for determining the concentration of the dissolved metal precursor, but usually require more preparation time. Development of such methods, possibly complementary to direct sample

analysis, can be useful for studies on the effect of metal to acid site ratio where very low and precise metal weight loadings are required.

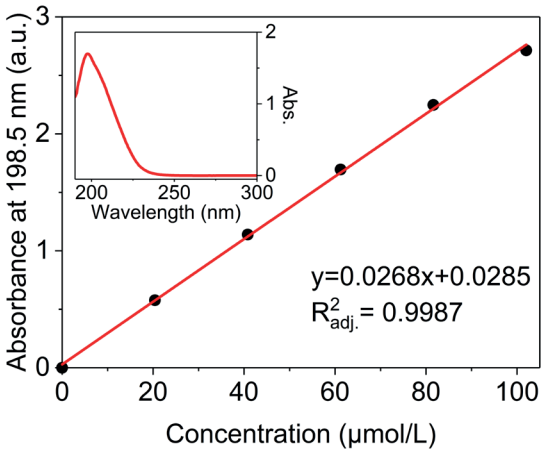

Figure 6.3. Calibration curve of the absorbance at 198.5 nm versus $[Pt(NH_3)_4]^{2+}$ (aq) concentration. Insert shows the absorption spectrum of a 60 μmol/L solution of $[Pt(NH_3)_4]^{2+}$ (aq).

References

[1] R. Moonen, J. Alles, E. J. Ras, C. Harvey, J. A. Moulijn, Chem. Eng. Technol. 2017, 40, 2025–2034.

[2] H. J. Cho, D. Kim, J. Li, D. Su, B. Xu, J. Am. Chem. Soc. 2018, 140, 13514–13520.

Chapter 6b

Nederlandse samenvatting

Nederlandse Samenvatting

Het onderwerp van dit proefschrift betreft bifunctionele katalysatoren (katalysatoren met twee katalytische functies) die gebaseerd zijn op zeolieten. De katalytisch actieve plekken op zeolieten (sites) zijn de zure functie van deze katalysatoren, en de metaalfunctie wordt geleverd door metaalnanodeeltjes die aanwezig zijn op het oppervlak van de katalysator. Dit type bifunctionele katalysatoren wordt gebruikt voor de omzetting van koolwaterstoffen in de aanwezigheid van waterstofgas. Koolwaterstoffen zijn moleculen die bestaan uit de elementen koolstof en waterstof en kennen zeer veel verschillende toepassingen, zoals brandstoffen of smeermiddelen. Bifunctionele katalysatoren worden gebruikt voor de productie van vloeibare brandstoffen en chemicaliën in grote industriële processen, zoals hydrokraken en hydroisomerisatie. Bijvoorbeeld, in hydrokraakprocessen worden per dag wereldwijd ongeveer 5.6 miljoen vaten olie omgezet, en dit proces word in ten miste 170 raffinaderijen ter wereld uitgevoerd. De grondstoffen voor deze processen zijn over het algemeen afgeleid van fossiele bronnen zoals aardolie of Fischer-Tropsch producten (ook wel Gas to Liquid producten genoemd) die worden gemaakt uit aardgas. Bifunctionele katalysatoren kunnen ook gebruikt worden voor de omzetting van meer duurzame grondstoffen zoals biomassa of afvalstromen. Deze grondstoffen kunnen in enkele gevallen direct omgezet worden, of worden verwerkt in een keten van processen. In het laatste geval worden de grondstoffen eerst vergast (omgezet naar koolmonoxide en waterstof), gevolgd door een Fischer-Tropsch proces en hydrokraken.

Zeolieten zijn microporeuze (poriën kleiner dan 2 nm) kristallijne materialen, bestaande uit alumina (Al_2O_3) en silica (SiO_2). Op zeoliet gebaseerde bifunctionele katalysatoren hebben over het algemeen een hoge katalytische activiteit, en de levensduur van industriële katalysatoren is vaak zeer lang. Ter illustratie, dezelfde lading katalysator kan voor meerdere jaren gebruikt worden in een industriële reactor voor hydroisomerisatie. Een van de grootste uitdagingen voor zeoliet gebaseerde katalysatoren is het optimaliseren van het massatransport van reactanten en producten door de katalysator. Moleculen die reageren in een microporie van het zeoliet kunnen vast komen te zitten, wat resulteert in volgreacties naar ongewenste kraakproducten (zoals gasvormige producten) of de vorming van kool. Idealiter beschikken zeoliet gebaseerde katalysatoren over een hiërarchische poriestructuur van poriën van verschillende grootte. Een onderling verbonden netwerk van macro-, meso- en microporiën maakt efficiënt transport van moleculen door de katalysator mogelijk.

Zeolietkristallen variëren in grootte van enkele nanometers (10^{-9} m) tot elke micrometers (10^{-6} m) en hebben de vorm van poeders die niet direct toegepast kunnen worden in industriële processen. Zeolietkristallen worden daarom verwerkt tot katalysatordeeltjes met een macroscopische structuur, wat de stabiliteit van de katalysator verhoogd, terwijl hoge drukvallen in reactoren

Figuur 6.4. De verschillende stappen van de bereiding van industriële metaal-zure bifunctionele katalysatoren.

met een vast katalysator-bed worden voorkomen. In Figuur 6.4. is een vereenvoudigd overzicht te zien van de verschillende bereidingstappen van een industriële katalysator. In de eerste stap wordt zeoliet-poeder gemengd met de voorloper van een binder en enkele additieven zoals water en een peptiseermiddel, gevolgd door extrusie en calcinatie om uiteindelijk extrudaten te verkrijgen. In de tweede stap wordt het metaal afgezet op de katalysator, wat over het algemeen uitgevoerd wordt door impregnatie met een oplossing van een metaalprecursor, gevolgd door een hittebehandeling. De exacte samenstelling en preparatiemethode kunnen verschillen per katalysatorfabrikant en zijn vaak onderdeel van het intellectuele eigendom en worden soms geheimgehouden.

Bifunctionele katalysatoren (gebaseerd op zeoliet Y), worden al decennia lang onderzocht en veel fundamentele studies zijn reeds uitgevoerd. Het reactiemechanisme voor de conversie van *n*-alkanen wordt over het algemeen bekend verondersteld en wordt daarom ook wel het klassieke bifunctionele mechanisme genoemd. Overige studies hebben het effect van de ratio van metallische en zure sites onderzocht en de maximale afstand tussen katalytische sites die acceptabel is voor efficiënt transport van tussenproducten voor optimale katalytische prestaties. Het zogenaamde nabijheids criterium ('intimacy criterion'), opgesteld door Paul B. Weisz rond 1960, kan gebruikt worden om de maximale afstand tussen metaal en zure sites te voorspellen bij bekende reactie omstandigheden, diffusiecoëfficiënt van tussenproducten en bekende reactiesnelheid. Over het algemeen is die maximale afstand in de orde van micrometers (1-1000 μm). Een aantal recente studies suggereren echter dat het plaatsen van metaalnanodeeltjes in het zeoliet, met een gemiddelde afstand van enkele nanometers tussen metallische en zure sites, schadelijk is voor de katalytische prestaties.

In **Hoofdstuk 1** van dit proefschrift word een introductie gegeven over het maatschappelijk belang van katalyse en worden de begrippen katalyse, zeolieten en bifunctionele katalysatoren meer uitgebreid geïntroduceerd.

Het onderzoek wat beschreven is in dit proefschrift gaat over de locatie van de metaalfunctie in Pt/zeoliet/γ-Al_2O_3 composiet katalysatoren. Voor de katalysatoren beschreven in deze dissertatie zijn Pt nanodeeltjes de metaal functie, die of in het zeoliet zitten of op de γ-Al_2O_3 component is aangebracht. Hierdoor wordt de gemiddelde afstand tussen metallische en zure sites van het zeoliet gevarieerd op de nanoschaal. Selectieve depositie van de metaal functie in het zeoliet werd verkregen door een kationisch Pt complex te gebruiken, $[Pt(NH_3)_4]^{2+}$ (aq) wat geadsorbeerd werd door ionenuitwisseling met protonen van het zeoliet, terwijl elektrostatische adsorptie van een anionisch Pt complex, $[PtCl_6]^{2-}$ (aq) gebruikt werd om Pt op de γ-Al_2O_3 component af te zetten.

In **Hoofstuk 2**, is een studie beschreven waarin verschillende karakterisatie methodes worden gebruikt om de locatie van Pt nanodeeltjes in Pt/zeoliet Y/γ-Al_2O_3 katalysatoren vast te stellen. Resultaten van Transmissie Elektronen Microscopie zijn vergeleken met technieken die enkele ordes van grootte hogere hoeveelheid katalysator bestuderen per meting. Kwantitatieve X-ray Photoelectronen Spectroscopie, CO infraroodspectroscopie en katalytische reacties konden succesvol worden gebruikt voor het vaststellen van de locatie van Pt nanodeeltjes in de katalysatoren. Uit de resultaten bleek dat Pt selectief kon worden afgezet op het zeoliet of op de γ-Al_2O_3 component, met slechts beperkte heterogeniteit per katalysator.

In **Hoofdstuk 3**, werden de effecten van de locatie van Pt nanodeeltjes en de grootte van de zeoliet microporiën onderzocht voor hydroisomerisatie van *n*-heptaan. Hierbij werden samengestelde dragermaterialen gebruikt bestaande uit zeoliet en γ-Al_2O_3, die gebaseerd waren op drie verschillende zeolieten: ZSM-5, zeoliet Beta en zeoliet Y. Daarnaast werd het effect van nabijheid tussen metallische en zure sites ook bestudeerd op de micrometerschaal door fysische mengsels te gebruiken van zeoliet poeders en Pt/γ-Al_2O_3. Door Pt nanodeeltjes op het γ-Al_2O_3 te plaatsen gecombineerd met zeolieten met relatief grote microporiën (zeoliet Beta, zeoliet Y) leverde positieve effecten op de katalytische activiteit en selectiviteit naar isomeren, terwijl voor een zeoliet met kleinere microporiën (ZSM-5) alleen een verhoogde katalytische activiteit werd waargenomen.

In **Hoofdstuk 4**, werden de effecten van kleine hoeveelheden chloor afkomstig van de Pt-verbinding, $H_2PtCl_6 \cdot 6H_2O$, op de katalysator onderzocht. Hitte behandelingen op verschillende temperaturen, ofwel in een stroom van waterstofgas of mengsels van waterdamp en waterstofgas, werden toegepast om het chloorgehalte op de katalysator te reguleren. Desorptie metingen van NH_3 duidden op een verhoogde opname van ammoniak voor katalysatoren met een hoger chloorgehalte, terwijl met infraroodspectroscopie het verlies van hydroxyl groepen werd bevestigd door substitutie met chloor. Desondanks werden in hydroisomerisatie experimenten geen effecten van de kleine hoeveelheden chloor gevonden, wat leidde tot de conclusie dat zuurheid als gevolg van chloor te zwak is om als zure site te functioneren in de condities van hydroisomerisatie van *n*-alkanen. Hiermee werd uitgesloten dat kleine hoeveelheden chloor een rol speelden in deze en voorgaande studies naar het effect van de nabijheid van metallische en zure sites.

In **Hoofdstuk 5** is een studie beschreven over de kinetiek van de conversie van *n*-alkanen over Pt/zeoliet Y/γ-Al_2O_3 katalysatoren waarin de effecten van contacttijd, temperatuur, druk, ordes in waterstof en *n*-alkaan, katalysatorkorrelgrootte en locatie van Pt nanodeeltjes werden onderzocht. Een hogere totale druk leidde tot een lagere katalytische activiteit, wat duidde op een zogenaamd 'ideaal' hydroisomerisatie proces. Voor katalysatoren met Pt nanodeeltjes in de zeoliet bleek dat de selectiviteit naar isomeren afhankelijk was van de korrelgrootte, terwijl voor katalysatoren met Pt nanodeeltjes op γ-Al_2O_3 geen effecten van korrelgrootte op de selectiviteit werden gevonden. Activeringsenergieën en ordes in waterstof en *n*-alkaan die werden bepaald, bleken niet afhankelijk te zijn van de locatie van Pt nanodeeltjes in de katalysatoren.

De resultaten in dit proefschrift beschrijven de effecten van de nabijheid tussen metallische en zure sites in samengestelde bifunctionele katalysatoren, bestaande uit zeoliet, γ-Al_2O_3 en Pt. Door één van twee Pt-complexen te gebruiken kon Pt selectief kon worden afgezet, of in het zeoliet of op de γ-Al_2O_3 component, met slechts beperkte heterogeniteit per katalysator. Verder werd een positief effect op de selectiviteit naar isomeren voor katalysatoren met Pt nanodeeltjes op de γ-Al_2O_3 component uitgebreid naar meerdere zeolieten en fysische mengsels. Voor relatief korte alkanen, die relatief snel diffunderen, waren effecten van de nabijheid tussen metallische en zure sites minder cruciaal, maar wel relevant. Verder konden mogelijke neveneffecten van chloor afkomstig van het toegepaste Pt-complex op de katalyse worden uitgesloten. Concluderend kan worden gesteld dat kraak reacties meer voorkomen voor composiet katalysatoren met Pt nanodeeltjes in zeoliet kristallen. De inzichten die voortkomen uit de resultaten in dit proefschrift

kunnen worden gebruikt voor het verder verbeteren van huidige industriële katalysatoren. Bovendien kunnen de methodes en resultaten uit deze thesis gebruikt worden voor vervolg studies naar bifunctionele katalysatoren voor andere toepassingen.

List of Publications

This thesis is based on the following publications:

Chapter 2: Assessment of the location of Pt nanoparticles in Pt/Zeolite Y/γ-Al_2O_3 composite catalysts
Jogchum Oenema, Jan P. Hofmann, Emiel J.M. Hensen, Jovana Zečević, Krijn P. de Jong, *ChemCatChem* 12, 2020, 2, 615-622.

Chapter 3: Influence of Nanoscale Intimacy and Zeolite Micropore Size on the Performance of Bifunctional Catalysts for *n*-Heptane Hydroisomerization
Jogchum Oenema, Justine Harmel, Roxana Pérez Vélez, Mark J. Meijerink, Willem Eijsvogel, Ali Poursaeidesfahani, Thijs J.H. Vlugt, Jovana Zečević, Krijn P. de Jong, *ACS Catalysis* 10, 2020, 23, 14245-14257.

Chapter 4: Influence of Residual Chlorine on Pt/γ-Al_2O_3/Zeolite Y Bifunctional Catalysts: Acidity and Performance
Jogchum Oenema, Renée A. van Alst, Mark J. Meijerink, Jovana Zečević, Krijn P. de Jong, *Applied Catalysis A: General A.* 605, 2020, 117815.

Chapter 5: Kinetic Analysis of the Conversion of *n*-Alkanes on Pt/Zeolite Y/γ-Al_2O_3 Catalysts: Effect of Catalyst Grain Size and Pt Nanoparticle Location
Jogchum Oenema, Lars. I van der Wal, Krijn P. de Jong, *in preparation.*

Other publications:

Vapor Phase Impregnation of Platinum(II)Acetylacetonate for the Preparation of Bifunctional Pt/Zeolite Y Catalysts for the Hydroisomerization of *n*-Hexadecane
Lars I. van der Wal, Jogchum Oenema, Luc C. J. Smulders, Hideto Yoshida, Robby van der Pluijm, Jovana Zečević, Krijn P. de Jong, *in preparation*

Maximizing platinum utilization in hydroisomerization of *n*-alkanes by nanoscale arrangement of metal and acid sites
Kang Cheng, Lars I. van der Wal, Jogchum Oenema, Luc C. J. Smulders, Glenn Sunley, Tegan Roberts, Zhuoran Xu, Eric Doskocil, Hideto Yoshida, Jovana Zečević, Petra E. de Jongh and Krijn P. de Jong, *submitted*

Impact and Control of Metal Heterogeneities on the Catalytic Performance of Pt/Zeolite Y Bifunctional Catalysts
Lars I. van der Wal, Jogchum Oenema, Luc C.J. Smulders, Nonne J. Samplonius, Karan R. Nandpersad, Jovana Zečević, Krijn P. de Jong, *ACS Catalysis* 11, 2021, 3842-3855.

Impact of the Spatial Organization of Bifunctional Metal-Zeolite Catalysts for Hydroisomerization of Light Alkanes
Kang Cheng, Lars I. van der Wal, Hideto Yoshida, Jogchum Oenema, Justine Harmel, Zhaorong Zhang, Glenn Sunley, Jovana Zečević, Krijn P. de Jong, *Angewandte Chemie* 59, 2020, 9, 3592-3600.

Effects of noble metal promotion for Co/TiO_2 Fischer-Tropsch catalysts
Thomas O. Eschemann, Jogchum Oenema, Krijn P. de Jong, *Catalysis Today* 261, 2016, 60-66.

Oral presentations

Controlling the Location of Pt Nanoparticles in Pt/Al_2O_3/Zeolite Composite Catalysts: Impact on Performance and Tools for Assessment of Location
Jogchum Oenema, Justine Harmel, Jan Philipp Hofmann, Emiel J.M. Hensen, Jovana Zečević, Krijn P. de Jong, 14th European Congress on Catalysis (EuropaCat 2019), Aachen, Germany (August 2019)

Controlling the Location of Pt Nanoparticles in Pt/Al_2O_3/Zeolite Composite Catalysts: Impact on Performance and Tools for Assessment of Location
Jogchum Oenema, Justine Harmel, Jan Philipp Hofmann, Emiel J.M. Hensen, Jovana Zečević, Krijn P. de Jong, 26th North American Catalysis Society Meeting (NAM26), Chicago, United States (June 2019)

Influence of intimacy and micropore size on the catalytic performance of bifunctional catalysts
Jogchum Oenema, Justine Harmel, Jovana Zečević, Krijn P. de Jong, 20th Netherlands' Catalysis and Chemistry Conference (NCCC), Noordwijkerhout, The Netherlands (March 2019)

Identifying the location of Pt nanoparticles in a Pt/Al_2O_3/zeolite Y catalyst
Jogchum Oenema, Jan Philip Hofmann, Emiel M.J. Hensen, Jovana Zečević, K.P. de Jong, 19th Netherlands' Catalysis and Chemistry Conference (NCCC), Noordwijkerhout, The Netherlands (March 2018)

Poster presentations

The influence of residual chlorine on $Pt/\gamma\text{-}Al_2O_3$/zeolite Y bifunctional catalysts: Acidity and Performance
Jogchum Oenema, Renée A. van Alst, Jovana Zečević, Krijn P. de Jong, 21th Netherlands' Catalysis and Chemistry Conference (NCCC), Noordwijkerhout, The Netherlands, (March 2020)

Effects of Pt nanoparticle location on selectivity in *n*-heptane hydroisomerisation
Jogchum Oenema, Justine Harmel, Roxana Pérez Vélez, Ali Poursaeidesfahani, Thijs J.H. Vlugt, Jovana Zečević, Krijn P. de Jong, CHAINS 2018 (6th edition), Veldhoven, The Netherlands (December 2018)

Effects of Pt nanoparticle location on selectivity in *n*-heptane hydroisomerisation
Jogchum Oenema, Justine Harmel, Roxana Pérez Vélez, Ali Poursaeidesfahani, Thijs J.H. Vlugt, Jovana Zečević, Krijn P. de Jong, Dutch Zeolite Association meeting, Amsterdam, The Netherlands (October 2018)

Identifying the location of Pt nanoparticles in Pt/Al_2O_3/Zeolite Y catalysts
Jogchum Oenema, Jan Philip Hofmann, Emiel M.J. Hensen, Jovana Zečević, K.P. de Jong, 12th International Symposium on the "Scientific Bases for the Preparation of Heterogeneous Catalysts" (PREPA12), Louvain-La-Neuve, Belgium (July 2018)

Identifying the location of metal nanoparticles in composite supports
Jogchum Oenema, Jan P. Hofmann, Emiel J.M. Hensen, Jovana Zečević, Krijn P. de Jong, 18th Netherlands' Catalysis and Chemistry Conference (NCCC), Noordwijkerhout, The Netherlands, (March 2017)

Acknowledgements | Dankwoord

Deze thesis markeert het einde van 4.5 jaar als PhD bij de vakgroep Anorganische Chemie en Katalyse. Ik beschouw dit als een zeer leerzame en waardevolle periode waarvoor ik graag meerdere mensen wil bedanken.

Krijn, allereest wil ik jou bedanken als promotor, zowel voor de mogelijkheid die je mij hebt gegeven om een promotie te kunnen doen in jouw onderzoeksgroep en voor de betrokken begeleiding. Het was fijn dat er altijd de mogelijkheid was om snel nieuwe of onverwachte resultaten te bespreken en ook de adviezen voor het geven van presentaties op conferenties waren zeer behulpzaam. Furthermore, I would like to thank Jovana for the very hands-on introduction on preparing and studying zeolite based catalyst. Since my PhD project directly resulted from your own PhD, it was really useful to have you as a supervisor from the start.

I also would like to thank Baira, Peter Ngene and Petra de Jongh for all the useful discussions, such as during team meetings, and for the support in supervision of students projects.

Within ICC, I was very grateful to be part of the 'Bifunctional team' that has operated very successfully due to a good and diverse mixture of both base players and substitute players. Bengisu, Hideto, Jovana, Justine, Kang, Krijn, Lars, Lennart, Luc, Mark, Roxana, many thanks for the very useful discussions and productive collaborations over the past years.

Lars en Mark wil ik graag zeer bedanken voor de vele TEM plaatjes die ze voor mij hebben gemaakt de afgelopen jaren. De resultaten van de samenwerking vormt een zeer waardevolle contributie voor deze thesis. Daarnaast was voor het succesvol lokaliseren van Pt nanodeeltjes met TEM, ultramicrotomie cruciaal en hiervoor wil ik graag Hans en Chris bedanken. Zowel voor de instructies als voor het regelen van praktische zaken, zoals ervoor zorgen dat de diamantmessen weer op tijd geslepen waren.

I would also like to thank the several members of the 'Flowrence team' for keeping the unit in operation for most of the time and for their contributions to realize the revamp. Allereerst Tom, zeer bedankt voor het geduldig uitleggen van werking van de Flowrence en het deskundig beantwoorden van mijn vele vragen. Also the support from Lennart was very useful to solve several technical problems on the Flowrence. Daarnaast wil ik ook graag Carlos, Justine, Kang, Lars, Luc, Nynke, Roxana en Dennie en Jan Willem bedanken voor de hulp tijdens de maintenance weeks en technische assistentie. Ook de hulp van de leden van het Flowrence II Team: Rolf, Remco, Nienke, Laura was vaak zeer nuttig. Aan de kant van Avantium zou ik ook graag Alexander, Robin Jastrzebski en Wilfred willen bedanken voor hun inzet die resulteerde in de succesvolle aanpassingen aan de Flowrence.

Van de technische staf wil ik graag Ad van der Eerden, Ad Mens, Dennie, Fouad, Herrick, Pascal, Oscar, Jan Willem, Dennie, Marjan, Jochem Wijten, Joris, Ramon bedanken het beantwoorden van vele vragen en verzoeken in de afgelopen jaren. Ad en Otto wil ik in het bijzonder bedanken voor alle hulp voor het ontwerpen en produceren van een nieuwe degelijke press tool, en voor het feit jullie uiteindelijk meer geduld hadden met oplossen van dit probleem dan ikzelf.

Verder wil ik graag Dymph, Ilonka, Iris en Monique bedanken voor het afhandelen van vele diverse administratieve taken in de afgelopen jaren. Jullie zijn absoluut een onmisbare schakel

voor het draaiende houden van de groep.

Ik beschouw het als een voorrecht dat ik tijdens mijn PhD meerdere master studenten heb mogen begeleiden. Tijdens het onderzoekproject van Renée was het een uitdaging om de mogelijke het effecten van chloor inzichtelijk te maken, hoewel we al vermoedden dat er geen effecten op de katalyse waren. Ik denk dat het uiteindelijk goed gelukt is om dit overtuigend aan te tonen wat heeft geresulteerd in hoofdstuk 4. De positieve reacties en vaak terugkerende vragen op o.a. conferenties geven aan het erg gewaardeerd wordt dat dit onderzocht is. Ook de resultaten van het synthese project van Robby - in samenwerking met Lars - waren erg nuttig en kunnen gebruikt worden voor publicatie. Zeer bedankt voor je nauwkeurige werken en het doorzettingsvermogen tijdens het afronden van je project. Ook ben ik erg dankbaar voor de inzet van Max, Nonne, Jochem van de Minkelis en Willem tijdens hun bachelorprojecten. De nieuwe inzichten en vele interessante resultaten waren erg nuttig voor deze thesis.

I would also like to thank my many desk neighbours: Mark, Jochem Wijten, Nynke, Nikos, Frank, Marisol, most of whom were replaced in the last months by Haissam, Daan, Franscesco and Shuang. Thank you for al the nice and funny conversations and discussions and for being the typical 'starting point' when for looking for information within the group. Your presence made the office routine at ICC fun and bearable during the past years.

Christa, Ilse, Lars, Laurens, Nynke wil ik graag bedanken voor de gezelligheid tijdens de tapas etentjes, verjaardagen en de andere uitjes tijdens onze PhD's en ook daarvoor. Lars en Laurens in het bijzonder bedankt dat jullie mijn paranimfen willen zijn. Also I would like to thank Carlos, Donglong, Hideto, Kang, Nynke, Lars, Luc, Miguel, Rolf, Xinwei for the occasional dinners, either with or without the Chinese chicken legs.

For all the good times during lunch breaks, coffee breaks, conferences, courses, barbeques, borrels, football games, bike rides, excursions, labuitjes, and other social activities, I would like to thank several people. Ana, Anne-Eva, Antonio, Baira, Bas, Beatriz, Carlos, Carolien, Caroline, Charlotte, Christa, Christia, Daan, Donglong, Egor, Erik, Fouad, Francesco, Frederique, Giorgio, Guusje, Haissam, Hebatalla, Hideto, Ilse, Ina, Iris, Javier, Jelle, Jeroen, Jessie, Jochem W, Joel, Johan, Joris Goetze, Joris Koek, Justine, JX, Kang, Katerina, Katinka, Koen, Lars, Laura B, Laura K, Laurens, Lennart, Lisette, Luc, Maarten, Manuel, Marjolein, Mark, Marianna, Martin, Matteo, Max, Micheal, Miguel, Nazila, Nienke, Nikos, Nynke, Oscar Brandt Corstius, Oscar Daoura, Peter Bramwell, Peter Ngene, Petra Keijzer, Rafael, Ramon, Remco, Robin Geitenbeek, Rolf, Romy, Roozbeh, Roxana, Roy, Sam, Sander, Savannah, Sebastian, Silvia, Sophie, Stanislav, Stijn, Suzan, Suzanne, Thomas, Tom, Ward, Wirawan, Wouter, Wouter, Xinwei, Yannick, Zoran and anyone else that I may have missed unintentionally.

Tot slot wil ik mijn zusje en mijn ouders bedanken. Jullie waren altijd heel geïnterresseerd in waar ik mee bezig was en ook een goed klankbord. Bedankt voor alle steun en de goede zorgen.

Curriculum Vitea

Jogchum Oenema was born on the 26th of September 1991 in Groningen. After finishing highschool (VWO) at the Zernike College in Haren, he started the bachelor Chemistry at Utrecht University in 2010. His bachelor thesis was entitled 'Oligomerisation of 4-Fluorostyrene in Zeolites: Correlation between Acidity, Framework Topology and Reaction Rate' and was performed under supervision of Hendrik van der Bij and prof. Bert Weckhuysen.

In 2013, he started his master 'Nanomaterials: Chemistry and Physics' in Utrecht. The master thesis project was performed in the group of Inorganic Chemistry and Catalysis under supervision of Thomas Eschemann and prof. Krijn de Jong, where the effect of noble metal promotion (Re, Ru, Ag, Pt) on titania supported cobalt catalysts for Fischer-Tropsch synthesis was investigated. The results of this project could be published in Catalysis Today. In addition, he performed a research project at the European Synchotron Research Facility in Grenoble under supervision of dr. Giovanni Agostini, dr. Sakura Pascarelli and prof. Frank de Groot.

In January 2016, he started a PhD project in the Inorganic Chemistry and Catalysis group under supervision of prof. Krijn de Jong and assistant prof. Jovana Zečević. His research focused on the location of Pt nanoparticles within Pt/zeolite/γ-alumina composite catalysts and its consequences for catalysis. Part of the work discussed in this thesis is published in peer-reviewed journals and was presented on national and international conferences. Besides scientific research, Jogchum taught practical courses to first year students and supervised several research projects of bachelor and master students. In his free time, he enjoys playing badminton, cycling, running and reading.